



TECHNISCHE
UNIVERSITÄT
DARMSTADT

Physik

Chiral Three-Nucleon Interactions in Ab-Initio Nuclear Structure and Reactions

Vom Fachbereich Physik
der Technischen Universität Darmstadt

zur Erlangung des Grades
eines Doktors der Naturwissenschaften
(Dr. rer. nat.)

genehmigte Dissertation von
Joachim Langhammer, M. Sc.
aus Groß-Umstadt

Darmstadt 2014

D 17

Referent	Prof. Dr. Robert Roth
Koreferent	Prof. Dr. Jochen Wambach
Tag der Einreichung	10. Februar 2014
Tag der Prüfung	23. April 2014

ABSTRACT

The prediction of nuclear structure and reaction observables based on nuclear Hamiltonians including two- and three-nucleon (NN+3N) interactions derived from chiral effective field theory constitutes a challenging task for ab-initio nuclear theory. In particular, the consistent inclusion of 3N interactions requires formal extensions of the many-body methods and, at the same time, causes a significant increase of the computational cost. This work presents the necessary steps for the inclusion and the subsequent application of 3N interactions in different ab-initio nuclear structure and reaction approaches.

The first part is dedicated to the preparation of the chiral nuclear forces before they enter the many-body methods. It addresses the similarity renormalization group (SRG) as a tool to soften the initial chiral interactions and its generalization to consistently include 3N interactions. Moreover, the technically important 3N matrix-element management in a convenient basis for the subsequent many-body methods including an efficient storage scheme is discussed. In addition, a possibility to derive approximative schemes for 3N interactions using normal ordering is presented.

In the second part the SRG-evolved chiral NN+3N Hamiltonians are applied in nuclear structure calculations using the importance truncated no-core shell model (IT-NCSM) as well as coupled-cluster theory. The impact of SRG-induced and chiral 3N interactions on ground-state energies and low-energy spectra of different p -shell nuclei is studied, including a sensitivity analysis concerning uncertainties of the chiral interactions in the ^{12}C and ^{10}B spectra. Furthermore, the first ab-initio study of even oxygen isotopes with explicit 3N interactions is presented, and by means of the normal-ordered two-body approximation the ground-state energy systematics of selected closed-shell nuclei throughout the calcium, nickel, and tin isotopic chains are obtained in qualitative agreement with experiment.

The third part of this work focuses on 3N interactions in ab-initio nuclear scattering approaches. This includes a detailed discussion of the inclusion of 3N interactions in the no-core shell model combined with the resonating-group method (NCSM/RGM) with emphasis on the ability to treat targets beyond the lightest nuclei. The extended formalism is then applied to nucleon- ^4He scattering, where the 3N interaction overall improves scattering phase shifts, differential cross sections and analyzing powers. Finally, the no-core shell model with continuum approach, which constitutes a unified ab-initio approach to bound and scattering states resulting from the combination of the NCSM and the NCSM/RGM, is generalized to 3N interactions and applied to the neutron- ^8Be system to study the impact of the continuum on the ^9Be energy levels. The results demonstrate the importance of the consistent treatment of continuum states.

ZUSAMMENFASSUNG

Ab-initio Vorhersagen von Kernstruktur- und Kernreaktionsobservablen, basierend auf Zwei- und Drei-Nukleonen (NN+3N) Wechselwirkungen hergeleitet aus chiraler effektiver Feldtheorie, stellen eine Herausforderung dar. Insbesondere die Berücksichtigung von 3N Wechselwirkungen verlangt formale Erweiterungen der Vielteilchenmethoden und erhöht den Rechenaufwand signifikant. Die vorliegende Arbeit befasst sich mit der Einbeziehung von 3N Wechselwirkungen in ab-initio Kernstruktur- und Kernreaktionsmethoden.

Der erste Teil der Arbeit diskutiert vorbereitende Schritte zur Einbeziehung der chiralen 3N Wechselwirkungen. Diese umfassen die technisch wichtige Handhabung von 3N Wechselwirkungsmatrixelementen in geeigneten Basen, sowie ein zugehöriges, effizientes Speicherschema. Desweiteren wird die Similarity Renormalization Group (SRG) Transformation zur Milderung der starken kurzreichweitigen Korrelationen mit konsistenter Berücksichtigung der 3N Wechselwirkungen diskutiert. Außerdem werden Näherungen der 3N Wechselwirkung im Rahmen des Formalismus der Normalordnung vorgestellt.

Der zweite Teil behandelt die Anwendung der SRG-transformierten chiralen NN+3N Wechselwirkungen in Kernstrukturechnungen mit Hilfe des Importance-Trunkierten No-Core Schalenmodells (IT-NCSM), sowie der Coupled-Cluster Theorie. Die Effekte von SRG-induzierten sowie von chiralen 3N Wechselwirkungen auf Grundzustands- und Anregungsenergien von Atomkernen der p -Schale, inklusive der Studie von Unsicherheiten der chiralen Wechselwirkungen in ^{12}C und ^{10}B Spektren, werden untersucht. Darüberhinaus werden erste ab-initio Berechnungen für Sauerstoffisotope gerader Massenzahl mit expliziten 3N Wechselwirkungen vorgestellt. Desweiteren zeigt die Systematik der Grundzustandsenergien für ausgewählte Atomkerne mit Schalenabschlüssen der Kalzium-, Nickel- und Zinn-Isotopenketten mit Berücksichtigung chiraler 3N Wechselwirkungen im Rahmen der Normalordnungsnäherung qualitative Übereinstimmung mit experimentellen Daten.

Im dritten Teil werden ab-initio Vorhersagen nuklearer Streuprozesse insbesondere mit Streuzentren jenseits der leichtesten Atomkerne behandelt. Die Einbeziehung von 3N Wechselwirkungen in die Kombination aus No-Core Schalenmodell und der Resonating Group Method (NCSM/RGM) wird im Detail diskutiert. Die anschließende Untersuchung von Nukleon- ^4He Streuung zeigt eine Verbesserung der Übereinstimmung von Streuphasen, differentiellen Wirkungsquerschnitten und Analysierstärken mit experimentellen Daten durch die 3N Wechselwirkung. Schließlich wird der Formalismus des No-Core Schalenmodells mit Kontinuum, eine Kombination von NCSM und NCSM/RGM, zur Berücksichtigung von 3N Wechselwirkungen erweitert. Die Anwendung auf Neutron- ^8Be demonstriert den Einfluss der konsistenten Beschreibung von Kontinuumszuständen anhand der ^9Be Energieniveaus.

CONTENTS

Abstract	iii
Zusammenfassung	v
Introduction	xi
I Chiral Nuclear Forces	1
Introduction to Part I	3
1 Chiral Effective Field Theory	5
1.1 The Chiral Nucleon-Nucleon Force up to N^3LO	10
1.2 The Three-Nucleon Force at N^2LO	11
2 Three-Nucleon Force Matrix Elements	17
2.1 Matrix Elements in the HO Jacobi Basis	18
2.2 Three-Nucleon Matrix Elements in the m -Scheme	20
2.2.1 Transformation of Jacobi Matrix Elements into the JT -Coupled Scheme	20
2.2.2 The Decoupling into m -Scheme Matrix Elements	23
2.2.3 Computational Aspects of the 3N Matrix-Element Handling	24
2.3 The Normal-Ordered Two-Body Approximation	29
2.3.1 Formalism	30
2.3.2 Normal-ordering Directly in the JT -Coupled Scheme	33
3 The Similarity Renormalization Group	37
3.1 General Formalism	38
3.2 Consistent Evolution of NN+3N Forces in Three-Body Space	41
3.3 The Frequency-Conversion Technique	44

II	Three-Nucleon Forces in Ab-Initio Nuclear Structure	47
Introduction to Part II		49
4	Many-Body Methods and their Extension to 3N Interactions	51
4.1	The No-Core Shell Model	52
4.2	The Importance Truncated No-Core Shell Model	55
4.3	Coupled-Cluster Theory for Ground-States	62
5	The Role of the SRG Model Space	67
5.1	Effects on Absolute Energies	68
5.2	Effects on Excitation Energies	70
6	Chiral 3N Forces in Ab-Initio Nuclear Structure of p-Shell Nuclei	73
6.1	Description of Ground-State Energies throughout the p -Shell	74
6.1.1	The Origin of SRG-Induced Multi-Nucleon Interactions	80
6.2	Nuclear Spectra with Chiral 3N Interactions	82
6.3	Chiral 3N Interactions with Reduced Cutoff	86
7	Sensitivity Analysis for Chiral Three-Nucleon Forces	91
8	Benchmark of the Normal-Ordered Two-Body Approximation	99
9	Ab-Initio Studies from Oxygen to Heavy Tin Isotopes	107
9.1	Even Oxygen Isotopes with Chiral NN+3N Interactions	107
9.2	Closed-Shell Nuclei up to ^{132}Sn with Chiral 3N Interactions	110
9.2.1	The SRG Model-Space — Revisited for Heavy Nuclei	111
9.2.2	Coupled-Cluster Model-Space Convergence	115
9.2.3	Iterative Normal Ordering for Large $E_{3\text{max}}$	116
9.2.4	HO Frequency Dependence	119
9.2.5	From ^{16}O to ^{132}Sn with Chiral Hamiltonians	119

III Three-Nucleon Forces in Ab-Initio Nuclear Reactions	125
Introduction to Part III	127
10 Generalities on Many-Body Scattering	129
11 The No-Core Shell Model / Resonating Group Method	137
11.1 General Formalism	138
11.2 The Norm and Hamiltonian Kernels	143
11.2.1 Derivation of the Kernels	143
11.2.2 Slater Determinant Channel States and Translational Invariant Kernels	148
11.2.3 Integration Kernels in the Slater Determinant Channel Basis	151
11.2.4 Summary of Kernels — Coupled vs. Uncoupled Densities	159
11.2.5 Implementation Details	163
12 The <i>R</i>-Matrix Theory	167
12.1 Calculation of the <i>R</i> -Matrix for Single-Channel Problems	167
12.2 The Calculable <i>R</i> -Matrix in Multi-Channel Scattering	174
12.3 <i>R</i> -Matrix Theory on a Lagrange Mesh	177
13 Nucleon-⁴He Scattering	181
13.1 Convergence Studies of Scattering Phase Shifts	182
13.1.1 Dependence on the Model-Space Truncation N_{\max}	182
13.1.2 Dependence on $E_{3\max}$	183
13.1.3 Dependence on the HO Frequency	184
13.1.4 Dependence on the Number of Excitations of the ⁴ He Target	184
13.1.5 Relevance of Discarded SRG-Induced Multi-Nucleon Forces	186
13.1.6 Benchmark of the Isospin Treatment	187
13.2 Three-Nucleon Force Effects on Scattering Phase Shifts	189
13.3 Cross Sections and Analyzing Powers	192
14 No-Core Shell Model with Continuum	197
14.1 Formalism	198
14.2 Ab-Initio Description of ⁹ Be via n- ⁸ Be Scattering	200
14.2.1 Monitoring the IT-NCSM Inputs in the NCSMC	201
14.2.2 Model-Space Convergence	203
14.2.3 Dependence on the SRG Flow Parameter	205
14.2.4 3N-force Effects on n- ⁸ Be Scattering Phase Shifts	207
14.2.5 Impact of the Continuum on the ⁹ Be Spectrum	208
Summary and Outlook	213

Appendices	217
A High-Order Padé-Resumed Many-Body Perturbation Theory	219
B Binary-Cluster Jacobi Coordinates	229
C List of Publications	231
References	235

INTRODUCTION

The scientific picture of atoms has been revolutionized in the early 20th century by a number of seminal experiments. Among these is the discovery of the atomic nucleus by scattering α particles off gold atoms by Ernest Rutherford in 1910 [1, 2]. Moreover, in 1919 he succeeded to accomplish the first man-made nuclear reaction by disintegrating nitrogen into protons and oxygen by bombardment with α particles [2]. In 1932 James Chadwick proved the existence of neutrons [3, 4, 5] that, together with the protons, build the atomic nucleus. Furthermore, it was realized that properties of atomic nuclei and nuclear reactions are crucial for the formation of the chemical elements in stars leading to the theory of nucleosynthesis in 1957 [6].

The quest for a fundamental understanding of nuclear properties and nuclear reactions and their potential consequences for astrophysics motivates the development of a universal theoretical framework for the description of nuclear systems. A crucial ingredient to the description of atomic nuclei built of nucleons, i.e. protons and neutrons, as quantum many-body system is the nuclear interaction. A seminal step towards the theoretical description of the nuclear interaction was the idea of Yukawa in 1935 to identify pions as mediators of the interaction between the nucleons [7]. Inspired by this approach a number of nuclear potentials also involving exchanges of heavier mesons have been developed and are successfully applied even until today [8, 9, 10].

However, over the past decade a paradigm shift to exploit a link to low-energy Quantum Chromodynamics (QCD) occurred. The latter is the underlying theory of nuclear physics describing the strong interaction between quarks and gluons as the fundamental degrees of freedom. The fact that QCD is confining for energies relevant in nuclear structure and low-energy reactions causes the failure of perturbative approaches to low-energy QCD [11, 12]. Therefore, one resorts to effective theories valid for the energies of interest in nuclear physics and with a firm inherent link to low-energy QCD. Currently, the most systematic approach in this respect is the so-called chiral effective field theory (EFT) that employs nucleons and pions as relevant degrees of freedom and additionally respects the symmetries of QCD, in particular the spontaneously broken chiral symmetry [13, 14, 15]. As a result it provides a systematic expansion of the nuclear two-, three- and multi-nucleon interactions and also current operators consistently in the framework of chiral perturbation theory [16, 17, 18].

Theoretical nuclear physics is then confronted with the challenge to exploit this link to low-energy QCD via chiral EFT Hamiltonians to arrive at rigorous and quantitative predictions of structural properties as well as of scattering and reaction observables of nuclei. Additionally, this is important to constrain, validate, and ideally also to optimize the chiral

nuclear forces on the basis of direct comparisons to experimental data. Accordingly, versatile methods to solve the many-body Schrödinger equation starting from a given Hamiltonian without any conceptual or uncontrolled approximations are essential. Such methods are typically referred to as *ab-initio* approaches. It follows from the definition above that one prerequisite to classify a method as 'ab initio' is the possibility to estimate and improve on the remaining uncertainties. Pioneering ab-initio calculations beyond the ${}^4\text{He}$ nucleus used the Green's function Monte Carlo approach [19, 20, 21], and since then ab-initio nuclear theory has made great progress. While the typical limit for ab-initio studies was located in mid- p -shell nuclei about ten years ago [22, 23, 24, 25, 26], in recent years active developments towards ab-initio methods applicable to medium-mass or even heavy nuclei and also to nuclear reactions have either extended existing many-body methods as, e.g., the importance-truncated extension of the no-core shell model [27, 28] or coupled-cluster theory [29], or have brought about new ab-initio methods. Among the latter are, e.g., self-consistent Green's function methods [30, 31], the (multi-reference) in-medium similarity renormalization group [32, 33, 34] or the nuclear lattice effective field theory [35, 36].

Precise results from various ab-initio methods have shown that for calculations using only two-nucleon (NN) interactions, often discrepancies to experimental data remain, even in the domain of light nuclei [24]. These issues have been traced back to the lack of three-nucleon (3N) interactions in the nuclear Hamiltonian. Prominent examples are the ground-state of ${}^{10}\text{B}$ [37], the nucleon-deuteron analyzing power [38], or the position of the neutron drip line in the oxygen isotopic chain [34]. Furthermore, in order to exploit the connection to the underlying physics of low-energy QCD using the nuclear forces derived via chiral EFT it is indispensable to consistently include the chiral 3N interactions at all stages of the calculations. It is a clear advantage of the chiral EFT that NN, 3N, and also multi-nucleon forces emerge consistently within the same framework. Hence, there is no principle choice about which 3N interaction to adopt along with which two-nucleon interaction as it is the case, e.g., for the combination of the more phenomenological Argonne V18 [8] or CD Bonn [9] NN interactions with the Tucson Melbourne or Urbana IX 3N interaction models [39].

However, the inclusion of 3N interactions into the different ab-initio techniques poses a supreme challenge. On the one hand the many-body methods need to be adapted to incorporate 3N interactions, on the other hand the computational cost typically increases significantly. Nuclear structure calculations of p -shell nuclei with explicit 3N interactions are currently possible with the Green's function Monte Carlo approach [24], the no-core shell model [40, 41] and its importance-truncated extension [42, 43, 44], coupled-cluster theory [45, 46], and nuclear lattice effective field theory [36] (for nuclei build of α -clusters), where only the latter four can use the non-local chiral EFT Hamiltonians. For ab-initio predictions of nuclear reactions the inclusion of explicit chiral 3N interactions into scattering processes involving more than four nucleons has been achieved only recently in the no-core shell model combined with the resonating group method [47, 48] and the no-core shell model with continuum [49, 50] approaches, and has been developed as part of this work [51]. The self-consistent Green's function as well as the (multi-reference) in-medium

similarity renormalization group resort to an approximate treatment of 3N interactions, which is of course also vitally important provided a solid validation of the accuracy of the used approximation.

In this work we apply the currently most advanced chiral NN+3N Hamiltonians available in terms of matrix elements in ab-initio nuclear structure throughout the p shell using the importance-truncated no-core shell model (IT-NCSM) and for ground-state energies up to heavy nuclei in the tin isotopic chain with the coupled-cluster (CC) method. Furthermore, we investigate effects of the chiral 3N interactions in ab-initio nucleon-nucleus scattering in the no-core shell model combined with the resonating group method and finally in the recently proposed no-core shell model with continuum that represents an ab-initio approach treating bound and scattering states on equal footing. For clarity we split this work into three main parts: Part I covers the chiral nuclear forces with focus on the necessary techniques to prepare the chiral Hamiltonians before they can enter the many-body calculations. This includes innovative strategies for the matrix-element handling of the 3N interactions, and the discussion of consistent similarity renormalization group (SRG) transformations [52] of the chiral NN+3N Hamiltonians, which is necessary to soften of the interactions to facilitate calculations with improved model-space convergence. Part II is dedicated to the application of the SRG-evolved chiral NN+3N Hamiltonians to ab-initio nuclear structure calculations with particular attention to the effects of SRG-induced and chiral 3N interactions on ground-state energies and excitation spectra, where we employ the IT-NCSM and CC approaches. The techniques presented in Part I permit to perform calculations for p -shell nuclei including 3N interactions in unprecedentedly large model spaces and precise enough to carry out first sensitivity analyses with respect to uncertainties of the chiral 3N interactions in spectra of p -shell nuclei. Furthermore, in combination with the so-called normal-ordered two-body approximation, which we prove to be accurate, we extend ab-initio studies to ground-state energies of selected nuclei with closed sub-shells up to ^{132}Sn , and explore the predictions of current ab-initio methods using chiral NN+3N Hamiltonians for the domain of heavy nuclei including a comprehensive uncertainty analysis. In Part III we concentrate on the ab-initio treatment of nuclear reactions with special emphasis on the inclusion of chiral 3N interactions. We present in detail the formalism to include 3N interactions into the no-core shell model combined with the resonating group method (NCSM/RGM) for nucleon-nucleus reactions. This paves the way for validations of the chiral NN+3N Hamiltonians also in context of scattering observables. After a brief discussion of R -matrix theory we apply the extended formalism to nucleon- ^4He scattering. Finally, we investigate 3N force effects in neutron- ^8Be scattering using the no-core shell model with continuum (NCSMC) approach that is able to describe bound and scattering states on equal footing. The former developments for the NCSM/RGM are crucial for the inclusion of 3N interactions into the NCSMC. If continuum effects are important this method exhibits a superior model-space convergence compared to both, the (IT-)NCSM and the NCSM/RGM approach.

Finally, we provide a brief summary and outlook on remaining challenges and future directions. In the appendices we discuss another promising many-body method based on

Padé-resumed high-order degenerate perturbation theory, so far applied with NN interactions only.

For a more detailed overview of the contents of the three parts please see their respective introductions on pages 3, 49, and 127.

Part I

Chiral Nuclear Forces

INTRODUCTION TO PART I

Chiral effective field theory currently provides the most systematic approach to nuclear forces based on low-energy QCD. It derives two-, three- and multi-nucleon interactions consistently within the same framework in a hierarchic manner and allows for predictions of nuclear structure and reaction observables rooted in QCD [17, 18].

Most many-body methods, in particular those we apply throughout this work, require matrix elements of the nuclear interaction with respect to a convenient basis. The most advanced chiral Hamiltonian available in terms of matrix elements suitable for calculations of finite nuclei consists of two-nucleon (NN) interactions up to next-to-next-to-next-to-leading order (N³LO) and three-nucleon (3N) interactions at next-to-next-to-leading order (N²LO) of chiral perturbation theory. However, before these matrix elements enter the different many-body methods, typically a number of manipulations are necessary in order to cast them into a more convenient form. While such procedures for NN interactions are used routinely, the 3N interactions pose a number of additional challenges, whose resolutions are crucial for the proper inclusion of the 3N interaction at all stages of the calculations. In this first part we address all relevant preparatory steps concerning the chiral 3N interactions for their applications in different nuclear structure and reaction scenarios in the Parts II and III.

We start with a brief summary of the basic concepts of chiral effective field theory and introduce the NN interaction at N³LO and 3N interaction at N²LO used throughout this thesis. In particular we discuss how the low-energy constants of the chiral 3N interactions are constrained by experiment.

Section 2 is dedicated to different aspects of the 3N matrix-element management. This includes the discussion of 3N matrix elements in the so-called Jacobi HO basis that build our starting point. Then we discuss how we arrive at 3N matrix elements in the m -scheme that are convenient for the calculations later on. As the number of 3N m -scheme matrix elements quickly becomes prohibitive we introduce the so-called JT -coupled matrix element scheme and give details about this scheme including its computational realization. Afterwards, we discuss how approximative schemes of the 3N interaction can be derived using the procedure of normal ordering.

It is a well-known fact that realistic nuclear interactions induce significant correlations in the eigenstates of atomic nuclei that need to be tamed in order to facilitate the convergence of many-body calculations. Different methods to achieve this exist and for the scope of this work we adopt the similarity renormalization group (SRG). In Section 3 we discuss the foundations of the SRG approach and focus on the consistent inclusion of 3N interactions in its framework.

SECTION 1

Chiral Effective Field Theory

A decisive input when aiming at the microscopic description and prediction of properties of the structure or collisions of nuclear many-body systems is the interaction between the constituents. In the context of atomic nuclei these constituents are protons and neutrons. However, they themselves consist of quarks and gluons, which are the fundamental degrees of freedom of the strong interaction within the Standard Model of particle physics. The underlying theory of the strong interaction is quantum chromodynamics (QCD), which has been formulated in the 1980s and is nowadays generally accepted for the description of interacting quarks and gluons. As a result, one should in principle be able to deduce nuclear properties and processes or at least the interaction between nucleons directly from QCD. However, this poses a formidable task hardly feasible in a comprehensive manner, as we discuss in the following. Afterwards, we present the basic concepts and steps towards the derivation of nuclear interactions in a systematic fashion within the so-called chiral effective field theory (EFT) approach, while maintaining the key features of low-energy QCD.

Since QCD is a field theory, it is formulated in terms of a Lagrangian density which is given by

$$\mathcal{L}_{\text{QCD}} = \bar{q}(i\gamma^\mu \mathcal{D}_\mu - \mathcal{M})q - \frac{1}{4} \mathcal{G}_{\mu\nu,a} \mathcal{G}_a^{\mu\nu}, \quad (1.1)$$

where we denote with q and \mathcal{M} the quark fields and the quark-mass matrix, respectively. Moreover, the covariant derivative is given by

$$\mathcal{D}_\mu = \partial_\mu - i g_s \frac{\lambda_a}{2} \mathcal{A}_{\mu,a}, \quad (1.2)$$

with the Gell-Mann matrices λ_a and the gluon fields $\mathcal{A}_{\nu,a}$. The Gluon field-strength tensor can be expressed as

$$\mathcal{G}_{\mu\nu,a} = \partial_\mu \mathcal{A}_{\nu,a} - \partial_\nu \mathcal{A}_{\mu,a} + g_s f_{abc} \mathcal{A}_{\mu,b} \mathcal{A}_{\nu,c}, \quad (1.3)$$

with the $SU(3)$ structure constants f_{abc} . The quantity describing the strength of the coupling of quarks and gluons is denoted by g_s . This coupling varies as function of momentum transfer and accordingly with energy: it has been found to be strong for low momentum transfers or low energies and is responsible for the confinement of quarks and gluons into colorless hadrons, whereas it becomes weak for high momentum transfers, i.e., at high energies, which is also referred to as asymptotic freedom [11, 12, 53]. This behavior leads to the fact that a perturbative treatment of QCD is meaningful at high energies only, which is opposite, e.g., to the running coupling of quantum electrodynamics. The relevant energy range of typical nuclear properties and processes we are interested in corresponds to the low-energy regime of QCD, i.e., the coupling constant is large and in particular $g_s \approx 1$. Consequently, a perturbative expansion of nuclear processes in terms of Feynman diagrams, which is equivalent to a power series in terms of the coupling constant, is non-convergent. Nevertheless, there are ongoing attempts to non-perturbatively extract information about nuclear systems directly from QCD treated numerically using a discretization over an Euclidean space-time grid, generally referred to as lattice QCD (LQCD) [54, 55]. The idea is to obtain, e.g., low-lying hadron masses and binding energies of light nuclei from the evaluation of the Feynman path-integral formalism on the lattice using Monte Carlo techniques [56, 57], and first attempts to derive the nuclear interaction [58, 59]. Besides statistical errors, LQCD encounters also systematic errors due to the finite volume of the lattice, due to the finite lattice spacing which is typically about 0.1 fm, and from the complication that the small physical up and down quark masses nowadays often cannot be simulated on the lattice [60]. Hence, the final results need to be obtained from extrapolations to infinite volume, to vanishing lattice spacing and to the physical quark masses. The reduction of these errors is directly linked to the available computational resources, which are exploited at their limits for the presently completed calculations. Although more sophisticated LQCD approaches are subject to current research [54, 55, 57] and supercomputers are approaching exa-scale computing capabilities, the expensive LQCD calculations cannot be done for the variety of nuclei and nuclear properties of interest in the foreseeable future. Nevertheless, LQCD is a valuable tool to cross-check issues of particular importance in few-nucleon systems [54], but for the description of nuclei and nuclear collisions beyond the few-body domain, which is the task we focus on in this thesis, we have to resort to an alternative approach that we cover in the remainder of this section and that delivers the nuclear interactions we apply throughout this work.

The intention is to develop an effective field theory valid in the low-energy regime of QCD, namely the regime where nuclear processes take place and can be considered as interactions between nucleons rather than resolving the complex dynamics of quarks and gluons. In a first step one needs to determine the relevant degrees of freedom that should be taken into account. At energy scales well below the pion mass it is possible to consider nucleons as degrees of freedom only, which results in the so-called pion-less effective field theory (see, e.g., [61]). However, if the nucleon energies are close to or above the pion mass, which is the case for the energies of interest for the different applications throughout this work, it becomes necessary to include the pions as explicit degrees of freedom. Thus,

one adopts nucleons and pions as relevant degrees of freedom, which is in line with the idea proposed in 1935 by Yukawa to describe the nucleon-nucleon interaction in terms of pion exchanges [7]. However, at the same time it is crucial to maintain a firm link to the underlying theory, i.e., QCD. This is possible by formulating the most general Lagrangian that reflects all symmetries of QCD but with nucleons and pions as the effective degrees of freedom, as discussed in the seminal papers [62, 13, 14, 15] by Weinberg. It was realized that in particular the so-called chiral symmetry plays an important role. This is a symmetry of the QCD Lagrangian in the limit of vanishing quark masses that can be rewritten in terms of left- and right-handed quark fields as

$$\mathcal{L}_{\text{QCD},0} = \bar{q}_L i \gamma^\mu \mathcal{D}_\mu q_L + \bar{q}_R i \gamma^\mu \mathcal{D}_\mu q_R - \frac{1}{4} \mathcal{G}_{\mu\nu,a} \mathcal{G}_a^{\mu\nu}, \quad (1.4)$$

where $q_R = \frac{1}{2}(1 + \gamma_5)q$ and $q_L = \frac{1}{2}(1 - \gamma_5)q$. One can show that this Lagrangian obeys the chiral symmetry, i.e., $SU(2)_R \times SU(2)_L$ symmetry, which corresponds to invariance under the unitary transformations

$$q_R = \begin{pmatrix} u_R \\ d_R \end{pmatrix} \longrightarrow e^{-i\vec{\Theta}^R \cdot \frac{\vec{\tau}}{2}} \begin{pmatrix} u_R \\ d_R \end{pmatrix} \quad (1.5)$$

$$q_L = \begin{pmatrix} u_L \\ d_L \end{pmatrix} \longrightarrow e^{-i\vec{\Theta}^L \cdot \frac{\vec{\tau}}{2}} \begin{pmatrix} u_L \\ d_L \end{pmatrix}. \quad (1.6)$$

Here, the quarks are restricted to up and down quarks, and the $\vec{\tau}$ denotes a vector containing the representation of the isospin operators as Pauli matrices. As consequence of this symmetry, Noethers theorem [63] predicts the existence of six conserved current densities, which can be divided into three vector and three axial-vector current densities. The three vector current densities can be assigned to isospin symmetry of the Lagrangian $\mathcal{L}_{\text{QCD},0}$, which is in accordance with the observation of approximately mass-degenerate isospin multiplets, e.g., the ρ^\pm and ρ^0 mesons. On the contrary, a signature of the conserved axial vector current densities cannot be identified in the hadron spectrum. This is evidence for a spontaneous breaking of the chiral symmetry, that is, the ground state of the system does not reflect the symmetry of the Lagrangian describing the system. Then, the Goldstone theorem postulates for each spontaneously broken symmetry a massless pseudo-scalar boson, also referred to as Goldstone boson [64, 65]. The Goldstone bosons assigned with the spontaneous breaking of the chiral symmetry of Lagrangian (1.4) are the pions π^\pm and π^0 . Of course, physical pions are not massless but acquire a mass of approximately $140 \text{ MeV}/c^2$. This is due to occurrence of the non-zero quark masses in the QCD Lagrangian which causes the explicit breaking of the chiral symmetry, i.e., the Lagrangian (1.1) is not invariant under the transformations (1.5) and (1.6). However, the up- and down-quark masses are small compared to typical hadron masses which are larger than $700 \text{ MeV}/c^2$. Therefore, chiral symmetry is formally broken explicitly but can still be interpreted as approximate symmetry of low-energy QCD, whose spontaneous breaking reasons the small mass of the pions in comparison to other hadrons which are no Gold-

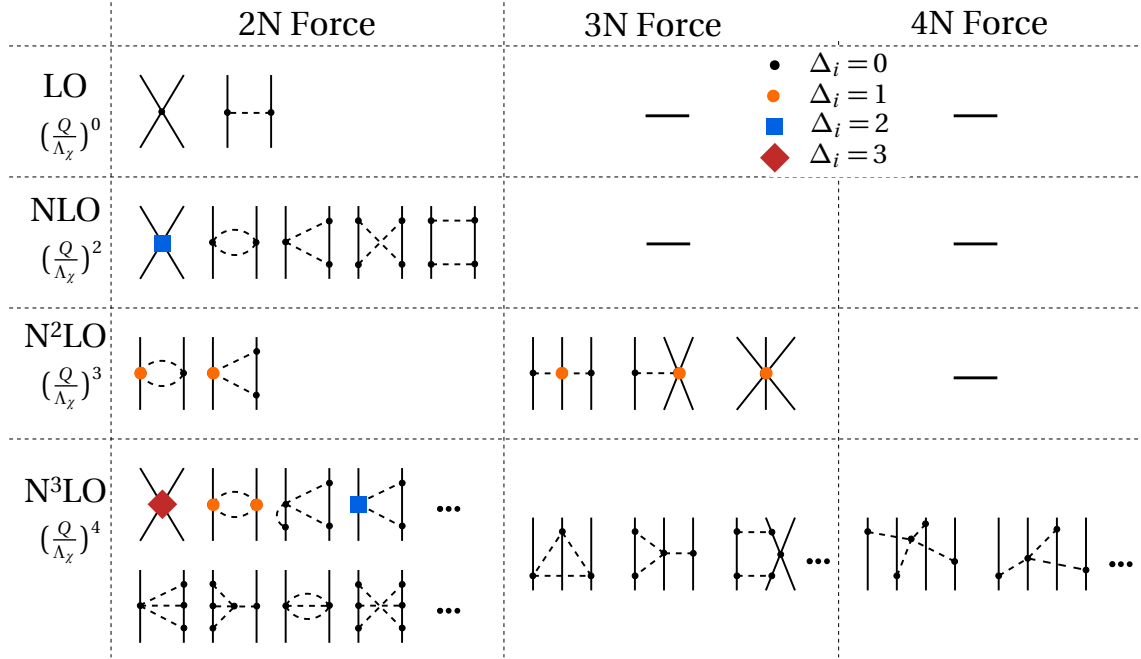


Figure 1.1 – Diagrams contributing to the nuclear interactions from chiral EFT at different orders of the expansion parameter $\frac{Q}{\Lambda_\chi}$. Solid lines represent nucleons and dashed lines denote pions. Figure adapted from [66].

stone bosons.¹ We note that also the isospin symmetry is broken due to the difference of the non-vanishing masses of the up and down quarks, which results in the small mass differences between the pions and likewise between neutrons and protons.

Having identified the important (broken) symmetries of QCD, one is left with the construction of the most general Lagrangian with nucleons and pions as effective degrees of freedom consistent with these symmetries, in particular with the (spontaneously) broken chiral symmetry. This has been accomplished first by Weinberg in Refs. [13, 14]. The effective Lagrangian may be written as

$$\mathcal{L}_{\text{eff}} = \mathcal{L}_{\pi\pi} + \mathcal{L}_{\pi N} + \mathcal{L}_{NN} + \mathcal{L}_{\pi\pi N} + \mathcal{L}_{\pi NN} + \mathcal{L}_{NNN} + \dots, \quad (1.7)$$

where each Lagrangian including pions contains an infinite number of terms. They are typically ordered in terms of the so-called interaction index Δ_i for vertex i

$$\Delta_i = d_i + \frac{n_i}{2} - 2, \quad (1.8)$$

where d_i denotes the number of derivatives, and n_i the number of nucleon fields. It can be shown that $\Delta_i \geq 0$ holds, because for NN contact interactions there are at least 4 nucleon fields. Nucleon-pion interactions enter with one derivative due to the Goldstone boson nature of the pion and there are at least two nucleon fields, and pion-pion interactions have at least two derivatives [17]. However, each of the Lagrangians ordered with increas-

¹If one also allows strange quarks in the QCD Lagrangian in the chiral limit, one finds eight Goldstone bosons, which are identified with the pions, kaons and eta particles [17].

ing interaction index Δ_i still contains infinitely many terms. Hence, one needs a measure of the importance of the individual diagrams contributing to scattering matrix elements. This can be achieved by an expansion in powers of $\frac{Q}{\Lambda_\chi}$ with a generic momentum Q of the order of the pion mass and the so-called chiral-symmetry breakdown scale $\Lambda_\chi \sim m_\rho$, which makes $\frac{Q}{\Lambda_\chi}$ a small quantity. The ordering of terms according to this expansion is accomplished using the so-called Weinberg power counting, which determines the exponent of the expansion parameter by

$$\nu = -4 + 2A + 2L + \sum_i \Delta_i \quad (1.9)$$

with i summed over all vertices of a connected diagram. In addition, A denotes the number of nucleons and L the number of loops. For a specific exponent ν , the number of diagrams contributing to the nuclear interaction is finite, and, furthermore, the importance of contributions with larger ν should decrease. A diagrammatic representation of the contributions to the nuclear interaction ordered in terms of powers ν is shown in Figure 1.1. Leading-order (LO) diagrams correspond to $(\frac{Q}{\Lambda_\chi})^{\nu=0}$, next-to-leading-order (NLO) contributions have $\nu = 2$, because all contributions for $\nu = 1$ vanish by parity or time-reversal symmetry arguments. Then, next-to-next-to-leading-order diagrams (N²LO) have $\nu = 3$ and next-to-next-to-next-to-leading-order contributions (N³LO) correspond to $\nu = 4$. In particular, Figure 1.1 illustrates the expected hierarchy of nuclear forces, that is NN interactions should be more important than three-nucleon (3N) interactions, which in turn should be more important than four-nucleon (4N) forces, and so on. This is of course a consequence of the Weinberg power-counting scheme (1.9): diagrams without loops and with vanishing interaction indices and including two nucleons can contribute at $\nu = 0$, while three-nucleon forces may contribute first at $\nu = 2$, as is evident from plugging $A = 3$ into Eq. (1.9). However, it has been shown that the 3N contributions at NLO vanish [15]. Hence, the leading 3N interactions contribute at N²LO only, and, therefore, their effects should be small compared to the NN interaction. Evaluation of the power-counting scheme for $A = 4$ reveals that leading 4N forces start contributing at N³LO.

Additionally, we note that chiral EFT provides a systematic expansion of electromagnetic and weak meson-exchange current operators consistently within the same framework [67, 68]. Although, we do not further investigate these current operators in this work it will be interesting to see their impact in calculations, e.g., of radii and electromagnetic transitions in future studies. Results from GFMC calculations using the Argonne V18 potential along with chiral meson-exchange currents can be found in Ref. [10].

Altogether, chiral effective field theory provides nuclear forces in a hierarchic manner by means of a systematic expansion in powers of $\frac{Q}{\Lambda_\chi}$, which are in addition solidly rooted in QCD through the consistency with its symmetries, in particular the chiral symmetry and its spontaneous breaking. Furthermore, NN, 3N, and multi-nucleon forces are treated on equal footing since the theory naturally predicts the 3N forces that should be used along with the chiral NN interaction. Nowadays, chiral NN forces are routinely used in different approaches for studies of many-nucleon systems. On the other hand, considerations

of chiral 3N interactions in context of different many-body approaches have become accessible over the past few years only. This is due to the fact that matrix elements of the nuclear interaction with respect to harmonic-oscillator (HO) bases are necessary, whose computation in large enough sets and their handling in the many-body calculations is significantly more demanding than for NN interactions. Currently, partial-wave decomposed momentum-basis matrix elements of the chiral NN interaction are available up to $N^3\text{LO}$ and up to $N^2\text{LO}$ for the 3N interaction which can then be transformed into the HO basis. We have developed the required techniques to handle also large sets of 3N matrix elements, which is the focus of Section 2. Prior to this, in the following two subsections, we discuss further general aspects of the chiral NN interaction at $N^3\text{LO}$ and the 3N interactions at $N^2\text{LO}$ which we apply and study throughout this thesis.

1.1 The Chiral Nucleon-Nucleon Force up to $N^3\text{LO}$

As can be seen from Figure 1.1 the NN interactions are given by NN contact terms and pion-exchange contributions. The LO contributions are given by two momentum-independent contact interactions and a one-pion-exchange (OPE) diagram. Due to the OPE contribution the tensor force appears already at LO, which is known to be essential, e.g., for the correct description of the deuteron. The contact interactions come with a so-called low-energy constant (LEC) each, which incorporate the short-range behavior of the interactions which may be mediated by heavy mesons that have been 'integrated out' by choosing pions as only degrees of freedom. Thus, these unknown constants are fitted to experimental data in particular to nucleon-nucleon scattering phase shifts to fix the short-range behavior of the nuclear potential. Contact terms can contribute only in LO, NLO and $N^3\text{LO}$ due to parity symmetry. Altogether, 24 such contact terms enter up to $N^3\text{LO}$ with according LECs, and play a crucial role for the renormalization of the chiral EFT [17]. The NLO contributions yield lots of spin-isospin structures that are known to be important from more phenomenological realistic interactions. At $N^2\text{LO}$, seven contact terms, and the $\Delta_i = 3$ pion-pion vertices are present, which are due to intermediate contributions of the $\Delta(1232)$ -isobar that also has been integrated out. Hence, these kind of vertices have also LECs attached which can be determined from NN or πN scattering data. Finally, at $N^3\text{LO}$ quadratic spin-orbit forces contribute and 15 new contact terms with according LECs are encountered. It was found that in particular these contact terms, i.e., NN interactions up to fourth order are mandatory to fit the NN scattering phase shifts with comparable quality as the more phenomenological realistic interactions, i.e., to obtain $\chi^2/\text{datum} \approx 1$ [69, 70]. The pion-exchange contributions depend on the axial-vector coupling constant $g_A = 1.29$, and the pion-decay constant $F_\pi = 92.4\text{MeV}$, and eight additional LECs. The first chiral NN potential at $N^3\text{LO}$ has been developed by Entem and Machleidt, which is also the NN interaction we will use in all applications throughout this work [71]. The details of the fitting procedure including a detailed discussion of the nucleon-nucleon phase shifts is described in Ref. [71]. We note that this NN potential includes charge dependence, which is important for the accurate fit of np, nn and pp phase shifts [71]. Moreover, in practical

applications of this potential it needs to be multiplied with a regulator function to avoid diverging integrals. This regulator function is chosen as [71]

$$f^{\text{NN}}(p', p) = e^{-\left(\frac{p'}{\Lambda}\right)^{2n} - \left(\frac{p}{\Lambda}\right)^{2n}}, \quad (1.10)$$

with p and p' as magnitude of the initial and final relative nucleon momenta, respectively. The parameter n is chosen such that the order of powers $\left(\frac{Q}{\Lambda}\right)^v$ generated by the exponentials are beyond N³LO. The cutoff momentum for the NN interaction we use throughout this work is $\Lambda = 500 \text{ MeV}/c$.

1.2 The Three-Nucleon Force at N²LO

As already mentioned above, the leading 3N interaction within the framework of chiral EFT appears at N²LO. It is evident from the power-counting scheme (1.9) that at this order only diagrams without loops but with one vertex with interaction index $\Delta_i = 1$ contribute. The corresponding diagrams, which first have been derived by van Kolck [16], can be seen in Fig. 1.1. We discuss them from left to right: the first contribution is a two-pion exchange (2PE) diagram, which resembles the Fujita-Miyazawa term that provided a first estimate of three-body force effects already in 1957 [72], of course disconnected from the chiral EFT efforts over the past two decades. Mathematically, the 2PE diagram is given by

$$\hat{V}_{2\text{PE}} = \sum_{i \neq j \neq k} \frac{1}{2} \left(\frac{g_A}{2F_\pi} \right)^2 \frac{(\hat{\sigma}_i \cdot \vec{q}_i)(\hat{\sigma}_j \cdot \vec{q}_j)}{(\vec{q}_i^2 + M_\pi^2)(\vec{q}_j^2 + M_\pi^2)} \hat{F}_{ijk}^{\alpha\beta} \hat{\tau}_i^\alpha \hat{\tau}_j^\beta \quad (1.11)$$

$$\hat{F}_{ijk}^{\alpha\beta} = \delta^{\alpha\beta} \left[-\frac{4c_1 M_\pi^2}{F_\pi^2} + \frac{2c_3}{F_\pi^2} \vec{q}_i \cdot \vec{q}_j \right] + \sum_\gamma \frac{c_4}{F_\pi^2} \epsilon^{\alpha\beta\gamma} \hat{\tau}_k^\gamma \hat{\sigma}_k \cdot [\vec{q}_i \times \vec{q}_j],$$

with $\hat{\sigma}$ and $\hat{\tau}$ as spin and isospin operators, respectively. Note that we adopt the notation of Ref. [73] in the mathematical expressions, which are matrix elements with respect to the nucleon momenta but operators with respect to spin and isospin. The momenta $\vec{q}_i = \vec{p}'_i - \vec{p}_i$ are the momentum transfers of nucleon i with \vec{p}_i and \vec{p}'_i as initial and final momenta. In the 2PE no new LECs are encountered, because the constants c_1 , c_3 and c_4 , or c_i for short, are already present in the πN vertices of NN interaction and are fixed during the fitting procedure of the NN interaction. However, we note that quite different values for the c_i constants can be obtained from different fits, which motivates a sensitivity study of 3N force effects on different LEC combinations. We will present such studies based on nuclear spectra of p -shell nuclei in Section 7. The second diagram is given by the two-nucleon contact one-pion exchange (OPE) term by the expression

$$\hat{V}_{\text{OPE}} = - \sum_{i \neq j \neq k} \frac{g_A}{8F_\pi^2} \frac{c_D}{F_\pi^2 \Lambda_\chi} \frac{\hat{\sigma}_j \cdot \vec{q}_j}{\vec{q}_j^2 + M_\pi^2} (\hat{\tau}_i \cdot \hat{\tau}_j) (\hat{\sigma}_i \cdot \vec{q}_j) \quad (1.12)$$

accompanied with the new LEC c_D arising from the two-nucleon contact. The three-nucleon contact diagram completes the 3N interaction at this order and contributes an-

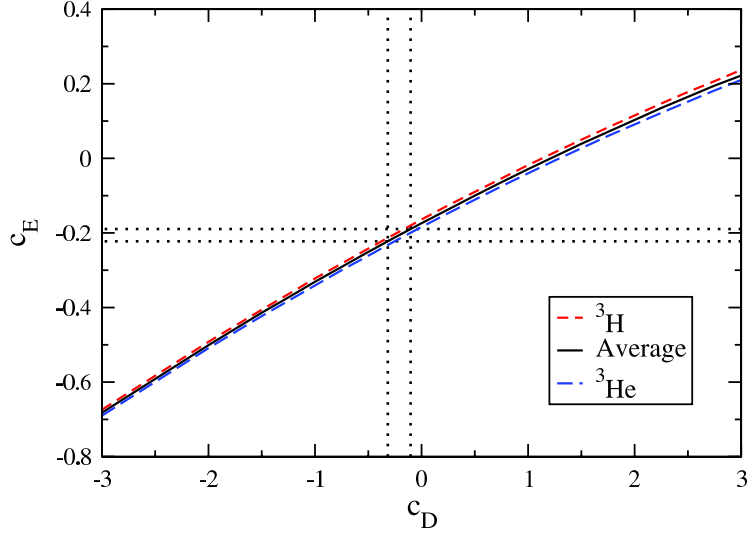


Figure 1.2 – Shown are trajectories in the c_D - c_E -parameter space reproducing the binding energies of ${}^3\text{H}$ and ${}^3\text{He}$ and their average. In addition, the vertical dotted black lines denote the parameter range of c_D for which the β -decay half-life of ${}^3\text{H}$ is reproduced. The intersections of the dotted and solid black lines define the values for LECs c_D and c_E of the 3N interaction at N²LO. Plot taken from [76].

other LEC, c_E , and reads mathematically

$$\hat{V}_{\text{cont}} = \frac{1}{2} \sum_{j \neq k} \frac{c_E}{F_\pi^4 \Lambda_\chi} (\hat{\tau}_j \cdot \hat{\tau}_k). \quad (1.13)$$

We note that throughout this thesis we use 3N interactions that have been regularized by means of a regulator function formulated in terms of the momentum transfer of the nucleons

$$f^{3\text{N}}(\vec{p}'_i - \vec{p}_i) = e^{-\frac{(\vec{p}'_i - \vec{p}_i)^4}{\Lambda_{3\text{N}}^4}}, \quad (1.14)$$

which leads to a local interaction as introduced in Ref. [74], where we denote the cutoff momentum of the 3N interaction as $\Lambda_{3\text{N}}$. Again, the power of the exponent has been chosen such that the order at which the calculations are conducted is smaller than the powers formally generated by the exponential. Finally, we note that we adopt a charge-symmetric 3N interaction in all applications throughout this thesis, accordingly we use an average pion mass of $M_\pi = 138\text{MeV}$ [74]. Chiral 3N forces including charge-symmetry-breaking effects can be found in Ref. [75].

Of course, as before for the NN interaction, the LECs c_D and c_E need to be fixed from experimental data. Various set-ups to tie down these parameters can be found in the literature, e.g., using the binding energies of ${}^3\text{H}$ and ${}^4\text{He}$ [77], or the neutron-deuteron doublet scattering length [73] or a fit to properties of light nuclei [78]. Throughout this work, we adopt the values $c_D = -0.2$ and $c_E = -0.205$ for the 3N interaction with the momentum cutoff $\Lambda_{3\text{N}} = 500\text{MeV}/c$, which is the cutoff consistent with the one used in the adopted

NN interaction. These values have been determined in Ref. [76] by exploiting the fact that the constant c_D emerges also in electro-weak chiral meson-exchange currents offering the possibility to use the β -decay half-life of ${}^3\text{H}$ computed by ab-initio calculations as constraint. Their procedure is illustrated in Figure 1.2: the red dashed and blue dash-dotted lines are trajectories in the c_D - c_E -parameter space that yield the experimental binding energies of ${}^3\text{H}$ and ${}^3\text{He}$, respectively. The average of both lines is drawn as black solid line which represents those parameter values that give the correct average binding energy of nuclei made of three nucleons. In addition, the vertical dotted lines denote the range in c_D for which one achieves the correct β -decay half-life of ${}^3\text{H}$ up to $\pm 0.54\%$. The center of this interval is at $c_D = -0.2$ which, with help of the black solid line, pins down c_E . In this way, both new LECs accompanying the 3N interaction are fixed entirely by data from 3N systems, which is the most consistent approach.

At first glance, it may seem most consistent to apply the same cutoff momentum $\Lambda_{3\text{N}}$ in the 3N interaction as in the NN interaction. However, full consistency between the N³LO NN and the N²LO 3N interactions is questionable already due to their different chiral orders, and the different functional forms of the used regular functions. When aiming at sensitivity studies of nuclear observables with respect to changing the cutoff momentum $\Lambda_{3\text{N}}$ and in this way the strength of the 3N interaction, it is valuable to determine further pairs of parameters c_D and c_E in $A = 3$ or 4 systems for different cutoff momenta $\Lambda_{3\text{N}}$ (see Section 7). Further reasons why the corresponding 3N interactions are of great practical interest will become clear later in Section 6.3. Hence, we keep the cutoff momentum of the NN interaction at $\Lambda = 500\text{MeV}/c$, but lower the cutoff momentum $\Lambda_{3\text{N}}$ of the 3N interaction and refit the LEC c_E such that the obtained Hamiltonian reproduces the ${}^4\text{He}$ binding energy. For convenience we keep $c_D = -0.2$, which warrants the reproduction of the triton β -decay half-life according to the findings in Ref. [76], namely the fact that the β -decay constant of triton is rather insensitive to the presence of 3N forces. We accomplish the fit of the ${}^4\text{He}$ binding energy utilizing matrix elements of the 3N interaction in a Jacobi HO basis within the no-core shell model (NCSM) with help of the `MANYEFF` code [79] provided by Petr Navrátil. We conduct the calculations for a sequence of model-space sizes up to $N_{\text{max}} = 20$ and extrapolate to infinite model-space size. We discuss the details of the HO Jacobi basis and the NCSM in Sections 2.1 and 4.1, respectively. We apply this procedure for 3N interactions with cutoff momenta $\Lambda_{3\text{N}} = 350\text{MeV}/c$, $400\text{MeV}/c$ and $450\text{MeV}/c$. The resulting LECs and also their values for the standard 3N interaction with $\Lambda_{3\text{N}} = 500\text{MeV}/c$ are summarized in Table 1.1. In addition, we show the convergence pattern of the ${}^4\text{He}$ ground-state energy with respect to the model-space size for the three cases in Figure 1.3 including the exponential function which we have fitted to energies obtained in three largest model spaces indicated by switching to the solid line, respectively. In all three cases the energies at $N_{\text{max}} = 20$ are sufficiently well converged so that the extrapolation is robust and contributes only a small correction to the energy obtained in the largest model space. The extrapolated energies can be seen from Table 1.1, where we also include the extrapolated energies for triton based on extrapolations from NCSM calculations at $N_{\text{max}} = 36, 38$ and 40 . For the 3N interactions fitted to the ${}^4\text{He}$ ground-state energies we

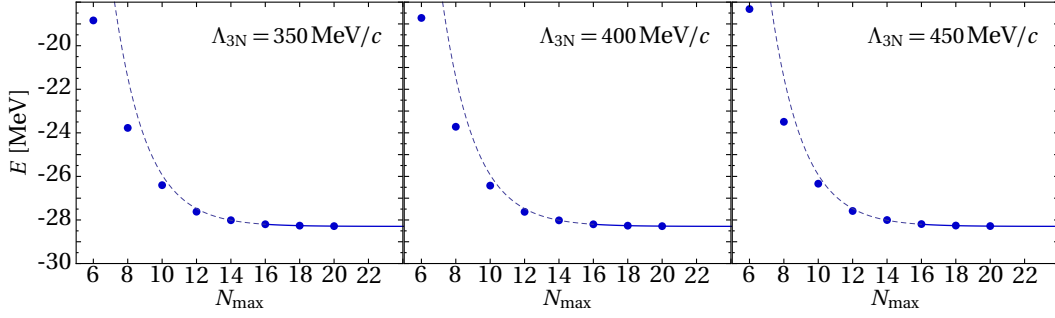


Figure 1.3 – Convergence pattern of the ${}^4\text{He}$ ground-state energy which was used to fit the LEC c_E for cutoff momenta $\Lambda_{3N} = 350, 400$ and $450 \text{ MeV}/c$ of the 3N interaction at $N^2\text{LO}$ as function of the NCSM model-space size. The solid line represents the extrapolation including the energies obtained from three largest model-spaces. The HO frequency is $\hbar\Omega = 36 \text{ MeV}$.

find deviations from the experimental triton energy of about 200 keV with $\Lambda_{3N} = 350$ and $400 \text{ MeV}/c$, and of about 150 keV with $\Lambda_{3N} = 450 \text{ MeV}/c$. In this way, we obtain alternative 3N interactions that are fixed by properties of three- and four-nucleon systems. Thus, their application in heavier systems remains completely predictive. We study and compare the properties of these different 3N interactions in particular in Sections 6.3, 7, and 9.

Finally, we note that the derivation of the Cartesian momentum operators of the sub-leading 3N interaction at $N^3\text{LO}$ is complete [82, 83]. They have been included in neutron and nuclear matter calculations which directly build on momentum-space matrix elements [84]. However, for applications to finite nuclei within the scope of the many-body methods discussed in Part II partial-wave decomposed matrix elements are needed. Because of the many different operator structures involved in the 3N interaction at $N^3\text{LO}$ this poses a formidable task, which cannot be accomplished manually, as done before in Ref. [74] for the five operator structures of the leading 3N interaction. Therefore, developments towards an automatized partial-wave decomposition of the $N^3\text{LO}$ 3N interaction as proposed in Ref. [85] are currently under way. The method relies on the numerical integra-

Table 1.1 – In the first three rows we quote the fitted LEC c_E to the ground-state energy of ${}^4\text{He}$ for different cutoff momenta Λ_{3N} of the $N^2\text{LO}$ 3N interaction and using the NN potential at $N^3\text{LO}$ described in Section 1.1, which determines the LECs c_i of the 3N interaction. The last two columns show the energies of ${}^4\text{He}$ and ${}^3\text{H}$ from extrapolations to infinite model-space size. The used HO frequency is $\hbar\Omega = 36 \text{ MeV}$. In the fourth row we quote the LEC combinations we use for $\Lambda_{3N} = 500 \text{ MeV}/c$ taken from Ref. [76], and the last row contains the experimental energies from Refs. [80, 81]. For further details see text.

$\Lambda_{3N} [\text{MeV}/c]$	c_D	c_E	$E({}^4\text{He}), N_{\text{max}}=\infty [\text{MeV}]$	$E({}^3\text{H}), N_{\text{max}}=\infty [\text{MeV}]$
350	-0.2	0.205	-28.2944	-8.276
400	-0.2	0.098	-28.2956	-8.283
450	-0.2	-0.016	-28.2920	-8.324
500	-0.2	-0.205	-28.50	-8.473
exp.			-28.2956	-8.482

tion of five-dimensional angular integrals and will eventually yield partial-wave decomposed 3N matrix elements on a four-dimensional Jacobi momentum grid. This requires a substantial amount of computing time and, therefore, has led to the joint efforts within the Low-Energy Nuclear Physics Collaboration (LENPIC) [86] we are part of. Once partial-wave decomposed matrix elements of these beyond-leading order 3N interactions become available, our machinery to use them in nuclear structure or reaction theory is completely developed and can be used immediately, because all input formats will be identical to the 3N interactions at N²LO. We discuss the necessary manipulations on the level of matrix elements to incorporate 3N interactions consistently in nuclear structure and reaction calculations in the remaining sections of Part I of this thesis.

SECTION 2

Three-Nucleon Force Matrix Elements

For an efficient description of finite nuclei with many-body methods that rely on a basis expansion of the Hamiltonian eigenstates it is mandatory to have access to matrix elements of the interaction with respect to basis states that are well-suited for the description of a localized system. This is in particular true for all many-body methods we discuss in Part II of this thesis. A basis composed of harmonic-oscillator (HO) eigenstates has proven to be suitable due to localized basis wave functions and the possibility to apply many analytic relations. In this section, we discuss the necessary procedure to transform the input matrix elements, given with respect intrinsic Jacobi HO states, into matrix elements that are convenient as input for the different many-body methods discussed later on. For NN interactions these steps are well-established and can be found, e.g., in Ref. [87]. Here, we focus on the treatment of 3N interaction matrix elements. As already mentioned above, our starting point are matrix elements of the 3N interaction with respect to antisymmetrized Jacobi HO 3N states, which are generated by Petr Navrátil's `MANYEFF` code [79] and are discussed in Section 2.1. Afterwards, in Section 2.2, we discuss the transformation into matrix elements with respect to angular-momentum and isospin coupled m -scheme states, which we refer to as JT -coupled scheme in the following. This JT -coupled scheme turns out to be key for an efficient inclusion of 3N matrix elements in many-body methods beyond the lightest nuclei. We briefly review our implementation and discuss the storage scheme tailored for an efficient on-the-fly decoupling of the matrix elements into the m -scheme, including our first attempts to evaluate this decoupling on graphics processing units, which is investigated in an ongoing collaboration with computer scientists [88]. Note that part of this discussion resulted in the publication [44]. In the last subsection we introduce the formalism of the so-called normal-ordering technique, which allows to approximate the 3N interaction by means of zero-, one-, and two-body interactions whenever the computational cost to include 3N interactions explicitly becomes prohibitive. A benchmark of this approximation is discussed in Section 8.

2.1 Matrix Elements in the HO Jacobi Basis

The 3N interaction matrix elements serving as input have been derived in Ref. [74], where the partial-wave decomposition has been performed manually with help of the partial-wave Jacobi HO basis states, which are given by

$$|N_1 N_2; \alpha\rangle = |N_1 N_2; [(L_1 S_1) J_1, (L_2 \frac{1}{2}) J_2] J_{12}; (T_1 \frac{1}{2}) T_{12}\rangle, \quad (2.1)$$

and are antisymmetric with respect to particle exchange $1 \leftrightarrow 2$ only, such that $(-1)^{L_1+S_1+T_1} = -1$. In addition, we have introduced the partial-wave index α which summarizes all orbital quantum numbers. Here, we adopt the notation of Ref. [44] which is similar to Ref. [74]. The quantum numbers N_1 and L_1 are the HO radial and orbital angular momentum quantum number, respectively, corresponding to an HO formulated in terms of the Jacobi coordinate

$$\vec{\xi}_1 = \frac{1}{\sqrt{2}}(\vec{r}_a - \vec{r}_b) \quad (2.2)$$

and the corresponding Jacobi momentum

$$\vec{\pi}_1 = \frac{1}{\sqrt{2}}(\vec{p}_a - \vec{p}_b), \quad (2.3)$$

with \vec{r}_i and \vec{p}_i being single-particle coordinates and momenta. Analogously, the N_2 and L_2 are the respective radial and the orbital angular momentum quantum numbers with respect to the Jacobi coordinate

$$\vec{\xi}_2 = \sqrt{\frac{2}{3}}\left(\frac{1}{2}(\vec{r}_a + \vec{r}_b) - \vec{r}_c\right) \quad (2.4)$$

and corresponding Jacobi momentum

$$\vec{\pi}_2 = \sqrt{\frac{2}{3}}\left(\frac{1}{2}(\vec{p}_a + \vec{p}_b) - \vec{p}_c\right). \quad (2.5)$$

The orbital angular momentum \hat{L}_1 couples with the total spin of the first two nucleons \hat{S}_1 to \hat{J}_1 ; the orbital angular momentum \hat{L}_2 couples with the spin of the third nucleon to \hat{J}_2 . In addition, the angular momenta \hat{J}_1 and \hat{J}_2 couple to the total angular momentum \hat{J}_{12} , and analogously the coupled isospin of the first two nucleons \hat{T}_1 and the isospin of the third nucleon couple to the total isospin \hat{T}_{12} . The projection quantum numbers of the total angular momentum $M_{J_{12}}$ and of the total isospin $M_{T_{12}}$ are suppressed for brevity. We note our general rule to denote quantum numbers characterizing more than one nucleons as capital letters while single-particle quantum numbers are denoted by lower-case letters. The states (2.1) are particularly well adapted to the translational invariant interactions because they are defined in the center-of-mass frame, i.e., they include intrinsic degrees of freedom of the 3N system only. Consequently, center-of-mass contaminations, which are an issue in certain applications, are ruled out by construction as long as one works with such states directly. We come back to this issue in context of the description of various

many-body methods in Section 4.

To arrive at completely antisymmetrized Jacobi HO states $|E_{12} i J_{12}^{\pi} T_{12}\rangle_a$, i.e., to fully antisymmetrize the partial-wave HO Jacobi states (2.1), we have to perform the transformation

$$|E_{12} i J_{12}^{\pi} T_{12}\rangle_a = \sum_{N'_1 N'_2 \alpha'} \delta_{E_{12}, 2N'_1 + L_1 + 2N'_2 + L_2} \delta_{J_{12}^{\pi}, J_{12}^{\pi'}} \delta_{T_{12}, T_{12}'} C_{N'_1 N'_2 \alpha'}^i |N'_1 N'_2 \alpha'\rangle. \quad (2.6)$$

The principal HO quantum number of the antisymmetrized Jacobi HO state is given by $E_{12} = 2N_1 + L_1 + 2N_2 + L_2$. The remaining good quantum numbers are the total angular momentum and parity J_{12}^{π} of the relative motion as well as the total isospin T_{12} . The index i does not correspond to a physically meaningful quantity, it labels different antisymmetrized Jacobi states for given quantum numbers E_{12} , J_{12}^{π} and T_{12} . The expansion coefficients are determined by the overlap of the antisymmetrized and non-antisymmetrized Jacobi HO states

$$C_{N_1 N_2 \alpha}^i = \langle N_1 N_2; \alpha | E_{12} i J_{12}^{\pi} T_{12} \rangle_a, \quad (2.7)$$

which are the so-called coefficients of fractional parentage (CFP) [74, 77, 89]. The CFPs are determined by diagonalization of the matrix obtained by representing the antisymmetrizer $\hat{\mathcal{A}}$ in the non-antisymmetrized Jacobi basis states $|N_1 N_2; \alpha\rangle$. Due to the fact that E_{12} , J_{12}^{π} and T_{12} are good quantum numbers in both representations these quantum numbers define a block structure of the matrix, so that the diagonalization can be carried out separately for each block. The eigenvectors of the antisymmetrizer with eigenvalue 1 define the fully antisymmetric Jacobi states $|E_{12} i J_{12}^{\pi} T_{12}\rangle$. For each $(E_{12}, J_{12}^{\pi}, T_{12})$ block multiple eigenvectors with eigenvalue 1 may exist, hence, they span a degenerate subspace with the index i as degeneracy index. In addition, we note that the CFPs are identical for all HO frequencies, i.e., in practice they need to be computed and stored to disk only once for a specific frequency. Altogether, this antisymmetrization procedure by means of CFPs is efficient and numerically easy to handle at least for the case of three-body states discussed here.

With help of Eqs. (2.1) and (2.6) we can express 3N interaction matrix elements with respect to antisymmetrized Jacobi HO states as

$$\begin{aligned} & {}_a \langle E'_{12} i' J_{12}^{\pi} T_{12} | \hat{V}^{3N} | E_{12} i J_{12}^{\pi} T_{12} \rangle_a \\ & = 3 \sum_{N_1 L_1} \sum_{N_2 L_2} \sum_{\alpha} \sum_{N'_1 L'_1} \sum_{N'_2 L'_2} \sum_{\alpha'} C_{N_1 N_2 \alpha}^i C_{N'_1 N'_2 \alpha'}^{i'} \langle N'_1 N'_2; \alpha' | \hat{V}_1^{3N} | N_1 N_2; \alpha \rangle, \end{aligned} \quad (2.8)$$

where the fact that the 3N interaction can be written as sum of three terms $\hat{V}^{3N} = \hat{V}_1^{3N} + \hat{V}_2^{3N} + \hat{V}_3^{3N}$ has been exploited [74]. The different \hat{V}_i^{3N} are related by particle permutations and yield identical contributions in terms of matrix elements with respect to fully antisymmetrized states leading to the factor 3 in Eq. (2.8). The matrix elements on the left-hand side build our starting point and are generated by the `MANYEFF` code of Petr Navrátil. This code computes matrix elements in the partial-wave Jacobi HO basis $|N_1 N_2; \alpha\rangle$ of the chiral 3N interactions shown in Eqs.(1.11)-(1.13) as described in Ref. [74], and performs

the transformation (2.8). For three-nucleon systems the obtained matrix elements can be used directly in calculations within the no-core shell model (NCSM) based on Jacobi coordinate HO states, as we briefly discuss in Section 4.1. However, for all applications of the 3N interaction discussed later we rely on matrix elements with respect to three-body Slater determinants $|n_a l_a j_a m_a m_{t_a}; n_b l_b j_b m_b m_{t_b}; n_c l_c j_c m_c m_{t_c}\rangle_a$ of HO single-particle states, typically called m -scheme states. The transformation of the antisymmetrized Jacobi matrix elements (2.8) into matrix elements with respect to m -scheme states is a computationally demanding step which will be the focus of the next subsection.

2.2 Three-Nucleon Matrix Elements in the m -Scheme

For the application of 3N interactions in the variety of many-body methods discussed in Part II of this thesis we have to prepare its matrix elements with respect to three-body Slater determinants of HO single-particle states, the so called m -scheme states

$$|abc\rangle_a = |n_a l_a j_a m_a m_{t_a}; n_b l_b j_b m_b m_{t_b}; n_c l_c j_c m_c m_{t_c}\rangle_a. \quad (2.9)$$

Here, n_a is the radial and l_a the orbital angular momentum quantum number of the spherical HO, respectively. The orbital angular momentum \hat{l}_a couples with the spin to the angular momentum \hat{j}_a with projection quantum number m_a . The projection-quantum number of the isospin is m_{t_a} . In addition, on the left-hand side we have introduced the short hand for the set of single-particle quantum numbers $a = \{n_a l_a j_a m_a m_{t_a}\}$ including all projection quantum numbers. Many of the first NCSM calculations including 3N interactions explicitly were performed using the modulus of computing and storing 3N m -scheme matrix elements before the actual many-body calculations, which subsequently reads in these matrix elements sets [78, 90, 91]. As we discuss in more detail in Section 2.2.3 and also in Refs. [44, 42] the memory requirements for their storage in fast memory during the many-body calculation quickly becomes prohibitive and, thus, limits the accessible model-space sizes. To overcome this complication we resort to a different strategy, namely to precompute matrix elements with respect to so-called JT -coupled states. The transformation into the JT -coupled scheme is discussed in Section 2.2.1. We will see that this reduces the memory needs significantly while the computationally demanding pieces are still part of the pre-computation step. Of course, most many-body methods still require m -scheme matrix elements so that an efficient on-the-fly decoupling of the matrix elements is necessary. To accomplish this we have developed an adapted storage scheme for the JT -coupled matrix elements, which we discuss in Section 2.2.2. Finally, we elaborate on the computational details of the 3N matrix element handling in Section 2.2.3.

2.2.1 Transformation of Jacobi Matrix Elements into the JT -Coupled Scheme

As we have motivated above, we aim at the transformation of 3N matrix elements with respect to antisymmetrized Jacobi states $|E_{12} i J_{12}^\pi T_{12}\rangle_a$ into matrix elements with respect to JT -coupled states composed of single-particle states. The corresponding JT -coupled

basis states are given by

$$|\bar{a}\bar{b}\bar{c}; J_{ab}J; T_{ab}T\rangle_a = |n_a l_a n_b l_b n_c l_c; [(j_a j_b)J_{ab}, j_c]J; [(\frac{1}{2} \frac{1}{2})T_{ab}, \frac{1}{2}]T\rangle_a, \quad (2.10)$$

where we have omitted the projection quantum numbers of the total angular momentum J and isospin T for brevity. In addition, we have introduced the notation $\bar{a} = \{n_a l_a j_a\}$ as short-hand for the set of single-particle quantum numbers without their projections. Since the states (2.10) are composed of single-particle states that depend on single-particle coordinates, they also include the description of the center of mass. Therefore, as starting point for the transformation we need to augment the partial-wave HO Jacobi state $|N_1 N_2; \alpha\rangle$ with an explicit center-of-mass degree of freedom by means of the HO states $|N_{\text{cm}} L_{\text{cm}} M_{\text{cm}}\rangle$, which after angular-momentum coupling reads

$$|N_1 N_2; \alpha; N_{\text{cm}} L_{\text{cm}}; J\rangle = \{|N_1 N_2; \alpha\rangle \otimes |N_{\text{cm}} L_{\text{cm}}\rangle\}^J, \quad (2.11)$$

where we couple the center-of-mass orbital angular momentum \hat{L}_{cm} and \hat{J}_{12} to \hat{J} . Afterwards, we can proceed by investigating the key element of the transformation, namely the overlap of the JT -coupled states (2.10) with the Jacobi states (2.11), which we refer to as T coefficients

$$T_{N_1 N_2 \alpha N_{\text{cm}} L_{\text{cm}}}^{\bar{a}\bar{b}\bar{c} J_{ab} J} = T_{N_1 L_1 S_1 J_1 N_2 L_2 J_{12} J_{12} N_{\text{cm}} L_{\text{cm}}}^{n_a l_a j_a n_b l_b j_b n_c l_c j_c J_{ab} J} = \langle N_1 N_2; \alpha; N_{\text{cm}} L_{\text{cm}}; J | \bar{a}\bar{b}\bar{c}; J_{ab} J; T_{ab} T \rangle. \quad (2.12)$$

We skip the detailed derivation of the T coefficients here because we have discussed it in a comprehensive manner in Refs. [92, 93]. Instead, we quote the final expression

$$\begin{aligned} & T_{N_1 L_1 S_1 J_1 N_2 L_2 J_{12} J_{12} N_{\text{cm}} L_{\text{cm}}}^{n_a l_a j_a n_b l_b j_b n_c l_c j_c J_{ab} J} \\ &= \sum_{\mathcal{L}} \sum_L \sum_{\Lambda} \sum_{S_{12}} \sum_{L_{12}} \sum_{L_{ab}} \delta_{(2n_a + l_a + 2n_b + l_b + 2n_c + l_c), (2N_{\text{cm}} + L_{\text{cm}} + 2N_1 + L_1 + 2N_2 + L_2)} \\ & \times (-1)^{l_c + \Lambda + L_{ab} + L + S_{12} + L_1 + J} \hat{j}_a \hat{j}_b \hat{j}_c \hat{J}_{ab} \hat{J} \hat{J}_1 \hat{J}_2 \hat{S}_1 \hat{S}_{12}^2 \hat{L}_{ab}^2 \hat{\mathcal{L}}^2 \hat{\Lambda}^2 \\ & \times \langle \langle \mathcal{N} \mathcal{L}, N_1 L_1; L_{ab} | n_b l_b, n_a l_a \rangle \rangle_1 \langle \langle N_{\text{cm}} L_{\text{cm}}, N_2 L_2; \Lambda | \mathcal{N} \mathcal{L}, n_c l_c \rangle \rangle_2 \\ & \times \begin{Bmatrix} l_a & l_b & L_{ab} \\ \frac{1}{2} & \frac{1}{2} & S_1 \\ j_a & j_b & J_{ab} \end{Bmatrix} \begin{Bmatrix} L_{ab} & l_c & L \\ S_1 & \frac{1}{2} & S_{12} \\ J_{ab} & j_c & J \end{Bmatrix} \begin{Bmatrix} L_1 & L_2 & L_{12} \\ S_1 & S_2 & S_{12} \\ J_1 & J_2 & J_{12} \end{Bmatrix} \\ & \times \begin{Bmatrix} l_c & \mathcal{L} & \Lambda \\ L_1 & L & L_{ab} \end{Bmatrix} \begin{Bmatrix} L_{\text{cm}} & L_2 & \Lambda \\ L_1 & L & L_{12} \end{Bmatrix} \begin{Bmatrix} L_{\text{cm}} & L_{12} & L \\ S_{12} & J & J_{12} \end{Bmatrix}, \end{aligned} \quad (2.13)$$

where we use the notation $\hat{x} = \sqrt{2x+1}$, and briefly outline the general strategy for its derivation: as evident from our discussion above, the T coefficients need to accomplish the change of the underlying coordinate system from Jacobi into single-particle coordinates. Because we are working with HO basis states this can be done with help of two Harmonic-Oscillator Brackets (HOBs) which we denote by $\langle \langle \dots | \dots \rangle \rangle_d$ and we follow the conventions of Kamuntavicius [94]. More detailed discussion on the HOBs may be found also in [92]. For the derivation of the T coefficients the most important property is their

requirement of coupled orbital angular momenta, which leads to the necessity of various angular momentum re-couplings which manifest themselves by the occurring $6j$ - and $9j$ -symbols. From Eq. (2.13) it is evident that the T coefficients are independent of the isospin quantum numbers, however they are defined only for $T_{ab} = T_1$ and $T = T_{12}$ as these are good quantum numbers in both bases. The remaining quantum numbers the T coefficients depend on are listed as upper and lower indices.

Having the expansion coefficients (2.12) we can tie up the pieces to arrive at the final transformation equation. We start with the targeted matrix elements of the 3N interaction with respect to antisymmetric JT -coupled states, i.e.,

$$\begin{aligned} & {}_a \langle \bar{a}\bar{b}\bar{c}; J_{ab} J; T_{ab} T | \hat{V}^{3N} | \bar{a}'\bar{b}'\bar{c}'; J'_{ab} J'; T'_{ab} T' \rangle_a \\ & = 6 \langle \bar{a}\bar{b}\bar{c}; J_{ab} J; T_{ab} T | \cdot \hat{\mathcal{A}} \hat{V}^{3N} \cdot \hat{\mathcal{A}} | \bar{a}'\bar{b}'\bar{c}'; J'_{ab} J'; T'_{ab} T' \rangle, \end{aligned} \quad (2.14)$$

where we made use of the projection property of the antisymmetrization operator for three-body states

$$| \bar{a}\bar{b}\bar{c}; J_{ab} J; T_{ab} T \rangle_a = \sqrt{6} \cdot \hat{\mathcal{A}} | \bar{a}\bar{b}\bar{c}; J_{ab} J; T_{ab} T \rangle, \quad (2.15)$$

which requires the factor $\sqrt{6}$. Next, we express the antisymmetrizer as projector explicitly with help of the antisymmetric Jacobi states augmented by a center-of-mass HO state in analogy to Eq. (2.11) as

$$\hat{\mathcal{A}} = \sum_{E_{12} i J_{12}^\pi T_{12}} \sum_{N_{\text{cm}} L_{\text{cm}}} \sum_J | E_{12} i J_{12}^\pi T_{12}; N_{\text{cm}} L_{\text{cm}}; J \rangle_a \langle E_{12} i J_{12}^\pi T_{12}; N_{\text{cm}} L_{\text{cm}}; J |. \quad (2.16)$$

This relation holds because the center-of-mass part is always symmetric with respect to particle transpositions. If we plug this expression for the antisymmetrizer in Eq. (2.15) and insert another identity in the non-antisymmetrized states (2.11)

$$\hat{\mathbb{1}} = \sum_{N_1 N_2} \sum_{\alpha} \sum_{N_{\text{cm}} L_{\text{cm}}} \sum_J | N_1 N_2; \alpha; N_{\text{cm}} L_{\text{cm}}; J \rangle \langle N_1 N_2; \alpha; N_{\text{cm}} L_{\text{cm}}; J | \quad (2.17)$$

we can identify again the CFPs $C_{N_1 N_2 \alpha}^i$ from the overlap

$$\begin{aligned} & \langle N_1 N_2; \alpha; N_{\text{cm}} L_{\text{cm}}; J | E'_{12} i' J_{12}^{\pi'} T'_{12}; N'_{\text{cm}} L'_{\text{cm}}; J' \rangle_a \\ & = C_{N_1 N_2 \alpha}^i \delta_{2N_1+L_1+2N_2+L_2, E_{12}} \delta_{J_{12}^\pi, J_{12}^{\pi'}} \delta_{T_{12}, T'_{12}} \delta_{N_{\text{cm}}, N'_{\text{cm}}} \delta_{L_{\text{cm}}, L'_{\text{cm}}} \delta_{J, J'}. \end{aligned} \quad (2.18)$$

Altogether, plugging Eq. (2.16) in Eq. (2.14) and using the identity (2.17) twice leads to the

final transformation formula

$$\begin{aligned}
 & {}_a \langle \bar{a} \bar{b} \bar{c}; J_{ab} J; T_{ab} T | \hat{V}^{3N} | \bar{a}' \bar{b}' \bar{c}'; J'_{ab} J; T'_{ab} T \rangle_a \\
 &= 6 \sum_{N_1 N_2 \alpha} \sum_{N'_1 N'_2 \alpha'} \sum_{i, i'} \sum_{N_{cm} L_{cm}} \delta_{T_{ab}, T_1} \delta_{T'_{ab}, T'_1} \delta_{T, T_{12}} \delta_{T', T'_{12}} \delta_{J_{12}, J'_{12}} \\
 & \times T_{N_1 L_1 S_1 J_1 N_2 L_2 J_{12} J_{12} N_{cm} L_{cm}}^{n_a l_a j_a n_b l_b j_b n_c l_c j_c J_{ab} J} T_{N'_1 L'_1 S'_1 J'_1 N'_2 L'_2 J'_{12} J'_{12} N_{cm} L_{cm}}^{n'_a l'_a j'_a n'_b l'_b j'_b n'_c l'_c j'_c J'_{ab} J} \\
 & \times C_{N_1 N_2 \alpha}^i C_{N'_1 N'_2 \alpha'}^{i'} {}_a \langle E_{12} i J_{12}^\pi T_{12} | \hat{V}^{3N} | E'_{12} i' J'_{12}{}^{\pi'} T'_{12} \rangle_a, \tag{2.19}
 \end{aligned}$$

where we also exploited the fact that the interaction does not connect different total angular momenta or isospins.

In fact, the isospin quantum numbers are not affected by the change of the underlying coordinate system, which is reflected in the formula by the corresponding Kronecker deltas. The advantage of using the JT -coupled scheme instead of matrix elements with respect to the m -scheme states (2.9) can be identified immediately in the final result (2.19): the number of coupled matrix elements that we need to compute and store is much reduced compared to the m -scheme case, because we can directly exploit the basic symmetries of the interaction such as its rotational invariance, i.e., different total angular momentum quantum numbers are not connected, and the matrix elements are independent of M_J . Likewise different total isospin quantum numbers are not connected and the matrix elements are independent of M_T , which is an approximation applied already in the matrix elements we start from. We study the memory needs of the JT -coupled matrix elements in more detail in Section 2.2.3.

Nevertheless, as we have mentioned already, most many-body methods rely on m -scheme matrix elements and accordingly an efficient angular-momentum decoupling during the many-body calculation is mandatory. We discuss this step in the next subsection. However, the key point of using the JT -coupled matrix-element scheme is the fact that the computationally most demanding steps are included in the pre-computation step and, thus, do not bother the many-body calculation. This is fulfilled due to the large number of T coefficients that need to be handled in the transformation (2.19), and also the computation of the T coefficients (2.13) is rather involved.

2.2.2 The Decoupling into m -Scheme Matrix Elements

After having computed the JT -coupled matrix elements using the formula derived above, we can utilize them in different many-body methods. The strategy is to store the matrix elements in fast memory and to retrieve the m -scheme matrix elements by an explicit decoupling. This decoupling is straightforwardly achieved and involves Clebsch-Gordan co-

efficients only

$$\begin{aligned}
 {}_a \langle abc | \hat{V}^{3N} | a' b' c' \rangle_a &= \sum_{J_{ab} J'_{ab}} \sum_J \sum_{T_{ab} T'_{ab}} \sum_T \\
 &\times \begin{pmatrix} j_a & j_b & | & J_{ab} \\ m_a & m_b & | & M_{ab} \end{pmatrix} \begin{pmatrix} J_{ab} & j_c & | & J \\ M_{ab} & m_c & | & M \end{pmatrix} \begin{pmatrix} \frac{1}{2} & \frac{1}{2} & | & T_{ab} \\ m_{t_a} & m_{t_b} & | & M_{T_{ab}} \end{pmatrix} \begin{pmatrix} T_{ab} & \frac{1}{2} & | & T \\ M_{T_{ab}} & m_{t_c} & | & M_T \end{pmatrix} \\
 &\times \begin{pmatrix} j'_a & j'_b & | & J'_{ab} \\ m'_a & m'_b & | & M'_{ab} \end{pmatrix} \begin{pmatrix} J'_{ab} & j'_c & | & J \\ M'_{ab} & m'_c & | & M \end{pmatrix} \begin{pmatrix} \frac{1}{2} & \frac{1}{2} & | & T'_{ab} \\ m'_{t_a} & m'_{t_b} & | & M'_{T'_{ab}} \end{pmatrix} \begin{pmatrix} T'_{ab} & \frac{1}{2} & | & T \\ M'_{T'_{ab}} & m'_{t_c} & | & M_T \end{pmatrix} \\
 &\times {}_a \langle \bar{a} \bar{b} \bar{c}; J_{ab} J; T_{ab} T | \hat{V}^{3N} | \bar{a}' \bar{b}' \bar{c}'; J'_{ab} J; T'_{ab} T \rangle_a.
 \end{aligned} \tag{2.20}$$

All projection quantum numbers that do not appear on the left-hand side are determined by the properties of the Clebsch-Gordan coefficients. Since the Clebsch-Gordan coefficients can be easily precached it is obvious that this decoupling can be included as intermediate step during the many-body calculation. However, we have developed further optimizations of this decoupling by introducing an adapted storage scheme that is tailored to guarantee a highly efficient decoupling procedure. Also, we have shown in a collaborative project with computer scientists that this decoupling can be ported efficiently to graphics-processing units. We discuss the details together with other computational aspects in the next subsection.

2.2.3 Computational Aspects of the 3N Matrix-Element Handling

After the discussion of the formal steps towards the access to 3N m -scheme matrix elements while storing JT -coupled matrix elements in fast memory, we now elaborate on some computational aspects and the implementation of the different steps in practice.

We start with a discussion of the memory requirements for the different matrix element schemes introduced in the previous subsections. In Figure 2.1 we show the memory needed for the 3N interaction matrix elements with respect to antisymmetrized Jacobi states (purple squares), the JT -coupled states (red triangles), and the m -scheme states (blue discs), respectively, as function of the maximum total energy quantum number $E_{3\max}$ of the three-body states. The latter is given by $2N_1 + L_1 + 2N_2 + L_2$ for the antisymmetric Jacobi states and by $e_a + e_b + e_c$ with $e_i = 2n_i + l_i$ in the JT -coupled scheme and the m -scheme. It is evident that the memory need depends on the extent of basic symmetries of the interaction reflected in the chosen three-body basis. The least memory is required to store the matrix elements with respect to the antisymmetrized Jacobi basis which takes advantage of all symmetries present, namely Hermiticity, rotational invariance (by means of the couplings to total \hat{J} and \hat{T}), antisymmetry and translational invariance since the center-of-mass part is completely omitted in this basis. The latter is included in the JT -coupled scheme and, as a consequence, two orders of magnitude more memory is needed for their storage beyond $E_{3\max} = 12$. This further increases when matrix elements in the m -scheme basis are considered, because here not even the rotational symmetry is exploited. How-

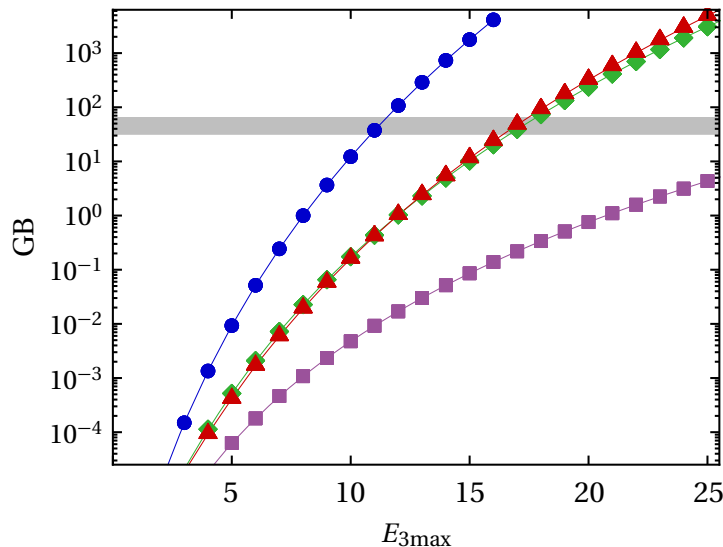


Figure 2.1 – Required memory to store the antisymmetrized Jacobi (■), m -scheme (●) and JT -coupled scheme (▲) matrix elements of \hat{v}^{3N} as well as the T coefficients (◆) of Eq. (2.13) as function of the maximum three-body energy quantum number $E_{3\max}$. Single-precision storage of the floating point numbers is assumed. The shaded area denotes the range of a 32-64 GB threshold that represents the typical available memory per node in current state-of-the-art supercomputers. (published in [44])

ever, we note that still all basic symmetries, i.e., antisymmetry, the fact that the sum of single-particle projection quantum numbers needs to be equal in the bra and ket states as well as time-reversal symmetry are considered. The different memory demands are crucial for practical applications and set the limits for current ab-initio nuclear structure calculations.

Many NCSM calculations including 3N interactions [78, 90, 91] originally followed the strategy to compute and store the set of m -scheme matrix elements before solving the many-body Hamiltonian eigenvalue problem. This defines a limit of accessible model-space sizes. For instance, an $N_{\max} = 8$ model space for a mid- p -shell nucleus requests 3N matrix elements up to $E_{3\max} = 11$, requiring the storage of about 33 GB matrix elements in single precision [95]. This is definitely borderline, because the memory per node typically available at current supercomputers is between 32 and 64 GB, shown as shaded area in Figure 2.1. But to converge NCSM-type calculations it is typically necessary to investigate model spaces with $N_{\max} = 12$ or beyond. Therefore, we have introduced the JT -coupled matrix-element scheme. As already emphasized, this reduces the necessary storage up to three orders of magnitude, e.g., for the example of an $N_{\max} = 8$ calculation in the mid- p -shell the JT -coupled matrix elements at $E_{3\max} = 11$ need 0.4 GB in single precision only. Thus, the JT -coupled scheme enables NCSM calculations for p -shell nuclei including 3N interactions for much larger model spaces and, thus, is key to obtain results that are converged or close to convergence with respect to model-space sizes. This applies as well to other nuclear structure methods, e.g., the coupled-cluster method [96, 97], the in-medium similarity renormalization group [32, 34] or the Gorkov-Green’s function approach [30],

and to nuclear reaction approaches as, e.g., the no-core shell model resonating group method [51] and the no-core shell model with continuum (see Part III), which have all adopted our storage scheme.

During the calculations of the JT -coupled 3N matrix elements the most critical objects are the T coefficients (2.13). Each T coefficient involves sums over products of two HOBs, three $9j$ -symbols and three $6j$ -symbols. We precompute all HOBs and angular-momentum coupling coefficients that are needed for the calculation of T coefficients up to $E_{3\max}$. Already from the large number of indices the T coefficients depend on, one may anticipate that the number of relevant coefficients is large. The memory demand of these coefficients is also included in Figure 2.1 as green diamonds and is approximately identical to that of the JT -coupled matrix elements. For an efficient realization of the transformation (2.19) it is necessary to fit all precomputed T coefficients in memory. For increasing $E_{3\max}$ this becomes more and more problematic, in particular due to the fact that besides the T coefficients also the antisymmetrized Jacobi matrix elements, the CFPs and of course the resulting JT -coupled matrix elements need to be stored. However, exploiting the fact that the computation of a given JT -coupled matrix element requires T coefficients depending on $\bar{a}\bar{b}\bar{c}$ and $\bar{a}'\bar{b}'\bar{c}'$ only, we split the transformation in different $(\bar{a}\bar{b}\bar{c}, \bar{a}'\bar{b}'\bar{c}')$ -blocks and thus circumvent memory limitations. In a post-processing step we join the matrix elements of all different blocks into a common file. This discussion clarifies that an on-the-fly evaluation of the transformation (2.19) during the many-body calculation itself is not favorable, because the cached T coefficients would not lead to further memory savings, since the breakdown into different $(\bar{a}\bar{b}\bar{c}, \bar{a}'\bar{b}'\bar{c}')$ -blocks is hardly feasible efficiently at this stage. A complete on-the-fly evaluation of JT -coupled matrix elements, i.e., without pre-computed T coefficients, would significantly increase the computing time. Therefore, the precomputation of JT -coupled matrix elements currently seems to be the optimal compromise.

Next, we focus on the optimized storage scheme of the JT -coupled 3N matrix elements tailored to facilitate a cache-optimized and, thus, efficient on-the-fly decoupling (2.20) into the m -scheme during the many-body calculation. We store all matrix elements as a single flat vector without further indices, i.e., the quantum numbers of the matrix elements are encoded by their sequence. The six outermost loops run over the orbital single-particle quantum numbers \bar{a} , \bar{b} , \bar{c} , \bar{a}' , \bar{b}' and \bar{c}' . At this stage we exploit antisymmetry, parity symmetry and Hermiticity. The combination of these indices mark the beginning of a region of JT -coupled matrix elements in memory that may contribute to m -scheme matrix elements with single-particle quantum numbers a, b, c, a', b', c' due to the fact that the orbital quantum numbers remain invariant during the decoupling. Hence, we do the bookkeeping of these positions with help of an auxiliary array for later usage in the angular-momentum decoupling. The inner loops that complete the definition of the storage scheme run over the coupled angular momenta and isospin quantum numbers of the JT -coupled matrix elements. We evaluate them in the specific order J_{ab} , J'_{ab} , J , T_{ab} , T'_{ab} and T . We constrain the loop bounds by the simple triangular conditions dictated by the single-particle quantum numbers, however, here we do not exploit antisymmetry for iden-

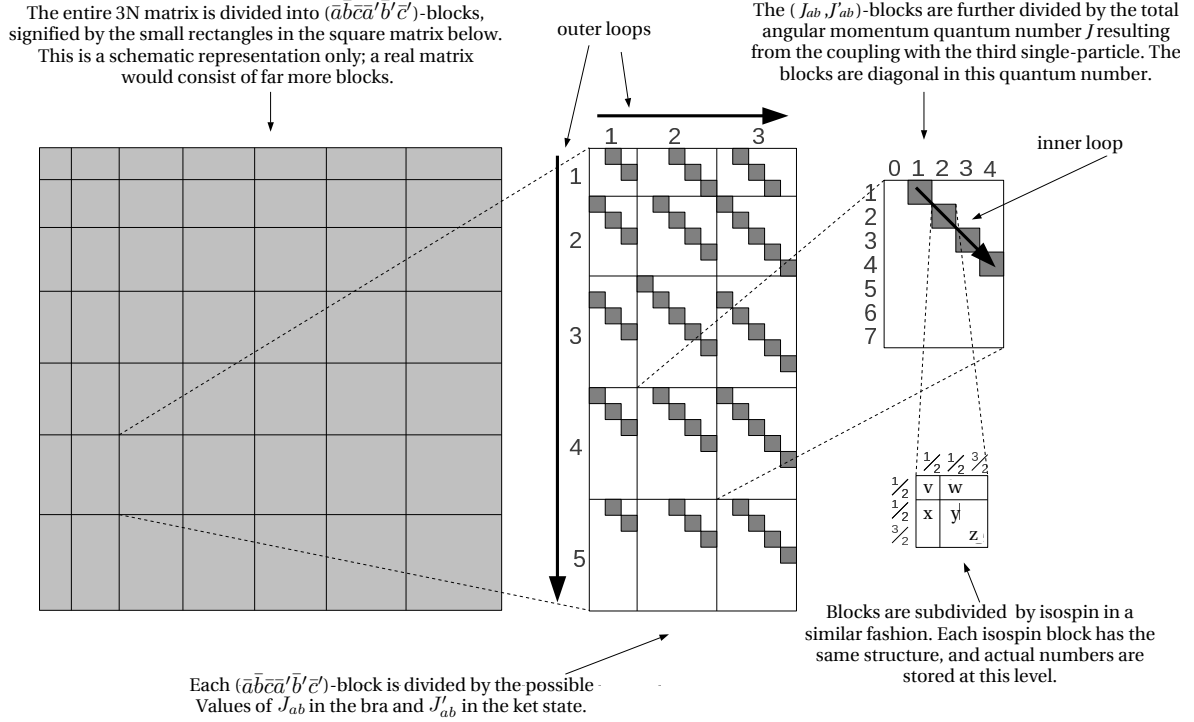


Figure 2.2 – Illustration of the storage scheme of the JT -coupled matrix elements in a matrix form. For further details and explanations see text. Figure published in [88] and modified to match notations.

tical single-particle orbitals in order to maintain a fixed stride for the innermost segment of the three isospin loops. An illustration of the storage scheme in terms of a matrix form is shown in Figure 2.2. To obtain a specific m -scheme matrix element, at first we jump to the beginning of the corresponding $(\bar{a}\bar{b}\bar{c}, \bar{a}'\bar{b}'\bar{c}')$ -block in the matrix-element vector with help of the book-keeping array mentioned above. By evaluating the decoupling loops in the same sequence as in the storage scheme we can evaluate the decoupling loops as a linear sweep over the storage vector of the JT -coupled matrix elements with additional weighting by the appropriate Clebsch-Gordan coefficients as shown in Eq. (2.20). The three isospin loops are rolled out explicitly for improved performance. In this way, the intermediate decoupling step relevant in the many-body calculations is accomplished in a simple and cache-efficient manner. The JT -coupled matrix elements with the storage scheme described here have already been adopted and proven to be efficient in different many-body methods for the inclusion of $3N$ interactions [33, 34, 51, 30, 95, 98, 46]. We note that we use an analogous scheme for the management of the NN matrix elements, too.

In collaboration with computer scientists we worked towards porting the decoupling of JT -coupled matrix elements onto graphics processing units (GPUs) to exploit their large number of cores by using a CUDA implementation [88]. The idea is to send requests for chunks of m -scheme matrix elements by specifying sets of indices $\{a, b, c, a', b', c'\}$ to the GPU, which computes the requested matrix elements using the algorithm described above and sends them back to the CPU. In order to accomplish this efficiently, the bookkeeping

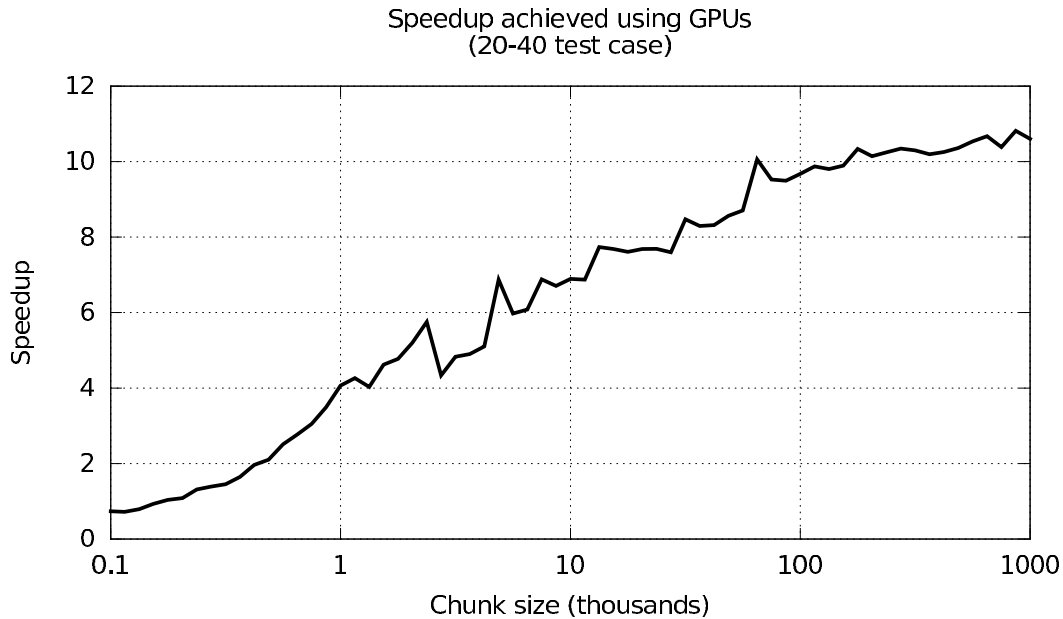


Figure 2.3 – Achieved speedup in the decoupling of JT -coupled matrix elements into the m -scheme by the evaluation on a single GPU relative to the execution on a single CPU using eight OpenMP threads. The test was performed on a GPU node on the Dirac cluster at NERSC², the GPU consists of 448 parallel CUDA cores and 3 GB memory. For further details see text. (published in [88])

array, the cached Clebsch-Gordan coefficients, and the JT -coupled matrix elements are stored on the accelerator card. Hence, the available memory on the GPU sets the limit for an efficient application. Each m -scheme matrix element is computed by a separate thread on the GPU, which can clearly be done independently and is well-suited for parallel execution. However, the performance is limited by the communication between the GPU and CPU. A first test of the speedup through the use of one GPU compared to a single CPU with eight OpenMP threads as function of the chunk size is shown in Figure 2.3 for a specific test case using a particular range of single-particle indices. The speedup increases as function of chunk sizes and reaches a factor of ten for chunk sizes of about 10^5 matrix elements. These results are promising and are under further investigations. For the first tests a stand-alone implementation concentrated just on the calculation of m -scheme matrix elements is used. One of the crucial next steps is the efficient inclusion of the preparation and retrieval of the chunks of m -scheme matrix elements into the many-body calculation, which is under investigation at the moment for the Many-Fermion Dynamics for nuclear structure code, which is a large-scale NCSM code [99, 100, 101]. For further details about the first GPU implementation we refer the interested reader to Ref. [88].

We end this section with a comment on the implementation of the transformation (2.19). Besides the already mentioned implementation of the transformation having the T coefficients in fast memory and evaluating the loops explicitly as efficiently as possible, a closer look at the transformation formula reveals the possibility to evaluate it in terms of matrix multiplications. Of course, this is not surprising: in spite of all complicated objects

²<https://www.nersc.gov>

contained Eq. (2.19), it is nevertheless nothing else than a simple basis transformation. In matrix form Eq. (2.19) reads

$$V_{JT}^{3N} = 3! \sum_{l_{cm}} T^\top(l_{cm}) V_{Jacobi}^{3N} T(l_{cm}). \quad (2.21)$$

A first implementation in this spirit using multi-threaded BLAS routines to accomplish the matrix multiplications reveals the opportunity of huge savings of computing time compared to our conventional implementation with the optimized evaluation of the loops in Eq. (2.19). Test calculations show that this computational scheme allows the calculation of JT -coupled matrix elements with maximum three-body energy $E_{3\max} = 14$ in one hour on a standard node, which reduces the computational burden of the production of 3N matrix elements in the JT -coupled scheme significantly.

2.3 The Normal-Ordered Two-Body Approximation

In the previous subsections we have shown that our realization of the JT -coupled scheme reduces the memory requirements of 3N matrix elements and facilitates many-body calculations with much larger $E_{3\max}$ truncations, which is usually key to provide converged results. Nevertheless, the explicit inclusion of the 3N interaction into the solution of the many-body Schrödinger equation still requires the generalization of the many-body framework, which is often a highly non-trivial task. Prime examples are the coupled-cluster theory with explicit 3N interactions as discussed briefly in Section 4.3 and in detail in Refs. [96, 45] or the no-core shell model combined with the resonating group method, which is the focus of Section 11 of this work. Even if the formal extensions are straightforward, the computational cost typically increases by orders of magnitude due to the explicit treatment of 3N interactions and, hence, may forbid calculations that are routinely done at the two-body level. In spite of the benefit from the JT -coupled scheme compared to the use of m -scheme matrix elements, for large $E_{3\max} \geq 16$ the memory needs again tend to become prohibitive as evident from Figure 2.1.

This predicament, namely the need for 3N interactions versus the immense computational costs, might motivate the development of controlled approximation schemes for the 3N interaction. Of course, the quantitative assessment of the quality of the approximation in terms of a benchmark against calculations including the 3N interaction explicitly is indispensable prior to its application. In the following subsection, we briefly recapitulate the basic formalism of normal ordering and highlight how it can be used to deduce a rigorous and improvable approximation scheme to the 3N interaction. The details about the practical computation of normal-ordered matrix elements by merging the normal ordering with the transformation into the JT -coupled matrix element scheme is the focus of Section 2.3.2. A comprehensive benchmark of the normal-ordering scheme in terms of ab-initio calculations of ground-state energies in light and medium-mass nuclei follows in Section 8 in Part II of this work.

2.3.1 Formalism

Normal ordering with respect to a reference state $|\Phi_0\rangle$ is a well-known tool in quantum many-body and field theory [102]. For the scope of single-reference normal ordering we are aiming at in this work, a string of operators in second quantization is said to be in normal order if all particle creation and hole annihilation operators are to the left of all particle annihilation and hole creation operators. Here, we refer to the occupied and unoccupied single-particle states in the reference Slater determinant as hole states and particle states, respectively. For convenience we assume HO single-particle states in the following, however, all formulas are valid for arbitrary orthonormal bases, e.g., Hartree-Fock bases. We denote the quantum numbers of particle states by a, b, \dots , quantum numbers of hole states by i, j, \dots , and those of generic states by q, r, \dots . From this definition follows that the standard operator expressions given in second quantization, e.g., for the 3N interaction

$$\hat{V}^{3N} = \frac{1}{36} \sum_{pqrst u} a \langle pqr | \hat{V}^{3N} | stu \rangle_a \hat{a}_p^\dagger \hat{a}_q^\dagger \hat{a}_r^\dagger \hat{a}_u \hat{a}_t \hat{a}_s, \quad (2.22)$$

are typically already in normal order with respect to the vacuum as reference state. To cast such operators into normal order with respect to the reference state $|\Phi_0\rangle$ we can make use of a variant of Wick's theorem [102], given by

$$\hat{A}\hat{B}\hat{C}\dots = \{\hat{A}\hat{B}\hat{C}\dots\}_{|\Phi_0\rangle} + \sum_{\text{all contractions}} \overline{\{\hat{A}\hat{B}\hat{C}\dots\}_{|\Phi_0\rangle}}, \quad (2.23)$$

where $\hat{A}\hat{B}\hat{C}\dots$ denote a generic string of operators and $\{\hat{A}\hat{B}\hat{C}\dots\}_{|\Phi_0\rangle}$ denotes the same string in normal order with respect to the reference state $|\Phi_0\rangle$ defined by

$$\{\hat{A}\hat{B}\hat{C}\dots\}_{|\Phi_0\rangle} = \text{sgn}(\mathcal{P}) \hat{D}\hat{F}\hat{A}\dots \quad (2.24)$$

with $\text{sgn}(\mathcal{P})$ as signature of the permutation \mathcal{P} necessary to accomplish the re-ordering of the operator string. In addition, a so-called contraction is denoted by the bracket connecting the two involved operators, see second term of Eq. (2.23). Wick's theorem for the special case of two operators yields

$$\overline{\hat{A}\hat{B}} = \hat{A}\hat{B} - \{\hat{A}\hat{B}\}_{|\Phi_0\rangle}, \quad (2.25)$$

and a normal ordered product of operators involving contractions is evaluated as

$$\overline{\{\hat{A}\hat{B}\dots\hat{F}\dots\hat{H}\dots\}_{|\Phi_0\rangle}} = \text{sgn}(\mathcal{P}) \hat{F}\hat{H}\overline{\{\hat{A}\hat{B}\dots\}_{|\Phi_0\rangle}}, \quad (2.26)$$

and accordingly for more contractions. Inserting in Eq. (2.25) all possible combinations of hole-hole, particle-particle and particle-hole operators reveals that only two non-vanishing

contractions remain, namely

$$\hat{i}^\dagger \hat{j} = \delta_{ij} \quad \text{and} \quad \hat{a} \hat{b}^\dagger = \delta_{ab}. \quad (2.27)$$

This will help to simplify the expressions in the following.

Applying Wick's theorem (2.23) to the 3N interaction operator (2.22) yields a sum of four contributions that differ by their number of contractions

$$\begin{aligned} \hat{V}^{3N} = & \frac{1}{36} \sum_{pqrst u} a \langle pqr | \hat{V}^{3N} | stu \rangle_a \{ \hat{a}_p^\dagger \hat{a}_q^\dagger \hat{a}_r^\dagger \hat{a}_u \hat{a}_t \hat{a}_s \}_{|\Phi_0\rangle} \\ & + \frac{1}{36} \sum_{pqrst u} a \langle pqr | \hat{V}^{3N} | stu \rangle_a \sum_{\text{single contractions}} \overbrace{\{ \hat{a}_p^\dagger \hat{a}_q^\dagger \hat{a}_r^\dagger \hat{a}_u \hat{a}_t \hat{a}_s \}_{|\Phi_0\rangle}} \\ & + \frac{1}{36} \sum_{pqrst u} a \langle pqr | \hat{V}^{3N} | stu \rangle_a \sum_{\text{double contractions}} \overbrace{\{ \hat{a}_p^\dagger \hat{a}_q^\dagger \hat{a}_r^\dagger \hat{a}_u \hat{a}_t \hat{a}_s \}_{|\Phi_0\rangle}} \\ & + \frac{1}{36} \sum_{pqrst u} a \langle pqr | \hat{V}^{3N} | stu \rangle_a \sum_{\text{triple contractions}} \overbrace{\{ \hat{a}_p^\dagger \hat{a}_q^\dagger \hat{a}_r^\dagger \hat{a}_u \hat{a}_t \hat{a}_s \}_{|\Phi_0\rangle}}. \end{aligned} \quad (2.28)$$

Further evaluation of the contractions using Eq. (2.27) and collecting identical terms leads to the decomposition

$$\begin{aligned} \hat{V}^{3N} = & \frac{1}{36} \sum_{pqrst u} a \langle pqr | \hat{V}^{3N} | stu \rangle_a \{ \hat{a}_p^\dagger \hat{a}_q^\dagger \hat{a}_r^\dagger \hat{a}_u \hat{a}_t \hat{a}_s \}_{|\Phi_0\rangle} \\ & + \frac{1}{4} \sum_{ipqrs} a \langle pqi | \hat{V}^{3N} | sti \rangle_a \{ \hat{a}_p^\dagger \hat{a}_q^\dagger \hat{a}_t \hat{a}_s \}_{|\Phi_0\rangle} \\ & + \frac{1}{2} \sum_{ijps} a \langle pij | \hat{V}^{3N} | sij \rangle_a \{ \hat{a}_p^\dagger \hat{a}_s \}_{|\Phi_0\rangle} \\ & + \frac{1}{6} \sum_{ijk} a \langle ijk | \hat{V}^{3N} | ijk \rangle_a, \end{aligned} \quad (2.29)$$

where we kept the order of the terms, i.e., the three-body operator originates from the term without contractions, the two-body operator follows from the contributions with one contractions, and the one- and zero-body body operators are from the doubly and triply contracted terms, respectively. The important detail of the contributions at lower particle ranks is that part of the summations now run over hole states only, which build for a given reference state a significantly reduced subset of all single-particle states. Now, we can rewrite the 3N interaction operator as sum of a zero-body (0B), one-body (1B), two-body (2B) and the residual three-body (3B) part as

$$\hat{V}^{3N} = \hat{V}_{0B}^{3N} + \hat{V}_{1B}^{3N} + \hat{V}_{2B}^{3N} + \hat{V}_{3B}^{3N}. \quad (2.30)$$

So far, we have obtained an operator identity of the original 3N interaction operator on the

left-hand side in terms of a sum of operators normal ordered with respect to the reference state $|\Phi_0\rangle$ on the right-hand side. Evidently, part of the information originally contained entirely in the three-body operator \hat{V}^{3N} has been demoted to lower particle ranks by means of the normal ordering with help of information about the many-body system under consideration encoded in the reference state. Thus, Eq. (2.30) brings us into the position to define different approximations of the 3N interaction, namely, the normal-ordered n -body (NO n B) approximations with $n \in \{0, 1, 2\}$, where $(n+1)$ -body operators are discarded. We benchmark these different approximations in detail in Section 8, and eventually use the NO2B approximation in different applications in Section 9.

For both, the benchmark aspects and the applications of the NO2B approximated interactions in many-body calculations we have to convert the truncated normal-ordered operator

$$\hat{V}_{\text{NO2B}}^{3N} = \hat{V}_{\text{0B}}^{3N} + \hat{V}_{\text{1B}}^{3N} + \hat{V}_{\text{2B}}^{3N} \quad (2.31)$$

back into vacuum normal order. This is achieved by reversed application of Wick's theorem for the operators $\{\hat{a}_p^\dagger \hat{a}_q^\dagger \hat{a}_t \hat{a}_s\}_{|\Phi_0\rangle}$ and $\{\hat{a}_p^\dagger \hat{a}_s\}_{|\Phi_0\rangle}$, i.e., using

$$\begin{aligned} \{\hat{a}_p^\dagger \hat{a}_q^\dagger \hat{a}_t \hat{a}_s\}_{|\Phi_0\rangle} &= \hat{a}_p^\dagger \hat{a}_q^\dagger \hat{a}_t \hat{a}_s + \overline{\hat{a}_p^\dagger \hat{a}_s \hat{a}_q^\dagger \hat{a}_t} - \overline{\hat{a}_p^\dagger \hat{a}_r \hat{a}_q^\dagger \hat{a}_s} - \overline{\hat{a}_q^\dagger \hat{a}_s \hat{a}_p^\dagger \hat{a}_t} \\ &\quad + \overline{\hat{a}_q^\dagger \hat{a}_r \hat{a}_p^\dagger \hat{a}_s} + \overline{\hat{a}_q^\dagger \hat{a}_s \hat{a}_p^\dagger \hat{a}_r} - \overline{\hat{a}_q^\dagger \hat{a}_r \hat{a}_p^\dagger \hat{a}_s}, \end{aligned} \quad (2.32)$$

$$\{\hat{a}_p^\dagger \hat{a}_s\}_{|\Phi_0\rangle} = \hat{a}_p^\dagger \hat{a}_s - \overline{\hat{a}_p^\dagger \hat{a}_s}. \quad (2.33)$$

Finally, we arrive at the normal-ordered 3N interaction operator at the NO2B approximation converted back in vacuum normal order given by

$$\hat{V}_{\text{NO2B}}^{3N} = v - \frac{1}{2} \sum_{pq} v_{pq} \hat{a}_p^\dagger \hat{a}_q + \frac{1}{4} \sum_{pqrs} v_{pqrs} \hat{a}_p^\dagger \hat{a}_q^\dagger \hat{a}_s \hat{a}_r \quad (2.34)$$

with the definitions

$$v = \frac{1}{6} \sum_{ijk} {}_a \langle ijk | \hat{V}^{3N} | ijk \rangle_a \quad (2.35)$$

$$v_{pq} = \sum_{ij} {}_a \langle pij | \hat{V}^{3N} | qij \rangle_a \quad (2.36)$$

$$v_{pqrs} = \sum_i {}_a \langle pqi | \hat{V}^{3N} | rsi \rangle_a. \quad (2.37)$$

Whenever we perform a many-body calculation using the NO2B approximation we use the operator (2.34) instead of explicitly including the original 3N interaction. Thus, we are technically left with a calculation at the two-body interaction level where the only additional complication is the treatment of the 0B- and 1B-part contributions in Eq. (2.34).

Obviously, this avoids the extension of the many-body framework to explicit 3N interactions, which was one of the reasons to resort to approximative schemes as motivated above. Nevertheless, we need to provide matrix elements of the 0B, 1B and 2B operators in Eq. (2.34) which internally requires the availability of 3N matrix elements. We present a new technique to efficiently provide 3N matrix elements in NO2B approximation for large $E_{3\max}$ in the following subsection.

2.3.2 Normal-ordering Directly in the JT -Coupled Scheme

The simplest way to produce matrix elements of $\hat{V}_{\text{NO2B}}^{3\text{N}}$ is the direct use of 3N m -scheme matrix elements as they are contained in Eqs. (2.35)-(2.37). But storing m -scheme 3N matrix elements becomes prohibitive already at relatively low $E_{3\max}$. This can be overcome by using the JT -coupled scheme in combination with the on-the-fly decoupling (2.20) during the calculation of matrix elements of $\hat{V}_{\text{NO2B}}^{3\text{N}}$. However, in the following we discuss a more elegant approach which is the key to obtain normal-ordered 3N matrix elements beyond $E_{3\max} = 16$. First, we realize that Eqs. (2.35)-(2.37) can be reformulated in terms of JT -coupled matrix elements. For the derivation we assume a closed-shell nucleus consistent with the single-reference normal ordering discussed here. As a consequence all single-particle states of a given j -orbital in the reference state are fully occupied. By expressing the 3N m -scheme matrix elements in the 0B contribution in terms of matrix elements in the JT -coupled scheme we obtain

$$\begin{aligned}
 v = & \sum_{\bar{i}\bar{j}\bar{k}} \sum_{J_{ij}} \sum_J \sum_{m_{t_i}} \sum_{m_{t_j}} \sum_{m_{t_k}} \sum_{T_{ij}M_{T_{ij}}} \sum_{T'_{ij}M_{T'_{ij}}} \sum_{TM_T} \\
 & \times \begin{pmatrix} \frac{1}{2} & \frac{1}{2} & \left| \begin{matrix} T_{ij} \\ m_{t_i} & m_{t_j} \end{matrix} \right. \\ & & M_{T_{ij}} \end{pmatrix} \begin{pmatrix} \frac{1}{2} & \frac{1}{2} & \left| \begin{matrix} T'_{ij} \\ m_{t_i} & m_{t_j} \end{matrix} \right. \\ & & M_{T'_{ij}} \end{pmatrix} \begin{pmatrix} T_{ij} & \frac{1}{2} & \left| \begin{matrix} T \\ M_{T_{ij}} & m_{t_k} \end{matrix} \right. \\ & & M_T \end{pmatrix} \begin{pmatrix} T'_{ij} & \frac{1}{2} & \left| \begin{matrix} T \\ M'_{T_{ij}} & m_{t_k} \end{matrix} \right. \\ & & M_T \end{pmatrix} \\
 & \times (2J+1)_a \langle \bar{i}\bar{j}\bar{k}; J_{ij} J; T_{ij} T | \hat{V}^{3\text{N}} | \bar{i}\bar{j}\bar{k}; J'_{ij} J; T'_{ij} T \rangle_a. \tag{2.38}
 \end{aligned}$$

We note that the Clebsch-Gordan coefficients involving angular momenta have been eliminated by their orthogonality relations due to the assumption of closed j -shells. This is not possible for the isospins in the general case of $N \neq Z$ nuclei, however their Clebsch-Gordan coefficients help to collapse the summations with respect to $M_{T_{ij}}$ and $M_{T'_{ij}}$.

We go on with the matrix elements of the 1B operator in Eq. (2.34) which includes the

matrix elements (2.36) and again introduce JT -coupled matrix elements

$$\begin{aligned}
 \langle p | -\frac{1}{2} \sum_{rs} v_{rs} \hat{a}_r^\dagger \hat{a}_s | q \rangle &= -\frac{1}{2} v_{pq} \\
 &= -\frac{1}{2} \sum_{\bar{i}\bar{j}} \sum_{J_{ij}} \sum_J \sum_{m_{t_i} m_{t_j}} \sum_{T_{ij} M_{T_{ij}}} \sum_{T'_{ij} M_{T'_{ij}}} \sum_{TM_T} \\
 &\times \begin{pmatrix} \frac{1}{2} & \frac{1}{2} & & T_{pi} \\ m_{t_p} & m_{t_i} & & M_{T_{pi}} \end{pmatrix} \begin{pmatrix} \frac{1}{2} & \frac{1}{2} & & T'_{pi} \\ m_{t_p} & m_{t_i} & & M_{T'_{pi}} \end{pmatrix} \begin{pmatrix} T_{pi} & \frac{1}{2} & & T \\ M_{T_{pi}} & m_{t_j} & & M_T \end{pmatrix} \begin{pmatrix} T'_{pi} & \frac{1}{2} & & T \\ M_{T'_{pi}} & m_{t_j} & & M_T \end{pmatrix} \\
 &\times \frac{2J+1}{2j_p+1} {}_a \langle \bar{p} \bar{i} \bar{j}; J_{pi} J; T_{pi} T | \hat{V}^{3N} | \bar{q} \bar{i} \bar{j}; J'_{pi} J; T'_{pi} T \rangle_a. \tag{2.39}
 \end{aligned}$$

Finally, we come to the matrix elements of the 2B part that we compute with respect to angular- and isospin-coupled two-body states as

$$\begin{aligned}
 &{}_a \langle \bar{p} \bar{q}; J_{pq} T_{pq} M_{T_{pq}} | \frac{1}{4} \sum_{tuvw} v_{tuvw} \hat{a}_t^\dagger \hat{a}_u^\dagger \hat{a}_w \hat{a}_v | \bar{r} \bar{s}; J_{pq} T_{pq} M_{T_{pq}} \rangle_a \\
 &= \sum_{m_p} \sum_{m_q} \sum_{m_r} \sum_{m_s} \begin{pmatrix} j_p & j_q & & J_{pq} \\ m_p & m_q & & M_{J_{pq}} \end{pmatrix} \begin{pmatrix} j_r & j_s & & J_{pq} \\ m_r & m_s & & M_{J_{pq}} \end{pmatrix} \begin{pmatrix} \frac{1}{2} & \frac{1}{2} & & T_{pq} \\ m_{t_p} & m_{t_q} & & M_{T_{pq}} \end{pmatrix} \begin{pmatrix} \frac{1}{2} & \frac{1}{2} & & T_{pq} \\ m_{t_r} & m_{t_s} & & M_{T_{pq}} \end{pmatrix} \\
 &\times \sum_i {}_a \langle pq i | \hat{V}^{3N} | r s i \rangle_a \\
 &= \sum_J \sum_T \sum_{M_T} \sum_{\bar{i}} \sum_{m_{t_i}} \begin{pmatrix} T_{pq} & \frac{1}{2} & & T \\ M_{T_{pq}} & m_{t_i} & & M_T \end{pmatrix} \begin{pmatrix} T_{pq} & \frac{1}{2} & & T \\ M_{T_{pq}} & m_{t_i} & & M_T \end{pmatrix} \\
 &\times \frac{2J+1}{2J_{pq}+1} {}_a \langle \bar{p} \bar{q}; J_{pq} T_{pq} \bar{i}; JT | \hat{V}^{3N} | \bar{r} \bar{s}; J_{pq} T_{pq} \bar{i}; JT \rangle_a. \tag{2.40}
 \end{aligned}$$

Again we stress that further simplifications of the isospin Clebsch-Gordan coefficients are not possible for $N \neq Z$ nuclei, and we emphasize that these formulas remain valid also for Hartree-Fock reference states and Hartree-Fock bases used to compute the matrix elements (2.38) to (2.40).

Altogether, using Eqs. (2.38)-(2.40) we are able to compute the necessary matrix elements of the 3N interaction in NO2B approximation directly from the JT -coupled matrix elements. However, as pointed out before it becomes practically challenging to store the complete set of JT -coupled 3N matrix elements beyond $E_{3\max} = 16$. As evident from Eqs. (2.38)-(2.40), for a given truncation $E_{3\max}$ only a subset of 3N matrix elements is needed because the summations over \bar{i} , \bar{j} and \bar{k} run over hole states, i.e., occupied orbitals in the reference state, only. In order to take full advantage of this we have merged our codes for the computation of the JT -coupled matrix elements starting from the antisymmetrized Jacobi matrix elements with the production code of the normal-ordered matrix elements using Eqs. (2.38)-(2.40). In addition, we exploit the fact that identical JT -coupled 3N matrix elements contribute to normal-ordered matrix elements of different reference states, e.g., of different nuclei, we start from. Therefore, we apply the following modus operandi: first we define a set of nuclei or, more generally, reference states we want to investigate.

Next, we identify all JT -coupled matrix elements that contribute to the normal-ordered matrix elements for all reference states under investigation, but without actually computing them during this process. In the next step we loop through the vector of JT -coupled 3N matrix elements and precompute the subset we have identified before. In this way JT -coupled matrix elements contributing to normal-ordered matrix elements of different reference states are computed only once. Finally, we compute the normal-ordered matrix elements according to Eqs. (2.38)-(2.40) using the precached JT -coupled matrix elements. To make each of the steps most efficient we use an OpenMP parallelization at each stage of the calculation. In practice an additional complication arises if JT -coupled matrix elements that differ from our standard storage scheme by the ordering of the single-particle orbitals are requested, since we choose a particular order to exploit antisymmetry. In these cases additional angular-momentum recouplings involving $6j$ -symbols may be necessary which, however, can be done very efficiently. The details about these recouplings can be found in Ref. [96]. Finally, another look at Figure 2.1 reveals that the T -coefficients, i.e., the transformation coefficients between the antisymmetrized HO Jacobi and JT -coupled scheme states, which we pre-cache during the calculation of the 3N matrix elements need the same amount of memory as the JT -coupled 3N matrix elements themselves. Thus, the available memory may again become critical. The key to overcome is at the heart of our storage scheme of the 3N matrix elements, namely the existence of the $(\bar{a}\bar{b}\bar{c}, \bar{a}'\bar{b}'\bar{c}')$ -blocks: for the computation of a given JT -coupled matrix elements only T -coefficients involving the specific quantum numbers $(\bar{a}\bar{b}\bar{c})$ and $(\bar{a}'\bar{b}'\bar{c}')$ enter. Therefore, we split the calculation of normal-ordered matrix elements into different runs, each covering the contributions from different sets of $(\bar{a}\bar{b}\bar{c}, \bar{a}'\bar{b}'\bar{c}')$ -blocks of JT -coupled 3N matrix elements. In a post-processing step we accumulate the contributions of all sets. In this way, we can decrease the memory needs per run simply by decreasing the number considered $(\bar{a}\bar{b}\bar{c}, \bar{a}'\bar{b}'\bar{c}')$ -blocks per run. Therefore, we can easily access normal-ordered 3N matrix elements at the NO2B approximation level for truncations $E_{3\max} \geq 16$ in an efficient manner while avoiding severe memory bottlenecks. The production of NO2B matrix-elements sets with large $E_{3\max}$ is limited only by the available computing time. However, one should always check how far this $E_{3\max}$ limit needs to be extended in practice, because other truncations of the many-body method may have artificial effects on the convergence pattern with respect to $E_{3\max}$. We will discuss this point in more detail in Section 9, where we present ab-initio calculations for heavy nuclei.

SECTION 3

The Similarity Renormalization Group

With the advent of nuclear forces rooted in QCD via chiral effective field theory and the technology to efficiently process the NN and 3N matrix elements, we would like to include those forces directly into many-body methods to solve the Schrödinger equation. However, nuclear interactions induce strong correlations in the exact many-body eigenstates, originating from the strong short-range repulsion at small inter-nucleon distances, which can be accounted for in huge many-body model spaces only. In comparison to traditional, more phenomenological NN potentials such as, e.g., the Argonne V18 potential [8], the chiral interactions already have a softer character due to the momentum-space cutoff. Nevertheless it is hardly feasible to converge, for instance, NCSM-type calculations beyond the very light nuclei, as we will also see in Part II of this work. Therefore, we have to insert an intermediate step before we can actually apply the chiral nuclear forces, that is, we need to soften the initial nuclear forces and, thus, tame the strong short-range correlations. This will lead to improved convergence properties in the subsequent solution of the Hamiltonian eigenvalue problem.

In this work, we concentrate on the Similarity Renormalization Group (SRG)[52, 103, 104, 105, 106, 107] as tool to soften the initial interactions. As we will see, the method yields a softened nuclear interaction independent of the many-body model space or nucleus under consideration, i.e., the resulting interactions remain universal and may enter identically in various many-body methods. Furthermore, the inclusion of 3N interactions into the SRG framework can be achieved in a consistent way. In the first subsection we introduce the general formalism of the SRG, and consider the treatment of 3N interactions in the formalism in more detail in Section 3.2. Finally, we discuss the frequency conversion of HO matrix elements, which can be used, e.g., to convert SRG-transformed matrix elements to a lower HO frequency than the one used for the transformation. In practice this is relevant to cure shortcomings of the SRG model space.

3.1 General Formalism

The basic concepts of the SRG are based on a unitary transformation of the Hamiltonian $\hat{H} = \hat{H}_{\alpha=0}$, given by

$$\hat{H}_\alpha = \hat{U}_\alpha^\dagger \hat{H}_{\alpha=0} \hat{U}_\alpha, \quad (3.1)$$

where α is a continuous parameter the unitary-transformation operator \hat{U}_α depends on. The transformed Hamiltonian is denoted by \hat{H}_α . By differentiating the transformed Hamiltonian with respect to the flow parameter and using $\hat{U}_\alpha^\dagger \hat{U}_\alpha = \hat{\mathbb{1}}$ we obtain the renormalization group flow equation

$$\frac{d}{d\alpha} \hat{H}_\alpha = [\hat{\eta}_\alpha, \hat{H}_\alpha], \quad (3.2)$$

where we have introduced a commutator on the right-hand side and defined the generator

$$\hat{\eta}_\alpha = [-\hat{U}_\alpha^\dagger \frac{d}{d\alpha} \hat{U}_\alpha, \hat{H}_\alpha] \quad (3.3)$$

that explicitly depends on the parameter α also referred to as flow parameter in the following. Following exactly the same steps one obtains the flow equations for all other observables \hat{O} of interest

$$\hat{O}_\alpha = \hat{U}_\alpha^\dagger \hat{O}_{\alpha=0} \hat{U}_\alpha \quad \Rightarrow \quad \frac{d}{d\alpha} \hat{O}_\alpha = [\hat{\eta}_\alpha, \hat{O}_\alpha]. \quad (3.4)$$

Thus, we have obtained first-order differential equations for the evolved Hamiltonian and observables with the initial conditions $\hat{H}_{\alpha=0} = \hat{H}$ and $\hat{O}_{\alpha=0} = \hat{O}$. Additionally, we have the differential equation

$$\frac{d}{d\alpha} \hat{U}_\alpha = -\hat{U}_\alpha \hat{\eta}_\alpha \quad (3.5)$$

with the initial condition $\hat{U}_{\alpha=0} = \hat{\mathbb{1}}$. For the applications in this work, we avoid the determination of the explicit form of the unitary operator \hat{U}_α , but instead we aim at the direct solution of the flow equation (3.2) for the evolved Hamiltonian. If one is interested in the consistent evolution of different operators \hat{O} [108, 109], one needs to solve Eqs. (3.2) and (3.4) simultaneously, because the generator $\hat{\eta}_\alpha$ typically depends on the evolved Hamiltonian \hat{H}_α itself, as we will see in the following. In this case it may be more convenient to solve Eq. (3.5) for \hat{U}_α and to apply it explicitly according to Eq. (3.4).

Evidently, the physics behind the SRG transformation is governed by the generator $\hat{\eta}_\alpha$ which fully determines the evolved Hamiltonian and operators. The only constraint for the choice of an appropriate generator is that it needs to be antihermitian, which follows from

$$\hat{\eta}_\alpha + \hat{\eta}_\alpha^\dagger = -\frac{d}{d\alpha} (\hat{U}_\alpha \hat{U}_\alpha^\dagger) = \frac{d}{d\alpha} \hat{\mathbb{1}} = 0. \quad (3.6)$$

Hence, one is very flexible to tune the generator. This freedom has been exploited and led to studies of various generators in the literature [110, 111, 112]. The generator we adopt in the following was proposed by Szpigel and Perry in Ref. [104] and was first applied in the context of nuclear theory by Bogner et al. in Ref. [52]. It is defined as the commutator of the intrinsic kinetic energy $\hat{T}_{\text{int}} = \hat{T} - \hat{T}_{\text{cm}}$ with the transformed Hamiltonian

$$\hat{\eta}_\alpha = \left(\frac{2\mu}{\hbar^2}\right)^2 [\hat{T}_{\text{int}}, \hat{H}_\alpha], \quad (3.7)$$

with the reduced nucleon mass $\mu = \frac{m_N}{2}$ and a prefactor that gives the flow-parameter the unit [length⁴]. From this definition it follows that a possible fix point of the SRG flow is defined by a transformed Hamiltonian that commutes with the intrinsic kinetic energy, because in this case the generator vanishes. If we think about the flow equation represented in the relative momentum eigenstates, it follows that the Hamiltonian matrix is transformed into a band-diagonal form if it approaches this fix point. This reflects the behavior we are aiming at, namely the decoupling of high- and low-momentum or energy components of the model space, because this coupling in the initial Hamiltonian has its origin in the strong correlations generated by the short-range repulsion. Stated differently, the generator (3.7) defines a continuous unitary transformation that tames the short-range correlations and consequently leads to improved convergence behavior with respect to the model-space size in many-body calculations. We show that this is indeed the case during the discussion in the next subsection and throughout Part II. Here, we stress that the choice of the generator is disconnected from the investigated nuclei or the many-body method, it is based on the general idea to decouple high- and low-momentum degrees of freedom only. Clearly, this is of practical importance since we can use the same interaction in different many-body approaches allowing, e.g., for cross-checks based on the identical inputs. This is an advantage compared to, e.g., the Okubo-Lee-Suzuki (OLS) renormalization scheme [113, 114], which is so far the only other method capable of explicitly including 3N interactions, see, e.g., Ref. [77].

So far, all equations and derivations we have discussed are operator relations valid in an A -body Hilbert space or a Fock space and, thus, are independent of the basis. A peculiarity is that the SRG flow induces irreducible higher-order many-body contributions to the evolved operators, which is also known from other renormalization schemes, e.g., the OLS method or the unitary correlation operator method (UCOM) [115, 103]. To understand this in the context of the SRG transformation we can assume, for instance, an initial irreducible two-body interaction, e.g., written in second quantization. Plugging this into the commutators on the right-hand side of the flow equation (3.2) reveals that an infinitesimal step in the flow parameter induces irreducible operator contributions beyond the two-body level. Hence, at any finite value of α irreducible contributions to all particle numbers are generated and the evolved Hamiltonian can be decomposed using a cluster expansion [115, 103]

$$\hat{H}_\alpha = \hat{H}_\alpha^{[1]} + \hat{H}_\alpha^{[2]} + \hat{H}_\alpha^{[3]} + \hat{H}_\alpha^{[4]} + \dots \quad (3.8)$$

with the irreducible k -body operators $\hat{H}_\alpha^{[k]}$. However, in practice it is not feasible to solve the flow equation and account for irreducible A -body interactions as formally required. We have to truncate the cluster expansion at the k -body level with $k < A$. We discuss why this is necessary and how it is achieved below. Formally, this truncation may pose a potential problem: the unitarity of the transformation is violated. As long as no induced contributions are omitted the eigenvalues of the Hamiltonian in A -body space are invariant under SRG transformations. But due to the truncation of (3.8) the eigenvalues are not necessarily invariant and instead depend on the SRG flow parameter if the neglected n -body operators with $n > k$ yield relevant contributions. As a consequence, we can study the dependence of eigenvalues of the transformed Hamiltonians on systematic variations of the SRG flow parameter as a diagnostic tool to assess the significance of the induced but discarded multi-nucleon forces. We will come back to this in Part II and in particular in Section 6.

For the solution of the flow equation (3.2) for the evolved Hamiltonian we represent the operator equation (3.2) in a convenient basis in k -body space. Obviously, the k -body basis is not capable to represent n -body operators with $n > k$, i.e., these induced n -body contributions cannot be extracted. Hence, the choice of a k -body basis implies the truncation of the cluster expansion at the k -body level. The matrix elements after the SRG evolution contain all operator contributions up to the k -body level. However, to maintain a universal interaction for later applications in many-body calculations it is necessary to separate the contributions of each individual k -body operator in terms of matrix elements. This can be accomplished by successive subtraction of the lower-body contributions represented in k -body space from the k -body matrix elements resulting from the SRG evolution, i.e.,

$${}_a \langle \alpha_1 \dots \alpha_k | \hat{H}_\alpha^{[k]} | \beta_1 \dots \beta_k \rangle_a = {}_a \langle \alpha_1 \dots \alpha_k | \hat{H}_\alpha | \beta_1 \dots \beta_k \rangle_a - \sum_{i=1}^{k-1} {}_a \langle \alpha_1 \dots \alpha_k | \hat{H}_\alpha^{[i]} | \beta_1 \dots \beta_k \rangle_a. \quad (3.9)$$

The SRG evolution in two-body space, i.e., neglecting all induced three- and multi-nucleon contributions, has become a standard tool to soften the nuclear interactions over the past years [52, 103, 116], therefore, we skip its discussion here. Instead, throughout this work, we investigate the SRG evolution in three-body space, i.e., we truncate the cluster expansion at the 3N interaction level and thus can include consistently the induced and initial 3N contributions and have the opportunity to distinguish their effects in many-body calculations later on. We discuss the details of the SRG evolution in three-body space in the next subsection. In this case, the subtraction procedure shown in Eq. (3.9) simplifies to a single step, namely the subtraction of the evolved irreducible NN interaction represented in three-body space from the SRG transformed NN+3N Hamiltonian. In addition, we note that first attempts to account for SRG-induced four-body contributions are currently ongoing and first results are presented in Refs. [117, 118] including a detailed analysis of the subtraction procedure (3.9) which is more involved in the four-body case.

3.2 Consistent Evolution of NN+3N Forces in Three-Body Space

As indicated already above, the solution of the SRG flow equation is de facto accomplished using a basis representation. We may choose any basis that is computationally convenient. Our initial Hamiltonian consists of the intrinsic kinetic energy, a NN interaction \hat{V}^{NN} and a 3N interaction \hat{V}^{3N}

$$\hat{H}_{\alpha=0} = \hat{T}_{\text{int}} + \hat{V}^{\text{NN}} + \hat{V}^{\text{3N}}. \quad (3.10)$$

For consistency it is required to include also the 3N interaction in the evolution and to account for the SRG-induced 3N contributions. Accordingly, we need to perform the SRG evolution using a convenient 3N basis. Remembering our discussions in Section 2, it is obvious that the antisymmetrized HO Jacobi basis states $|E_{12}iJ_{12}T_{12}\rangle_a$ are the most convenient set. Thus, we represent the flow equation in this basis by inserting corresponding identities on the right-hand side of Eq. (3.2) and obtain

$$\begin{aligned} \frac{d}{d\alpha} \langle E_{12}iJ_{12}T_{12} | \hat{H}_\alpha | E'_{12}i'J'_{12}T_{12} \rangle &= \left(\frac{2\mu^2}{\hbar^2} \right)^2 \sum_{E''_{12}i''}^{E''_{12} \leq E_{\text{SRG}}(J_{12})} \sum_{E'''_{12}i'''}^{E'''_{12} \leq E_{\text{SRG}}(J_{12})} \left[\right. \\ &\langle E_{12}iJ_{12}T_{12} | \hat{T}_{\text{int}} | E''_{12}i''J_{12}T_{12} \rangle \langle E''_{12}i''J_{12}T_{12} | \hat{H}_\alpha | E'''_{12}i'''J_{12}T_{12} \rangle \langle E'''_{12}i'''J_{12}T_{12} | \hat{H}_\alpha | E'_{12}i'J_{12}T_{12} \rangle \\ &- 2 \langle E_{12}iJ_{12}T_{12} | \hat{H}_\alpha | E''_{12}i''J_{12}T_{12} \rangle \langle E''_{12}i''J_{12}T_{12} | \hat{T}_{\text{int}} | E'''_{12}i'''J_{12}T_{12} \rangle \langle E'''_{12}i'''J_{12}T_{12} | \hat{H}_\alpha | E'_{12}i'J_{12}T_{12} \rangle \\ &\left. + \langle E_{12}iJ_{12}T_{12} | \hat{H}_\alpha | E''_{12}i''J_{12}T_{12} \rangle \langle E''_{12}i''J_{12}T_{12} | \hat{H}_\alpha | E'''_{12}i'''J_{12}T_{12} \rangle \langle E'''_{12}i'''J_{12}T_{12} | \hat{T}_{\text{int}} | E'_{12}i'J_{12}T_{12} \rangle \right]. \end{aligned} \quad (3.11)$$

We exploit the fact that the Hamiltonian and the generator do not connect Jacobi basis states with different quantum numbers J_{12}^π and T_{12} . Thus, the evolution equation can be solved independently for each channel characterized by $(J_{12}^\pi T_{12})$. For each channel we have to solve a set of coupled first-order differential equations for the matrix elements ${}_a \langle E_{12}iJ_{12}T_{12} | \hat{H}_\alpha | E'_{12}i'J'_{12}T_{12} \rangle_a$. An important detail in Eq. (3.11) is the truncation of the formally infinite sums over the antisymmetrized HO Jacobi states by defining a maximum energy quantum number $E_{\text{SRG}}(J_{12})$ that we choose to depend on the total relative angular momentum J_{12} . We typically use a larger SRG model space for small J_{12} , which are expected to contain the most important contributions, and use a somewhat smaller model space for larger J_{12} . We refer to this truncated space as SRG model space. Of course the convergence of this truncation needs to be checked explicitly, which we do in ab-initio many-body calculations of light to medium-mass nuclei in Section 5 and for medium-mass to heavy nuclei in Section 9.

Technically, we use a standard Runge-Kutta solver with adaptive step-size control to evolve the Hamiltonian up to a certain flow-parameter α by means of Eq. (3.11). The adaptive step size is crucial to resolve the significant changes at the beginning of the flow with high precision, while it is adequate to increase the step size for larger values of α . The SRG transformation in three-body space can still be performed very efficiently due to the fact that the right-hand side of the flow equation can be expressed by matrix multiplications which can be implemented using cache-optimized, parallelized BLAS routines [119]. For

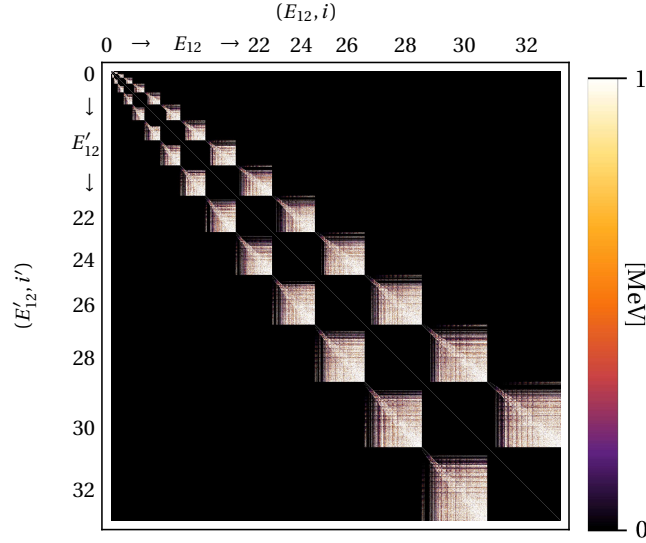


Figure 3.1 – Matrix plot of the absolute values of the intrinsic kinetic-energy matrix elements ${}_a \langle E'_{12} i' J_{12} T_{12} | \hat{T}_{\text{int}} | E_{12} i J_{12} T_{12} \rangle_a$ that build a fix point of the SRG flow. The used HO frequency is $\hbar\Omega = 20 \text{ MeV}$.

instance, the triton-channel $(J_{12}^\pi T) = (\frac{1}{2}^+ \frac{1}{2})$ matrix elements can be transformed for a typical value of $\alpha = 0.08 \text{ fm}^4$ with the typical model model-space truncation $E_{\text{SRG}}(\frac{1}{2}) = 40$ in less than one hour on a standard compute node.

Having the SRG transformation in three-body space under control, we are in the position to define the following three types of Hamiltonians emerging from different truncations of the SRG transformation: we refer to the *NN+3N-full* Hamiltonian when the initial Hamiltonian contains NN and 3N interactions and the SRG transformation is done in a three-body basis. Thus, the 3N contributions of this Hamiltonian stem from SRG-induced contributions and the transformed initial 3N interaction. Additionally, we define the *NN+3N-induced* Hamiltonian, where the initial Hamiltonian contains an NN interaction only, but the SRG transformation is done in three-body space as shown in Eq. (3.11). Accordingly, this Hamiltonian accounts for the induced 3N contributions originating from the initial NN interaction. These contributions are neglected in the *NN-only* Hamiltonian which results from an SRG transformation in two-body space and the initial Hamiltonian contains a NN force only. In all three Hamiltonians four- and multi-nucleon contributions are neglected and can, thus, be assessed only indirectly via the sensitivity of observables, e.g., the energy eigenvalues, to variations of the flow parameter α .

To confirm that the SRG transformation does as intended and behaves as described in the formal part above, it is crucial to investigate a number of cross-checks. Therefore, we show in Figure 3.1 a matrix plot of the absolute value of matrix elements of the intrinsic kinetic energy which is the fix point of the SRG flow. The color code is defined in the legend where absolute values larger than 1 MeV are represented by white colors. It can be seen that non-vanishing matrix elements exist only on the diagonal and in super- and sub-diagonal (E_{12}, E'_{12}) blocks. This means, we expect the transformed Hamilton matrix

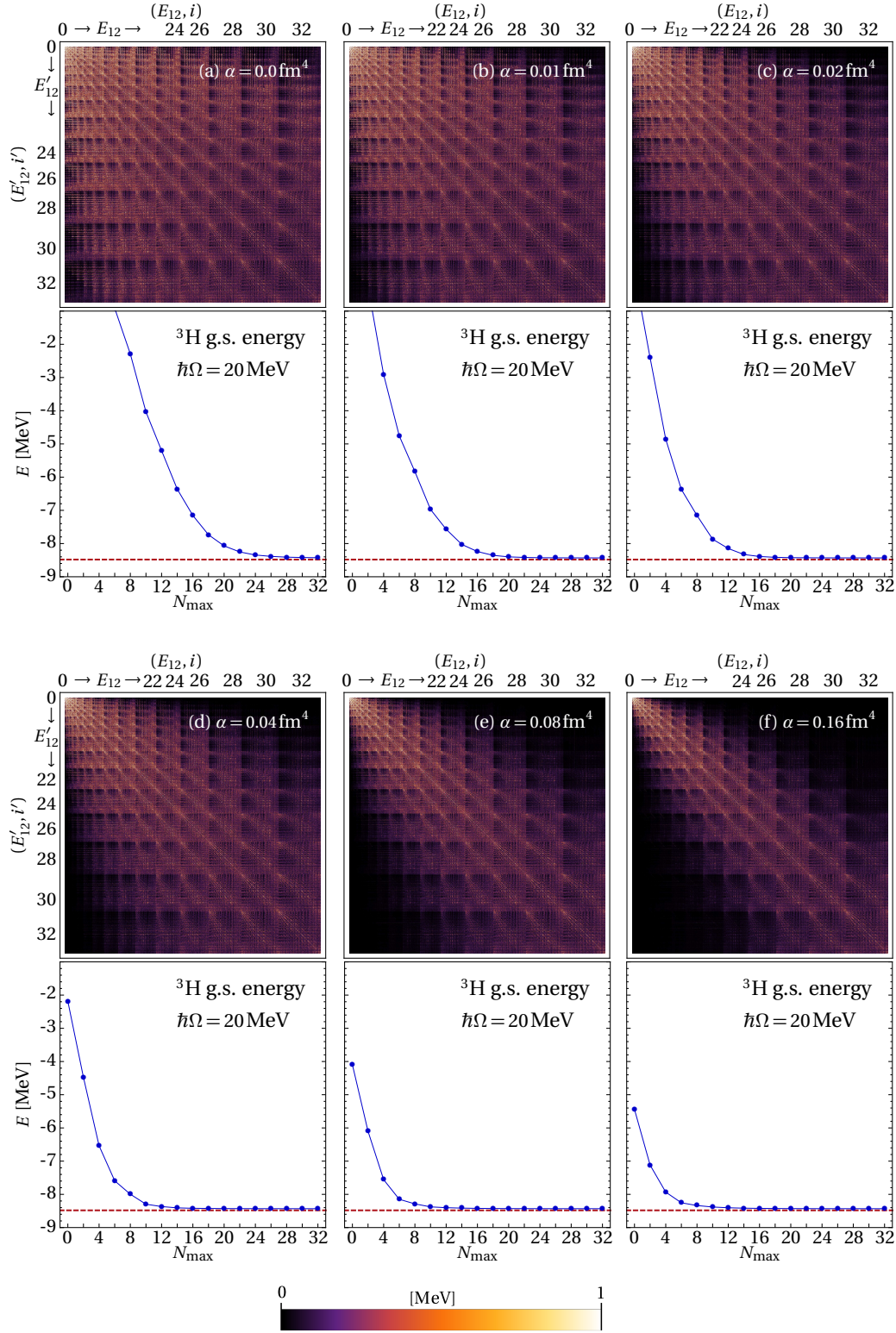


Figure 3.2 – Upper panels: Matrix plots of the absolute values of the SRG transformed interaction matrix elements ${}_a\langle E'_{12}i'J_{12}T_{12}|\hat{H}_\alpha - \hat{T}_{\text{int}}|E_{12}iJ_{12}T_{12}\rangle_a$ for the triton channel ($J^\pi T = \frac{1}{2}^+ \frac{1}{2}$) up to energy quantum number $E_{12} = 32$ for the NN+3N-full Hamiltonian for increasing SRG flow parameter α . Lower panels: Convergence of the triton ground-state energy as function of the NCSM model space for the flow parameter corresponding to the upper matrix plot, respectively. (published in [44])

to converge towards this form with increasing flow parameter. To confirm this, we show in Figure 3.2 matrix plots of the evolved interactions for different flow parameters in the triton channel, i.e., $(J_{12}^\pi T_{12}) = (\frac{1}{2}^+ \frac{1}{2})$ using the same color code as before. Panel (a) shows the bare interaction, i.e., $\alpha = 0\text{fm}^4$, where we can identify the strong coupling between low- and high-lying energetic states originating from the short-range repulsion. One major goal of the SRG is to decouple these low and high energy (or similarly momentum) regimes by suppressing far off-diagonal matrix elements. From Figure 3.2 it is evident that this is indeed accomplished since the matrix evolves into a more band-diagonal form with increasing flow parameter. As argued above, a connected objective of the SRG transformation is to obtain an improved convergence behavior with respect to model-space sizes of the subsequent many-body calculations. To investigate this we show the corresponding ground-state energies of the triton as function of the model-space size of NCSM calculations as lower panels in Figure 3.2. We find a dramatic improvement of the model-space convergence with increasing flow parameter compared to the bare interaction. Whereas for the bare interaction a $N_{\text{max}} = 28$ model space is necessary to reach sufficient convergence, for the $\alpha = 0.08\text{fm}^4$ Hamiltonian we need only $N_{\text{max}} = 12$. This improvement on the convergence is key for the results we study in Part II in various many-body methods and reflects the taming of the strong correlations in the exact many-body eigenstates. Furthermore, the converged energies are identical for all flow parameters confirming the unitarity of the transformation, which is exact here, since all induced interactions relevant for the triton are retained due to the SRG evolution in the three-body space. This may change when we use these SRG transformed interactions in calculations for heavier nuclei as we discuss in detail in Section 6.

3.3 The Frequency-Conversion Technique

In this section we deal with a rather technical but important detail when performing the SRG transformation in the HO basis with a fixed frequency Ω . For variations of the HO frequency in the many-body calculations the SRG transformation is done for each frequency separately, which may seem as a disadvantage of performing the SRG transformation in HO space instead of using, e.g., a momentum-space representation [103, 120] and transforming the SRG transformed matrix elements into the HO basis with convenient frequency afterwards. Another, more formal argument, which indicates that using an inappropriate HO frequency during the SRG evolution might be problematic, is that the energy range covered by the SRG model space is given by the product $E_{\text{SRG}}(J_{12}) \cdot \hbar\Omega$, i.e., for a given truncation $E_{\text{SRG}}(J_{12})$ the energy range is smaller for low frequencies Ω . If this is the case, the subsequent many-body calculations may exhibit an artificial frequency dependence due to an insufficient coverage of the relevant energies or momenta of the interaction.

However, there is a simple workaround that avoids this complication: we perform the SRG evolution for a sufficiently large parent frequency $\tilde{\Omega}$ that guarantees the proper representation of the Hamiltonian. Afterwards, we convert the matrix elements with respect to the parent frequency Ω_{SRG} into matrix elements with the targeted frequency Ω used in

the many-body calculation. This can be accomplished by means of a basis transformation for which the overlaps of two antisymmetrized HO Jacobi basis states are necessary. These are given by

$$\begin{aligned}
 & \langle E_{12} i J_{12}^\pi T_{12} | E'_{12} i' J_{12}^\pi T_{12} \rangle \\
 &= \sum_{N_1 N_2} \sum_{\tilde{N}_1 \tilde{N}_2} \sum_{\alpha} \delta_{E_{12}, 2N_1+L_1+2N_2+L_2} \delta_{\tilde{E}_{12}, 2\tilde{N}_1+L_1+2\tilde{N}_2+L_2} C_{N_1 N_2 \alpha}^i C_{\tilde{N}_1 \tilde{N}_2 \alpha}^{\tilde{i}} \\
 & \int d\pi_1 \pi_1^2 R_{N_1 L_1}(\pi_1) \tilde{R}_{\tilde{N}_1 L_1}(\pi_1) \int d\pi_2 \pi_2^2 R_{N_2 L_2}(\pi_2) \tilde{R}_{\tilde{N}_2 L_2}(\pi_2), \tag{3.12}
 \end{aligned}$$

where the radial HO wave functions corresponding to the parent frequency are denoted by $\tilde{R}_{\tilde{N}_i L_i}$ and those with respect to the target frequency by $R_{N_i L_i}$. In addition, the $C_{N_1 N_2 \alpha}^i$ are the CFPs as defined in Eq. (2.7).

Of course, also this transformation can be performed only within a finite model space and we use a truncation consistent with the SRG model space. However, due to the fact that both the SRG-transformed Hamiltonian matrix and the transformation matrices given by the overlaps (3.12) are band-diagonal, only matrix elements from limited energy regions are mixed. Accordingly, we find the 3N matrix elements which enter the subsequent many-body calculations up to a given $E_{3\max} < E_{\text{SRG}}(J_{12})$ in practice not affected by this truncation, since $E_{3\max}$ is usually much smaller than the limits for the energy quantum numbers used in the SRG transformation.

We come back to this frequency-conversion technique in Section 5, where we also test different SRG model spaces. Further details on this topic can also be found in Refs. [44, 118].

Part II

Three-Nucleon Forces in Ab-Initio Nuclear Structure

INTRODUCTION TO PART II

The inclusion of chiral 3N interactions into ab-initio nuclear structure calculations is vital for predictions of nuclear properties and to confront chiral NN+3N Hamiltonians with the wealth of experimental data. Over the past five years ab-initio nuclear theory with chiral 3N interactions has seen significant progress in the domain of light nuclei but also for the medium-mass regime, for which a number of new nuclear structure approaches have emerged. The inclusion of explicit 3N interactions often requires formal extensions and additionally the computational cost is significantly increased. Therefore, also approximate treatments of the 3N interactions are of importance, in particular in the medium mass regime. The discussion in the second part of this work builds on the SRG-evolved chiral NN+3N Hamiltonians and include them in different contexts in ab-initio calculations throughout the p -shell for ground states and nuclear spectra, and for binding energies up to the heavy-mass regime. We use different types of SRG-evolved Hamiltonians to allow for the discussion of effects of SRG-induced 3N interactions and of effects caused by the initial chiral 3N interactions.

We start with the description of the ab-initio nuclear structure methods applied throughout this part with emphasis on their extension to include 3N interactions. This includes the discussion of the no-core shell model (NCSM) and its importance truncated extension (IT-NCSM) as well as coupled-cluster (CC) theory for ground-state energies. Note that another promising approach, namely Padé-resummed degenerate perturbation theory at high-orders, is discussed in Appendix A.

In Section 5 we investigate the consequences of the finite HO model space that is used during the SRG transformation for ground-state energies and excitation spectra. This is necessary to exclude for the remaining studies artificial effects from the model-space truncations used during the SRG transformation.

In Section 6, we apply the SRG-evolved chiral NN+3N interactions in ab-initio studies throughout the p -shell for the discussion of 3N-force effects on binding energies and nuclear spectra. We encounter significant effects of SRG-induced multi-nucleon interactions and discuss a possibility to circumvent these.

In Section 7 we study excitation spectra with 3N interactions and perform a first sensitivity analysis in the ^{12}C and ^{10}B excitation spectra with respect to uncertainties of the chiral Hamiltonian encoded by variations of the low-energy constants or the cutoff momentum of the chiral 3N interaction.

Then, we validate the normal-ordered two-body approximation introduced in Section 2.3 by several benchmark calculations in the p -shell but also for selected closed-shell medium-mass nuclei up to ^{56}Ni . The excellent quality of this approximation gives con-

confidence in ab-initio predictions of ground-state energies also for heavy-mass nuclei. We present first ab-initio studies for the even oxygen isotopes including the neutron-rich isotopes at the neutron drip line using the IT-NCSM and ab-initio calculations for selected closed-shell nuclei up to ^{132}Sn using the coupled-cluster approach in Section 9. For the latter we pay special attention to a careful analysis of the uncertainties and discuss how most of them can be eliminated.

SECTION 4

Many-Body Methods and their Extension to 3N Interactions

Before starting the investigation of the effects of 3N interactions in nuclei throughout the light-, medium-, and also heavy-mass regime, we briefly introduce different ab-initio nuclear structure methods which we apply in the following sections. In particular, we emphasize for each method how and at what level of complication the generalization to an explicit inclusion of 3N interactions is realized. We start with the no-core shell model, which is a standard tool for the 'exact' solution of the Schrödinger equation by means of converting it into a large-scale matrix-eigenvalue problem [121]. From the eigenvectors one can compute any observable of interest. The applicability of this approach is limited by the dimension of the many-body matrix. In Section 4.2, we discuss the importance-truncated no-core shell model which also aims at the solution of the matrix-eigenvalue problem of the Hamiltonian, but using an a priori importance measure of the individual many-body basis states. The strategy is to reduce the model-space dimension from the outset by excluding basis states that are assumed to be less relevant. We will see that this extends the applicability compared to the conventional no-core shell model in terms of model-space size and nucleon number. In Section 4.3 we discuss the generalities of coupled-cluster theory with focus on the coupled cluster with singly- and doubly-excited clusters, and mention briefly triples corrections. This approach has been developed further in the nuclear physics context over the recent years [97], and is particularly successful for nuclei with closed sub-shells. Instead of a large-scale matrix eigenvalue problem, one needs to solve a set of coupled nonlinear so-called amplitude equations, whose number scales more gently compared to the above mentioned matrix dimension. In this work we apply the coupled-cluster framework for studies of ground-state energies for medium-mass and heavy nuclei. Finally, we discuss the possibility to extract ground- and excited-state energies from high-order degenerate many-body perturbation theory in combination with Padé approximants that yields excellent agreement with results from the exact no-core shell model. However, so far we did not apply 3N interactions in this approach and, therefore, present

Hamiltonian	included interactions
NN-only	SRG-transformed chiral NN interaction no 3N interaction
NN+3N-induced	SRG-transformed chiral NN + SRG-induced 3N interactions
NN+3N-full	SRG-transformed chiral NN and 3N + SRG-induced 3N interactions

Table 4.1 – Definition of the different types of Hamiltonians used throughout Parts II and III. For further details see Section 3.

it in Appendix A.

The nuclear Hamiltonian used in these methods and during the rest of Part II of this work has the general form

$$\hat{H} = \hat{T}_{\text{int}} + \hat{V}^{\text{NN}} + \hat{V}^{\text{3N}}, \quad (4.1)$$

where $\hat{T}_{\text{int}} = \hat{T} - \hat{T}_{\text{cm}}$ is the intrinsic kinetic energy operator, where \hat{T}_{cm} denotes the center-of-mass kinetic energy. For the NN interaction we typically adopt the SRG-evolved chiral N³LO potential by Entem and Machleidt as described in Section 1.1. If we conduct a calculation at the NN-only level, the \hat{V}^{3N} term in the Hamiltonian is not present. For calculations with the NN+3N-induced or NN+3N-full Hamiltonian, the term \hat{V}^{3N} corresponds to the SRG-induced 3N interaction or the SRG-induced plus SRG-transformed initial chiral 3N interaction, respectively. For later reference we summarize the different types of Hamiltonians that result after the SRG transformation in Table 4.1.

4.1 The No-Core Shell Model

The no-core shell model (NCSM) is an established and powerful ab-initio method aiming at the exact solution of the time-independent Schrödinger equation for a few energetically low-lying eigenstates [121, 41]. The method is based upon representing the A -body Hamilton operator eigenvalue problem $\hat{H}|\Psi_\nu\rangle = E_\nu|\Psi_\nu\rangle$, with energy eigenvalue E_ν and corresponding eigenstate $|\Psi_\nu\rangle$, in an A -body model space \mathcal{M} spanned by harmonic oscillator (HO) eigenstates $\{|\Phi_i\rangle\}$. Moreover, ν represents a collective index summarizing the good quantum numbers total angular momentum I , its projection M_I , parity π , and of course the energy eigenvalue E_ν , i.e., $\nu = \{E_\nu, I^\pi M_I\}$.

Multiplication of the Schrödinger equation from the left by a basis state $\langle\Phi_i|$ we obtain the matrix-eigenvalue problem of the Hamiltonian matrix

$$\begin{pmatrix} H_{11} & H_{12} & \cdots \\ H_{21} & H_{22} & \cdots \\ \vdots & \vdots & \ddots \end{pmatrix} \begin{pmatrix} C_1^{(\nu)} \\ C_2^{(\nu)} \\ \vdots \end{pmatrix} = E_\nu \begin{pmatrix} C_1^{(\nu)} \\ C_2^{(\nu)} \\ \vdots \end{pmatrix}, \quad (4.2)$$

with $H_{ij} = \langle \Phi_i | \hat{H} | \Phi_j \rangle$ and the $C_i^{(v)}$ are the expansion coefficients of the eigenstate in terms of the A -body HO basis states given by

$$|\Psi_v\rangle = \sum_{|\phi_i\rangle \in \mathcal{M}} |\Phi_i\rangle \langle \Phi_i | \Psi_v \rangle = \sum_{|\phi_i\rangle \in \mathcal{M}} C_i^{(v)} |\Phi_i\rangle. \quad (4.3)$$

Of course, in practice the model space needs to be truncated at a manageable finite size, which determines the number of unknown coefficients $C_i^{(v)}$ and the dimension of the matrix in Eq. (4.2). A defining element of the NCSM is its model-space truncation allowing only HO basis states $|\Phi_i\rangle$ whose excitation energy is at most $N_{\max} \hbar \Omega$ above the HO minimum-energy configuration. We illustrate this in Figure 4.1 for ^{12}C . Practical calculations are done for a series of model spaces with increasing N_{\max} and the convergence of the investigated observables with respect to this model-space truncation parameter is studied. Frequently, convergence cannot be reached due to computational limitations, and various extrapolation techniques are applied to obtain results for infinite model space, i.e., $N_{\max} \rightarrow \infty$. In case of absolute energies one benefits from the fact that the NCSM obeys the Ritz variational principle, and typically decreasing exponentials are chosen for the extrapolations [122, 123, 124, 44]. The variational character is maintained also when SRG transformed interactions are used, in contrast to Hamiltonians obtained from, e.g., Okubo-Lee-Suzuki transformations [114, 113]. Another advantage of the NCSM is its freedom to formulate the HO basis states $|\Phi_i\rangle$ either based on single-particle coordinates in terms of Slater determinants or using antisymmetrized Jacobi states. The latter are particularly suited to describe translational-invariant systems such as nuclei, because they separate the center-of-mass degree of freedom from the outset and render spurious center-of-mass contaminations impossible. We have used this variant already in Section 3.2 to obtain the triton ground-state energies shown in Figure 3.2. A crucial part is the antisymmetrization of the Jacobi basis states accomplished by diagonalizing the A -body antisymmetrization operator in a model space of non-antisymmetrized Jacobi states [79]. Then, eigenvectors with eigenvalue 1 define the antisymmetrized states as expansion in the non-antisymmetrized Jacobi states. We have encountered this procedure for the specific case of three-nucleon states before in the transformation of $3N$ matrix elements in Section 2. However, the setup of the matrix representation of the antisymmetrizer and its full diagonalization becomes computationally demanding with increasing nucleon number. Hence, the NCSM with antisymmetrized Jacobi basis states is usually not applied beyond nuclei with $A = 5$ [79]. Instead, one resorts to the second, equivalent formulation employing many-body Slater determinant (SD) states of ls -coupled HO single-particle states. In this case the antisymmetrization is trivially accomplished explicitly by the antisymmetrizer. The unique properties of the HO together with the N_{\max} -truncation scheme generate the advantage that the obtained eigenstates can be written as direct product of the intrinsic $|\Psi_{v,\text{int}}\rangle$ and the center-of-mass $|\Psi_{v,\text{cm}}\rangle$ parts of the state, i.e.,

$$|\Psi_v\rangle = |\Psi_{v,\text{int}}\rangle \otimes |\Psi_{v,\text{cm}}\rangle \quad (4.4)$$

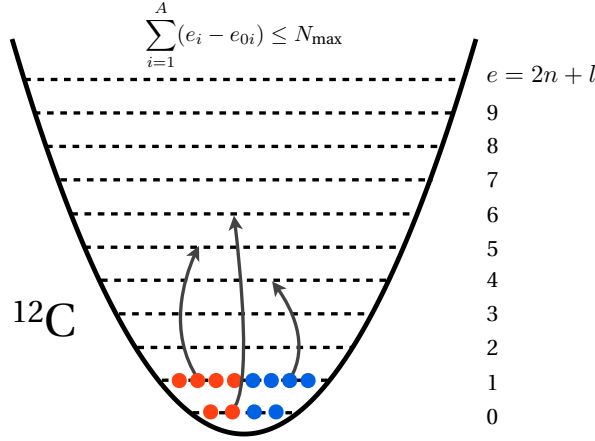


Figure 4.1 – Illustration of the N_{\max} -truncation scheme exemplarily for ^{12}C . The red and blue dots represent respectively the occupied proton and neutron single-particle states which form the unperturbed HO Slater determinant. Their energy quantum numbers are denoted by e_{0i} , quantum numbers of unoccupied state by e_i . The dashed lines indicate the single-particle energy shells. The NCSM model space includes all possible Slater determinants with excitation energy up to $N_{\max}\hbar\Omega$. All nucleons may contribute to the excitation energy — there exists no core of inert nucleons.

holds for any value of N_{\max} . We stress that this is not the case for other single-particle bases or different model-space truncation schemes. Property (4.4) is important to guarantee a proper description of the intrinsic states and observables of nuclei, without center-of-mass contaminations. In practice one uses the so-called Lawson method [125] to avoid solutions with excitations of the center-of-mass part by adding to the intrinsic Hamiltonian \hat{H}_{int} a HO Hamiltonian \hat{H}_{cm} in terms of the center-of-mass position $\vec{\xi}_0$ and momentum $\vec{\pi}_0$ with additional energy shift leading to vanishing zero-point energy, i.e.,

$$\hat{H}_{\text{cm}} = \frac{1}{2mA} \hat{\pi}_0^2 + \frac{mA\Omega^2}{2} \hat{\xi}_0^2 - \frac{3}{2}\hbar\Omega. \quad (4.5)$$

In this way one can avoid redundant states that differ only by their center-of-mass part, which we are not interested in for the description of the intrinsic properties of nuclei. In all calculations the Hamiltonian is replaced by $\hat{H}_\beta = \hat{H}_{\text{int}} + \beta \hat{H}_{\text{cm}}$. The parameter β is chosen such that no states with non-zero center-of-mass energies are encountered when solving the matrix eigenvalue problem for a set of targeted low-energy eigenstates.

A convenient property of the NCSM is that the inclusion of 3N interactions into its general framework is straightforward and requires no additional formal developments. This is due to the fact that the whole approach is formulated in terms of A -body states. The matrix elements of the 3N interaction (and also of the NN interaction) enter only during the setup of the A -body Hamilton matrix, i.e., when computing the Hamiltonian matrix elements H_{ij} . The inclusion of 3N interactions during the evaluation of such matrix elements with respect to SDs can be achieved easily, e.g., using Slater-Condon rules [126, 127]. Nevertheless, pioneering NCSM calculations with 3N interactions were particularly demanding, because they stored in memory the precomputed set of 3N matrix elements in the m -scheme

[78, 91, 90, 128, 89]. This implies a severe limitation to small model spaces due to the vast memory requirements of the $3N$ matrix elements discussed in Section 2.2.3. However, the benefit from our development of the JT -coupled $3N$ matrix-element scheme in combination with the efficient on-the-fly decoupling leads to a major breakthrough in this respect and, thus, allows to proceed to larger model spaces. Consequently, our scheme has been adopted in various NCSM codes, e.g., in the Many-Fermion Dynamics for nuclear structure (MFDn) code [99, 100, 101].

To obtain the set of low-lying eigenvalues and eigenvectors of the sparse Hamilton matrix, typically an iterative Lanczos algorithm is used [129, 130]. Each iteration requires a matrix-vector multiplication involving the the sparse Hamiltonian matrix (4.2). The inclusion of $3N$ interactions leads to an increased computational cost of these iterations because, compared to calculations with NN interactions, the Hamiltonian matrix becomes more dense, with one to two orders of magnitude more nonzero matrix elements [95]. Since the large-scale Hamiltonian matrix easily requires tens of TB memory if one approaches the model-space sizes that are necessary to converge the results, it is evident that a suitable distribution of the sparse matrix across a large number of compute nodes is mandatory. For details about this issue see, e.g., Ref. [95].

After all, the limitations of the NCSM are set by the model-space dimension, which grows factorially with N_{\max} and nucleon number A . Diagonalizations for 10^9 -dimensional model spaces are routinely feasible today, however, going beyond dimensions of 10^{10} remains prohibitive at this moment. We discuss a method to overcome this limitation by a reduction of the model-space sizes based upon a selection of the relevant basis states in the next subsection.

Finally, we mention that the long-range behavior of the HO wave functions that serve as many-body basis is problematic for the description of states of loosely bound systems such as halo nuclei or even scattering processes, which require the treatment of continuum effects. To account for this different extensions of the NCSM exist, and we cover this topic in Part III.

4.2 The Importance Truncated No-Core Shell Model

In the previous subsection we have discussed the NCSM as a method aiming at the exact solution of the large-scale Hamiltonian matrix eigenvalue problem with its advantages to provide access to all observables of interest through the eigenstates. The only drawback are the limitations due to the factorial increase of the model-space size with nucleon number A and truncation parameter N_{\max} which hinders the study of nuclei beyond the p -shell or to reach results close to convergence even for p -shell nuclei. Correspondingly, the aim for developments of alternative ab-initio methods must be to preserve the advantages of the NCSM as far as possible and to extend the range of accessible nuclei. If one sticks to the general approach to directly solve the matrix-eigenvalue problem of the Hamiltonian, a variant of the NCSM that requires a somehow reduced model-space size needs to be found. For the scope of this work we focus on the so-called importance-truncated no-core

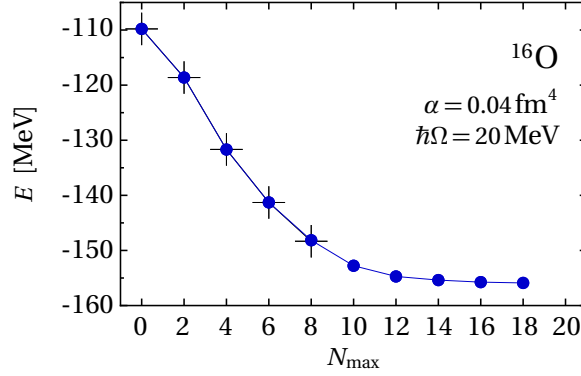


Figure 4.2 – Comparison of NCSM (+) to IT-NCSM (●) ^{16}O ground-state energies obtained with SRG-evolved NN-only Hamiltonian as function of the model-space size N_{\max} . The IT-NCSM energies coincide with those obtained within the NCSM and extend the accessible model spaces significantly beyond the NCSM regime, see also Ref. [27].

shell model (IT-NCSM) [42, 28, 27].

As already indicated, the general framework of the NCSM and IT-NCSM is the same. In particular, the IT-NCSM also employs A -body Slater determinants of single-particle HO states for a basis representation of the Hamiltonian, and the obtained matrix is diagonalized using a Lanczos algorithm targeting the low-energy eigenstates. However, the IT-NCSM model space is reduced to those configurations that are important for the description of the eigenstates of interest. In general, the selection of these most relevant configurations poses of course a formidable task. However, one can exploit the fact that we typically target the low-energy eigenstates of the Hamiltonian only, and the experience that for these states many of the amplitudes $C_i^{(v)}$ in expansion (4.3) are negligible. Of course, the size of the amplitudes depends strongly on the targeted states. Nevertheless, we can obtain a variational approximation of the states if we drop these less relevant configurations beforehand. This is exactly the procedure implemented in the IT-NCSM with the aid of an a priori importance measure for the individual basis configurations. However, we emphasize that a crucial part of the IT-NCSM formalism is the a posteriori recovery of contributions from the omitted configurations. Before we deal with the details of this method, we show in Figure 4.2 a proof-of-principle calculation of the ground-state energy of ^{16}O as function of N_{\max} obtained in the IT-NCSM and NCSM, where the latter is feasible. Both methods use identical inputs including an SRG-evolved NN interaction at flow parameter $\alpha = 0.04 \text{ fm}^4$, and the HO frequency $\hbar\Omega = 20 \text{ MeV}$ is used. The NCSM calculations shown as black crosses are feasible up to $N_{\max} = 8$, while $N_{\max} = 10$ would require the treatment of a 10^{10} -dimensional model space beyond present computational limits. Evidently, from the energies obtained within the NCSM it is hardly possible to provide a robust extrapolation $N_{\max} \rightarrow \infty$. The IT-NCSM energies are shown as blue discs and are on top of those obtained with the NCSM, which clearly demonstrates the reliability of the IT. At the same time the IT-NCSM delivers the ground-state energies up to $N_{\max} = 18$ model spaces and thus is able to reach convergence with respect to the model-space size. This allows for

stable extrapolations to the infinite model-space limit. Obviously, the IT-NCSM is able to treat significantly larger N_{\max} compared to the NCSM, and, therefore, facilitates ab-initio nuclear structure beyond the domain of NCSM while the results are in excellent agreement where both methods are applicable. More detailed benchmarks of the IT-NCSM versus NCSM also including different observables can be found in Refs. [28, 44].

The general procedure of the IT-NCSM is the following: one starts from a set of initial approximations of the M targeted eigenstates, which are the reference states $|\Psi_{\text{ref}}^{(m)}\rangle$. Usually we employ states obtained from previous NCSM calculations in a conveniently accessible small model space \mathcal{M}_{ref} , i.e.,

$$|\Psi_{\text{ref}}^{(m)}\rangle = \sum_{|\Phi_i\rangle \in \mathcal{M}_{\text{ref}}} C_{\text{ref},i}^{(m)} |\Phi_i\rangle. \quad (4.6)$$

Based on these reference states we sample the relevance of basis states outside the reference space using an a priori importance measure given by

$$\kappa_i^{(m)} = -\frac{\langle \Phi_i | \hat{H} | \Psi_{\text{ref}}^{(m)} \rangle}{\Delta \epsilon_i}, \quad (4.7)$$

where the denominator is given by the excitation energy of $|\Phi_i\rangle$ relative to the unperturbed Slater determinant. This measure is guided by the first-order state correction of multi-configurational perturbation theory [131, 132]. This importance measure is computed for all basis states $|\Phi_i\rangle \notin \mathcal{M}_{\text{ref}}$ and we construct the so-called importance-truncated model space $\mathcal{M}_{\text{IT}}(\kappa_{\min})$ by retaining the states contained in \mathcal{M}_{ref} and all basis states that fulfill $|\kappa_i^{(m)}| \geq \kappa_{\min}$ for at least one of the reference states. All other basis states are discarded. Since the importance measure (4.7) is linked to the perturbative state correction at first order, it opts for the description of the eigenstates and is, therefore, suitable for all observables, i.e., not only the energy. Moreover, it gives consideration to a number of different aspects: first of all it suppresses high-energy basis states due to the energy denominator which is consistent with the effect of the underlying N_{\max} -truncation scheme. In addition, information about the full Hamiltonian, the targeted states carried by the reference states, and the many-body basis states enters via the matrix element in the numerator. Altogether, it is a state-specific, adaptive and physics-guided measure. Clearly, a variation of the threshold κ_{\min} allows for tuning the dimension of the model-space $\mathcal{M}_{\text{IT}}(\kappa_{\min})$ in which the eigenvalue problem needs to be solved. A variation of the threshold provides an additional assessment of the discarded states and is used for a subsequent extrapolation of the results to vanishing threshold as we will discuss in more detail below.

During an NCSM calculation one is typically interested in an N_{\max} -sequence, because the convergence with respect to this parameter needs to be monitored. It turns out that steps $N_{\max} \rightarrow N_{\max} + 2$ yielding the next same-parity model space can be efficiently combined with the IT scheme. The typical modus operandi is as follows: we begin with eigenstates of the Hamiltonian obtained from the N_{\max} model space, and keep those configurations with expansion coefficients $|C_i^{(m)}| \geq C_{\min}$ to define the reference model space \mathcal{M}_{ref} .

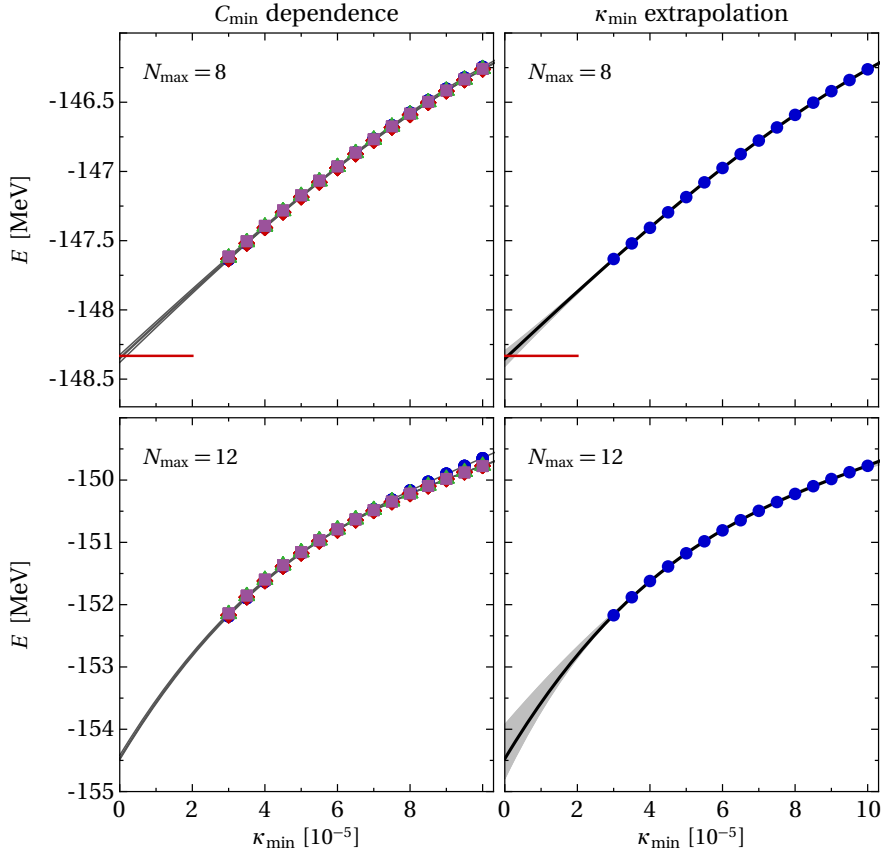


Figure 4.3 – ^{16}O ground-state energy dependencies on the importance threshold κ_{\min} obtained with the NN-only Hamiltonian at $\alpha = 0.04 \text{ fm}^4$ and $\hbar\Omega = 20 \text{ MeV}$. The left-hand panels show the κ_{\min} dependence for different thresholds $C_{\min} = 10^{-4}$ (\bullet), $2 \cdot 10^{-4}$ (\blacklozenge), $3 \cdot 10^{-4}$ (\blacktriangle), $5 \cdot 10^{-4}$ (\blacksquare). The right-hand panels show the simple threshold extrapolation at $C_{\min} = 2 \cdot 10^{-4}$ using a third-order polynomial as solid black lines, and the shaded area corresponds to the uncertainty obtained as explained in the text. Red bars mark results from the full-NCSM code ANTOINE [133] where accessible. (published in [44])

This means not the complete decomposition of the eigenstates is used to construct the reference space, but their renormalized projections on \mathcal{M}_{ref} . However, in practice the parameter C_{\min} is chosen small enough not to affect the observables as discussed below. In the next step, the reference configurations are used to construct the importance-truncated model space $\mathcal{M}_{\text{IT}}(\kappa_{\min})$, where all states of the reference model space are kept and all configurations of the full $N_{\text{max}} + 2$ space not contained in \mathcal{M}_{ref} are subject to the importance selection. The latter is performed for the smallest value of a sequence of κ_{\min} thresholds yielding the largest model space. The next-smaller model space with larger κ_{\min} is constructed by eliminating configurations based on the perviously computed importance measures. The eigenvectors obtained in the largest model space are then the starting point for the next step in N_{max} . This procedure has the important formal property that the full NCSM results obtained in the complete N_{max} spaces are recovered if $(\kappa_{\min}, C_{\min}) \rightarrow 0$.

Having obtained the eigenvalues $E_m(\kappa_{\min})$ and the corresponding eigenstates for a fixed N_{max} but for a series of importance thresholds κ_{\min} , a crucial final step of the IT-NCSM protocol is the assessment of contributions from discarded configurations. Although their

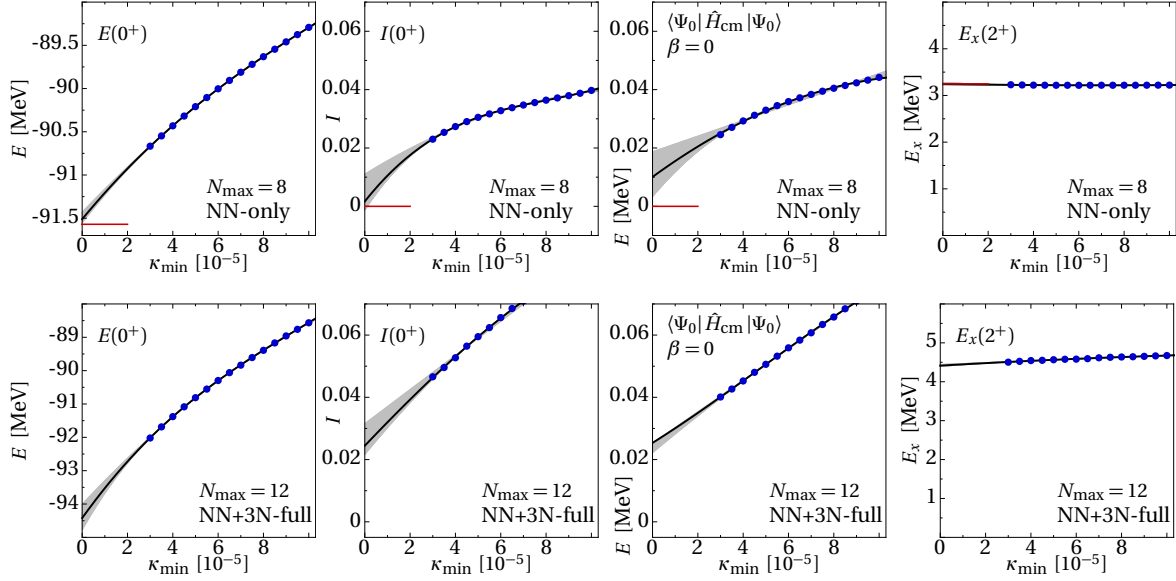


Figure 4.4 – Threshold extrapolation from left to right for the ^{12}C ground-state energy, angular momentum and expectation value of the center-of-mass Hamiltonian (4.5), and excitation energy of first 2^+ state based on the extrapolation protocol described in the text. The results in the upper and lower panels are obtained with the NN-only and NN+3N-full Hamiltonian using $C_{\min} = 2 \cdot 10^{-4}$ and $C_{\min} = 3 \cdot 10^{-4}$, respectively. The remaining parameters are $\alpha = 0.04 \text{ fm}^4$, $\hbar\Omega = 20 \text{ MeV}$. (published in [44])

amplitudes have been estimated to be very small, they will have an effect on the many-body observables. These effects are recovered by means of extrapolations of the observables to $(\kappa_{\min}, C_{\min}) \rightarrow 0$. Usually, the IT-NCSM calculations are conducted for a sequence of κ_{\min} values in the interval $[3 \cdot 10^{-5}, 10 \cdot 10^{-5}]$ with a fixed C_{\min} which is chosen low enough to not influence the results. Then, a polynomial $P_n(\kappa_{\min})$, typically of third order, is fitted to the data set and provides the $\kappa_{\min} \rightarrow 0$ extrapolated result. Additional fits with polynomials of orders $n + 1$ and $n - 1$ as well as further n th-order polynomials but with the lowest and the lowest two κ_{\min} values dropped are produced. The additional extrapolations for $\kappa_{\min} \rightarrow 0$ define the uncertainty for the threshold extrapolation of the given observable, and the procedure is repeated for each individual observable of interest. This is discussed in the following for ground-state energies in context of Figure 4.3, and additionally for excitation energies, angular momentum and the expectation value of the center-of-mass Hamiltonian (4.5) in Figure 4.4, where the respective uncertainties are depicted as shaded bands.

We start with investigating the impact of different thresholds C_{\min} shown in the left-hand panels of Figure 4.3. For this demonstration we use the NN-only Hamiltonian for SRG flow parameter $\alpha = 0.04 \text{ fm}^4$, and the upper and lower panels depict the results at $N_{\max} = 8$ and 12, respectively, which are obtained using the sequential update scheme described above starting from a full NCSM vector at $N_{\max} = 4$ as initial reference state. The different plot markers represent data sets with different C_{\min} resulting from different IT-NCSM runs as function of the importance threshold κ_{\min} , and the grey lines the respective ex-

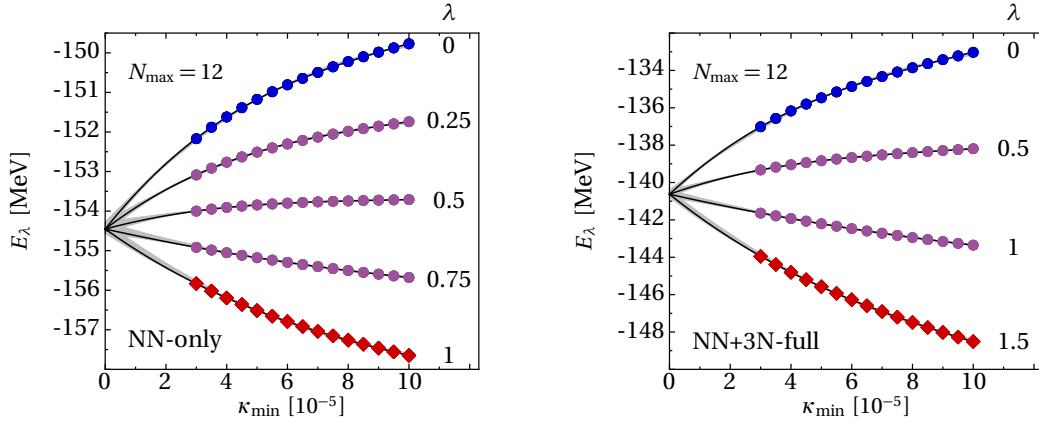


Figure 4.5 – ^{16}O Ground-state energy as function of the importance threshold κ_{\min} for different families of energy sets obtained from Eq. (4.9) as function of λ . Shown as black curves with gray bands are the obtained extrapolations with uncertainties, respectively, received from the simultaneous fit as described in the text. The results are obtained using the SRG-transformed chiral NN-only (left-hand panel) and NN+3N-full (right-hand panel) Hamiltonian at $\alpha = 0.04 \text{ fm}^4$, $\hbar\Omega = 20 \text{ MeV}$, $C_{\min} = 2 \cdot 10^{-4}$ and $N_{\max} = 12$. (published in [44])

trapolations to vanishing threshold κ_{\min} . Basically, the results throughout the whole range $C_{\min} = 10^{-4}$ to $5 \cdot 10^{-4}$, for $N_{\max} = 8$ and 12 are on top of each other, i.e., the dependence on the reference threshold C_{\min} is negligible as long it is below $5 \cdot 10^{-4}$. Typically we use $C_{\min} = 2 \cdot 10^{-4}$. The right panels of Figure 4.3 illustrate the threshold extrapolation $\kappa_{\min} \rightarrow 0$ using the protocol discussed above. First of all, we note that the energies decrease with increasing model-space size, i.e., with decreasing κ_{\min} . This is of course expected due to the variational character of the calculation. The extrapolation using a third-order polynomial is depicted as black curve, and the shaded area represents the uncertainty estimate. In the $N_{\max} = 8$ case the exact result, marked as red bar, is available from an independent NCSM calculation using the ANTOINE code [133]. We find excellent agreement within the small shaded uncertainty band. The extrapolation for $N_{\max} = 12$ yields slightly larger uncertainties but the extrapolation is still well under control.

Further examples for the extrapolation procedure are depicted in Figure 4.4, involving from left to right the ^{12}C ground-state energy, the corresponding angular momentum and expectation value of the center-of-mass Hamiltonian \hat{H}_{cm} , and the excitation energy of the first 2^+ state. The upper panels show the results as function of the importance threshold for the NN-only Hamiltonian, and the lower panels for the NN+3N-full Hamiltonian, i.e., including the initial chiral 3N interaction, at $N_{\max} = 12$. The energies obtained in a full NCSM calculations with the ANTOINE code are again marked as red bars where available. The discussion for the ground-state energy of ^{12}C is analogous to the one above for ^{16}O . Nevertheless, note that the inclusion of the initial 3N interaction does not harm the robustness of the extrapolation. Interestingly, the excitation energies are almost insensitive to κ_{\min} for both Hamiltonians. This means the pattern of the κ_{\min} dependence for the ground- and excited state is very similar and, therefore, cancels when computing the excitation energy. Hence, excitation energies are subject to much reduced extrapolation

uncertainties compared to absolute energies. Note again the excellent agreement of the excitation energy with the available exact result for the NN-only Hamiltonian. The third column shows the analysis for the angular momentum which is computed via the expectation value of \hat{I}^2 with respect to the eigenvectors corresponding to the individual values of κ_{\min} . Recall that individual Slater determinants do not have a good angular momentum quantum number and in the NCSM only a suitable superposition generates the value of the angular momentum. The importance truncation affects this superposition, however, from the extrapolations for the ground-state angular momentum we see that the threshold extrapolation yields good agreement with the exact result, although the uncertainty band does not include the $I = 0$ point for the NN+3N-full Hamiltonian. Finally, we investigate the extrapolation of the expectation value of the auxiliary center-of-mass Hamiltonian, i.e., a measure for the center-of-mass contaminations of the eigenstate, in the third column. A full NCSM calculation using the Lawson method would yield a vanishing expectation value due to the exact factorization (4.4) in N_{\max} -truncated model spaces. The IT technique clearly introduces additional truncations, and the factorization is not perfect. However, the κ_{\min} -dependence reveals small deviations from the vanishing expectation value only, and its extrapolation yields it acceptably close to zero.

For the special case of absolute energies we can exploit the second-order energy correction arising from the excluded model-space configurations to stabilize the threshold extrapolation. This correction is given by

$$\Delta_{\text{excl}}^{(m)}(\kappa_{\min}) = - \sum_{\substack{i \\ |\Phi_i\rangle \notin \mathcal{M}(\kappa_{\min})}} \frac{|\langle \Phi_i | \hat{H} | \Psi_{\text{ref}}^{(m)} \rangle|^2}{\Delta \epsilon_i} \quad (4.8)$$

and can be accumulated at essentially no additional cost, because the necessary matrix elements are identical to those computed during the importance selection. Of course, this correction, besides being of lowest order, is pretty crude because the contributions of configurations contained in $\mathcal{M}(\kappa_{\min})$ which are not in \mathcal{M}_{ref} are not considered. But it has the practically important property to vanish if we approach $\kappa_{\min} \rightarrow 0$ which can be used as constraint for the extrapolation: we generate a family of energy curves by adding the energy correction (4.8) multiplied by different auxiliary parameters λ to the eigenvalue obtained from the diagonalization, i.e.,

$$E_{\lambda}^{(m)}(\kappa_{\min}) = E^{(m)}(\kappa_{\min}) + \lambda \Delta_{\text{excl}}^{(m)}(\kappa_{\min}). \quad (4.9)$$

The values of λ are chosen such that the individual curves approach their common value at $\kappa_{\min} = 0$ from larger and lower values symmetrically as shown exemplarily in Figure 4.5. The additional constraint $E_{\lambda}^{(m)}(\kappa_{\min} = 0) = E_0^{(m)}(\kappa_{\min} = 0)$ for all λ stabilizes the simultaneous fit of the generated family of data sets. In this case, the uncertainty band is obtained by augmenting the different extrapolation variants discussed above by additionally dropping the largest or lowest λ set from the simultaneous extrapolation. As evident from Figure 4.5 for the example of the ground-state energy of ^{16}O the uncertainty band obtained

with this extrapolation method is significantly reduced compared to the simpler extrapolations shown in Figure 4.3.

Altogether, the different extrapolation techniques allow to assess the systematic uncertainties of the IT compared to the full NCSM results. These uncertainties will be represented by error bars in all plots showing IT-NCSM results for a given N_{\max} throughout this work. Of course, the IT-NCSM uses in addition the same extrapolation techniques to infinite model spaces as the NCSM.

The extension of the IT-NCSM formalism to include explicit 3N interactions is analogous to the NCSM and, hence, requires no formal developments. Thus, the discussion in the previous section about the increased computational demand due to a more dense many-body Hamiltonian matrix and the benefit through the JT -coupled scheme for the 3N interaction matrix elements applies here, too. However, we stress that it is the interplay between advances in the many-body method due to the IT technique and the progress on the computational side that is key for extending NCSM-type ab-initio nuclear structure calculations beyond the p -shell: the IT technique allows for the efficient extension of the NCSM to make large N_{\max} model spaces tractable and the JT -coupled 3N matrix elements permits the proper inclusion of the necessary 3N matrix elements at large $E_{3\max}$.

In the remainder of this work we apply the IT-NCSM framework mainly for studies throughout the p -shell but also for the investigation of even oxygen isotopes. In addition, it also delivers input vectors relevant for our investigation of nuclear reactions with target nuclei heavier than ${}^4\text{He}$ discussed in Part III. For studies of nuclei in the medium-mass regime and beyond we use a different method, namely coupled-cluster theory, which we discuss in the following subsection.

4.3 Coupled-Cluster Theory for Ground-States

In this section we focus on a brief overview of coupled-cluster (CC) theory, which is another ab-initio approach to the solution of the Schrödinger equation for the ground state. After its successful application in quantum chemistry [134], coupled-cluster has been subject to significant developments also in the nuclear-structure context over the past several years [97], and has been found to be most efficient for nuclei with closed sub-shells.

The general ansatz of the CC approach is the parametrization of the ground state $|\Psi_{\nu_0}\rangle$ (we omit the label ν_0 for brevity in the following) by applying the so-called wave operator $e^{\hat{T}}$ to a single Slater-determinant reference state $|\Phi_0\rangle$, i.e.,

$$|\Psi\rangle = e^{\hat{T}} |\Phi_0\rangle, \quad (4.10)$$

where the operator

$$\hat{T} = \sum_{m=1}^A \hat{T}_m \quad (4.11)$$

consists of m -particle- m -hole excitation operators given by

$$\hat{T}_m = \frac{1}{(m!)^2} \sum_{a_1 \dots a_m} \sum_{i_1 \dots i_m} t_{i_1 \dots i_m}^{a_1 \dots a_m} \{\hat{a}_{a_1}^\dagger \hat{a}_{a_2}^\dagger \dots \hat{a}_{a_m}^\dagger \hat{a}_{i_1} \dots \hat{a}_{i_2} \hat{a}_{i_1}\}_{|\Phi_0\rangle}. \quad (4.12)$$

Each particular excitation contributes with an amplitude $t_{i_1 \dots i_m}^{a_1 \dots a_m}$. We adopt the same notation as in Section 2.3, i.e., a, b, \dots denote single-particle quantum numbers of particle states, i.e., unoccupied states in $|\Phi_0\rangle$, and indices i, j, \dots represent of hole states, i.e., occupied states in the reference state. In addition, $\{\dots\}_{|\Phi_0\rangle}$ denotes normal ordering with respect to $|\Phi_0\rangle$. Note that the amplitudes are antisymmetric under transpositions among their upper and lower indices, respectively, such that different permutations of the m particle or hole indices yield identical contributions to \hat{T}_m , and the pre-factor in Eq. (4.12) corrects for such redundancies. Obviously, the objective is to determine the amplitudes $t_{i_1 \dots i_m}^{a_1 \dots a_m}$ of the excitation operators, which are the unknowns in this approach. The truncation of the sum over particle states defines the model space of the CC calculation, and is specified by a maximum single-particle energy of the underlying HO single-particle basis e_{\max} . Note that also in the case of a Hartree-Fock reference state and single-particle basis still the underlying HO basis is consistently truncated by e_{\max} . The number of unknown amplitudes in Eq. (4.12) can be shown to increase polynomially with nucleon number and model-space size [97], i.e., it scales more gently than the matrix dimension in NCSM-type approaches.

Typically, CC theory is formulated directly using the normal-ordering technique of the complete Hamiltonian. Formally, the result resembles Eq. (2.30), i.e., the Hamiltonian is rewritten as sum of a normal-ordered zero-, one-, two- and three-body parts \hat{H}_{0B} , \hat{H}_{1B} , \hat{H}_{2B} , and \hat{H}_{3B} , respectively. Assuming the inclusion of an initial 3N interaction it reads

$$\hat{H} = \hat{H}_{0B} + \hat{H}_{1B} + \hat{H}_{2B} + \hat{H}_{3B}. \quad (4.13)$$

The difference to Eq. (2.30) is that the different terms now contain also contributions of the one-body part and the NN interaction of the original Hamiltonian (4.1). The normal-ordered three-body part is identical to Eq. (2.30), i.e., $\hat{H}_{3B} = \hat{V}_{3B}^{3N}$. We proceed by plugging Eq. (4.13) and the CC ansatz for the eigenstate (4.10) in the time-independent Schrödinger equation and arrive at

$$(\hat{H}_{0B} + \hat{H}_{1B} + \hat{H}_{2B} + \hat{H}_{3B}) e^{\hat{T}} |\Phi_0\rangle = E e^{\hat{T}} |\Phi_0\rangle. \quad (4.14)$$

We multiply by $e^{-\hat{T}}$ from the left to eliminate the wave operator on the right-hand side and subtract the so-called reference energy

$$E_{\text{ref}} = \langle \Phi_0 | \hat{H} | \Phi_0 \rangle = \langle \Phi_0 | \hat{H}_{0B} | \Phi_0 \rangle. \quad (4.15)$$

Hence, we obtain

$$e^{-\hat{T}} (\hat{H}_{1B} + \hat{H}_{2B} + \hat{H}_{3B}) e^{\hat{T}} |\Phi_0\rangle = \Delta E |\Phi_0\rangle. \quad (4.16)$$

To arrive at this expression we introduced the CC correlation energy $\Delta E = E - E_{\text{ref}}$. For the further discussion it is convenient to define the so-called effective Hamiltonian via

$$\hat{\mathcal{H}} = e^{-\hat{T}} (\hat{H}_{1B} + \hat{H}_{2B} + \hat{H}_{3B}) e^{\hat{T}}. \quad (4.17)$$

Having converted the Schrödinger equation into the eigenvalue problem of the effective Hamiltonian (4.16), we still need conditional equations for the CC amplitudes and the correlation energy. Due to the increasing computational cost and the complexity of these equations in the context of nuclear structure, the cluster operator \hat{T} is approximated at the level of singly and doubly excited clusters leading to the coupled-cluster method at the singles and doubles level (CCSD), i.e., $\hat{T} \approx \hat{T}_{\text{CCSD}} = \hat{T}_1 + \hat{T}_2$. The equations determining the corresponding amplitudes $\{t_i^a, t_{ij}^{ab}\}$ are obtained by projecting Eq. (4.16) onto the reference state $|\Phi_0\rangle$, and onto one-particle-one-hole $|\Phi_{0,i}^a\rangle$ and two-particle-two-hole $|\Phi_{0,ij}^{ab}\rangle$ excitations of the reference state. Thus, we obtain

$$\langle \Phi_0 | \hat{\mathcal{H}} | \Phi_0 \rangle = \Delta E_{\text{CCSD}}, \quad (4.18)$$

$$\langle \Phi_{0,i}^a | \hat{\mathcal{H}} | \Phi_0 \rangle = 0 \quad \forall a, i, \quad (4.19)$$

$$\langle \Phi_{0,ij}^{ab} | \hat{\mathcal{H}} | \Phi_0 \rangle = 0 \quad \forall a, b, i, j. \quad (4.20)$$

Note that the amplitude equations (4.19) and (4.20) are decoupled from the energy equation (4.18) due to the multiplication by $e^{-\hat{T}}$ from the left in Eq. (4.16). Therefore, the solution of the coupled and nonlinear Eqs. (4.19) and (4.20) for the amplitudes $\{t_i^a, t_{ij}^{ab}\}$, typically in an iterative fashion, completely determines the eigenstate (4.10) in terms of the amplitudes. Inserting these amplitudes in Eq. (4.18) yields the CCSD energy ΔE_{CCSD} , and together with the reference energy E_{ref} the total energy E .

All formally as well as computationally demanding pieces are still implicit in the equations above. First the effective Hamiltonian $\hat{\mathcal{H}}$ needs to be manipulated and simplified to allow for an efficient implementation of the matrix elements of the operator structures that enter Eqs. (4.18)-(4.20). Detailed discussions on these steps for CCSD for NN and NN+3N interactions within the NO2B approximation can be found in Refs. [135] and [45], respectively. Pioneering CCSD calculations including the \hat{H}_{3B} contribution explicitly can be found in Ref. [45], while a systematic application to medium-mass nuclei can be found in Refs. [46, 136], and a comprehensive dissertation on this topic including formal details in Ref. [96].

At this point we take the opportunity to distinguish different possible types of calculations depending on which operator contributions of the Hamiltonian are being included on the left-hand side of Eq. (4.16). Therefore, we split the effective Hamiltonian into a part relevant for CCSD at the NO2B level, $\hat{\mathcal{H}}_{\text{NO2B}}$, and the part corresponding to the normal-ordered three-body part, $\hat{\mathcal{H}}_{3B}$, defined as

$$\hat{\mathcal{H}}_{\text{NO2B}} = e^{-\hat{T}} (\hat{H}_{1B} + \hat{H}_{2B}) e^{\hat{T}} \quad \text{and} \quad \hat{\mathcal{H}}_{3B} = e^{-\hat{T}} \hat{H}_{3B} e^{\hat{T}}. \quad (4.21)$$

If all operators shown in Eq. (4.16) are included, the CC calculations are conducted including the complete 3N interaction, i.e., $\hat{\mathcal{H}} = \hat{\mathcal{H}}_{\text{NO2B}} + \hat{\mathcal{H}}_{3\text{B}}$ and the normal-ordered 3N interaction is kept explicitly. If instead the $\hat{H}_{3\text{B}}$ contribution is discarded in Eq. (4.16), the CC theory is formulated at the level of the NO2B approximation introduced in Eq. (2.31). That is, 3N interaction effects are only partly included through contributions at the lower-particle ranks in normal ordering. The NN interaction is of course fully accounted for at the NO2B level. It follows from this discussion that a CC formalism required for a calculation at the NN-only level and at the NN+3N level with NO2B approximation is identical. The only difference occurs in the content of the operators $\hat{H}_{0\text{B}}$, $\hat{H}_{1\text{B}}$ and $\hat{H}_{2\text{B}}$.

As before for the NCSM-type approaches, we add a brief discussion that highlights the efforts that become necessary for the inclusion of 3N interactions in the CCSD approach. We have seen above it is natural to include the 3N interaction at the NO2B approximation level in the CCSD framework. In this case the necessary NO2B matrix elements are provided by a preparatory step discussed in Section 2.3.2, and, therefore, do not burden the CCSD calculation. On the contrary, significantly more work, including formal developments and the derivation and implementation of new formulas, becomes necessary when aiming at the complete inclusion of 3N interaction, i.e., explicitly retaining the $\hat{H}_{3\text{B}}$ part. This can be seen as follows: the first step beyond the energy and amplitude equations in their generic form, shown in Eqs. (4.18)-(4.20) above, is the evaluation of the effective Hamiltonians $\hat{\mathcal{H}}_{\text{NO2B}}$ and $\hat{\mathcal{H}}_{3\text{B}}$. In general, expressions like in Eq. (4.21) can be evaluated using the non-terminating Baker-Campbell-Hausdorff commutator expansion. Fortunately, for the special case of \hat{T} being an excitation operator, the commutator expansion terminates, which can be proven by means of Wick's theorem (cf. Eq. (2.23)) for the evaluation of the emerging commutators [102]. For CCSD calculations at the NN-only or the NO2B level, the expansion of $\hat{\mathcal{H}}_{\text{NO2B}}$ terminates after the four-fold commutator, caused by the Hamiltonian being a two-body operator. Instead, the explicit inclusion of the complete 3N interaction requires the evaluation of $\hat{\mathcal{H}}_{3\text{B}}$ for which the commutator expansion terminates only after the six-fold commutator. Consequently, significantly more operator structures appear, whose contributions to the energy and amplitude equations need to be accounted for, which leads to a significantly larger expense of the CCSD calculations. Altogether, the inclusion of explicit 3N interactions in the CCSD framework in comparison to NCSM-type approaches is clearly more sophisticated, in particular, because formal generalizations of the CCSD framework to include explicit 3N interactions are required.

In many practical cases it is necessary to go beyond CCSD in order to obtain an accurate description of nuclear properties, i.e., one needs to account for effects of triply excited clusters [98, 137, 138]. However, the full treatment of the \hat{T}_3 operator in the cluster operator via the CCSDT approach, is prohibitively expensive. Therefore, one resorts to approximative schemes, through a non-iterative treatment of the connected triply excited clusters a posteriori, also referred to as triples corrections, that one adds on top of the CCSD energies [98]. The two approaches we employ in this respect, mainly relevant for our discussions in Section 9, are the completely-renormalized coupled-cluster(2,3) [CR-CC(2,3)] approach [139, 140, 141], and the Λ CCSD(T) method [135, 142]. The former has proven

to produce the best approximations to a full CCSDT calculation for several benchmark cases in quantum chemistry [143], and the latter can be obtained as approximation to CR-CC(2,3) [98]. Both methods are highly sophisticated and require besides the solution of the amplitude equations discussed above also so-called Λ equations which determine amplitudes of de-excitation operators that generate the left eigenstate of the non-Hermitian effective Hamiltonian. We do not go into further details here, but refer the interested reader to Refs. [96, 98] about the inclusion of explicit 3N interaction into Λ CCSD(T), and references therein.

SECTION 5

The Role of the SRG Model Space

Before we start discussing the effects of the chiral NN+3N Hamiltonians on different nuclear observables, we need to cover one more technical point, namely the impact of the model-space truncations used during the SRG evolution. As we have discussed in Section 3.2, the consistent inclusion of 3N interactions into the SRG framework is achieved by representing the flow equation (3.2) in the antisymmetrized three-body Jacobi HO basis, leading to first-order differential equations for the Hamiltonian matrix elements. Since in practice only finite-dimensional matrices can be handled we have introduced a truncation of the SRG model space by specifying a maximum relative energy quantum number $E_{\text{SRG}}(J_{12})$ which may vary for the different angular momenta J_{12} . A crucial part of such a truncation is the validation of its accuracy, which is discussed in this section. The findings presented in this section are also included in the publication [44].

From the physics perspective, 3N channels ($J_{12}^{\pi} T_{12}$) with large relative angular momenta J_{12} should be less important for the description of low-energy properties of light nuclei, whereas small angular momenta should be crucial. This motivates the angular-momentum dependent model-space truncation $E_{\text{SRG}}(J_{12})$. We employ SRG model-space truncations that are largest for small angular momenta and then decrease with increasing relative angular momentum. Note that such truncation schemes are convenient also from a practical point of view, since the basis dimension for fixed E_{SRG} grows with increasing J_{12} . To test the convergence with respect to the SRG model-space size, we define three different choices of $E_{\text{SRG}}(J_{12})$, the so-called 'ramps'. They are sketched in Figure 5.1: the overall largest SRG model space studied here will be our default choice and is denoted as 'ramp \mathcal{A} ' represented by the blue solid line. It employs $E_{\text{SRG}} = 40$ for $J_{12} \leq \frac{5}{2}$ and is then reduced in steps of 4 until we reach $E_{\text{SRG}}(J_{12}) = 24$ for $J_{12} \geq \frac{13}{2}$. For 'ramp $\mathcal{A}_{\text{slope}}$ ', shown as red-dashed line, the model-space reduction starts already at $J_{12} = \frac{5}{2}$ and employs $E_{\text{SRG}} = 24$ for $J_{12} \geq \frac{11}{2}$, i.e., the slope is shifted to smaller J_{12} . Consequently, comparing results obtained with ramp \mathcal{A} to those from ramp $\mathcal{A}_{\text{slope}}$ tests the convergence and relevance of channels beyond the lowest J_{12} . In contrast, the convergence of channels with small angular momenta is checked by comparing results obtained with ramp \mathcal{A} and ramp \mathcal{A}_{low} that is identical to ramp \mathcal{A}

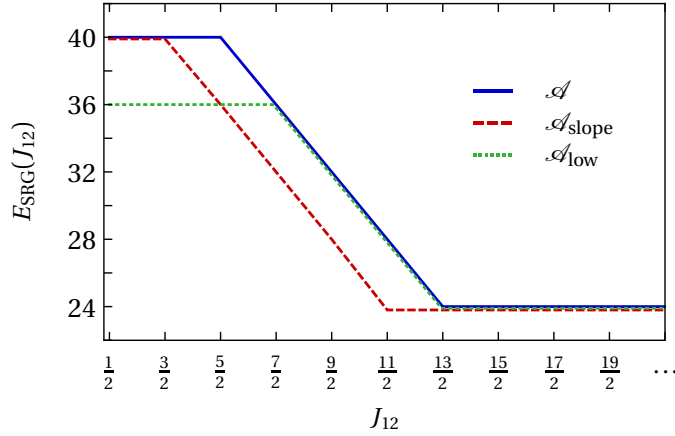


Figure 5.1 – Illustration of the angular momentum dependent SRG model-space truncation $E_{\text{SRG}}(J_{12})$. Plotted are the ramps \mathcal{A} , $\mathcal{A}_{\text{slope}}$, and \mathcal{A}_{low} . For further explanations see text. (published in [44])

for $J_{12} \geq \frac{7}{2}$ but uses the smaller $E_{\text{SRG}} = 36$ for $J_{12} \leq \frac{5}{2}$, as indicated by the green-dotted line. We stress that these SRG model spaces are adapted for applications in light nuclei as mentioned above. For medium-mass or even heavy nuclei much larger SRG model spaces may be necessary, in particular if single-particle shells with large angular momenta become relevant. Therefore, we critically reinvestigate the SRG model space and revise the convergence tests when we aim at the description of nuclei beyond ^{24}O in Section 9.

Because it is difficult to decide on convergence based on deviations in the different resulting 3N matrix elements, we address this issue directly in the nuclear-structure observables we are interested in. All results presented throughout this section are obtained using the chiral NN+3N-full Hamiltonian, as it is defined in Table 4.1, using the standard 3N interaction with cutoff of $\Lambda_{3\text{N}} = 500\text{MeV}/c$ described in Section 1.2. In all cases we evolve the Hamiltonian up to an SRG flow-parameter $\alpha = 0.08\text{fm}^4$. We begin with the investigation of ground-state energies in the following subsection and investigate excitation energies in Section 5.2.

5.1 Effects on Absolute Energies

We start with the investigation of the impact of the different SRG model spaces on ground-state energies for ^4He and ^{16}O . Figure 5.2 shows their dependence on the IT-NCSM model-space size N_{max} for the two HO frequencies $\hbar\Omega = 16$ and 20MeV . For ^4He at frequency $\hbar\Omega = 20\text{MeV}$ we find essentially no dependence of the ground-state energy on the different SRG model spaces. The same holds for ^{16}O , where we again find negligible deviations. This changes for the ground-state energies obtained at $\hbar\Omega = 16\text{MeV}$. The ^4He ground-state energies obtained with ramp \mathcal{A} and $\mathcal{A}_{\text{slope}}$ remain on top of each other, but ramp \mathcal{A}_{low} exhibits a deviation of 0.4%. This means the ^4He ground-state energy is sensitive to the smaller model-space size for the smallest relative angular momenta. For the heavier nucleus ^{16}O the deviations become larger and, in addition, also sensitive to ramp $\mathcal{A}_{\text{slope}}$, i.e., short-comings of the SRG model space for the larger angular momenta are revealed.

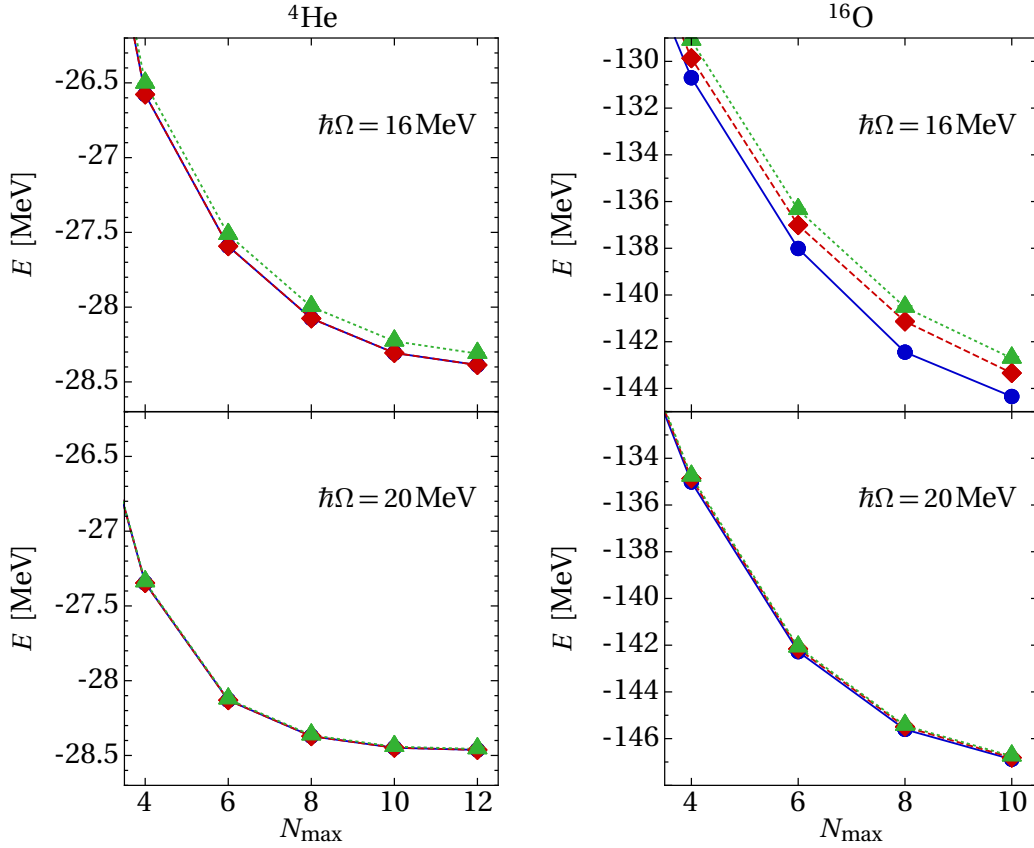


Figure 5.2 – Ground-state energies of ${}^4\text{He}$ (left-hand panels) and ${}^{16}\text{O}$ (right-hand panels) as function of the IT-NCSM model-space size N_{max} obtained with the NN+3N-full Hamiltonian at HO frequency $\hbar\Omega = 16\text{ MeV}$ (upper panels) and 20 MeV (lower panels). The different curves denote results obtained with ramp \mathcal{A} (\bullet), ramp $\mathcal{A}_{\text{slope}}$ (\blacklozenge) and ramp \mathcal{A}_{low} (\blacktriangle) as SRG model-space truncations. (published in [44])

In conclusion we find that for HO frequencies $\hbar\Omega = 20\text{ MeV}$ and larger the SRG model space of ramp \mathcal{A} is sufficiently large to obtain accurate results. This is not the case for the lower frequency $\hbar\Omega = 16\text{ MeV}$, which may be related to an insufficient coverage of the relevant energy-range defined by $E_{\text{SRG}} \cdot \hbar\Omega_{\text{SRG}}$.

To remedy such SRG model-space truncation artifacts at small HO frequencies we can use the frequency-conversion technique introduced in Section 3.3. That is, we choose a sufficiently large parent frequency $\hbar\Omega_{\text{SRG}}$ to perform the SRG evolution, and afterwards we convert the matrix elements with help of Eq. (3.12) to the smaller frequencies $\hbar\Omega$ at which we perform the many-body calculations. We discuss the impact of this procedure in context of Figure 5.3: the left panel shows again the ${}^{16}\text{O}$ ground-state energies obtained with the three different SRG model spaces, where the SRG transformation and the IT-NCSM calculation use the same HO frequency, i.e., $\Omega_{\text{SRG}} = \Omega$. In contrast, for the results shown in the right panel the SRG is always performed at $\hbar\Omega_{\text{SRG}} = 24\text{ MeV}$ and the matrix elements are subsequently converted to the frequencies used in the IT-NCSM calculations. The upper panels contain the absolute energies, and the lower panels show the energy differences relative to our default ramp \mathcal{A} . Obviously, the frequency-conversion technique is able

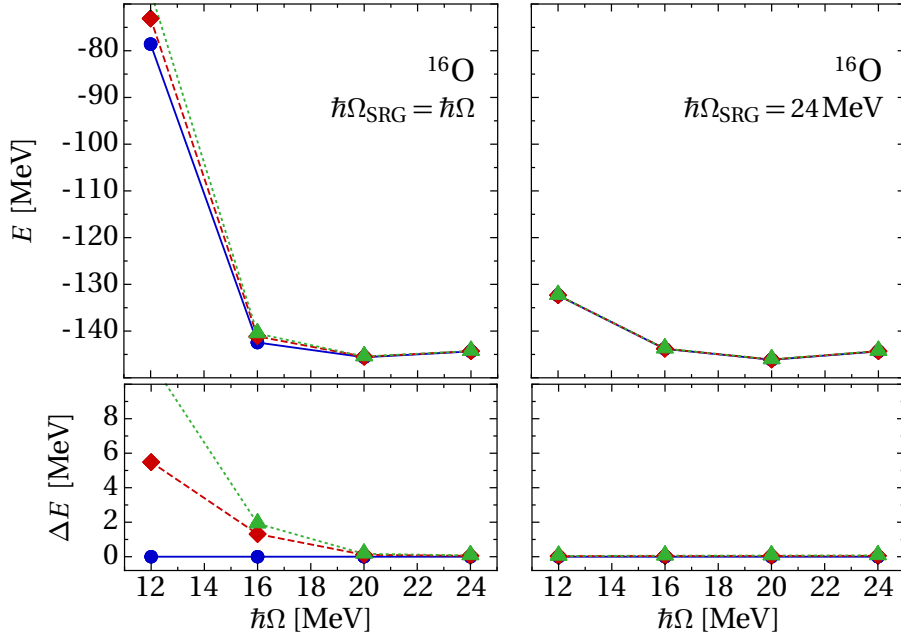


Figure 5.3 – Comparison of the ^{16}O ground-state energy as function the oscillator frequency obtained without frequency conversion, meaning $\hbar\Omega_{\text{SRG}} = \hbar\Omega$ (left-hand panels), to energies obtained when the SRG transformation is performed at fixed $\hbar\Omega_{\text{SRG}} = 24$ MeV and the subsequent frequency conversion (right-hand panels). Results are shown for the three different SRG model space truncations \mathcal{A} (●), $\mathcal{A}_{\text{slope}}$ (◆), and \mathcal{A}_{low} (▲). The upper panels show the absolute energies, and in the lower panels the deviations from energies obtained with ramp \mathcal{A} are plotted. The NN+3N-full Hamiltonian is used with parameters $N_{\text{max}} = 8$ and $\alpha = 0.08 \text{ fm}^4$. (published in [44])

to cure the problems with the SRG model space completely, since for all frequencies no difference between the energies obtained from different ramps exists. This is particularly impressive for the smallest frequency $\hbar\Omega = 12$ MeV, where drastic deviations caused by the different SRG model spaces are apparent. At such small frequencies significant contributions of the initial Hamiltonian relevant for the binding energy are not accounted for by the SRG transformation, while they are included when using a sufficiently larger frequency with identical SRG model-space truncation $E_{\text{SRG}}(J_{12})$. It is evident from this discussion that the frequency-conversion technique is key for proper calculations with 3N interactions at small frequencies. This can be particularly relevant, e.g., to reliably study expectation values of long-range operators.

For absolute energies we conclude that the SRG model-space truncation \mathcal{A} is sufficient for the light nuclei considered here at HO frequencies $\hbar\Omega \geq 20$ MeV, and for smaller frequencies in combination with the frequency-conversion technique. For medium-mass nuclei one may expect that this analysis needs to be repeated, as is done in Section 9.

5.2 Effects on Excitation Energies

For excitation energies we find much less impact of the three different SRG model-space truncations compared to the absolute energies. In Figure 5.4 we show two ^{12}C spectra in-

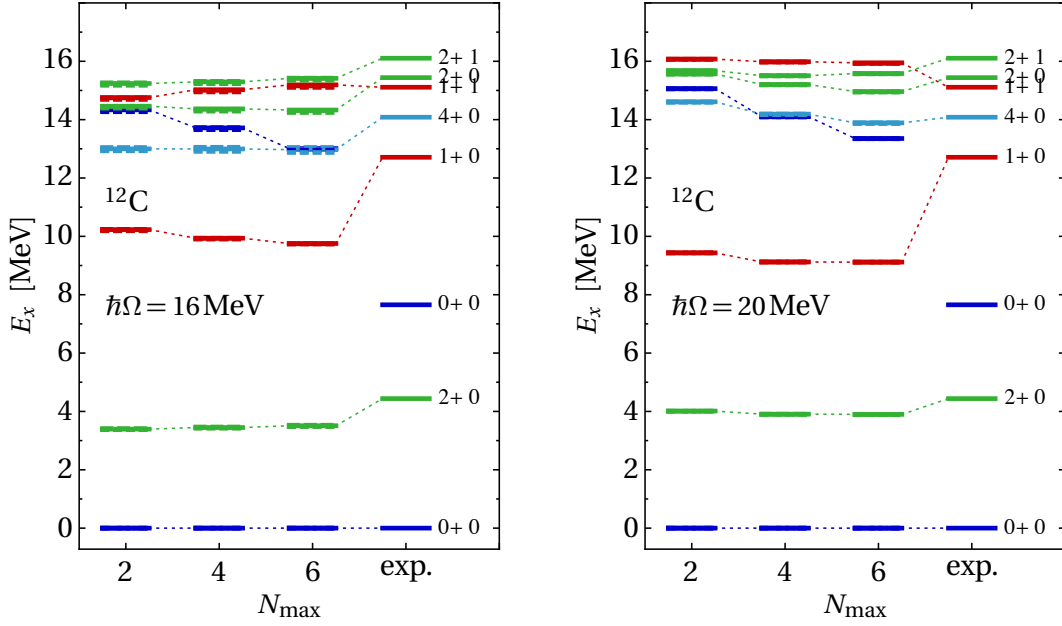


Figure 5.4 – Positive-parity excitation spectra of ^{12}C obtained with the different SRG model space truncations \mathcal{A} (—), $\mathcal{A}_{\text{slope}}$ (---), and \mathcal{A}_{low} (····) for HO frequency $\hbar\Omega = 16\text{MeV}$ (left-hand panel), and $\hbar\Omega = 20\text{MeV}$ (right-hand panel). Differences between different SRG model-space truncations are hardly visible, because the excitation energies are to a large extent on top of each other. The IT-NCSM calculations are conducted with the NN+3N-full Hamiltonian at SRG flow parameter $\alpha = 0.08\text{fm}^4$. (published in [44])

cluding the first eight low-energy positive-parity states for frequency $\hbar\Omega = 16\text{MeV}$ in the left panel and for $\hbar\Omega = 20\text{MeV}$ in the right panel. In addition, the results obtained with the three different ramps are superimposed using different line styles in each panel, respectively. The resulting excitation energies are practically on top of each other, in particular also for the smaller frequency $\hbar\Omega = 16\text{MeV}$. Note that no frequency conversion has been used, i.e., $\hbar\Omega = \hbar\Omega_{\text{SRG}}$. Apparently, possible shortcomings covering the relevant energy range of the Hamiltonian during the SRG evolution lead to overall identical energy shifts of all states, which cancel out when nuclear spectra are considered. Consequently, we can establish our default ramp \mathcal{A} as sufficient to obtain SRG-transformed Hamiltonians which can serve for quantitative analyses of nuclear spectra of light nuclei even at low frequencies.

SECTION 6

Chiral 3N Forces in Ab-Initio Nuclear Structure of p -Shell Nuclei

In this section we aim at ab-initio predictions for a variety of p -shell nuclei starting from SRG-evolved chiral NN+3N Hamiltonians. The discussion is guided by IT-NCSM calculations using the chiral NN interaction at N³LO as described in Section 1.1 along with the chiral 3N interaction at N²LO introduced in Section 1.2 exploiting the JT -coupled matrix-element scheme. If not stated otherwise, we use the momentum-scale cutoff $\Lambda_{3N} = 500\text{MeV}/c$ for the chiral 3N force, which is included explicitly without any further approximation. We soften the Hamiltonian by means of the SRG evolution described in Section 3 and use the SRG model space 'ramp \mathcal{A} ', which we validated for p -shell nuclei in the previous section. All IT-NCSM results for a given model-space truncation N_{max} are obtained by extrapolations to vanishing importance threshold using the protocol described in Section 4.2, and the provided uncertainties are shown as error bars in all subsequent plots.

Thus, for now all preparatory steps have been clarified in the previous sections and we concentrate on consequences of the chiral Hamiltonians for nuclear structure observables. We start to explore the effects of 3N interactions on ground-state energies for a variety of p -shell nuclei in comparison to experiment and, in particular, disentangle the effects of SRG-induced and initial 3N interactions in the first subsection. We find that discarded SRG-induced contributions beyond the three-body level, which are negligible for the lightest nuclei, become significant in the upper p -shell and beyond, and we trace back their origin in Section 6.1.1. We clarify the relevance of SRG-induced forces for low-energy excitations with help of energy spectra in Section 6.2. Finally, we discuss the option to circumvent significant SRG-induced multi-nucleon contributions by lowering the cutoff momentum Λ_{3N} of the initial 3N interactions in Section 6.3. The different aspects discussed in this section have resulted in the publications [42, 44, 43].

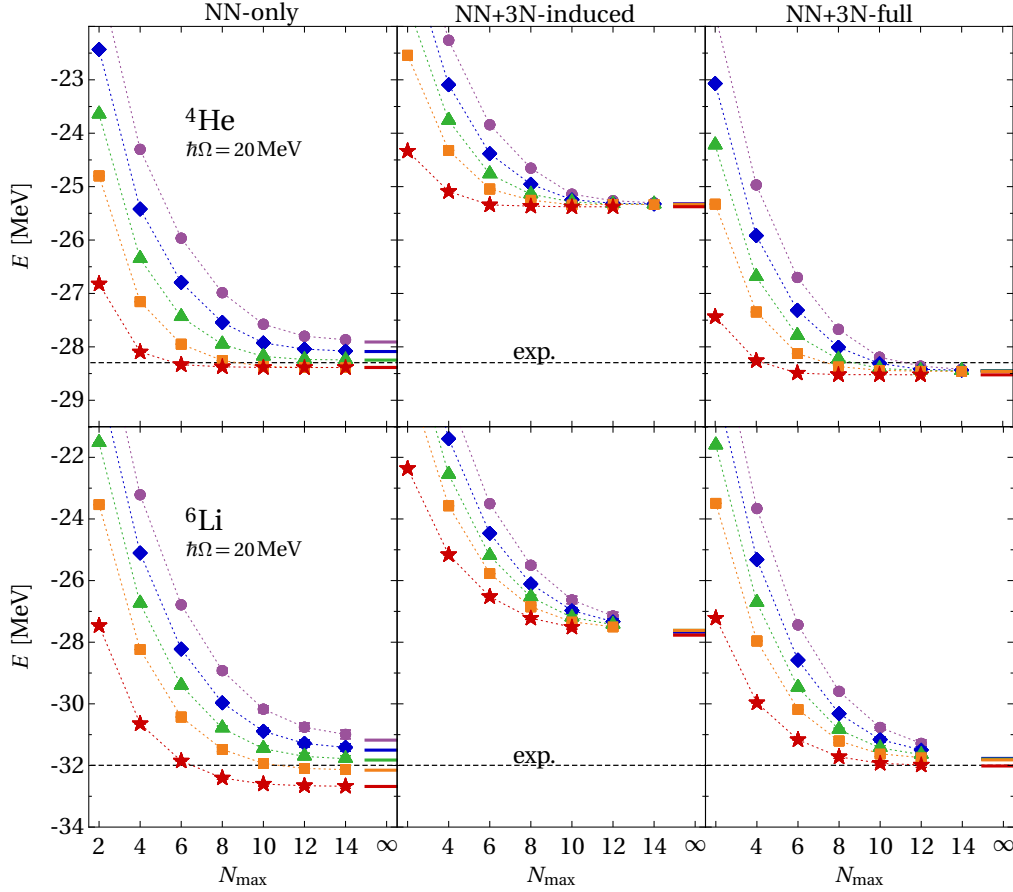


Figure 6.1 – ${}^4\text{He}$ (upper panels) and ${}^6\text{Li}$ (lower panels) ground-state energies obtained in the IT-NCSM as function of the model-space size N_{max} for different SRG flow parameters $\alpha = 0.04$ (\bullet), 0.05 (\blacklozenge), 0.0625 (\blacktriangle), 0.08 (\blacksquare), 0.16fm^4 (\star). Uncertainties of the IT threshold extrapolation are indicated as error bars (mostly hidden by the plot markers). The horizontal bars mark the exponentially extrapolated energies at infinite model space (see text), and the black dashed lines represent the experimental energies [144]. (published in [42])

6.1 Description of Ground-State Energies throughout the p -Shell

We begin our investigations with the ground-state energies of ${}^4\text{He}$ and ${}^6\text{Li}$ obtained with the NN-only, NN+3N-induced and NN+3N-full Hamiltonians. They are depicted in Figure 6.1 as function of the IT-NCSM model-space size and for the set of SRG flow parameters $\alpha = 0.04, 0.05, 0.0625, 0.08$ and 0.16fm^4 . First of all, we notice systematically for all three Hamiltonians and both nuclei the improved rate of convergence with respect to the model-space size N_{max} with increasing SRG flow parameter. Hence, the SRG works as desired in this respect, that is, with the IT-NCSM calculations up to $N_{\text{max}} = 12$ we can reach convergence for soft the interactions and achieve energies close to convergence already at moderate model-space sizes. However, note that the use of SRG-transformed Hamiltonians is mandatory, because calculations at $\alpha = 0$, i.e., for the initial Hamiltonian, lack convergence in spite of the large model-spaces we can handle. The improved convergence behavior offers the possibility for stable extrapolations to infinite model-space size to simplify the interpretation of the results. Therefore, we use a simple extrapolation by fitting

the exponential $E_\infty + ae^{-bN_{\max}}$ to the energies from the three or four largest model spaces and mark the average for E_∞ as horizontal bars in Figure 6.1. The extrapolated energies obtained with the NN-only Hamiltonian shown in the left panel of Figure 6.1, exhibit a sizeable dependence on the SRG flow parameter and scatter around the experimental result. This is well known from different applications of SRG-transformed NN-only Hamiltonians in nuclear-structure calculations [52, 145, 40], and is caused by the omission of the SRG-induced 3N interactions which we can confirm by including them explicitly. This is achieved by performing the SRG transformation consistently in three-body space, which leads to the NN+3N-induced Hamiltonian. The corresponding IT-NCSM results using this Hamiltonian are shown in the middle panel of Figure 6.1. The extrapolated energies for all flow parameters are on top of each other and the inclusion of the repulsive SRG-induced 3N interactions yields them at larger values compared to the NN-only results for both nuclei, respectively. The energies are independent of the flow parameter, meaning that SRG-induced four- and multi-nucleon interactions originating from the initial NN interaction are negligible, and the NN+3N-induced Hamiltonian is unitarily equivalent to the initial NN Hamiltonian. The same is true once the initial 3N interaction is accounted for using the NN+3N-full Hamiltonian, as shown in the right panel of Figure 6.1. The ground-state energies remain α -independent and the attractive initial 3N forces yields ${}^4\text{He}$ slightly overbound, and ${}^6\text{Li}$ in good agreement with experiment. The vanishing flow-parameter dependence again points towards the irrelevance of SRG-induced four- and multi-nucleon contributions for nuclei in the lower p -shell. These results and conclusions are also in excellent agreement with the full-NCSM calculations of Refs. [145, 40] using a comparably SRG-transformed Hamiltonian starting from the identical initial Hamiltonian.

We repeat an analogous analysis for nuclei in the upper p -shell. Therefore, we present first accurate ab-initio calculations of the ground-state energies of ${}^{12}\text{C}$ and ${}^{16}\text{O}$ including chiral 3N interactions up to $N_{\max} = 12$ model space in Figure 6.2. The overall conclusion from the calculations at the NN-only and NN+3N-induced level is very similar to the light-nuclei domain: the extrapolated ground-state energies of ${}^{12}\text{C}$ and ${}^{16}\text{O}$ at the NN-only level show an even stronger dependence on the SRG flow parameter α . To resolve this we include SRG-induced 3N interactions for both nuclei, and achieve flow-parameter independent energies, which are underbound compared to experiment. We find the NN+3N-induced ground-state energies in good agreement with coupled-cluster $\Lambda\text{CCSD(T)}$ calculations by Hagen et al. using the unitarily equivalent initial NN interaction without softening [135]. However, when we proceed to include the initial chiral 3N interaction into the IT-NCSM calculations we find evidence for a non-negligible SRG flow-parameter dependence shown in the right panel of Figure 6.2. Thus, the observed pattern indicates the presence of significant SRG-induced four- and multi-nucleon contributions which have been omitted and, thus, lead to the observed flow-parameter dependence. We emphasize that it is mandatory to have well-converged results which are independent of all many-body truncations to be able to draw conclusions from the observed flow-parameter dependence. This is indeed the case for the presented IT-NCSM calculations due to the large accessible N_{\max} , which is the only truncation involved in case of NCSM-type calculations.

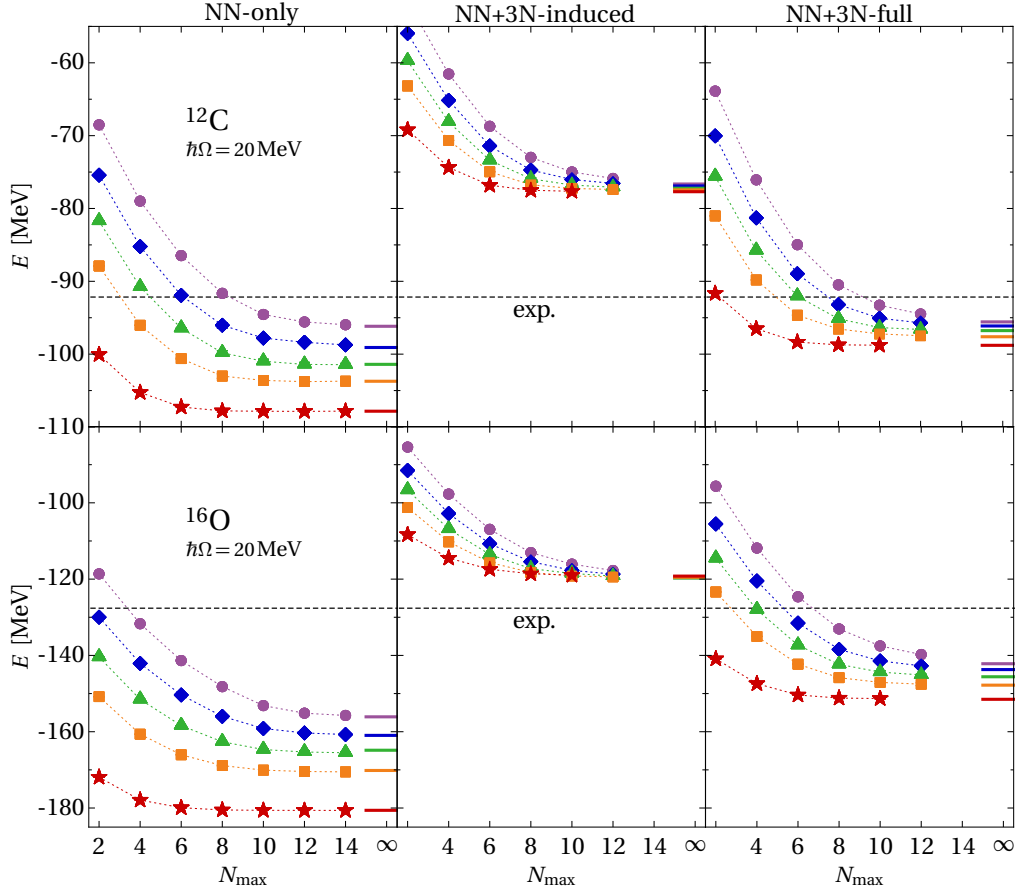


Figure 6.2 – IT-NCSM ground-states energies of ^{12}C (upper panels) and ^{16}O (lower panels) as function of N_{max} for the three types of Hamiltonians and for the set of SRG flow-parameters given in Figure 6.1. Experimental energies are taken from [144]. (published in [42])

This is more complicated for other many-body methods [34, 51, 33, 46, 136]

For a more direct comparison of the flow-parameter dependencies we plot in Figure 6.3 the ground-state energies of ^4He and ^{16}O as function of α . Hence, flow-parameter independent results occur in this format as horizontal lines. The results obtained at the NN-only level, shown as blue discs, in the range $\alpha = 0.04$ to 0.16fm^4 show a flow-parameter dependence of 0.7 MeV for ^4He and 25 MeV for ^{16}O due to the spoiled unitarity of the SRG transformation. This is cured for both nuclei by the inclusion of SRG-induced 3N contributions which remedies the α dependence leading to nearly horizontal lines represented by the green diamonds. Whereas the flow-parameter dependence remains absent for ^4He after the inclusion of the initial 3N interaction, we encounter for the spread $\alpha = 0.04 - 0.08\text{fm}^4$ a flow-parameter dependence of about 10 MeV in ^{16}O originating from induced but discarded four- and multi-nucleon contributions. This means the discarded induced beyond-3N interactions reach approximately half the size of the total contribution from the initial 3N interaction and, thus, the hierarchy of the chiral nuclear forces may not be preserved by the SRG. Consequently, these omitted contributions degrade the predictive power of the results, since the recovery of the $\alpha = 0$ result is a highly non-trivial, hardly feasible task. Altogether, based on these results we can state that part of the overbinding

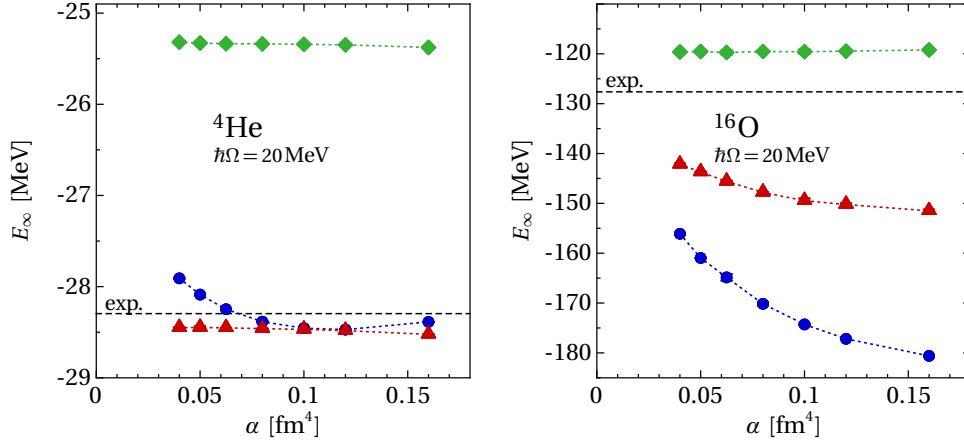


Figure 6.3 – IT-NCSM ground-state energies of ${}^4\text{He}$ and ${}^{16}\text{O}$ extrapolated to infinite model-space size as function of the SRG flow parameter α for the NN-only (●), NN+3N-induced (◆) and NN+3N-full (▲) Hamiltonian. (published in [42])

observed for the NN+3N-full Hamiltonian is due to discarded SRG-induced contributions. However, we cannot assess possible deficiencies of the initial chiral Hamiltonian, since we cannot exclude that the complete overbinding originates from discarded multi-nucleon interactions.

To investigate the emergence of SRG-induced four- and multi-nucleon forces more systematically over the mass range covered here, we present additional ground-state energy calculations of ${}^8\text{Be}$, ${}^{10}\text{Be}$, ${}^{14}\text{C}$ for the NN+3N-induced and NN+3N-full Hamiltonians in Figure 6.4. The observations are similar to those discussed above. Calculations starting from an NN+3N-induced Hamiltonian do not lead to an SRG flow-parameter dependence in the ground-state energies. For calculations with the NN+3N-full Hamiltonian the ${}^8\text{Be}$ ground-state energy remains α independent, while a slight dependence becomes visible for ${}^{10}\text{Be}$. Then starting from mass number $A \approx 10$ the flow-parameter dependence in the NN+3N-full results starts to increase with increasing mass number and is clearly present for ${}^{14}\text{C}$.

In Table 6.1 we summarize the extrapolated ground-state energies for the considered nuclei for the set of flow-parameters $\alpha = 0.04, 0.0625$ and 0.08 fm^4 , which is the range we will typically investigate in further applications. The numbers given are the average of the simple extrapolations involving the last three or four data points and we quote as a rough uncertainty estimate the difference between the extrapolated energies. Typically, these uncertainties are somewhat smaller for increasing α due to more stable extrapolations caused by the improved rate of convergence. Note that the uncertainties from the extrapolations to vanishing importance threshold (cf. Section 4.2) are not taken into account for the extrapolations.

We can further confirm the presence of the flow parameter dependence also beyond the p -shell with coupled-cluster calculations at the singles and doubles level (CCSD). In Figure 6.5 we show the ground-state energies of ${}^{16}\text{O}$, ${}^{24}\text{O}$, ${}^{40}\text{Ca}$, and ${}^{48}\text{Ca}$ as function of the CCSD model-space truncation parameter e_{max} , which we published in Ref. [43]. We note that the presented calculations are conducted using a underlying HO basis and using the

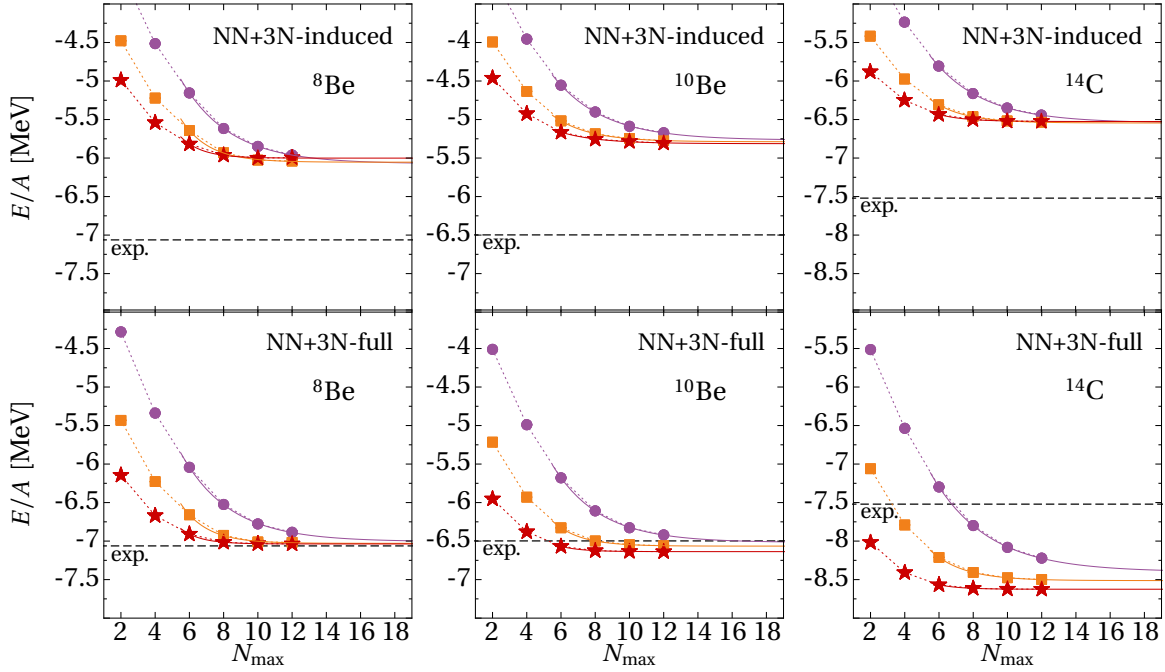


Figure 6.4 – IT-NCSM ground-state energies per nucleon for ${}^8\text{Be}$, ${}^{10}\text{Be}$, and ${}^{14}\text{C}$ as function N_{max} obtained with the NN+3N-induced (upper panels) and NN+3N-full Hamiltonian (lower panels). The different data sets correspond to results for SRG flow parameters $\alpha = 0.04$ (\bullet), 0.08 (\blacksquare), and 0.16fm^4 (\star). The HO frequency $\hbar\Omega = 20\text{MeV}$ is used. The horizontal dashed lines denote experimental energies [144]. (published in [44])

Table 6.1 – IT-NCSM ground-state energies in MeV of various p -shell nuclei for the three types of Hamiltonians at SRG flow parameters $\alpha = 0.04, 0.0625,$ and 0.08fm^4 extrapolated to the infinite model-space limit using the simple exponential ansatz $E(N_{\text{max}}) = E_{\infty} + a e^{-bN_{\text{max}}}$ with $\{E_{\infty}, a, b\}$ as fit parameters. The quoted energies are the average for E_{∞} from extrapolations based on either the three or four largest N_{max} spaces. As rough uncertainties we quote the difference between the energies obtained from the two extrapolations. Note that uncertainties from the IT threshold extrapolation are not accounted for in the extrapolations to $N_{\text{max}} \rightarrow \infty$. These are, e.g., for ${}^8\text{Be}$ at $N_{\text{max}} = 12$ on the order of 100keV and reach about 400keV for ${}^{16}\text{O}$. In the last row we quote the experimental energies [144].

\hat{H}	$\alpha[\text{fm}^4]$	${}^4\text{He}$	${}^6\text{Li}$	${}^8\text{Be}$	${}^{10}\text{Be}$	${}^{12}\text{C}$	${}^{14}\text{C}$	${}^{16}\text{O}$
NN-only	0.04	-27.90(1)	-31.2(1)	-	-	-96.2(1)	-	-156.1(3)
NN-only	0.0625	-28.25(1)	-31.8(1)	-	-	-101.4(3)	-	-164.9(7)
NN-only	0.08	-28.38(1)	-32.2(1)	-	-	-103.7(1)	-	-170.2(4)
3N-ind.	0.04	-25.32(1)	-27.7(3)	-48.5(1)	-52.5(3)	-76.6(1)	-91.5(2)	-119.6(5)
3N-ind.	0.0625	-25.34(1)	-27.6(2)	-	-	-77.2(1)	-	-119.7(5)
3N-ind.	0.08	-25.34(1)	-27.6(1)	-48.2(4)	-52.9(2)	-77.4(1)	-91.6(1)	-119.5(1)
3N-full	0.04	-28.45(1)	-31.8(3)	-55.9(3)	-65.0(3)	-95.6(4)	-117.3(6)	-142.2(2)
3N-full	0.0625	-28.45(1)	-31.8(1)	-	-	-96.8(2)	-	-145.6(2)
3N-full	0.08	-28.46(1)	-31.8(1)	-56.1(4)	-65.6(1)	-97.6(1)	-119.2(1)	-147.8(1)
exp. [144]		-28.30	-32.0	-56.5	-65.0	-92.3	-105.3	-127.6

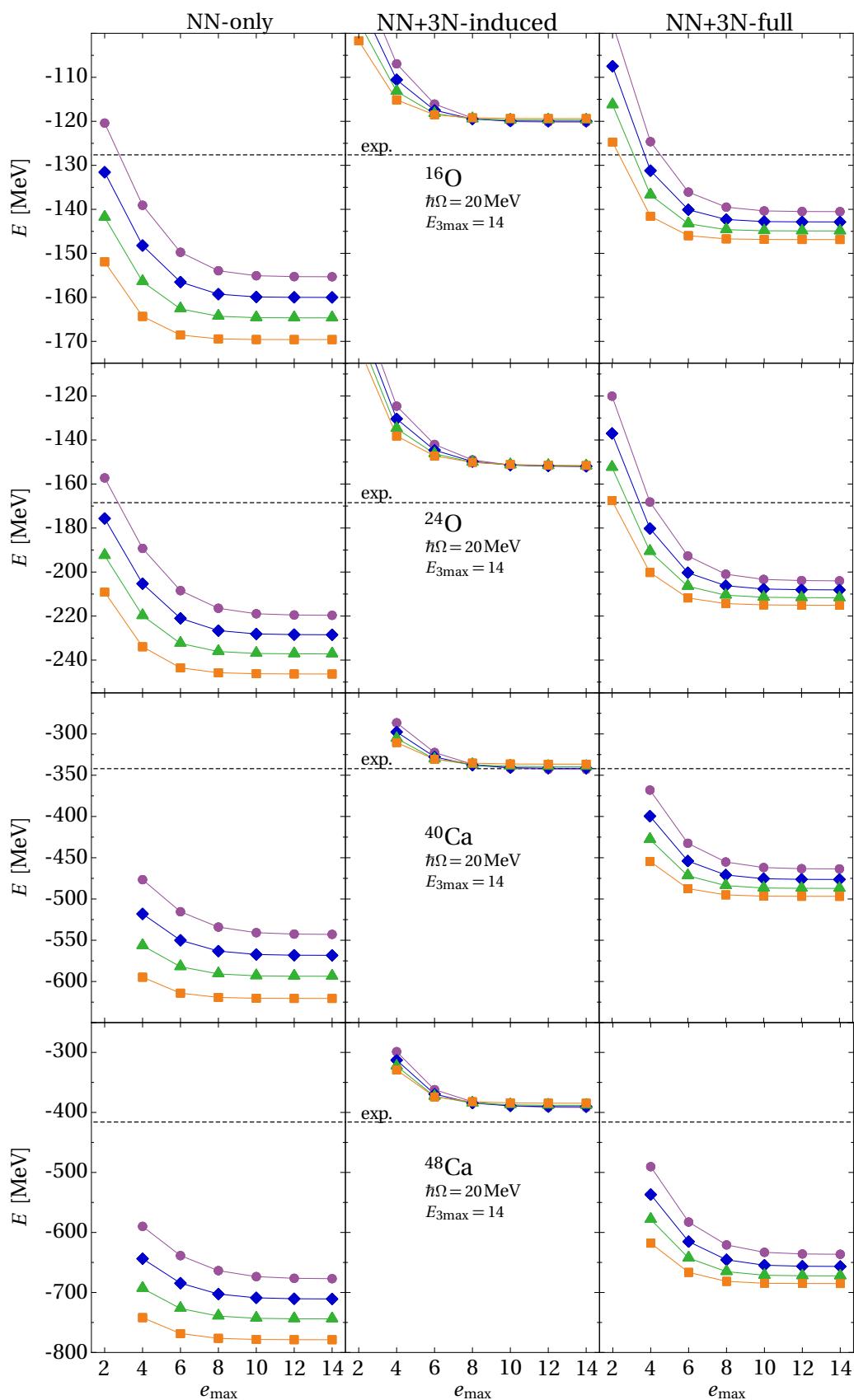


Figure 6.5 – CCSD ground-state energies for ^{16}O , ^{24}O , ^{40}Ca , and ^{48}Ca as function of the CC model-space truncation e_{max} for the three types of Hamiltonians (see column headings) using the NO2B approximation for flow parameters $\alpha = 0.04$ (\bullet), 0.05 (\blacklozenge), 0.0625 (\blacktriangle), and 0.08 fm^4 (\blacksquare). Dashed lines denote the experimental energies [144]. (published in [43])

NN+3N-full Hamiltonian at the normal-ordered two-body approximation (cf. Section 2.3), which we can safely anticipate here to be a very accurate approximation as we confirm in Section 8. For ^{16}O , where we can compare the CCSD to IT-NCSM results, and also for the medium-mass nuclei the observed pattern is consistent: the energies resulting from the NN-only Hamiltonian exhibit a strong dependence on the SRG flow parameter which becomes negligible once the SRG-induced 3N interactions are included. But the α dependence returns once the initial chiral 3N interaction is included. For completeness we state that also triples corrections, which are discarded here, would not alter this conclusion.

In summary, α dependence of the ground-state energies obtained with the standard NN+3N-full Hamiltonian can be clearly identified for nuclei with $A \gtrsim 10$, and unfortunately sophisticates the assessment of the untransformed Hamiltonian. Thus, conclusions about the initial chiral 3N interactions may be difficult.

6.1.1 The Origin of SRG-Induced Multi-Nucleon Interactions

Since we have identified the chiral 3N interaction as the origin of sizable α dependence of ground-state energies in nuclei beyond the mid- p -shell, we now disentangle the role of the individual parts of the chiral 3N interaction for the emergence of beyond-3N SRG-induced interactions. The findings discussed in the following are part of our publications [42, 44].

The chiral 3N interaction at N^2LO consists of a two-pion exchange (TPE), a one-pion exchange two-nucleon contact (OPE) and of a three-nucleon contact contribution, each of them accompanied by low-energy constants (LECs). We can switch off individual contributions to the 3N interactions in the initial Hamiltonian and study the consequences for the α dependence of the ground-state energies. Of course, if one or more LECs are changed, it is necessary to refit the remaining LECs and we adopt the procedure discussed in detail in Section 1.2. That is, we refit c_E to the ^4He binding energy at the bare interaction level and keep $c_D = -0.2$, which warrants the reproduction of the triton β -decay half life. The only exception is the case $c_E = 0$, where we instead use c_D to refit the ^4He binding energy. We emphasize that the 3N interactions are still fixed entirely in three- and four-body systems, and, thus are predictive for the ^{16}O ground-state energy we consider in the following. We quote all sets of LECs in Table 6.2.

Our results for the ^{16}O ground-state energy obtained with the different Hamiltonians are shown in Figure 6.6 for $\alpha = 0.04, 0.08$ and 0.16fm^4 including the exponential extrapolations to infinite model-space sizes indicated by the solid curves. As reference for the analysis we also include the results for the standard Hamiltonian exhibiting the strong flow-parameter dependence in panel (a). In panels (b) and (c) we show the results obtained when switching off the OPE terms ($c_D = 0$), or the 3N contact terms ($c_E = 0$), respectively. In both cases we observe small overall shifts of the energies, but almost no change of the flow-parameter dependence compared to the standard Hamiltonian. Therefore, these two terms can be ruled out as sources of significant SRG-induced many-body forces. In panel (d) we show the results with switched-off TPE contributions ($c_i = 0$), where the flow-parameter dependence of the extrapolated energies has collapsed and vanishes com-

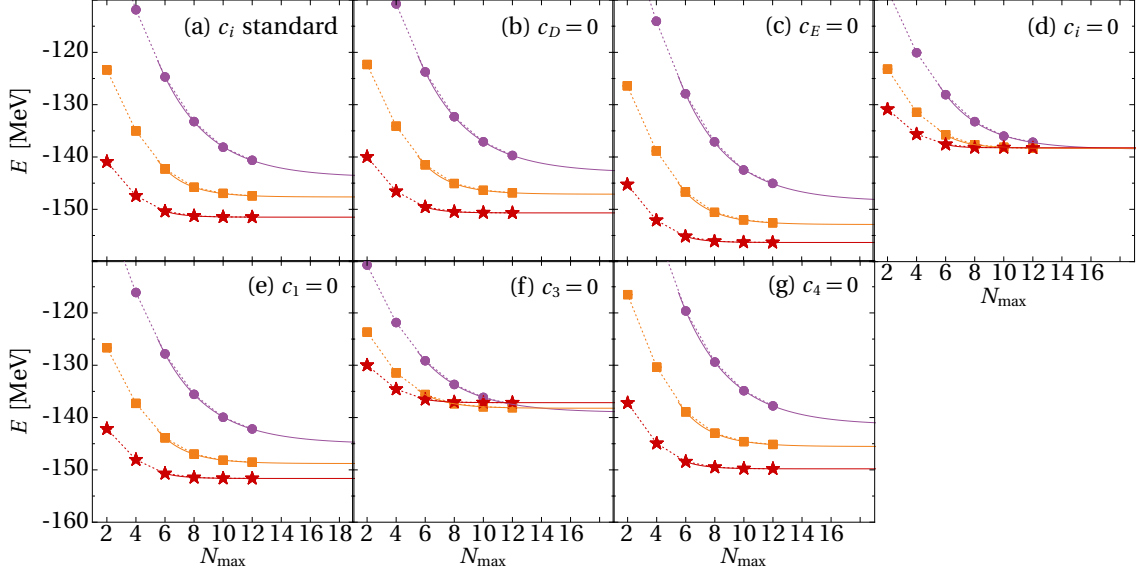


Figure 6.6 – IT-NCSM ground-state energy of ^{16}O obtained with the NN+3N-full Hamiltonian as function of N_{max} for SRG flow parameters $\alpha = 0.04$ (\bullet), $\alpha = 0.08$ (\blacksquare), $\alpha = 0.16 \text{ fm}^4$ (\star). Panel (a) shows results for the standard Hamiltonian. In addition, we show results for $c_D = 0$ in (b), $c_E = 0$ in (c), all $c_i = 0$ in (d), $c_1 = 0$ in (e), $c_3 = 0$ in (f), and $c_4 = 0$ in (g). For further details see text. (published in [44])

pletely. We conclude that solely the long-range TPE terms of the leading chiral 3N interactions are the key drivers of induced many-body forces during the SRG flow. The operator structure of the TPE diagram, see Eq. (1.11), is rather complicated and contains tensor- and spin-orbit-type terms. Bearing in mind that tensor interactions in the NN force are the origin of significant induced 3N interactions (see Ref. [103]), our findings above may not be unexpected. However, we can proceed further with our analysis and try to answer the question which operator structure within the TPE term is most relevant for the flow-parameter dependence. As before, we accomplish this by setting individual LECs, now the individual c_i , to zero. The results are shown in panels (e)-(f) of Figure 6.6. We find only mi-

Table 6.2 – Sets of LECs of the chiral 3N interaction at N^2LO for the standard Hamiltonian and different variants used for the analysis of the origin of SRG-induced beyond-3N contributions as described in the text. All individual sets are refitted by means of NCSM calculations at the bare Hamiltonian level to reproduce the ^4He binding energy. We used the identical fitting procedure presented in Section 1.2.

LEC types	c_1 [GeV^{-1}]	c_3 [GeV^{-1}]	c_4 [GeV^{-1}]	c_D	c_E
standard	-0.81	-3.2	5.4	-0.2	-0.205
$c_i = 0$	0	0	0	-0.2	0.444
$c_D = 0$	-0.81	-3.2	5.4	0	-0.205
$c_E = 0$	-0.81	-3.2	5.4	1.238	0
$c_1 = 0$	0	-3.2	5.4	-0.2	-0.207
$c_3 = 0$	-0.81	0	5.4	-0.2	-0.228
$c_4 = 0$	-0.81	-3.2	0	-0.2	0.141

nor effects on the flow-parameter dependence by switching off the c_1 or c_4 contributions. In contrast, a vanishing c_3 leads to ground-state energies that are almost independent of α . Thus, we identify the operator structure corresponding to c_3 as the main driver of the SRG-induced four- and multi-nucleon many-body forces originating from the chiral 3N interaction at N²LO. The uniqueness of c_3 in this respect remains rather unclear based on comparisons of the different contributing operator structures. Also the contributions to the ⁴He binding energy, which we identify indirectly via the necessary change of LEC c_E to recover the experimental energy, is of similar size for c_3 and c_4 , and only for c_1 quite small. Nevertheless, our findings about the critical role of c_3 may provide important information for the construction of next-generation chiral forces or optimized interactions using automated fitting algorithm as, such as POUNDERS in the recently proposed N²LO_{opt} interaction [146]. Furthermore, they might be taken into account for future developments of alternative SRG generators that are designed to suppress sizable many-body contributions from the outset.

6.2 Nuclear Spectra with Chiral 3N Interactions

After having observed a sizable SRG flow-parameter dependence of absolute energies in the upper p -shell, in this subsection we concentrate on its impact on excitation energies. We start our investigation with the excitation energies of the first 3^+ and 0^+ states of ⁶Li shown in the upper panels of Figure 6.7 as function of N_{\max} from left to right for the NN-only, NN+3N-induced and NN+3N-full Hamiltonian, respectively. We plot the excitation energies for the same set of flow parameters as previously for absolute energies using the identical plot-marker scheme. Obviously, we find much reduced flow-parameter dependence compared to our results for the absolute energies discussed above. At the NN-only level the converged results for $N_{\max} \geq 12$ for both excited states of ⁶Li, show a very small α dependence, where the largest deviation is generated by the $\alpha = 0.16 \text{ fm}^4$ Hamiltonian. As a consequence, despite the significant flow-parameter dependence of the absolute ⁶Li energies, the flow-parameter dependence is strongly reduced for the excitation energies. Therefore, the latter are less sensitive to SRG-induced many-body interactions. This is confirmed by including the 3N-induced contributions explicitly, as shown in the upper-middle panel of Figure 6.7. Both excitation energies are converged with respect to the model-space size at $N_{\max} = 12$, and independent of α as expected in this case, because already the absolute energies are α independent. The slight differences between the converged NN-only and NN+3N-induced excitation energies result from the small α dependence of the NN-only energies. Finally, we include also the initial chiral 3N interaction yielding the results in the right panel. Again, the converged excitation energies become independent of the flow parameter and may be compared to experiment. Compared to the NN+3N-induced Hamiltonian, the 3^+ state is pushed towards its experimental value due to the initial 3N interaction, but the opposite is the case for the 0^+ state. Already from this example it is clear that the chiral 3N interaction will not simultaneously improve all excitation energies compared to experiment.

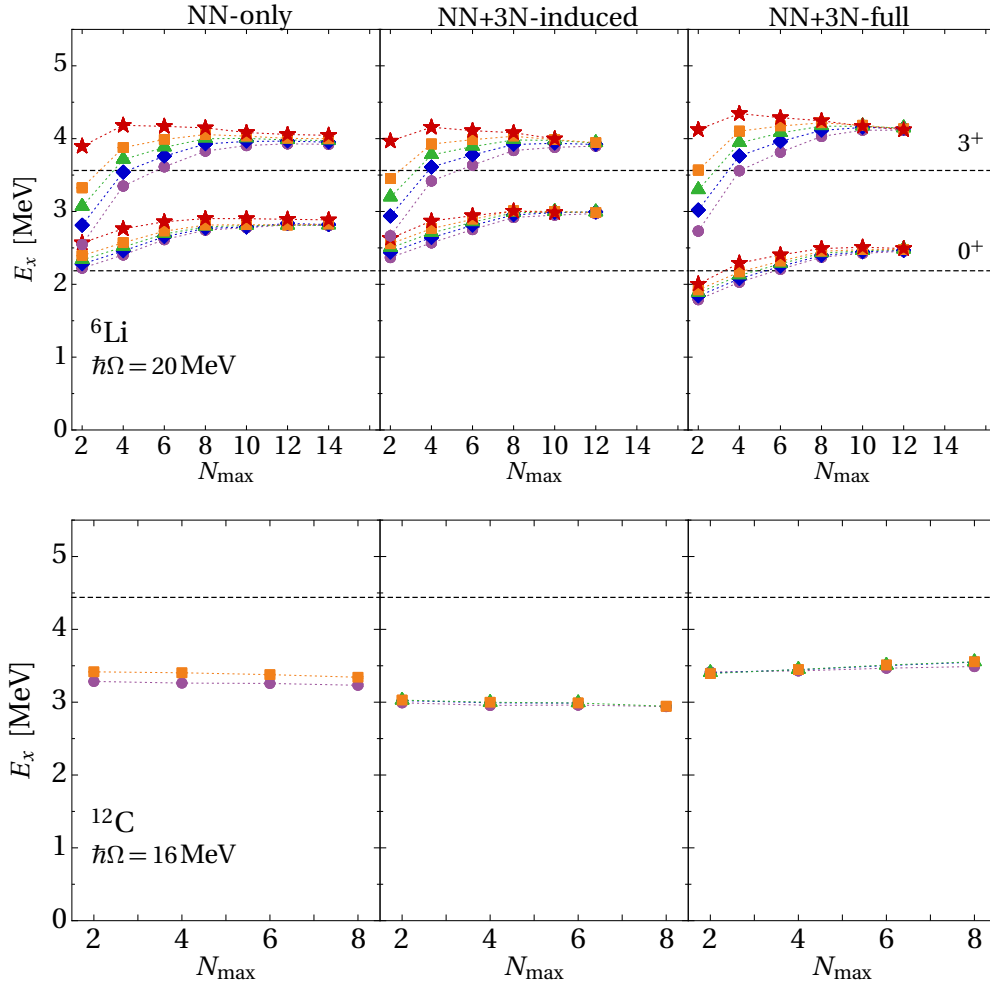


Figure 6.7 – Excitation energies of the first two excited states of ${}^6\text{Li}$ (upper panels) and the first excited 2^+ state in ${}^{12}\text{C}$ (lower panels) as function of the model-space size for the three different Hamiltonians obtained in the IT-NCSM for the SRG flow parameters $\alpha = 0.04$ (\bullet), 0.05 (\blacklozenge), 0.0625 (\blacktriangle), 0.08 (\blacksquare), and 0.16fm^4 (\star). The horizontal dashed lines denote experimental energies [144].

Moreover, we note the rather different pattern of the flow-parameter dependence for the two excited states of ${}^6\text{Li}$ before they reach convergence. The difference between the $\alpha = 0.04$ and 0.16fm^4 excitation energies at $N_{\text{max}} = 4$ is roughly twice as large for the 0^+ state than for the 3^+ state at the NN-only level and even larger in the NN+3N-full case. This shows that the SRG parameter dependence of excitation energies needs to be studied state by state in particular if they are not yet close to convergence.

The lower panels of Figure 6.7 show the excitation energy of the first excited state of ${}^{12}\text{C}$ again for the three types of Hamiltonians up to $N_{\text{max}} = 8$. Because of the increased computational cost for these calculations, we consider only a subset of flow parameters. For all three Hamiltonians the excitation energy of the first 2^+ state seems to be converged at $N_{\text{max}} = 8$. Concerning the flow-parameter dependence, the situation is similar to ${}^6\text{Li}$: although we observe a significant α dependence for the ${}^{12}\text{C}$ ground-state energy, both, the NN-only and NN+3N-full Hamiltonian results reveal that the SRG-induced multi-nucleon interactions are much less relevant for the excitation energy. As expected the NN+3N-

induced results are completely independent of α and the α -dependence of the NN+3N-full energies remains negligible, too. In conclusion these findings provide the possibility of investigations of nuclear spectra throughout the p -shell including explicit chiral 3N interactions and to distinguish effects from SRG-induced 3N interactions from those generated by initial 3N forces.

We emphasize that spectra obtained in the (IT-)NCSM often depend on the used HO frequency $\hbar\Omega$. Such dependencies are due to a lack of convergence with respect to model-space size, because converged results should be independent of the chosen basis, i.e., of $\hbar\Omega$. Examples for a direct comparison of spectra obtained at different HO frequencies are shown in Figures 5.4 or 6.11. For the spectra of ${}^6\text{Li}$, ${}^{10}\text{B}$ and ${}^{12}\text{C}$ discussed in the following and also for the spectra shown in Section 7 we choose the HO frequency for which the majority of investigated excited states seem to be most stable with respect to increasing N_{max} .

The three top panels of Figure 6.8 show the spectra of ${}^6\text{Li}$ up to $N_{\text{max}} = 12$ including the first four positive parity states for the three Hamiltonians with two flow parameters $\alpha = 0.08$ (solid bars) and 0.04fm^4 (dashed bars). We have already discussed the first two excited states above. The discussion of the 2^+ state follows essentially the same lines. With the NN+3N-induced Hamiltonian we find it practically α independent and in good agreement with experiment at $N_{\text{max}} = 12$, however it is not yet fully converged with respect to model-space size. The same holds for this state computed with the NN+3N-full Hamiltonian. From its N_{max} -convergence pattern one might anticipate that its excitation energy will continue to decrease and to further approach the experimental value. Altogether, the only state whose description compared to experiment is clearly improved by the initial 3N interaction is the 3^+ state.

In the second row of Figure 6.8 we depict the four lowest positive parity eigenstates of ${}^{10}\text{B}$ for the three types of Hamiltonians (see columns headings) and again for the two α values at $\hbar\Omega = 16\text{MeV}$. In the spectrum obtained with the NN-only Hamiltonian the ground-state of ${}^{10}\text{B}$ is a 1^+ state contrary to the experimentally found 3^+ ground state. Also the inclusion of SRG-induced 3N interactions, which yields the unitarily equivalent description based on the chiral NN interaction, cannot cure this problem. Only by including the initial 3N interaction we obtain the correct ground state, as shown in the right panel. This has been first discussed with chiral 3N interactions in Ref. [78] using the NCSM, and we can confirm it via the IT-NCSM. Furthermore, this is a well-known example for the necessity of including the initial 3N interaction, as also confirmed in ab-initio Green's function Monte-Carlo calculations [24]. Another interesting detail is the presence of rather α independent and seemingly relatively well-converged excitation energy of a 2^+ state obtained with the NN+3N-induced Hamiltonian that is shifted by about 2 MeV upwards in energy by the initial chiral 3N interaction towards its experimentally known excitation energy of about 3.6 MeV [148], (not shown in Figure 6.8, but cf. Figure 7.3). Therefore, despite some remaining flow-parameter dependence at $N_{\text{max}} = 8$, the spectrum of ${}^{10}\text{B}$ has been improved significantly by the initial chiral 3N interaction.

Finally, we investigate the low-lying positive-parity spectrum of ${}^{12}\text{C}$ shown in the lower

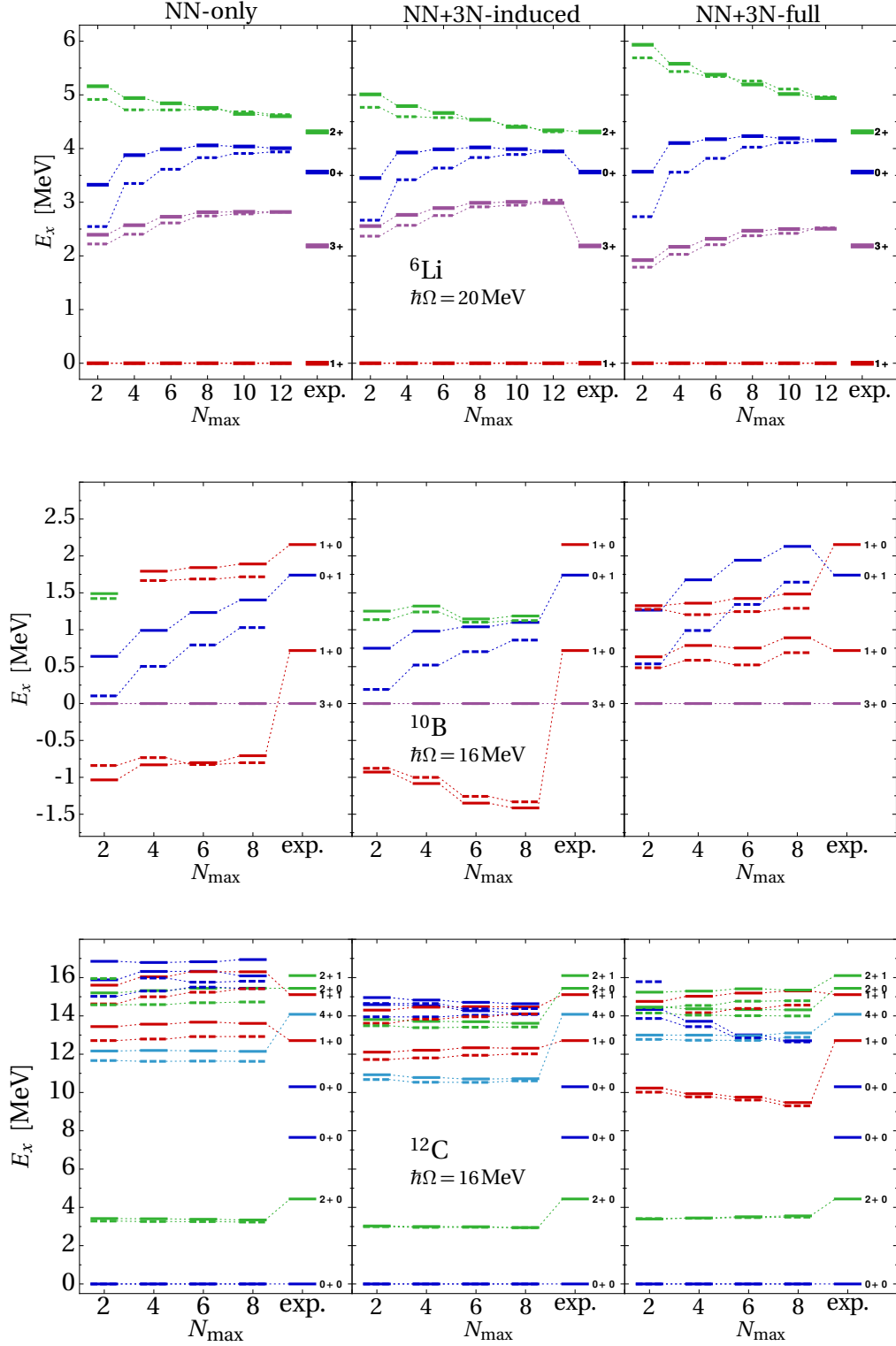


Figure 6.8 – Low-lying positive-parity excitation spectra of ${}^6\text{Li}$ (top panels), ${}^{10}\text{B}$ (middle panels) and ${}^{12}\text{C}$ (bottom panels) as function of model-space size for the three types of Hamiltonians (see column headings) and for SRG flow parameters $\alpha = 0.04$ (---) and 0.08fm^4 (—) obtained from the IT-NCSM. Note that uncertainties from the importance-threshold extrapolation using the protocol described in Section 4.2 are hidden by the plot markers. In the right columns we show in addition the experimental energies taken from Refs. [147, 148, 149].

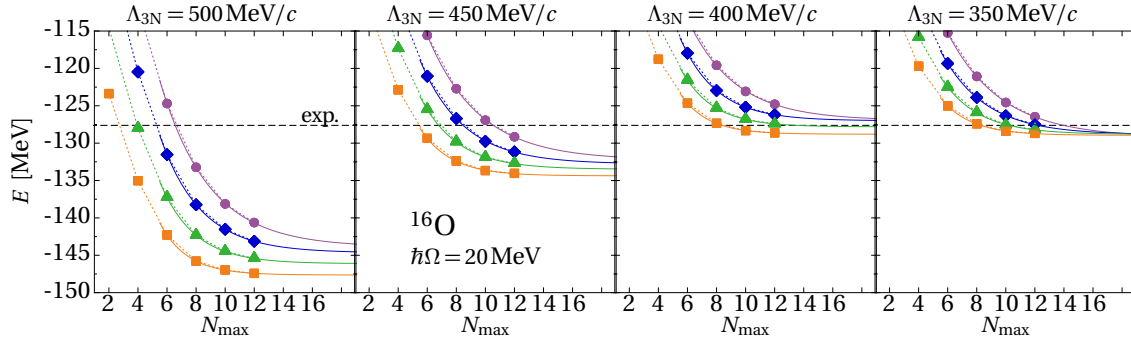


Figure 6.9 – Dependence of the IT-NCSM ground-state energy of ^{16}O obtained with the NN+3N-full Hamiltonian on the model-space size for the different 3N cutoffs Λ_{3N} (see column headings), and for the different SRG flow parameters $\alpha = 0.04$ (\bullet), 0.05 (\blacklozenge), 0.0625 (\blacktriangle) and 0.08 fm⁴ (\blacksquare). The horizontal dashed line denotes the experimental energy [144]. (published in [44])

three panels of Figure 6.8. We note that our results agree well with the spectra obtained in Ref. [78] using the Okuko-Lee-Suzuki transformed chiral 3N interaction, and most of the states seem to be well converged at $N_{\max} = 8$. The sole exception is the first excited 0^+ state that is a candidate for the famous Hoyle state [150, 151], which is known to be a α -particle-cluster state [152, 153]. Therefore, huge model spaces would be required to converge this state using a basis of Slater determinants of HO single-particle states [154]. From a comparison of the left-hand to the middle panel it is evident that the inclusion of the SRG-induced 3N interactions leads to an overall compression of the ^{12}C spectrum and to a reduced SRG flow-parameter dependence for all states at $N_{\max} = 8$. In contrast, the inclusion of the initial chiral 3N interaction leads to shifts of individual levels resulting in changed level orderings. These improve, e.g., the agreement of the first 2^+ and 4^+ states with experiment. On the downside the first 1^+ state needs to be mentioned whose excitation energy is reduced significantly resulting in noticeable disagreement with experiment. This state is clearly most sensitive to the inclusion of the initial 3N interaction, and hence lends itself for more detailed investigations of the role of details, e.g., the LECs, of the chiral 3N interaction. In addition, the stability of the ^{12}C spectrum with respect to N_{\max} convergence and flow parameter variations makes it an ideal candidate for such case studies. We come back to this in Section 7, including also the sensitive ground state of ^{10}B .

6.3 Chiral 3N Interactions with Reduced Cutoff

We now return to absolute energies and discuss options to reduce the SRG flow-parameter dependence that we have analyzed in Section 6.1. Motivated by the vanishing of the flow-parameter dependence when switching off the TPE 3N interaction, we study ground-state energies for Hamiltonians with different lowered cutoff momenta Λ_{3N} of the 3N interaction. In this way we decrease far off-diagonal 3N matrix elements, which are significantly affected by the prediagonalization in the SRG flow, from the outset. We have discussed the construction of these reduced-cutoff 3N interactions already in Section 1.2: after reducing the cutoff of the initial 3N interaction we keep $c_D = -0.2$ and refit c_E to the ^4He ground-state energy, while the c_i 's keep their original values dictated by the N³LO NN force. For

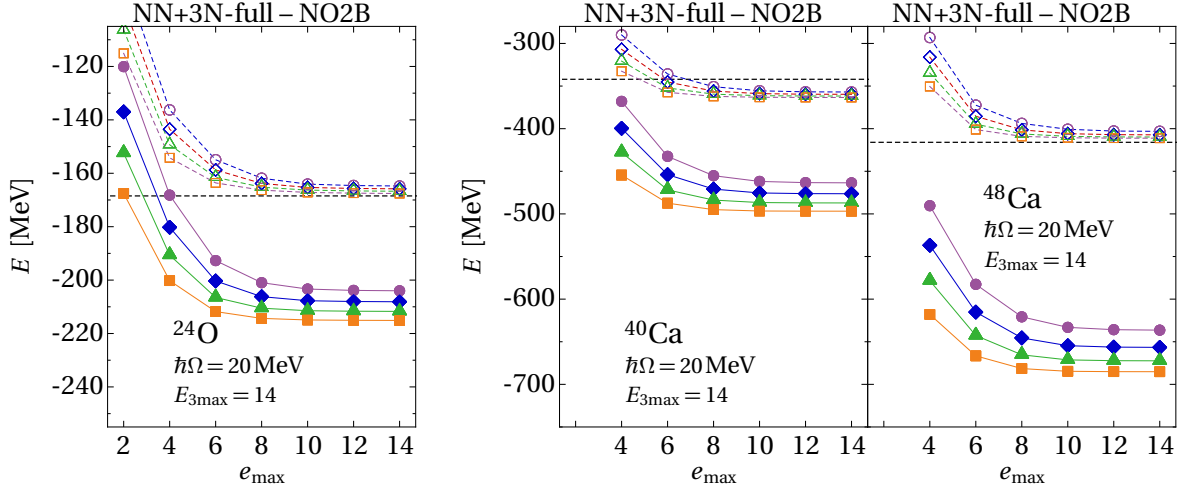


Figure 6.10 – CCSD ground-states energies of ^{24}O (left-hand panel), ^{40}Ca (middle panel), and ^{48}Ca (right-hand panel) as function of the CC model-space parameter e_{\max} for the NN+3N-full Hamiltonian using the NO2B approximation, for the set of SRG flow-parameters given in Fig. 6.9 and for three-body cutoffs $\Lambda_{3\text{N}} = 500\text{MeV}/c$ (filled symbols), and the reduced $\Lambda_{3\text{N}} = 400\text{MeV}/c$ (open symbols). (published in [43])

the details of the fitting procedure see Section 1.2, and for the obtained LECs see Table 1.1. In this way we have obtained additional 3N interactions with cutoff momenta of 350, 400 and $450\text{MeV}/c$.

We discuss the obtained ^{16}O ground-state energy using the different 3N interactions in the NN+3N-full Hamiltonian as function of model-space size and for a range of SRG flow-parameters from $\alpha = 0.04$ to 0.08fm^4 in context of Figure 6.9. The left panel shows for reference the ^{16}O ground-state energy obtained with the standard 3N interaction regularized with $\Lambda_{3\text{N}} = 500\text{MeV}/c$, where we have diagnosed the significant missing contributions of SRG induced four- and multi-nucleon interactions through the sizable α dependence. The remaining panels show the IT-NCSM results using the reduced-cutoff 3N interactions. The pattern of the flow-parameter dependence of the N_{\max} -extrapolated ground-state energies is obvious: the more we reduce the cutoff of the initial chiral 3N interaction the more the flow-parameter dependence, and accordingly the relevance of beyond-3N SRG-induced contributions, is suppressed. For $\Lambda_{3\text{N}} = 400\text{MeV}/c$ the flow-parameter dependence varies only by 2%. At $\Lambda_{3\text{N}} = 350\text{MeV}/c$ the extrapolated ground-state energies are identical for all α parameters. Based on this finding, we can sharpen our conclusions of Section 6.1.1: the high-momentum components of the TPE contributions, and mostly those coming with LEC c_3 , are the origin of SRG-induced beyond-3N interactions.

Furthermore, in Figure 6.9 we observe that for decreasing $\Lambda_{3\text{N}}$ and accordingly decreasing relevance of missing SRG-induced repulsive beyond-3N contributions the ^{16}O ground-state energy approaches its experimental value. We stress that the ground-state energies in case of vanishing α dependence are completely predictive since the LECs of the reduced-cutoff 3N interaction have been fixed entirely in the three- and four-body system. Therefore, the good agreement with experiment, e.g., with the 3N interaction using $\Lambda_{3\text{N}} = 400\text{MeV}/c$ is remarkable. We confirm this trend in Figure 6.10 also for the heav-

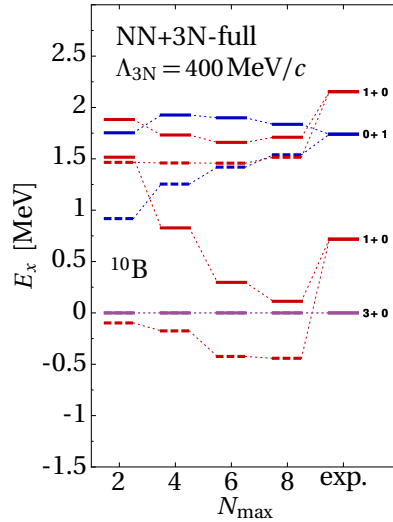


Figure 6.11 – Low-lying positive-parity spectrum of ^{10}B as function of N_{max} obtained with the NN+3N-full Hamiltonian using the 3N interaction with reduced cutoff to $\Lambda_{3\text{N}} = 400\text{MeV}/c$ at $\alpha = 0.08\text{fm}^4$. Shown are spectra obtained with HO frequency $\hbar\Omega = 16\text{MeV}$ (---) and $\hbar\Omega = 20\text{MeV}$ (—).

ier nuclei ^{24}O , ^{40}Ca , and ^{48}Ca computed in the CCSD approach, where we have used the normal-ordered two-body approximation introduced in Section 2.3. Here we anticipate already the good accuracy of this approximation, which we verify in detail in Section 8. Results obtained with the standard 3N interaction are shown as filled symbols and those obtained employing the $\Lambda_{3\text{N}} = 400\text{MeV}/c$ cutoff are represented by the open symbols. Even over of this mass-range we find a significantly reduced flow-parameter dependence and in addition ground-state energies in good agreement with experiment. This is a first hint towards the predictive power of the chiral interactions in this medium-mass regime. We validate the 3N interaction with $\Lambda_{3\text{N}} = 400\text{MeV}/c$ throughout the remaining sections of Part II. Moreover, we note that this interaction has also been adopted already by other groups and has triggered a number of publications, e.g., Refs. [34, 30, 33, 31, 155, 29].

We close our discussion of the reduced-cutoff 3N interactions here with another critical test in light nuclei. One consequence of lowering the cutoff $\Lambda_{3\text{N}}$ too far is the elimination of interaction components that are crucial for the proper description of certain nuclear properties. We concentrate on energies here because this is the main observable studied in this work. One crucial cross-check is, e.g., the ground-state of ^{10}B as we have discussed already above. Therefore, we present in Figure 6.11 the ^{10}B spectrum including the first three excited states computed with the NN+3N-full Hamiltonian using $\Lambda_{3\text{N}} = 400\text{MeV}/c$ as function of the model-space size N_{max} , and for the two HO frequencies $\hbar\Omega = 16\text{MeV}$ (dashed bars) and $\hbar\Omega = 20\text{MeV}$ (solid bars). For $\hbar\Omega = 16\text{MeV}$ the 1^+ state seems to be the ground-state of ^{10}B , which is in contradiction to experiment. The spectrum is not fully converged as evident from the strong influence of the change of the HO frequency to $\hbar\Omega = 20\text{MeV}$. In this case the 1^+ state at $N_{\text{max}} = 8$ remains an excited state, however, due to the still significant decrease of its excitation energy from $N_{\text{max}} = 6$ to 8 and the overall convergence

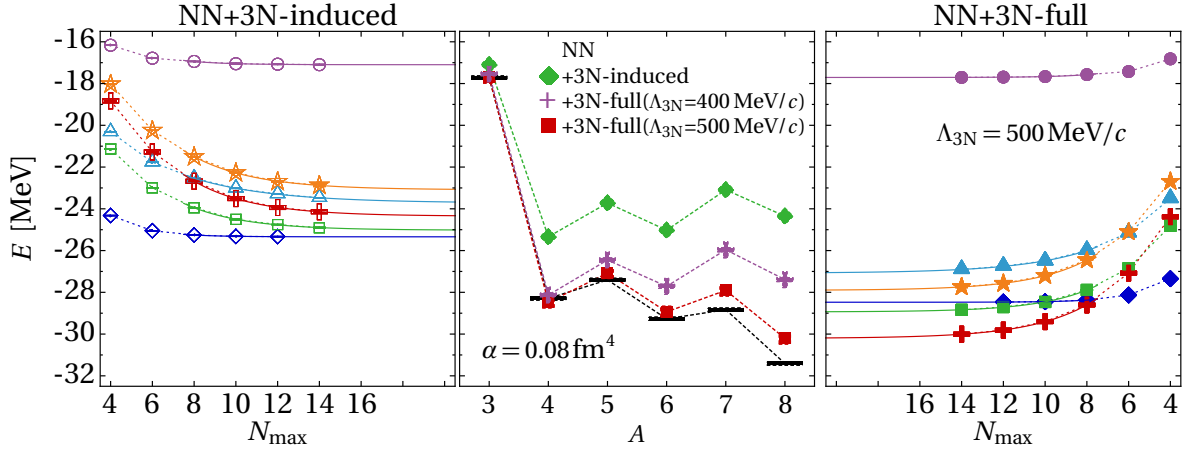


Figure 6.12 – Left- and right-hand panels show the convergence of IT-NCSM ground-state energies with respect to the model-space size for ${}^3\text{He}$ (\bullet , shifted by -10 MeV), ${}^4\text{He}$ (\blacklozenge), ${}^5\text{He}$ (\blacktriangle), ${}^6\text{He}$ (\blacksquare), ${}^7\text{He}$ (\blackstar) and ${}^8\text{He}$ (\blackplus) obtained at their respective optimal frequency for the NN+3N-induced and NN+3N-full Hamiltonians, respectively. Solid curves depict the extrapolations to infinite model space size. The middle panel shows the extrapolated ground-state energies of the ${}^A\text{He}$ isotopes for the NN+3N-induced (\blacklozenge), the NN+3N-full ($\Lambda_{3\text{N}} = 500$ MeV/ c) (\blacksquare), and the reduced-cutoff NN+3N-full ($\Lambda_{3\text{N}} = 400$ MeV/ c) (\blackplus) Hamiltonians compared to experiment (\blacksquare).

pattern with respect to N_{max} we again expect the 1^+ state to become the ground state once convergence is reached, i.e., beyond $N_{\text{max}} = 10$. On the other hand, a comparison to Figure 6.8 shows that the remaining excited states are rather insensitive to the change of $\Lambda_{3\text{N}}$.

As second test we study the helium isotopic chain using IT-NCSM calculations up to $N_{\text{max}} = 14$ model spaces, which is sufficient to obtain robust extrapolations to infinite model-space size in all isotopes as evident from the N_{max} sequences shown for the NN+3N-induced and NN+3N-full Hamiltonians in the left- and right-hand panel of Figure 6.12, respectively. In the middle panel of Figure 6.12 we show the N_{max} -extrapolated ground-state energies of ${}^3\text{He}$ to ${}^8\text{He}$ based on the four largest model spaces for the NN+3N-induced Hamiltonian (green diamonds) and the two NN+3N-full Hamiltonians with $\Lambda_{3\text{N}} = 500$ MeV/ c (red boxes) and $\Lambda_{3\text{N}} = 400$ MeV/ c (violet crosses) after SRG evolution up to $\alpha = 0.08$ fm 4 . With the NN+3N-induced Hamiltonian, which is unitarily equivalent to the initial chiral NN Hamiltonian, we find a severe underbinding for all helium isotopes. The inclusion of the initial 3N interaction with $\Lambda_{3\text{N}} = 400$ MeV/ c provides attractive contributions, however, they remain too weak and the isospin-dependence is at variance with experiment. In contrast, the NN+3N-full Hamiltonian with the $\Lambda_{3\text{N}} = 500$ MeV/ c yields ${}^3\text{He}$, ${}^4\text{He}$, ${}^5\text{He}$ and ${}^6\text{He}$ in good agreement with experiment. For ${}^7\text{He}$ and ${}^8\text{He}$ roughly 1 MeV underbinding is still present, but we find ${}^8\text{He}$ bound with respect to ${}^6\text{He}$ in agreement with experiment. Altogether, we can conclude that the chiral NN interaction at N 3 LO fails to reproduce the experimentally observed binding-energy systematics in the helium isotopic chain, but it is correctly described using the standard chiral 3N interaction with $\Lambda_{3\text{N}} = 500$ MeV/ c cutoff. However, the reduced-cutoff 3N interaction seems to be too weak and fails in this respect. Finally, we emphasize that for the description of the halo nuclei ${}^6\text{He}$ and ${}^8\text{He}$ and the unbound isotopes ${}^5\text{He}$ and ${}^7\text{He}$ also a proper description of the continuum may be relevant.

The formal developments to extend the NCSM in this direction are discussed in Part III of this thesis. However, given the robustness of the extrapolations shown in the left- and right-hand panels of Figure 6.12 we do not expect an altered general conclusion here.

In summary, in this section we have identified sizable SRG-induced beyond-3N interactions, which become relevant in studies of absolute energies beyond $A \gtrsim 10$, observed via strong flow-parameter dependencies. This effect is significantly reduced for excitation energies due to cancellations and, therefore, reliable predictions of relative energies are possible. To address this issue for absolute energies, we have investigated 3N interactions with reduced momentum cutoffs and have identified these as possibility to circumvent strong α dependencies also for absolute energies. Furthermore, we briefly highlighted that the 3N interaction with $\Lambda_{3N} = 400 \text{ MeV}/c$, in spite of deficiencies in light nuclei, yields ground-state energies in remarkably good agreement with experiment even in calcium isotopes. We expand on this in more detail in the dedicated Section 9, where we apply these interactions throughout the oxygen isotopic chain and in medium-mass and heavy nuclei up to ^{132}Sn .

SECTION 7

Sensitivity Analysis for Chiral Three-Nucleon Forces

So far we have discussed the developments allowing for the application of 3N interactions derived from chiral effective field theory, and investigated effects of the chiral NN+3N Hamiltonians on nuclear structure observables in the upper p -shell with particular focus on 3N interactions. The possibility to accurately study nuclear spectra in this mass region, which is due to the strongly reduced SRG flow-parameter dependence of excitation energies discussed in the previous section, we are in the position to close the circle and to provide feedback about uncertainties of, e.g., the low-energy constants (LECs) of the chiral interactions based on ab-initio predictions of nuclear structure properties. We proceed along these lines and study the sensitivity of nuclear structure observables to variations of the LECs and the cutoff momentum of the chiral 3N interaction at N²LO. Such sensitivity analyses are important to consistently propagate possible uncertainties in the chiral EFT inputs into nuclear observables and to provide error bands obtained directly for the relevant quantities. In this way we can provide direct feedback for future constructions or improvements of the chiral nuclear interactions.

We undertake first steps in this direction by a sensitivity study with respect to variations in the LECs present in the leading chiral 3N interaction. Its operator structures have been discussed in Eqs. (1.11), (1.12) and (1.13). The two-pion exchange contribution depends on LECs c_1 , c_3 and c_4 , the one-pion exchange two-nucleon contact on c_D , and the three-nucleon contact term on c_E . Due to the fact that the c_i constants appear already in contributions to the N³LO NN force these are determined already during the fitting procedure of the NN interaction. We list different sets of possible values for these c_i constants in Table 7.1. The first row shows the LECs of the NN interaction we use throughout this work. This table reveals sizable variations among the individual c_i constants, which might have consequences for the nuclear spectroscopy. However, we stress that we keep the LECs in the NN interaction at their original values, and concentrate on the effects of LEC variations in the 3N interaction only. Recall that otherwise a complete refit of NN scattering phase

shifts for each parameter set would be necessary.

Another motivation for the variation of the LECs in the 3N interaction has been pointed out in Refs. [82, 160]: selected TPE diagrams that contribute to the 3N interaction at N³LO can be included simply by using the following shifted LECs \bar{c}_i in the N²LO operator structures

$$\bar{c}_1 = c_1 - \frac{g_A^2 M_\pi}{64\pi F_\pi^2} = (-0.81 - 0.13)\text{GeV}^{-1}, \quad (7.1)$$

$$\bar{c}_3 = c_3 + \frac{g_A^4 M_\pi}{16\pi F_\pi^2} = (-3.20 + 0.89)\text{GeV}^{-1}, \quad (7.2)$$

$$\bar{c}_4 = c_4 - \frac{g_A^4 M_\pi}{16\pi F_\pi^2} = (5.40 - 0.89)\text{GeV}^{-1}, \quad (7.3)$$

where the first number corresponds to the original values c_i dictated by the NN interaction [71], respectively. We adopt these shifts of the LECs for our sensitivity studies in nuclear spectra throughout this section, where we also distinguish between shifting all c_i constants simultaneously or shifting them individually. Of course, each time we have to refit the remaining LECs c_D and c_E to properties of light nuclei, and we make use of the fitting procedure described in Section 1.2, which we used before for the construction of the reduced-cutoff 3N interactions. For completeness, we provide the used LECs for the sensitivity studies in Table 7.2.

We begin the sensitivity study with the low-energy positive-parity spectrum of ¹²C, which we discussed already in the previous section for the standard NN+3N Hamiltonian in Figure 6.8 and found the excitation energies robust with respect to changes of the SRG flow-parameter. In addition, we have identified the first 1⁺ state as very sensitive to the inclusion of the initial chiral 3N interaction. Hence, this state may serve as an ideal candidate for our sensitivity studies. In Figure 7.1 we depict the ¹²C spectrum obtained with the IT-NCSM at $N_{\text{max}} = 8$ with $\hbar\Omega = 16\text{MeV}$ and SRG flow-parameter $\alpha = 0.08\text{fm}^4$. The first column shows the spectrum resulting from the NN+3N-induced Hamiltonian, i.e., without an initial 3N interaction. As can be seen from the second column, the inclusion of the initial chiral 3N interaction causes several level crossings and the first excited 1⁺ and 4⁺ states are affected most. The next column shows the results when we adopt the shifted LECs \bar{c}_i

Table 7.1 – Possible sets of the LECs c_i obtained from different fit procedures. The constants quoted in the first line correspond to the NN interaction used throughout this work. Note that each individual set of LECs can have in addition sizable errors from the depending on the respective fit procedure. For details we refer to the respective references given below.

	c_1 [GeV ⁻¹]	c_3 [GeV ⁻¹]	c_4 [GeV ⁻¹]
Entem et al. – Ref. [71]	-0.81	-3.20	5.40
Rentmeester et al. – Ref. [156]	-0.76	-4.78	3.96
Büttiker et al. – Ref. [157]	-0.81	-4.70	3.40
Fettes et al. – Ref. [158]	-1.23	-5.94	3.47
Entem et al. – Ref. [70]	-0.81	-3.40	3.40
Bernard et al. – Ref. [159]	-0.93	-5.29	3.63

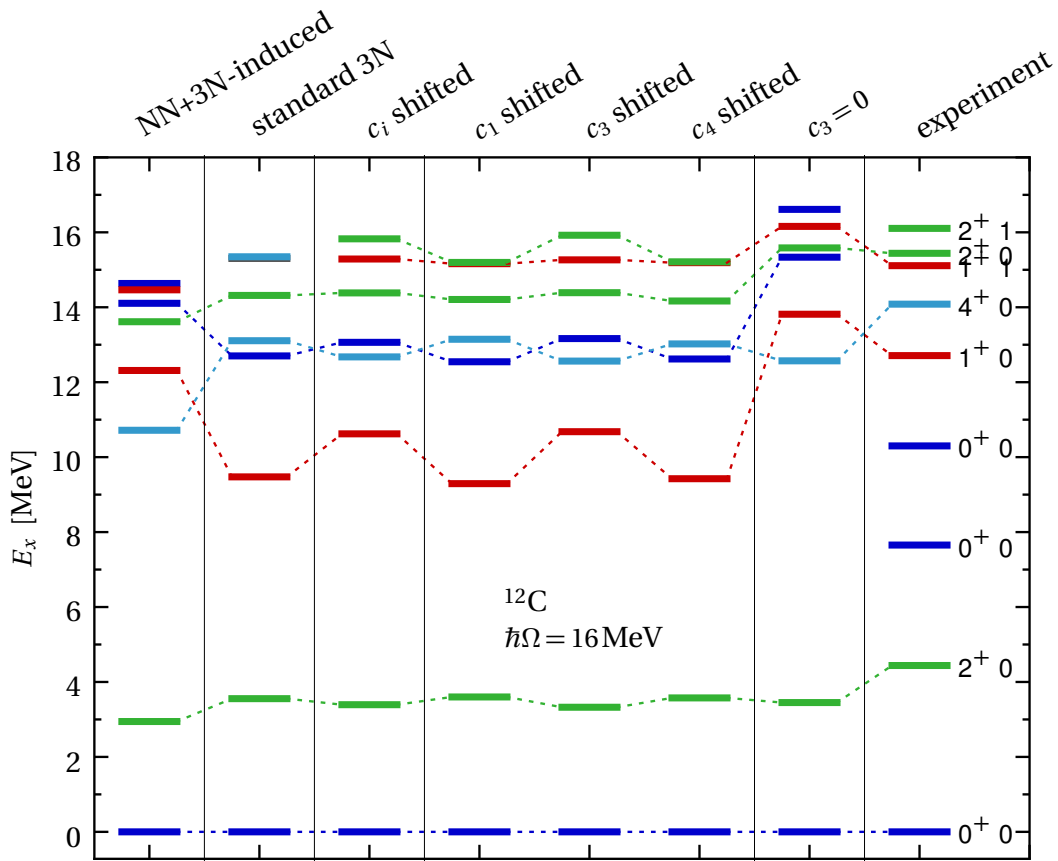


Figure 7.1 – IT-NCSM excitation spectrum of ^{12}C obtained for different Hamiltonians specified in the column headings and differing in the values of LECs c_i . The details are explained in the text. The IT-NCSM model space is truncated at $N_{\text{max}} = 8$, the HO frequency is $\hbar\Omega = 16\text{MeV}$ and the SRG flow-parameter $\alpha = 0.08\text{fm}^4$. Experimental energies are taken from Ref. [149]. (published in [161])

of Eqs. (7.1)-(7.3), i.e., in effect here we include selected N^3LO TPE contributions as argued above. We find most of the excitation energies rather insensitive. However, a prominent exception is the first 1^+ state, whose excitation energy is increased significantly. We investigate the question if this effect is due to a single LEC or if it is a cumulative effect of all three shifted LECs with help of the spectra shown in columns four to six, where in each column only a single c_i has been shifted while the remaining LECs are kept at their original values. Comparing the spectra of the columns labeled ‘ c_1 shifted’ and ‘ c_4 shifted’ to the original NN+3N-full spectrum shown in the second column reveals that the shifts of LECs c_1 and c_4 do not change the spectrum at all — not even the first 1^+ state. This is different for the individual shift of c_3 , where we observe a significant change of the first 1^+ excitation energy by about the same amount as for the simultaneous shift of all c_i s shown in column three. An interesting detail is that although the sensitivity of all other states are rather small, the pattern observed in columns four to six for the first 1^+ , the first 0^+ and the second and third 2^+ states is identical, which is a (slight) increase of their excitation energy for the c_3 shift. Similarly the first 2^+ and first 4^+ states react with a slight decrease of their excitation energy. In conclusion, we find the LEC c_3 playing an important role for the

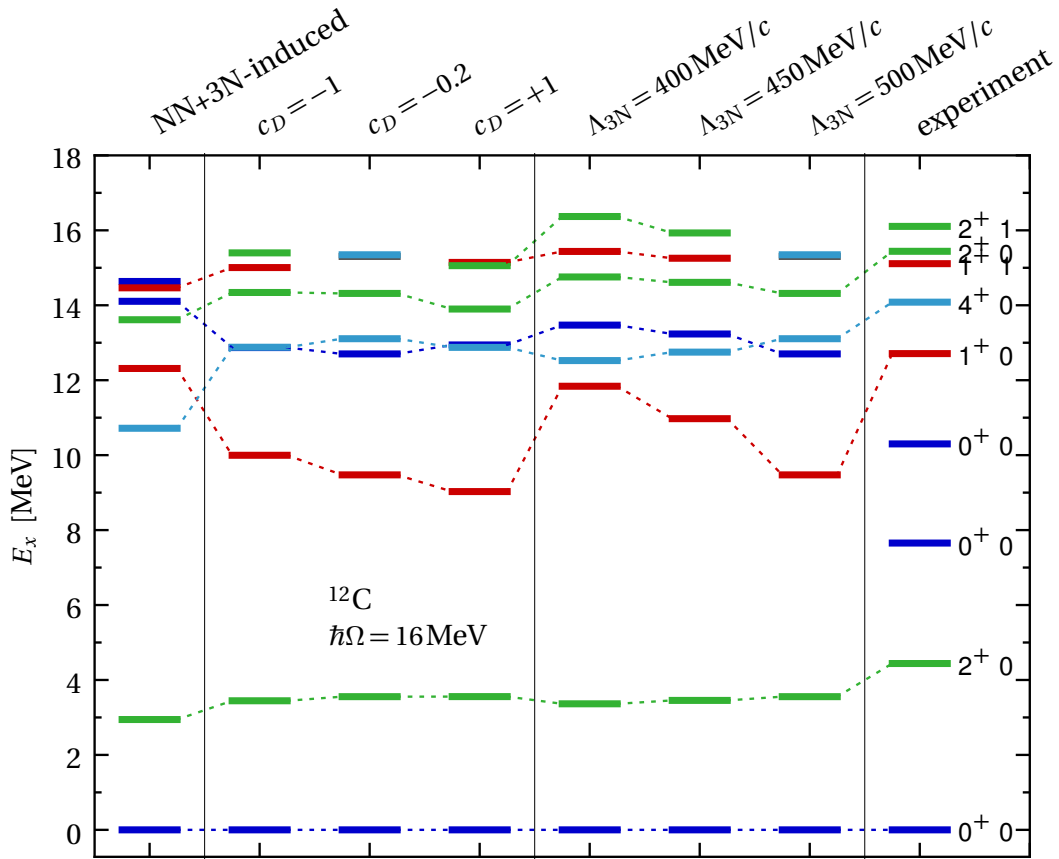


Figure 7.2 – IT-NCSM excitation spectrum of ^{12}C obtained for different Hamiltonians specified in the column headings and differing in the values of LEC c_D or the 3N cutoff Λ_{3N} . The details are explained in the text. Remaining parameters are identical to Figure 7.1. (published in [161])

excitation energy of the first 1^+ state in ^{12}C , while the excitation energies of other states are only slightly affected by c_3 and are essentially independent of c_1 and c_4 . To confirm the important role of c_3 we depict in the next-to-last column the spectrum obtained with $c_3 = 0$. The corresponding value for the refitted c_E can be found in Table 6.2. We find again a dramatic change of the excitation energy of the first 1^+ state. Also most of the high-lying states are affected, while the first 2^+ and 4^+ energies remain unaltered.

In the same way we can extend our sensitivity analysis to the LEC c_D attached to the OPE diagram of the leading chiral 3N interaction and the 3N cutoff Λ_{3N} . The refitted values for c_E are listed in Tables 7.2 and 6.2, respectively. The corresponding spectra are shown in Figure 7.2 starting again with the NN+3N-induced spectrum for reference. Columns two to four depict the spectrum for the increasing LEC $c_D = -1$, -0.2 (corresponding to the standard NN+3N-full Hamiltonian) and $+1$, respectively. Again the largest effect is observed for the excitation energy of the first excited 1^+ state, while the remaining energies stay essentially unaffected. The discussion is very similar for the sensitivities with respect to the variations of Λ_{3N} shown in columns five to seven. The only significant change is observed for the first 1^+ excitation energies while all other energies show only minor changes. At this point we briefly summarize: we clearly identified c_3 as the most important LEC for the ^{12}C spectrum, and the first 1^+ state in ^{12}C shows by far the largest sensitivity to details of the

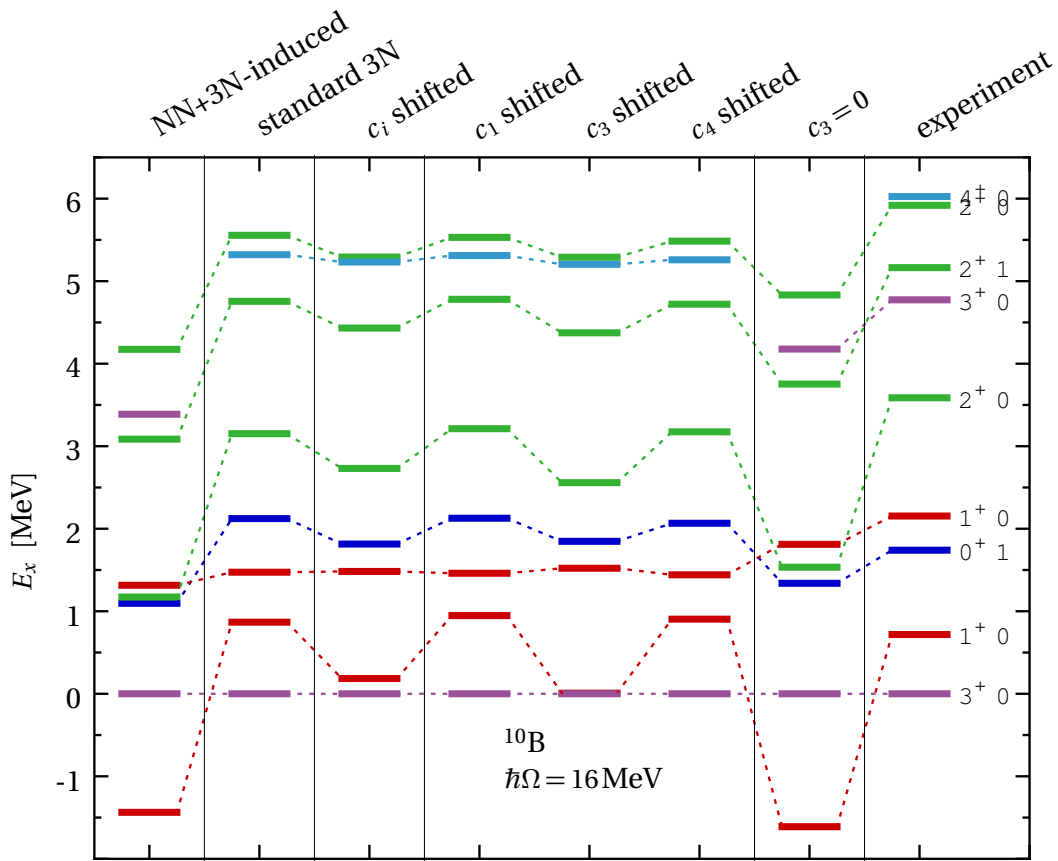


Figure 7.3 – Identical to Figure 7.1 but for nucleus ^{10}B . For further details see text. Experimental energies are taken from Ref. [148].

3N interaction, in particular to c_3 , c_D and Λ_{3N} .

Another prime example of an excitation energy of a 1^+ state strongly controlled by 3N forces is contained in the ^{10}B spectrum as we have discussed already in the previous section. Accordingly, we repeat the sensitivity study presented above for the low-energy positive-parity spectrum of ^{10}B . One should keep in mind that the ^{10}B spectrum, and in particular the energy difference between the first 1^+ and 3^+ states, is not yet fully converged at $N_{\text{max}} = 8$ as evident from Figure 6.11, and, connected to this, a slight dependence on the SRG flow parameter remains, see Figure 6.8. Consequently, differences of excitation energies observed in the following may also incorporate effects of different rates of convergence for the individual Hamiltonians. Nevertheless, we carry out the sensitivity analysis for ^{10}B using the fixed model-space parameters $N_{\text{max}} = 8$ and $\hbar\Omega = 16\text{MeV}$ and at $\alpha = 0.08\text{fm}^4$. The comparison of the first two columns of Figure 7.3 demonstrates the sensitivity of the excitation energy of the first 1^+ state to the inclusion of initial 3N interactions. Analogously to the study of ^{12}C above, column three depicts the spectrum where we adopted the shifted LECs \bar{c}_i and the spectra for the individual shifts are shown in columns four to six. Bearing in mind the convergence issue mentioned above, the significant changes in the spectrum obtained with \bar{c}_i are limited to the first 1^+ state and perhaps the first 2^+ state. Analogously to ^{12}C we find c_3 responsible for these effects while shifts of c_1 and c_4 do not change the excitation energies of these states. Interestingly, the individual

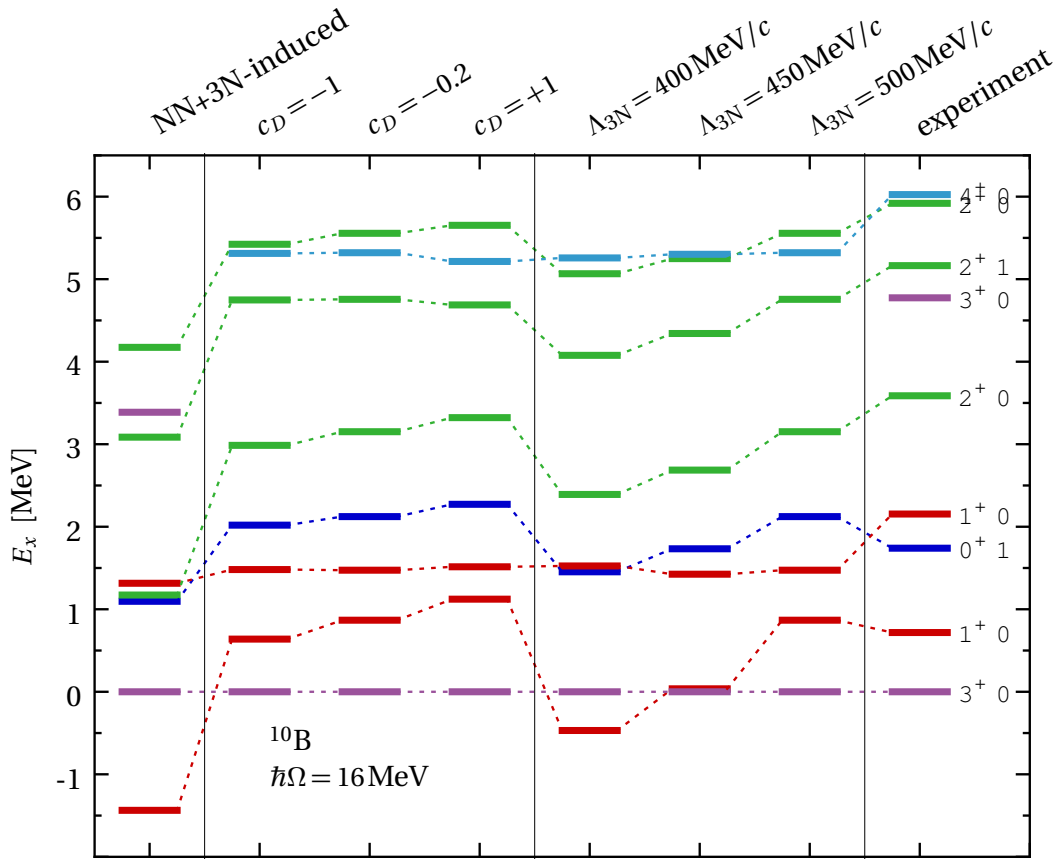


Figure 7.4 – Identical to Figure 7.2 but for nucleus ^{10}B . For further details see text. Experimental energies are taken from Ref. [148].

shift of c_3 yields the 1^+ state degenerate with the 3^+ ground state. The next-to-last column confirms the important role of c_3 by setting it to zero. This yields the wrong ground-state spin of ^{10}B , but interestingly the correct ordering of the first 0^+ and second 1^+ states. In addition, we briefly discuss the sensitivity of the ^{10}B spectrum to variations of c_D and the 3N momentum cutoff $\Lambda_{3\text{N}}$ in context of Figure 7.4. The spectrum is generally very insensitive to the variation of c_D from -1 to $+1$, where the largest change is again observed in the first 1^+ excitation energy. For the increase of the chiral 3N cutoff momentum from $400\text{MeV}/c$ to $500\text{MeV}/c$ many excitation energies in the spectrum increase, while only the excitation energies of the second 1^+ and the first 4^+ remain almost constant. Of course, as before we find that the reduced-cutoff 3N interactions do not produce the correct ground-state spin of ^{10}B , whereas $\Lambda_{3\text{N}} = 450\text{MeV}/c$ yields almost degenerate 3^+ and 1^+ states. Also the level ordering of the second 1^+ and first 0^+ state depends on the cutoff momentum and is not correct for the larger cutoffs. However, note that the ^{10}B spectrum may also change to some extent due to a lack of convergence as suggested from Figure 6.8.

For our concluding remarks we focus on the excitation energy of the first 1^+ state in ^{12}C and the energy difference between the first 3^+ and 1^+ states in ^{10}B , which have shown clear sensitivities to the varied parameters. We found that an increase of c_3 is lowering the excitation energy of the first 1^+ state (and likewise for the first 2^+ state) of ^{10}B , i.e., its agreement with experiment (righter-most column) becomes worse. In contrast, for ^{12}C

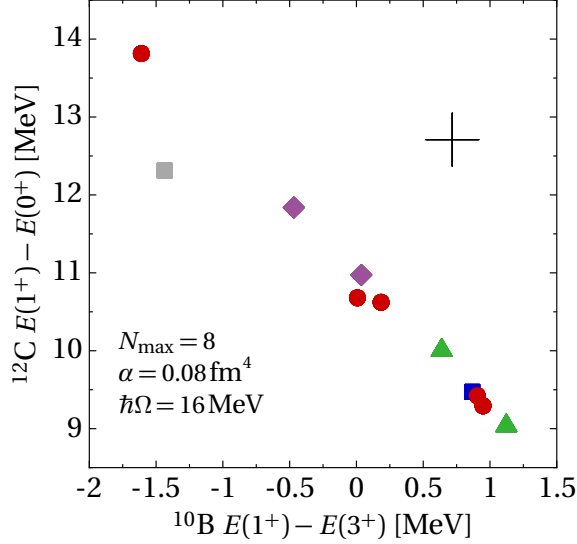


Figure 7.5 – Correlation plot between the excitation energy of the first 1^+ state of ^{12}C and the energy difference between the first 3^+ and 1^+ state in ^{10}B . The black cross marks the experimental value, and the remaining plot markers correspond to the sensitivity studies and result from the NN+3N-induced Hamiltonian (■), the NN+3N-full std. (■), the c_i variations (●), the c_D variations (▲), and the $\Lambda_{3\text{N}}$ variations (◆). For further explanations see text. (published in [161])

the increase of c_3 increases the excitation energy of the first 1^+ state and leads to a better description of the experimental value. This hints at a potential problem to describe both 1^+ excitation energies starting from one Hamiltonian. To obtain a better overview of the effects on the respective 1^+ excitation energies we present a correlation plot showing the excitation energy of the 1^+ state of ^{12}C as function of the energy difference between the 3^+ and 1^+ state in Figure 7.5 for all kinds of variations discussed above. In addition we mark the experimental point by the black cross. Strikingly, all excitation energies fall on a single line which is well separated from the experimental point. This may be interpreted as indication that the initial Hamiltonian needs to be augmented by further operator structures to improve on this. Such operator structures may enter from sub-leading 3N interactions, i.e., more generally from higher orders in the chiral power counting, or, alternatively from taking the $\Delta(1232)$ degree of freedom explicitly into account [162]. One should note that

Table 7.2 – List of different LEC combinations for the N^2LO chiral 3N interaction as applied for the sensitivity studies. All of them reproduce the triton β -decay half-life and the ^4He binding energy, when combined with the N^3LO NN interaction of Ref. [71].

	$c_1 [\text{GeV}^{-1}]$	$c_3 [\text{GeV}^{-1}]$	$c_4 [\text{GeV}^{-1}]$	c_D	c_E
standard 3N	-0.81	-3.20	5.40	-0.2	-0.205
c_i -shift	-0.94	-2.31	4.51	-0.2	-0.085
c_1 -shift	-0.94	-3.2	5.4	-0.2	-0.247
c_3 -shift	-0.81	-5.94	5.4	-0.2	-0.2
c_4 -shift	-0.81	-3.20	4.51	-0.2	-0.13
$c_D = 1$	-0.81	-3.40	3.40	1.0	-0.038
$c_D = -1$	-0.81	-3.40	3.40	-1.0	-0.386

we did not change the NN interaction in the sensitivity study presented here. First results along these lines will be presented in Ref. [118] and do not resolve this issue.

Altogether, we have presented first steps towards rigorous sensitivity studies and a consistent propagation of uncertainties from chiral effective field theory to the nuclear structure observables of interest. By varying the LECs of the leading chiral 3N interaction we confirm the important role of the LEC c_3 for the description of the first 1^+ states in ^{12}C and ^{10}B , which in the latter case is important to obtain the correct ground-state spin. Moreover, c_3 is also known to be important for the accurate fit of nucleon-nucleon phase-shift data as stated in Ref. [71]. In conclusion, careful attention should be paid to the determination of c_3 and it might be interesting to repeat such sensitivity studies for next-generation chiral interactions.

SECTION 8

Benchmark of the Normal-Ordered Two-Body Approximation

So far, we have focussed on the application of the full 3N interaction in the IT-NCSM framework without any further approximations. The aim of the applications of 3N forces in the remaining discussions of Part II is to study chiral nuclear Hamiltonians beyond the p -shell up into the heavy-mass regime including the tin isotopic chain with emphasis on the importance of 3N-force contributions. However, the explicit inclusion of 3N interactions comes with a significantly increased computational cost and, furthermore, often-times significant formal developments of the many-body methods are required (cf. Sections 4 and 11). Therefore, it is favorable to exploit controlled and reliable approximation schemes for the 3N interaction that are sufficiently accurate. One such approximation scheme can be defined with help of the normal ordering of the 3N interaction with respect to a nucleus-specific reference state. As a result, the 3N interaction can be rewritten as a sum of zero-, one-, two-, and three-body operators

$$\hat{V}^{3N} = \hat{V}_{0B}^{3N} + \hat{V}_{1B}^{3N} + \hat{V}_{2B}^{3N} + \hat{V}_{3B}^{3N}, \quad (8.1)$$

where information contained in the reference state, i.e., information about the many-body system, is used to demote parts of the vacuum-normal-ordered three-body force \hat{V}^{3N} to lower particle ranks. With help of the operator identity (8.1) we can define the different $\text{NO}n\text{B}$ approximations where $(n+1)$ -body operators on the right-hand side of Eq. (8.1) are discarded. We have discussed the general formalism of this recipe in Section 2.3, including the discussion how to obtain the required matrix elements for the case of the $\text{NO}2\text{B}$ approximation in particular for large model spaces. Throughout this section, we study the anatomy of the different $\text{NO}n\text{B}$ approximations and focus on the benchmark of the $\text{NO}2\text{B}$ approximation by comparison to calculations using the full 3N interaction explicitly, thus, quantifying the quality of this approximation. We note that the SRG evolution is still performed consistently at the 3N level and only afterwards the $\text{NO}2\text{B}$ approximation

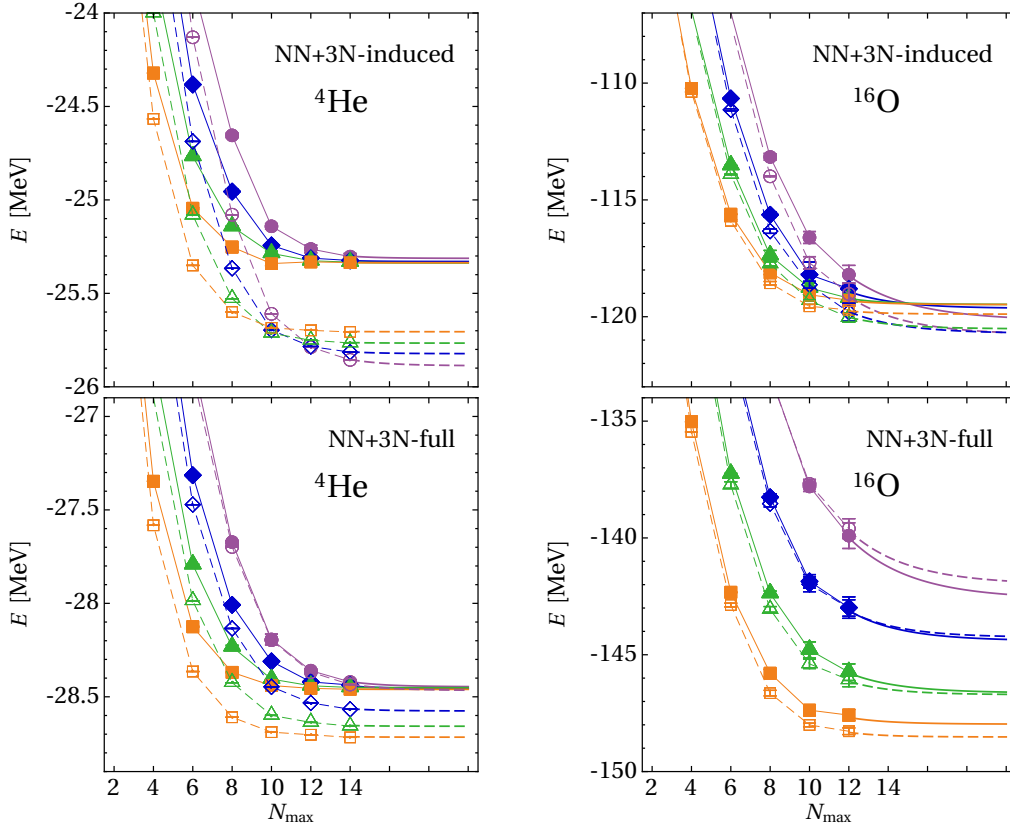


Figure 8.1 – Benchmark of the NO2B approximation for ground-state energies of ${}^4\text{He}$ (left-hand panels) and ${}^{16}\text{O}$ (right-hand panels) as function of the IT-NCSM model-space size and for SRG flow parameters $\alpha = 0.04$ (\bullet), $\alpha = 0.05$ (\blacklozenge), $\alpha = 0.0625$ (\blacktriangle), $\alpha = 0.08\text{fm}^4$ (\blacksquare) for the NN+3N-induced (upper panels) and NN+3N-full (lower panels) Hamiltonians, respectively. Filled symbols represent results obtained with the full 3N interaction, open symbols correspond to results using the NO2B approximation. Beyond the largest N_{max} the extrapolations to infinite model-space size is shown. For further explanations see text. (published in [43])

of the 3N interactions is applied. The reference states we use in the following are either the unperturbed HO Slater determinants for the IT-NCSM calculations, or the Hartree-Fock ground-state Slater determinant for CCSD. That is, we study the single-reference NO2B approximation as introduced in Section 2.3. A discussion of multi-reference normal ordering can be found in Refs. [163, 164]. The results presented in the following have been published in Refs. [43, 46].

We begin with a comparison of the ground-state energies of ${}^4\text{He}$ and ${}^{16}\text{O}$ obtained with and without using the NO2B approximation. In Figure 8.1 these energies are shown as function of the IT-NCSM model-space size N_{max} and for different SRG flow parameters, where the filled symbols represent the ground-state energies obtained with the full 3N interaction, whereas for the energies shown as open symbols the NO2B approximation is used. In addition, the lines beyond the data points of the largest model spaces depict the exponential extrapolations to $N_{\text{max}} = \infty$. The upper left panel shows the results for ${}^4\text{He}$ obtained with the NN+3N-induced Hamiltonian which shows the largest difference between the calculation using the NO2B approximation and the full 3N interaction on the

order of 2%. In addition, we see that the NO2B approximation leads to a dependence on the SRG flow parameter which is absent in the full calculation. For the NN+3N-induced Hamiltonian the NO2B approximation leads to approximately 0.6 MeV more binding for $\alpha = 0.04 \text{ fm}^4$ whereas for $\alpha = 0.08 \text{ fm}^4$ only 0.4 MeV more binding is encountered. Also in case of the NN+3N-full Hamiltonian we observe an α dependence triggered by the NO2B approximation. However, note that the pattern of the flow-parameter dependence is inverted compared to the NN+3N-induced case and for $\alpha = 0.04 \text{ fm}^4$ the results obtained with the full 3N interaction and with the NO2B approximation are essentially identical. The largest difference is found here for $\alpha = 0.08 \text{ fm}^4$ and amounts to about 0.3 MeV, which is on the order of 1%.

The right panels of Figure 8.1 show the analogous analysis for ^{16}O . Again we observe a slightly altered α dependence in the results obtained with the NO2B approximation. In contrast to ^4He , the deviations of the results with NO2B approximations from the exact results are below 1% for ^{16}O . In the NN+3N-induced case the NO2B approximation yields up to 1 MeV more binding for the smaller α parameters. For the NN+3N-full Hamiltonian the NO2B approximation gives about 1 MeV less binding for $\alpha = 0.04 \text{ fm}^4$ and a 1 MeV larger binding energy for $\alpha = 0.08 \text{ fm}^4$ compared to the exact result. In summary, up to this point we have found very good agreement of the ground-state energies obtained with the NO2B approximation with the exact results. The largest deviations are at the level of 2% for ^4He , and they decrease below the 1% level for ^{16}O .

For a more systematic analysis also of the NO n B approximations we investigate their anatomy by the following procedure: we compute the ground state using the exact NN+3N Hamiltonian without approximation and use it to compute the expectation value of the 3N interactions resulting from the different NO n B approximations. We perform this analysis within the IT-NCSM at fixed N_{max} for the NN+3N-induced and NN+3N-full Hamiltonians, for two SRG flow parameters and for the ground states of ^4He , ^{16}O and ^{40}Ca , respectively. The results are shown in Figure 8.2 in form of bar charts. Apparently, the systematics of the expectation values for ^4He is different compared to ^{16}O and ^{40}Ca , while the latter are rather similar. A second general observation is that the patterns for a given Hamiltonian are largely insensitive to the different SRG parameters. For ^4He using the NN+3N-induced Hamiltonian we obtain continuously increasing expectation values when we go step by step from the NO0B approximation to the exact result. The 0B, 1B, 2B and 3B contributions are all repulsive and the individual contributions of the 1B and 2B part is comparable to the contribution of the 3B part. This changes when we consider the NN+3N-full Hamiltonian, where the contribution of the 3B part becomes smaller compared to the 2B contribution and, accordingly, the NO2B approximation becomes more accurate. Also the pattern is completely different to the one observed for the NN+3N-induced Hamiltonian, because of different signs of the single n B contributions. In particular, the 0B contribution is rather small and attractive. This is completely different for ^{16}O and ^{40}Ca , where the 0B contribution is largest, repulsive and overestimates the exact result. This pattern is rather similar for both nuclei, even when switching from the NN+3N-induced to the NN+3N-full Hamiltonian, where we find the opposite sign for the 2B contribution. Finally, and most

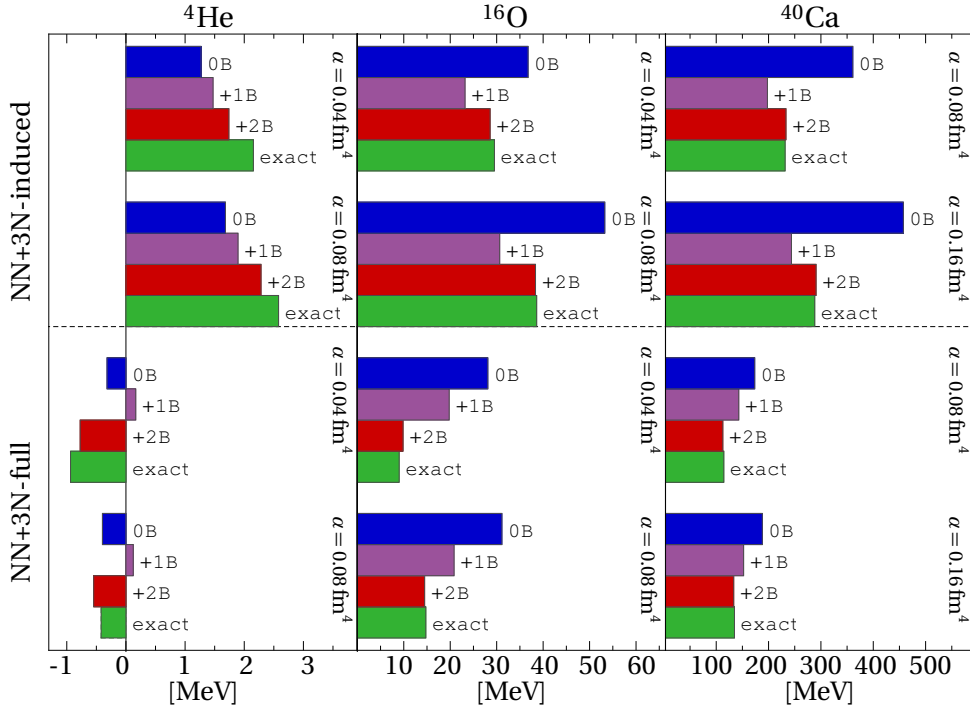


Figure 8.2 – Anatomy of NO_nB approximations obtained by IT-NCSM ground-state expectation values of the 3N interaction using the NO0B , NO1B , NO2B approximation and the full 3N interaction shown as bars. The ground states are computed with the $\text{NN}+3\text{N}$ -induced (upper panels) and $\text{NN}+3\text{N}$ -full (lower panels) Hamiltonians without approximation, and results for ^4He , ^{16}O and ^{40}Ca are shown for two SRG flow-parameters α . Remaining parameters are $\hbar\Omega = 20 \text{ MeV}$ and $N_{\text{max}} = 10$ for ^4He and ^{16}O and $N_{\text{max}} = 8$ for ^{40}Ca . (published in [43])

importantly for practical applications, the contribution of the 3B part is very small, and the expectation value of the exact 3N interaction is in good agreement with the expectation value of the NO2B operator. Note that this agreement is significantly improved compared to the ^4He results. In summary, we cannot identify a clear hierarchy in the different NO_nB approximations, which is at variance with the findings for ^4He in Ref. [45]. Instead, the individual contributions depend on the Hamiltonian, the SRG flow-parameter and the nucleus under consideration. Nevertheless, overall we can state that the NO2B approximation works very well in particular for heavier nuclei, where the deviation from the exact result is smaller than 1%.

These findings clearly motivate to use the NO2B approximation in ab-initio studies beyond p -shell nuclei entering the medium-mass regime. The many-body method of choice in this mass regime is coupled-cluster theory, which we have briefly introduced in Section 4.3. To make sure that the quality of the NO2B approximation is equally accurate for this many-body method and the medium-mass regime, we need to perform CC calculations with explicit 3N interactions. This is a non-trivial task on its own as already emphasized in Section 4.3. First CCSD calculations with explicit 3N interactions have been reported in Ref. [45] for ^4He , and independently this task has been accomplished by Sven Binder, who in particular managed to facilitate first CCSD and Λ -CCSD(T) calculations with explicit 3N interactions in the medium-mass regime [96, 46, 98]. Due to this, we can

explicitly benchmark the NO2B approximation in closed-shell nuclei for various values of α , the two types of Hamiltonians, and also for different HO frequencies. The calculations are conducted up to a maximum single-particle energy quantum number $2n + l \leq e_{\max}$, and we consider the range $e_{\max} = 4$ to 12. For each parameter set a Hartree-Fock calculation is performed to optimize the single-particle basis and to stabilize the iterations for the solution of the CC equations (4.18) - (4.20). As already mentioned in Section 4.3, the CC approach in principle requires $3N$ matrix elements up to $E_{3\max} = 3 \cdot e_{\max}$, which is clearly prohibitive for $e_{\max} = 12$ (cf. Section 2.2.3). Therefore, we use the truncation $E_{3\max} = 12$ for the benchmark of the NO2B approximation. For further technical details about the CC calculations with explicit $3N$ interactions we refer to Ref. [96].

In Figure 8.3, we present CCSD ground-state energies of ^{24}O , ^{40}Ca , ^{48}Ca and ^{56}Ni as function of the model-space truncation e_{\max} computed using the NO2B approximation shown as open symbols in comparison to the results of CCSD calculations explicitly including the exact $3N$ interaction (CCSD3B) denoted as filled symbols. The calculations are conducted at the optimal frequency for the respective nucleus (we discuss the frequency dependence in context of Figure 8.4 below). The left columns show the results obtained with the NN+3N-induced Hamiltonian, and in the right column we show the ground-state energies for the NN+3N-full Hamiltonian, where we use the reduced-cutoff $3N$ interaction with $\Lambda_{3N} = 400 \text{ MeV}/c$, since this choice reduces the SRG flow-parameter dependence significantly as discussed in Section 6.3. As evident from Figure 8.3, all CCSD calculations are converged or are very close to convergence with respect to e_{\max} . This encourages more systematic studies of chiral Hamiltonians in comparison to experimental results, which are shown as horizontal lines and, overall, reveal remarkable agreement with the CCSD results. However, a number of technical points need to be clarified in order to be able to quantify the remaining uncertainties of the calculations, related to , e.g., the SRG model space, the $3N$ matrix element truncation $E_{3\max}$, and to triples corrections to the CCSD calculations. Therefore, we postpone these discussions into the next section and concentrate here exclusively on the benchmark aspect of the NO2B approximation.

Indeed, Figure 8.3 demonstrates the quality of the NO2B approximation: for all resulting ground-state energies regardless of the nucleus, Hamiltonian, e_{\max} , or SRG flow parameter the NO2B approximation proves to be very accurate. The deviations from the CCSD3B energies are below 1% for all cases, e.g., for ^{56}Ni the largest deviation is about 4 MeV. In addition, we confirm the accuracy of the NO2B approximation in Figure 8.4, where we show the dependence of the ground-state energies for the same set of nuclei on the used HO frequency $\hbar\Omega$, again for the NN+3N-induced and NN+3N-full Hamiltonians obtained from CCSD3B as filled symbols and from CCSD with NO2B approximation as open symbols. We find the HO frequency irrelevant for the quality of the NO2B approximation as the deviations from the CCSD3B results are almost constant across the frequency range. Moreover, we find the effect of the residual $3B$ contributions, i.e., the step towards the exact treatment of the $3N$ interaction, always repulsive. Thus, it has the same sign as the total contribution of the SRG-induced plus initial $3N$ interactions. We have published the quantitative results for these studies with and without NO2B approximation in Ref. [43]. In

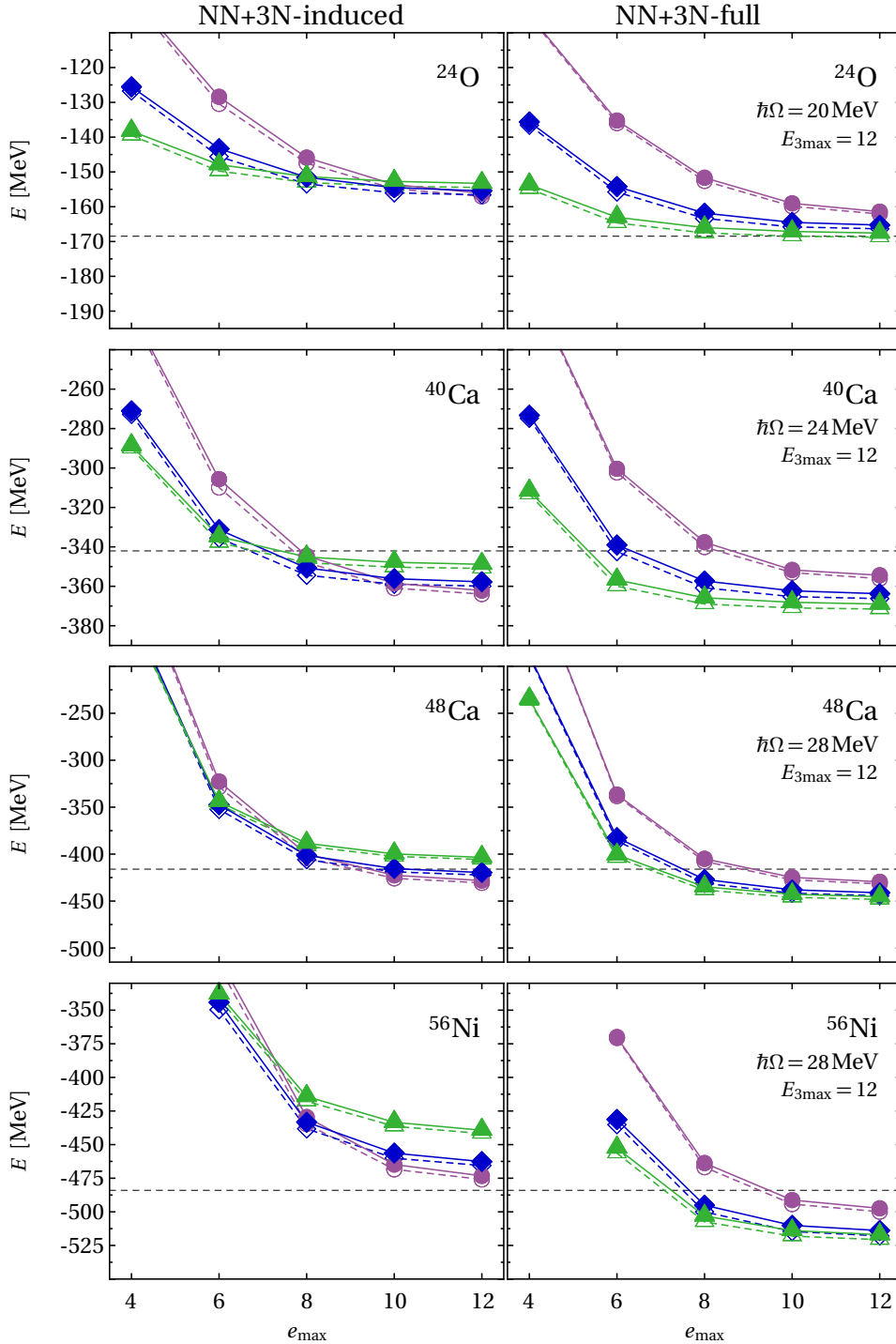


Figure 8.3 – Ground-state energies of ^{24}O , ^{40}Ca , ^{48}Ca and ^{56}Ni as function of the model-space truncation e_{max} obtained from CCSD in Hartree-Fock basis with explicit chiral 3N interaction (filled symbols) in comparison to CCSD calculations using the NO2B approximation (open symbols) for SRG flow parameters $\alpha = 0.02$ (\bullet), $\alpha = 0.04$ (\blacklozenge), $\alpha = 0.08 \text{ fm}^4$ (\blacktriangle), and at the optimal HO frequency. Results for the NN+3N-induced and the NN+3N-full ($\Lambda_{3\text{N}} = 400 \text{ MeV}/c$) Hamiltonian are shown in the left- and right-hand columns, respectively. Dashed lines mark the experimental energies [144]. (published in [46])

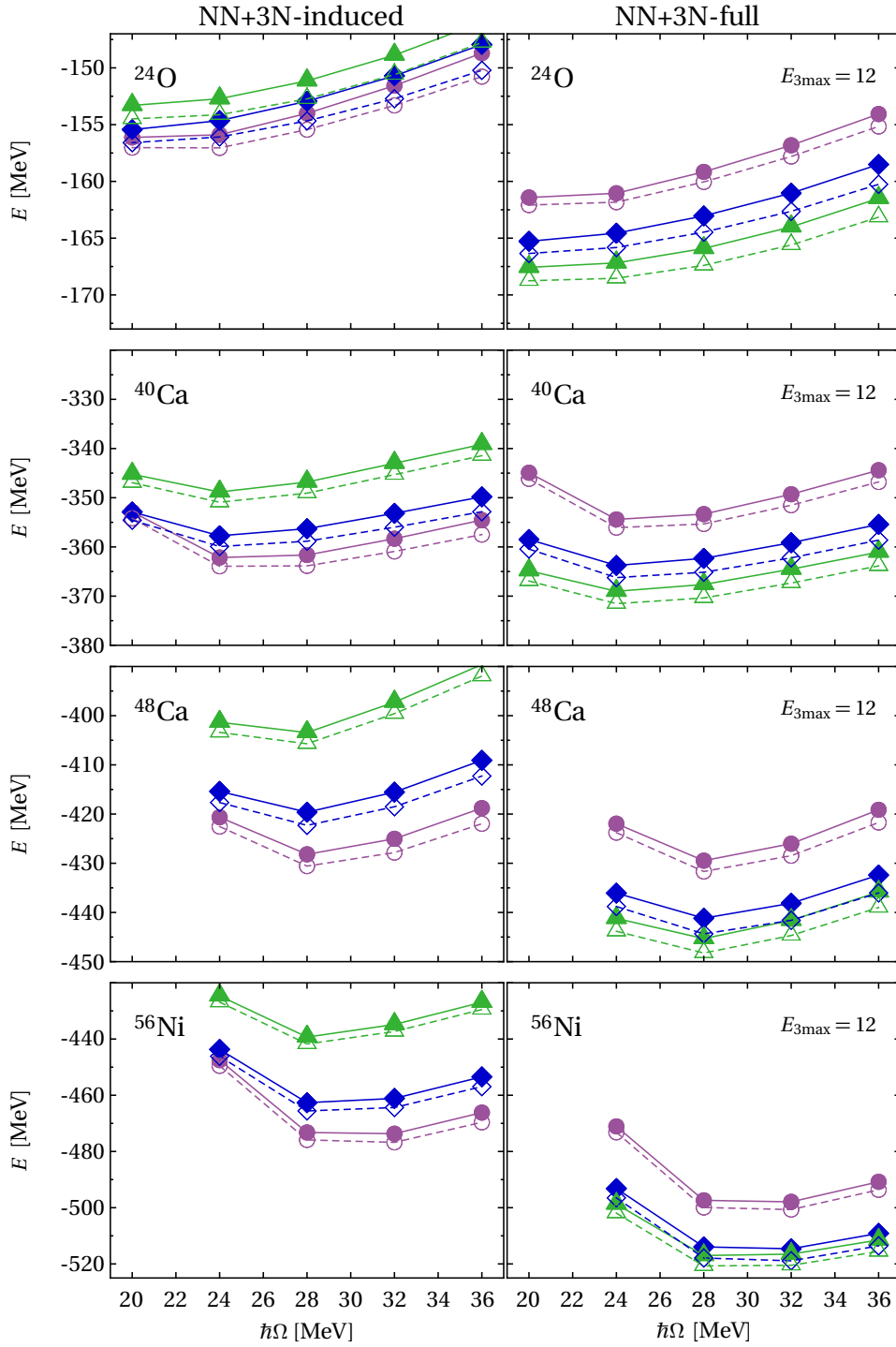


Figure 8.4 – Ground-state energies of ^{24}O , ^{40}Ca , ^{48}Ca and ^{56}Ni as function of the HO frequency $\hbar\Omega$ obtained from CCSD in Hartree-Fock basis at $e_{\text{max}} = 12$ with explicit chiral 3N interaction (filled symbols) in comparison to CCSD calculations using the NO2B approximation (open symbols) for SRG flow parameters $\alpha = 0.02$ (\bullet), $\alpha = 0.04$ (\blacklozenge), $\alpha = 0.08 \text{ fm}^4$ (\blacktriangle). Results for the NN+3N-induced Hamiltonian and the NN+3N-full ($\Lambda_{3\text{N}} = 400 \text{ MeV}/c$) Hamiltonian are shown in the left- and right-hand columns, respectively. (published in [46])

conclusion, we found the NO2B approximation to be extremely accurate even in medium-mass nuclei, and for a variety of combinations of the parameters e_{\max} , $\hbar\Omega$ and α , and for both, the NN+3N-induced and NN+3N-full Hamiltonian. In the next section we build on these findings and systematically analyze all remaining uncertainties in CC calculations with 3N interactions and proceed to even heavier closed-shell nuclei.

A further aspect of the validation of the NO2B approximation is its effect on the non-iterative triples corrections that are typically added on top of the CCSD energies (cf. Section 4.3 and Ref. [98]). Such investigations require the inclusion of explicit 3N interactions in the triples corrections, which has been worked out by Sven Binder [96]. The main conclusion, relevant for the remaining studies in this work, is that contributions of the normal-ordered 3B part to the triples correction are in general negligible. However, if the size of the total triples correction becomes comparable to the effect of the NO2B approximation on the CCSD energy as it is found for soft interactions, the normal-ordered 3B part should be explicitly included at the level of CCSD. For further details we refer to the detailed discussions in Refs. [96, 98].

SECTION 9

Ab-Initio Studies from Oxygen to Heavy Tin Isotopes

In this section we apply chiral NN+3N Hamiltonians in ab-initio calculations to study nuclei beyond the p -shell with particular focus on features triggered by the inclusion of 3N interactions. This discussion benefits from our previous developments of the reduced-cutoff 3N interactions that lead to suppressed contributions of SRG-induced four- and multi-nucleon interactions to ground-state energies, see Section 6.3. We start with the investigation of even isotopes throughout the oxygen chain and pay special attention to the neutron-rich isotopes and the position of the drip line, which has been shown before in more approximate calculations to be sensitive to the inclusion of 3N interactions [165]. Furthermore, the NO2B approximation, which we found to be extremely accurate in the previous section, facilitates investigations of still heavier nuclei at moderate computational cost. This allows for the extension of our studies well beyond the oxygen chain, towards nuclei with closed sub-shells in the calcium, nickel, and even tin isotopic chains using the coupled-cluster approach. We present the corresponding results in Section 9.2 including a detailed analysis of the theoretical uncertainties from the different truncations.

9.1 Even Oxygen Isotopes with Chiral NN+3N Interactions

As first systematic application of the chiral NN+3N Hamiltonians beyond p -shell nuclei we consider the even oxygen isotopes starting from ^{12}O up to the neutron drip line including the neutron-rich isotopes ^{24}O and ^{26}O . The oxygen isotopic chain has attracted significant attention over the past years [165, 30, 166], since it was found that shell-model calculations fail to predict the position of its neutron drip line correctly with NN interactions, and that 3N interactions resolve this issue [165]. However, so far all previous calculations had to resort to (uncontrolled) approximative treatments of the 3N interactions. The calculations presented in the following constitute the first ab-initio study of all even oxygen isotopes including chiral 3N interactions and have been published in Ref. [34]. Moreover,

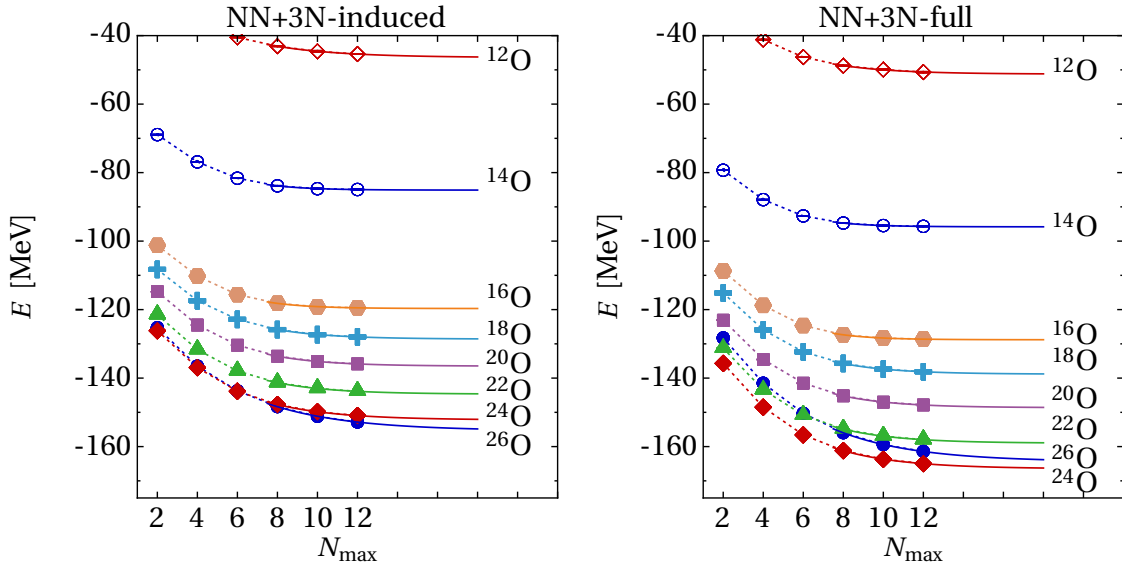


Figure 9.1 – IT-NCSM ground-state energies of even oxygen isotopes for the NN+3N-induced Hamiltonian (left-hand panel) and the NN+3N-full Hamiltonian (right-hand panel) as function of N_{\max} . The solid lines represent extrapolations to infinite model-space size. The SRG flow parameter is $\alpha = 0.08 \text{ fm}^4$, and we work at the optimal frequency $\hbar\Omega$ for each nucleus and use the frequency conversion for $\hbar\Omega < 20 \text{ MeV}$. The errors bars from the IT-NCSM threshold extrapolation are smaller than the plot markers. For further details see text. (published in [34])

concerning the IT-NCSM, the isotope ^{26}O is the heaviest nucleus studied so far with full 3N interactions.

In Figure 9.1 we present IT-NCSM ground-state energies of even oxygen isotopes ranging from ^{12}O to ^{26}O for the NN+3N-induced (left-hand panel) and NN+3N-full Hamiltonian (right-hand panel), both SRG-evolved to $\alpha = 0.08 \text{ fm}^4$ and for model-space sizes up to $N_{\max} = 12$. In addition, the solid curves denote the corresponding extrapolations to the infinite model-space limit based on the energies obtained in the three largest model spaces. Except for ^{26}O , the rate of convergence is very similar for all nuclei and for both Hamiltonians, and the $N_{\max} = 12$ energies are close enough to convergence to allow for stable extrapolations using simple exponentials. Because it is known experimentally, that ^{26}O is unbound with respect to ^{24}O , i.e., its ground-state is a resonance, the reduced rate of convergence for the ^{26}O energy compared to the other considered oxygen isotopes is expected. This is due to the fact that the localized HO basis states are not well suited for the description of continuum effects, and we try to compensate this issue to some extent by using the smaller HO frequency $\hbar\Omega = 14 \text{ MeV}$ for this nucleus. The proper description of continuum states would require an extended formalism that we cover in Part III of this work. Nevertheless, also the ^{26}O ground-state energy does come close enough to convergence to allow for a stable extrapolation to $N_{\max} \rightarrow \infty$.

We plot the extrapolated IT-NCSM ground-state energies in Figure 9.2 as red discs over the nucleon number A , and include experimental ground-state energies as black bars. For the NN+3N-induced Hamiltonian, which is unitarily equivalent to the initial chiral NN interaction, we observe a significant underbinding of all oxygen isotopes. In addition, we

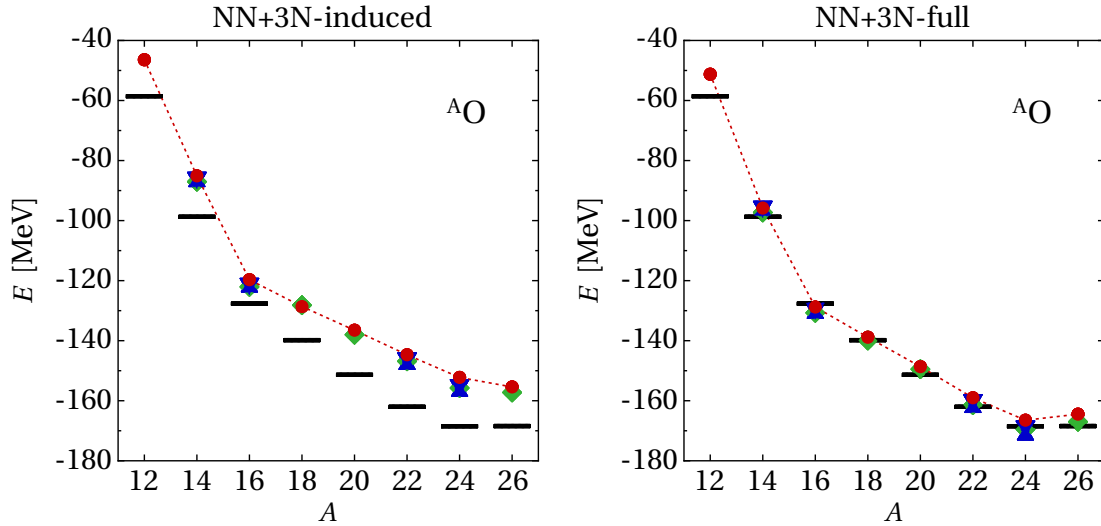


Figure 9.2 – Ground-state energies of even oxygen isotopes for the NN+3N-induced (left-hand panel) and the NN+3N-full (right-hand panel) Hamiltonian with $\Lambda_{3N} = 400 \text{ MeV}/c$ at $\alpha = 0.08 \text{ fm}^4$. The IT-NCSM energies (\bullet) have been extrapolated to infinite model space. The CCSD (\blacktriangle), ACCSD(T) (\blacktriangledown) and MR-IM-SRG (\blacklozenge) energies are obtained at optimal frequency, $e_{\text{max}} = 14$, $E_{3\text{max}} = 14$, and use the NO2B approximation. Experimental energies (—) taken from Refs. [167, 168]. (published in [34])

find ^{26}O clearly bound by about 3 MeV with respect to ^{24}O from extrapolations based on either the three or four largest model spaces using simple exponentials (cf. Section 6). Altogether, we are in the position to confirm by means of ab-initio calculations that the initial chiral NN interaction does not reproduce the experimental ground-state energies in the oxygen chain and, in particular, fails to produce the correct drip line position. This is different for the results obtained with the NN+3N-full Hamiltonian using $\Lambda_{3N} = 400 \text{ MeV}/c$ shown in the right-hand panel of Figure 9.2. We find remarkable agreement with experiment for all even oxygen isotopes. The sole exception is ^{12}O , where we find a larger deviation from experiment. Concerning the neutron drip line the extrapolated energies based on the results from the three or four largest model spaces yield ^{26}O unbound with respect to ^{24}O by about 2 MeV and, thus, predict the drip line in accordance with experiment. However, we note that the uncertainties from the threshold extrapolation of the IT-NCSM, which reach about 0.4 MeV for ^{26}O , are not taken into account by the simple exponential extrapolation used here. Also effects of the continuum could in principle contribute further corrections.

Another important role of the quasi-exact IT-NCSM energies for sd -shell nuclei is to provide benchmark points for the validation of approximate or alternative ab-initio methods. In Figure 9.2 we include ground-state energies obtained from CCSD and ACCSD(T) calculations using a Hartree-Fock (HF) single-particle basis for oxygen isotopes with closed sub-shells, and energies obtained from the ab-initio multi-reference in-medium SRG (MR-IM-SRG) recently proposed by Heiko Hergert et al. [34] for all even isotopes. For both methods the energies are computed using the NO2B approximation for the 3N interaction with $E_{3\text{max}} = 14$, which is sufficient to obtain accurate results in this mass range as

discussed in the following subsection. Furthermore, the CC and MR-IM-SRG calculations are performed at model-space truncations $e_{\max} = 14$ that lead to well-converged energies as shown in Ref. [34]. Nevertheless, the underlying basis for both methods is still the HO basis and, therefore, not ideally suited for the description of continuum effects. For all isotopes we find very good agreement between the three different many-body methods, regardless of the used Hamiltonian. The smaller computational cost of the MR-IM-SRG approach compared to the IT-NCSM, allowed for the more detailed study of the oxygen drip line including variations of the SRG flow parameter and the sensitivity to the cutoff momentum Λ_{3N} of the 3N interaction that has been presented in Ref. [34]. The drip-line position has been found to be robust against different combinations of SRG flow parameters and $\Lambda_{3N} = 350, 400$ and $450 \text{ MeV}/c$, and to be predicted correctly at ^{24}O in spite of a uncertainty of the MR-IM-SRG method of 1% [33]. In combination these findings confirm the position of the neutron drip line at ^{24}O as previously suggested, e.g., by shell-model calculations [165].

By comparison to the results obtained with the NN+3N-induced Hamiltonian we conclude that the inclusion of the initial chiral 3N interaction is vital for studies of ground-state energy systematics throughout isotopic chains and has crucial effects on neutron-rich isotopes. Thus, the investigation of 3N force effects in (neutron-rich) medium-mass and heavy nuclei is desirable.

9.2 Closed-Shell Nuclei up to ^{132}Sn with Chiral 3N Interactions

Over the past few years the ab-initio description of nuclei has been subject to vital progress resulting in the development of several many-body methods suitable for calculations in the medium-mass domain [33, 27, 169, 31]. One of these is CC theory which we adopt in the following for the ab-initio description of medium-mass and heavy nuclei, such as neutron-rich tin isotopes. One important milestone is evidently the benchmark of the NO2B approximation and its validation as very accurate approximation presented in Section 8. We focus on ground-state energies of closed-shell nuclei spanning the range from the oxygen chain across the calcium and nickel isotopes up to the tin isotopic chain. We consider the NN+3N-induced and NN+3N-full Hamiltonians to be able to distinguish between effects caused by SRG-induced forces and effects originating from the initial chiral 3N interactions. The coupled-cluster calculations are performed using a HO single-particle basis which has been optimized via the HF method. Moreover, the Hartree-Fock ground state is used as reference state $|\Phi_0\rangle$ to obtain the normal-ordered 3N matrix elements in the NO2B approximation. The latter is important to include the contributions from matrix elements with large $E_{3\max}$ for which the storage of complete sets of JT -coupled 3N matrix elements becomes inconvenient or prohibitive (cf. Sections 2.2.3 and 2.3).

For a proper ab-initio description of medium-mass and heavy nuclei a careful error analysis is mandatory to provide reliable conclusions. Therefore, we commit ourselves to an analysis of uncertainties resulting from all involved truncations and highlight in particular the technical developments necessary to reduce or eliminate these uncertainties.

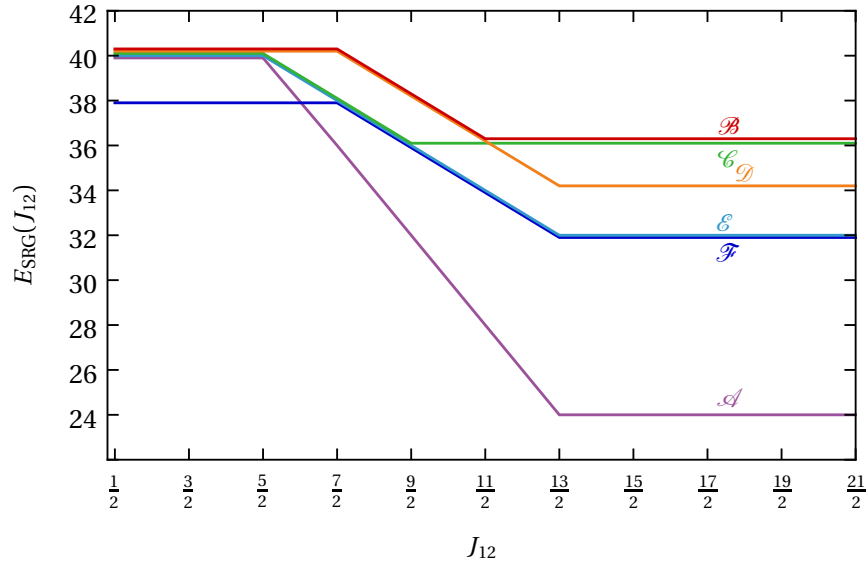


Figure 9.3 – Illustration of different SRG model-space truncations used to investigate corresponding uncertainties. See text for the detailed discussion.

Eventually, we deal with the question of whether present ab-initio techniques can reliably access the heavy mass regime. The results discussed in the following have been published in Ref. [136].

9.2.1 The SRG Model-Space — Revisited for Heavy Nuclei

To start the uncertainty analysis we come back to the investigation of the sufficiency of the finite SRG model space, which we investigated in Section 5 for light nuclei only. We truncate the SRG model space by specifying a maximum Jacobi HO energy quantum number $E_{\text{SRG}}(J_{12})$ that we vary as function of the angular momentum (ramps). If the SRG transformation is performed at low frequencies the relevant momentum range of the initial Hamiltonian may not be covered sufficiently. In the domain of light nuclei this has been the case for frequencies $\hbar\Omega < 20\text{MeV}$, and we have remedied this issue by means of the frequency-conversion technique introduced in Section 3.3. In Figure 9.4, we show CCSD ground-state energies obtained without and with frequency conversion as solid and open symbols, respectively. We investigate the NN+3N-induced and NN+3N-full Hamiltonians for the set of SRG flow parameters $\alpha = 0.02, 0.04, \text{ and } 0.08\text{fm}^4$, and the parent frequency for the SRG transformation of $\hbar\Omega_{\text{SRG}} = 36\text{MeV}$. Already for ^{40}Ca we observe a slight increase of the ground-state energies at frequency $\hbar\Omega = 24\text{MeV}$ similarly for both types of Hamiltonians. With increasing mass of the nuclei this effect is enhanced and also promoted to larger frequencies, i.e., it shifts the frequency minimum to larger frequencies. For ^{78}Ni the artificial increase at $\hbar\Omega = 24\text{MeV}$ amounts to more than 100 MeV compared to the results obtained with frequency conversion, and even slight effects at $\hbar\Omega = 32\text{MeV}$ can be observed. All remaining results presented in this section are obtained using the frequency-conversion technique, so that we can exclude artificial behaviors at low frequencies caused by the SRG transformation model-space truncation.

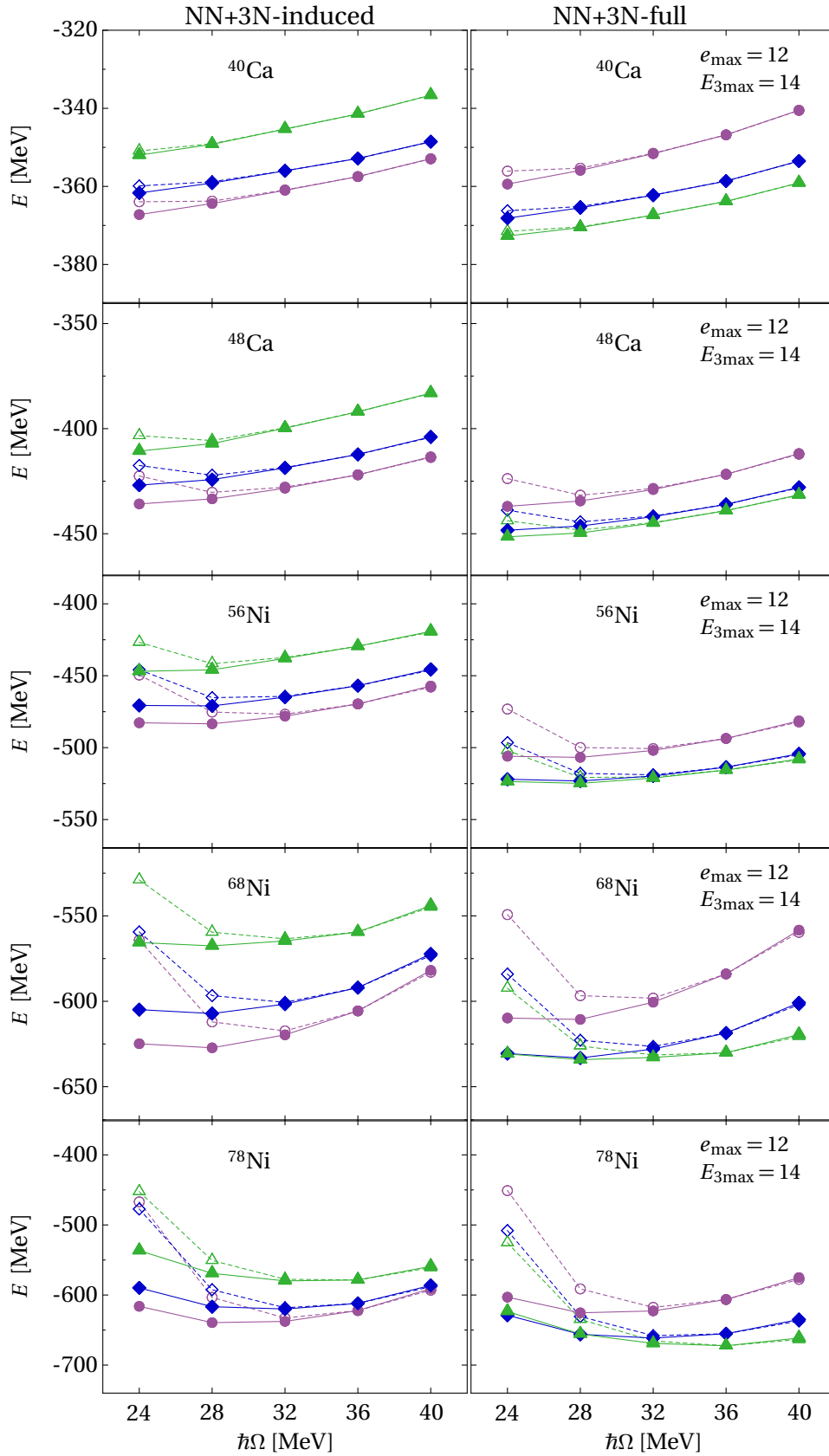


Figure 9.4 – Frequency dependence of CCSD ground-state energies using HF single-particle bases without (open symbols) and with (filled symbols) frequency conversion ($\hbar\Omega_{\text{SRG}} = 36$ MeV) for the two types of Hamiltonians (see column headings) in NO2B approximation, and for $\alpha = 0.02$ (\bullet), $\alpha = 0.04$ (\blacklozenge), $\alpha = 0.08$ fm⁴ (\blacktriangle). (published in [136])

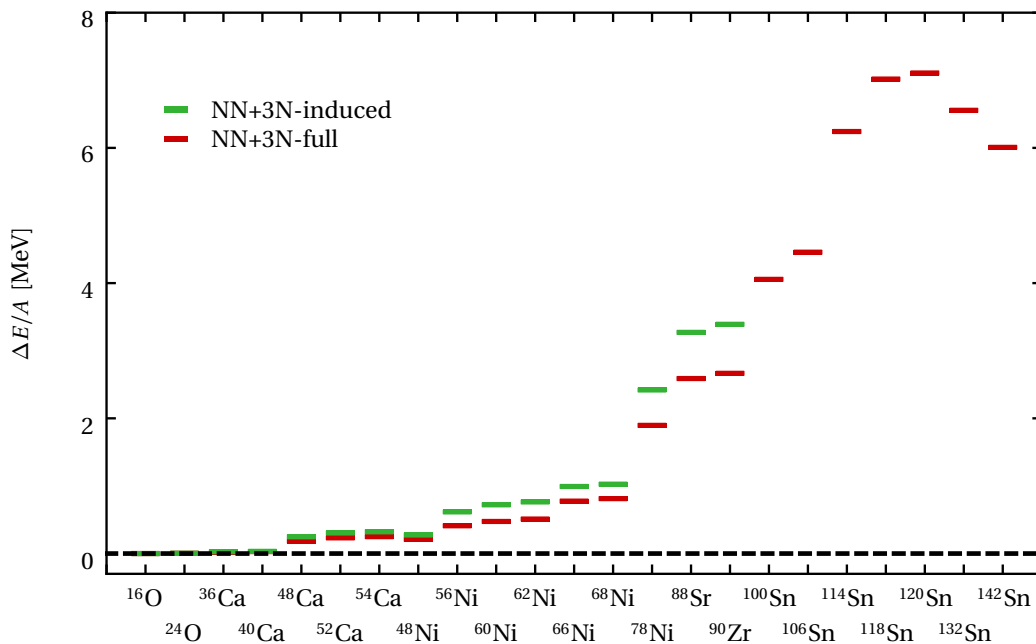


Figure 9.5 – Differences of CCSD ground-state energies per nucleon obtained with 3N interactions prepared by SRG transformations with model-space truncation ramp \mathcal{A} relative to ramp \mathcal{B} for the NN+3N-induced (up to ^{90}Zr) and NN+3N-full Hamiltonian. CCSD uses a HF basis, and the remaining parameters are $e_{\max} = 12$, $\hbar\Omega = 24\text{ MeV}$, $E_{3\max} = 14$, and $\alpha = 0.08\text{ fm}^4$, and the NO2B approximation is used. (published in [136])

Next, we study the dependence of the energies on the SRG model-space truncation $E_{\text{SRG}}(J_{12})$, i.e., on the different ramps. For clarity we illustrate the different truncations used in the following in Figure 9.3. The ramp labeled \mathcal{A} , defined by $E_{\text{SRG}}(J_{12} \leq \frac{5}{2}) = 40$, $E_{\text{SRG}}(J_{12} \geq \frac{13}{2}) = 24$ with a linear decrease in steps of four in between, has been used as default for the previous studies in the p -shell and also throughout the oxygen isotopic chain. Due to the fact that with increasing nucleon number more single-particle orbitals with relatively large single-particle angular momenta are occupied in the reference state, one may anticipate that large relative angular momenta during the SRG transformation in three-body space become more and more important, and hence the SRG model-space truncation \mathcal{A} might be too small to maintain accurate results. To check this explicitly we employ the significantly larger SRG model space \mathcal{B} with $E_{\text{SRG}}(J_{12} \leq \frac{7}{2}) = 40$, $E_{\text{SRG}}(J_{12} = \frac{9}{2}) = 38$ and $E_{\text{SRG}}(J_{12} \geq \frac{11}{2}) = 36$ to study the deviations from the ground-state energies obtained from Hamiltonians evolved within model-space truncation \mathcal{A} . These energetic deviations per nucleon are plotted in Figure 9.5 for the set of closed-shell nuclei ranging from ^{16}O to ^{132}Sn . Up to ^{40}Ca the results obtained with both model-space truncations are basically identical, i.e., in particular for the discussion of the oxygen isotopes in the previous subsection the SRG model-space truncation \mathcal{A} is sufficient. Starting from ^{48}Ca , with increasing mass number the deviations become significantly larger. For ^{56}Ni , which is the heaviest nucleus we studied in the previous section, the deviations amount to about 0.4 MeV per nucleon for the NN+3N-full Hamiltonian, which might be still acceptable. However, the deviations

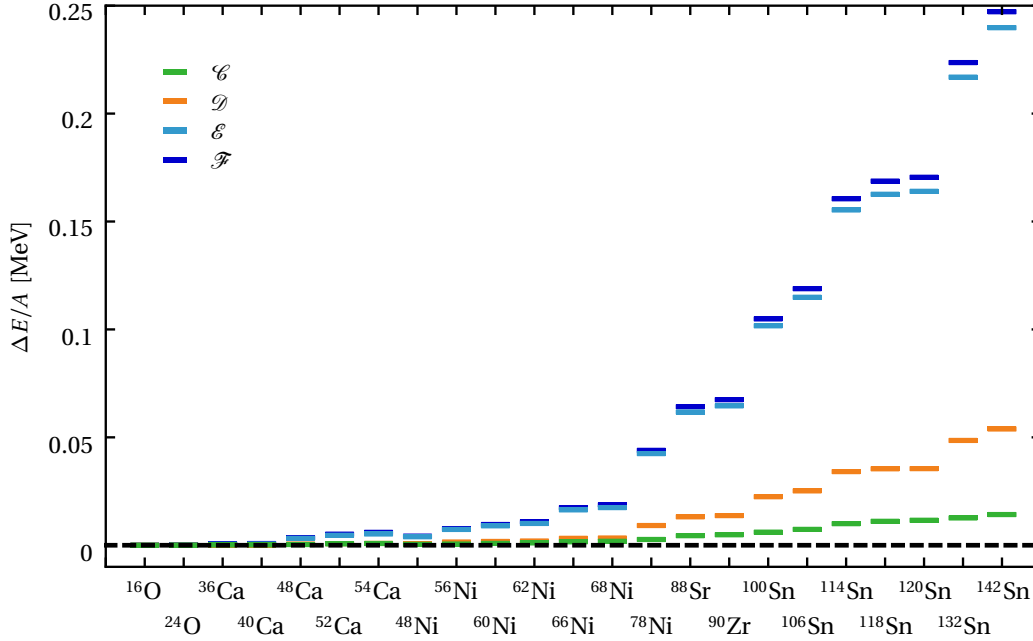


Figure 9.6 – Differences of CCSD ground-state energies per nucleon corresponding to ramp \mathcal{C} , \mathcal{D} , \mathcal{E} and \mathcal{F} relative to the largest SRG model space \mathcal{B} for the NN+3N-full Hamiltonian. CCSD uses a HF basis, and the remaining parameters are $e_{\max} = 12$, $\hbar\Omega = 24$ MeV, $E_{3\max} = 14$, and $\alpha = 0.08$ fm⁴, and the NO2B approximation is used. (published in [136])

grow to more than 7 MeV per nucleon in the tin isotopes, i.e., the SRG model space \mathcal{A} dramatically fails when we aim at accurate descriptions of nuclei in this mass region. This clearly underlines the importance of the proper investigation of the involved truncations present during the preparation of the Hamiltonian, in particular, if one enters the heavy-mass regime.

This implies of course the necessity to ensure that the larger SRG model space \mathcal{B} is sufficient in this respect. We study this in context of Figure 9.6, where we depict the difference relative to the ramp \mathcal{B} of the ground-state energies per nucleon obtained with four different SRG model spaces which are also illustrated in Figure 9.3. We start to assess the large relative angular momentum part of the SRG model space by introducing the auxiliary ramp \mathcal{C} which is identical to \mathcal{B} for $J_{12} \leq \frac{5}{2}$ and $J_{12} \geq \frac{11}{2}$ but for the intermediate J_{12} uses $E_{\text{SRG}}^{\mathcal{B}}(J_{12}) - 2$, i.e., the slope is shifted to smaller J_{12} . In addition, we employ ramp \mathcal{D} identical to \mathcal{B} up to $J_{12} = \frac{11}{2}$ but uses $E_{\text{SRG}}^{\mathcal{B}}(J_{12}) - 2$ for larger J_{12} . For both auxiliary ramps we conduct CCSD calculations and plot the deviations of the ground-state energies for ramp \mathcal{C} and ramp \mathcal{D} from the largest ramp \mathcal{B} in Figure 9.6 as green and orange bars, respectively. The deviations are negligible for both ramps throughout the oxygen, calcium and nickel isotopic chains. In the latter they are largest for ⁷⁸Ni for ramp \mathcal{D} but remain below 20 keV per nucleon. Throughout the tin isotopic chain the deviations continuously increase but stay below 20 keV per nucleon for ramp \mathcal{C} , and below 50 keV per nucleon even up to ¹³²Sn. Given the accuracy we aim at in this mass regime these are only minor deviations, and we conclude that the large- J_{12} part of the Hamiltonian is cov-

ered sufficiently well by our largest ramp \mathcal{B} . We proceed with the analogous check for the small- J_{12} part of the SRG model space, again defining two auxiliary ramps. We choose ramps \mathcal{E} and \mathcal{F} to be identical for $J_{12} \geq \frac{7}{2}$, but for small angular momenta ramp \mathcal{F} is defined to be smaller by $E_{\text{SRG}}^{\mathcal{F}}(J_{12} \leq \frac{5}{2}) = E_{\text{SRG}}^{\mathcal{E}}(J_{12}) - 2$. For computational convenience we use here smaller SRG model spaces for large relative angular momenta, since we have investigated their influence already above. Accordingly, we observe large deviations (around 250 keV per nucleon for the heaviest nuclei) of the CCSD ground-state energies obtained with ramps \mathcal{E} and \mathcal{F} from the largest ramp \mathcal{B} . However, since we are now after probing the small angular-momentum part of the SRG model space we are interested in the difference between ramps \mathcal{E} and \mathcal{F} , i.e., the difference between the light-blue and blue bars in Figure 9.6. Up to ^{88}Sr these bars are basically on top of each other, and also for the heavy tin isotopes this difference remains clearly below 20 keV per nucleon. In this way we have demonstrated that the SRG model space for partial waves with small relative angular momenta is sufficiently covered by ramp \mathcal{E} , and consequently also by means of ramp \mathcal{B} . Altogether, this confirms the convergence with respect to the SRG model-space size also in the heavy tin isotopes when using ramp \mathcal{B} , which we apply as standard for all calculations presented in the remainder of this section.

9.2.2 Coupled-Cluster Model-Space Convergence

Next, we discuss the convergence of the coupled-cluster calculations with respect to their model-space truncations. First we study the convergence pattern concerning the underlying HO single-particle basis shown in Figure 9.7 for ^{48}Ni , ^{68}Ni , ^{100}Sn and ^{132}Sn obtained with the NN+3N-full Hamiltonian at SRG flow parameters 0.04 and 0.08 fm⁴. Shown are CC ground-state energies including triples corrections at the level of $\Lambda\text{CCSD(T)}$ and CR-CC(2,3) as open and filled symbols, respectively. Again, we observe an improved convergence for the softer interactions. This facilitates to obtain for all nuclei energies reasonably close to convergence for $e_{\text{max}} = 12$. However, note that one might expect contributions of about 0.5 MeV per nucleon from larger model spaces for the heaviest tin isotope ^{132}Sn .

The second model-space truncation we need to assess is the contribution of beyond-doubly excited clusters. Therefore, we mark in Figure 9.7 the energies obtained at the level of CCSD with $e_{\text{max}} = 12$ as arrows that serve as reference to compare the contributions of the two triples correction methods. Overall, we find the usual pattern that the size of the triples correction is larger for the Hamiltonian with smaller SRG flow parameter [46]. In addition, we note that the $\Lambda\text{CCSD(T)}$ results are systematically below those obtained from the CR-CC(2,3) method. This complies with findings from quantum chemistry, where $\Lambda\text{CCSD(T)}$ typically overestimates the exact triples correction, while the approximative triples correction obtained via CR-CC(2,3) rather accurately reproduces the full CCSDT results [143]. In the following, we use the size of the CR-CC(2,3) triples contributions also as estimate of the convergence of the cluster expansion, and, accordingly, as measure for uncertainties from its truncation.

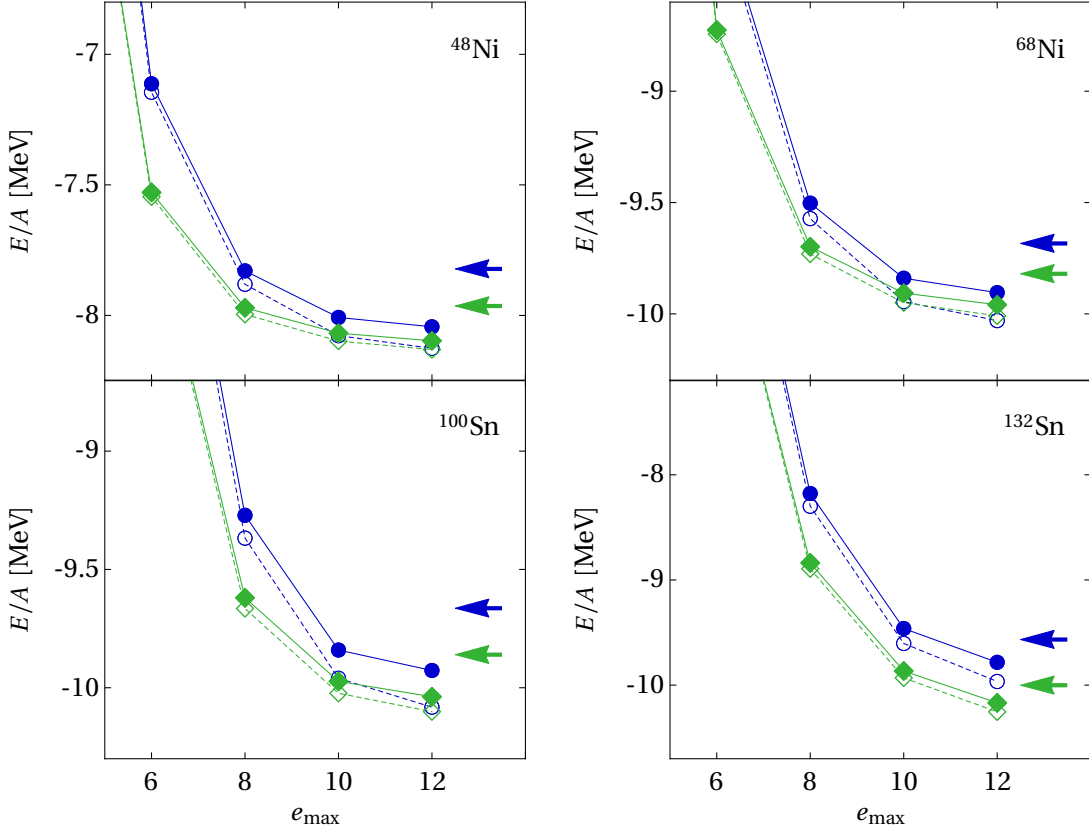


Figure 9.7 – CR-CC(2,3) (filled symbols) and Λ CCSD(T) (open symbols) ground-state energies as function of the single-particle model-space truncation parameter e_{max} computed for the NN+3N-full Hamiltonian. In addition, the arrows mark the CCSD ground-state energies at $e_{\text{max}} = 12$ using a HF basis. Blue and green symbols correspond to $\alpha = 0.04 \text{ fm}^4$ and $\alpha = 0.08 \text{ fm}^4$, respectively. Remaining parameters are $\hbar\Omega = 24 \text{ MeV}$ and $E_{3\text{max}} = 14$, and the NO2B approximation is used. (published in [136])

9.2.3 Iterative Normal Ordering for Large $E_{3\text{max}}$

Due to the fact that the coupled-cluster approach is not consistent with the $E_{3\text{max}}$ truncation of the 3N matrix elements sets, but would formally require matrix elements up to $E_{3\text{max}} = 3 \cdot e_{\text{max}}$, we also need to look into the convergence with respect to $E_{3\text{max}}$. As discussed in detail in Section 2.2.3, full 3N matrix element sets become inconveniently large even in the JT -coupled scheme at $E_{3\text{max}} \gtrsim 16$. To overcome this problem we have developed the normal-ordering scheme discussed in Section 2.3.2 that avoids the storage of full 3N matrix element sets, and instead precompute only those 3N matrix elements that are actually required. To ensure that the information contained in the large $E_{3\text{max}}$, i.e., $E_{3\text{max}} > 14$ matrix elements is included consistently in the reference state used to derive the NO2B approximation we take advantage of the following iterative scheme: we start with the calculation of the Hartree-Fock ground-state including the full 3N matrix-element set with $E_{3\text{max}} = 14$. Then we use the Hartree-Fock ground-state as reference state for computing the NO2B matrix elements for the large $E_{3\text{max}}$ we target. These matrix elements enter another Hartree-Fock calculation at the NO2B level yielding a reference state including in-

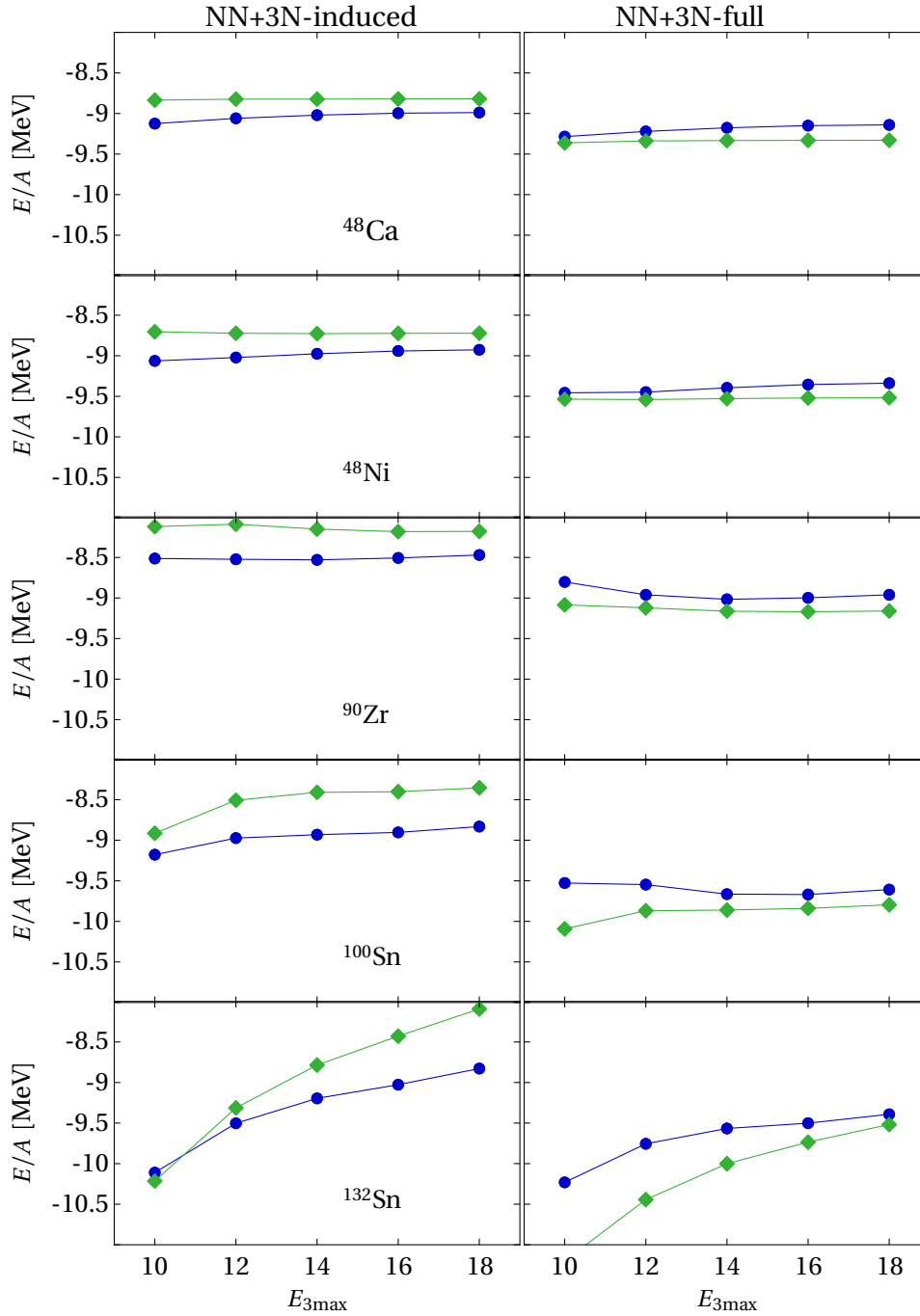


Figure 9.8 – Convergence of CCSD ground-state energies with respect to $E_{3\text{max}}$. CCSD is performed at $e_{\text{max}} = 12$ using a HF basis and for SRG flow parameters $\alpha = 0.04$ (●) and 0.08 fm^4 (◆) for the NN+3N-induced (left-hand column) and NN+3N-full (right-hand column) Hamiltonians. Remaining parameters are $\hbar\Omega = 24 \text{ MeV}$, the SRG model-space truncation \mathcal{B} and the NO2B approximation is used. (published in [136])

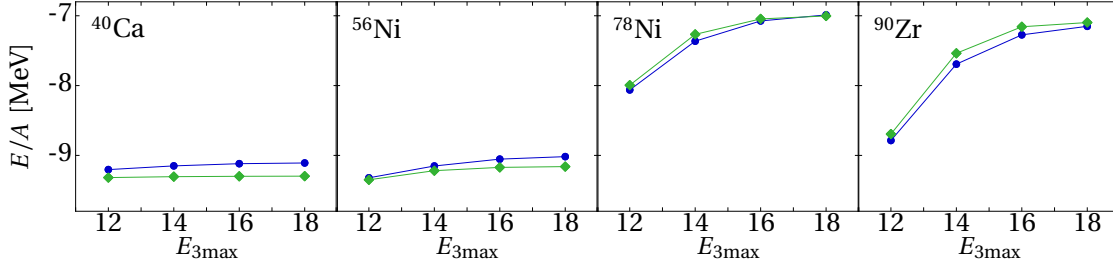


Figure 9.9 – Convergence of CCSD ground-state energies with respect to $E_{3\max}$ here using the too small SRG model space \mathcal{A} . CCSD is performed at $e_{\max} = 12$ and for SRG flow parameters $\alpha = 0.04$ (●) and 0.08 fm^4 (◆) for the NN+3N-full Hamiltonians at $\hbar\Omega = 24 \text{ MeV}$ and using the NO2B approximation. Note the different convergence pattern compared to Figure 9.8.

formation of large $E_{3\max}$, which is then used to again compute the normal-ordered matrix elements. This procedure can be iterated until we reach consistency. However, typically a single iteration is sufficient due to the excellent accuracy of the NO2B approximation. In this way we can easily produce NO2B matrix elements with $E_{3\max} = 18$ or even beyond if necessary.

In Figure 9.8, we present the convergence of the ground-state energies for ^{48}Ca , ^{48}Ni , ^{90}Zr , ^{100}Sn and ^{132}Sn with respect to $E_{3\max}$ for the NN+3N-induced and NN+3N-full Hamiltonian. The results for SRG parameters $\alpha = 0.04$ and 0.08 fm^4 are depicted as blue discs and green diamonds, respectively. For nuclei up to ^{90}Zr convergence with respect to $E_{3\max}$ is essentially reached at $E_{3\max} = 14$ independently of the used Hamiltonian or SRG flow parameter. For the heavier nuclei between ^{100}Sn and ^{132}Sn the access to the large $E_{3\max}$ matrix element sets is crucial to reach converged results. We note that the convergence pattern is changing throughout the tin isotopic chain: while the energies for ^{100}Sn are well converged with respect to $E_{3\max}$, we find slightly larger contributions from $E_{3\max} = 18$ for ^{132}Sn and a slower convergence for $\alpha = 0.08 \text{ fm}^4$. For ^{132}Sn the energies seem to be closer to convergence for the NN+3N-full Hamiltonian compared to the NN+3N-induced Hamiltonian, hinting at ongoing cancellations and we come back to this point in Section 9.2.5. Overall, we can state that we can largely suppress uncertainties due to the $E_{3\max}$ truncation as evident from Figure 9.8.

Furthermore, as we have briefly discussed at the end of Section 8 and in Refs. [46, 98], the triples corrections for soft interactions can become comparable to the uncertainties introduced by the NO2B approximation at the level of CCSD calculations. Therefore, in order to improve the accuracy of our final calculations discussed in Section 9.2.5 further, we include the normal-ordered 3B part explicitly up to $E_{3\max} = 12$, and include the contributions beyond that up to $E_{3\max} = 18$ using the NO2B approximation. According to this we practically remedy uncertainties stemming from the NO2B approximation at least throughout the oxygen, calcium and nickel isotopic chains.

Another interesting detail about the convergence pattern of the CCSD ground-state energies with respect to $E_{3\max}$ is its dependence on the SRG model space. In Figure 9.9 we present the convergence behavior for ^{40}Ca , ^{56}Ni , ^{78}Ni and ^{90}Zr analogously to Figure 9.8 but

here with an NN+3N-full Hamiltonian resulting from the SRG evolution using the much smaller SRG model-space truncation \mathcal{A} , which has been our default for light nuclei, instead of the significantly larger ramp \mathcal{B} . See Figure 9.3 to recall their definition. We have discussed the insufficiency of the small SRG model space \mathcal{A} , which leads to significant underbinding of heavy nuclei already above. In addition, we see now from Figure 9.9 that also the convergence pattern with respect to $E_{3\text{max}}$ is spoiled by the severe limitation of the SRG model space: we observe deviations from $E_{3\text{max}} = 14$ to 16 in ^{56}Ni that occur in the results obtained with the sufficiently large SRG model space \mathcal{B} only in the heavy tin isotopes. For ^{78}Ni and ^{90}Zr we find significant changes of the energies when we increase $E_{3\text{max}}$ from 12 through 14 to 16, which are completely absent when we use model space \mathcal{B} (cf. Figure 9.8). This highlights once more the problematic of using too small SRG model spaces, as they would lead to increased computational costs caused by the spurious demand for matrix element sets at unnecessarily large $E_{3\text{max}}$.

9.2.4 HO Frequency Dependence

As the last point on our path towards the validation of chiral Hamiltonians by means of comparing to experimental energies we investigate the dependence of ground-state energies on the HO frequency of the underlying single-particle basis. We depict the corresponding results for the NN+3N-full Hamiltonian in Figure 9.10 where we in addition include curves for different $E_{3\text{max}}$. Although the coupled-cluster approach is formally non-variational calculation, one typically adopts the energy minima as function of the frequency as working point. We find the frequency dependence for ^{40}Ca , ^{48}Ca and ^{56}Ni essentially flat where $\hbar\Omega = 24\text{MeV}$ yields the minimal energy for all $E_{3\text{max}}$, although the energy is subject to a slight increase with increasing $E_{3\text{max}}$. The somewhat steeper frequency dependence for the heavier nuclei is consistent with the e_{max} convergence pattern observed in Figure 9.7. Interestingly, for the tin isotopes the energy minimum moves as function of $E_{3\text{max}}$: it seems to be located around the larger frequencies 32 or 36 MeV for $E_{3\text{max}} = 12$, but with increasing $E_{3\text{max}}$ to 16 the minimum is shifted to smaller frequencies and we again identify $\hbar\Omega = 24\text{MeV}$ as minimum position over the studied frequency range. Overall, we have found moderate frequency dependence, and we choose the optimal frequency $\hbar\Omega = 24\text{MeV}$ for all nuclei and calculations presented in the following subsection.

9.2.5 From ^{16}O to ^{132}Sn with Chiral Hamiltonians

The detailed uncertainty analysis presented in the previous four subsections together with the benchmark of the NO2B approximation in Section 8 paves the way for first accurate ab-initio calculations for the regime of heavy nuclei. Facilitated by a number of technical developments we have demonstrated that we can avoid spurious results from shortcomings of the SRG model space, and that we are able to provide (NO2B) matrix elements computed with sufficiently large $E_{3\text{max}}$ to reach model-space convergence and to guarantee that we adopt the energy minimum as function of the HO frequency of the underlying single-particle basis of the coupled-cluster approach. Altogether, we find an accuracy

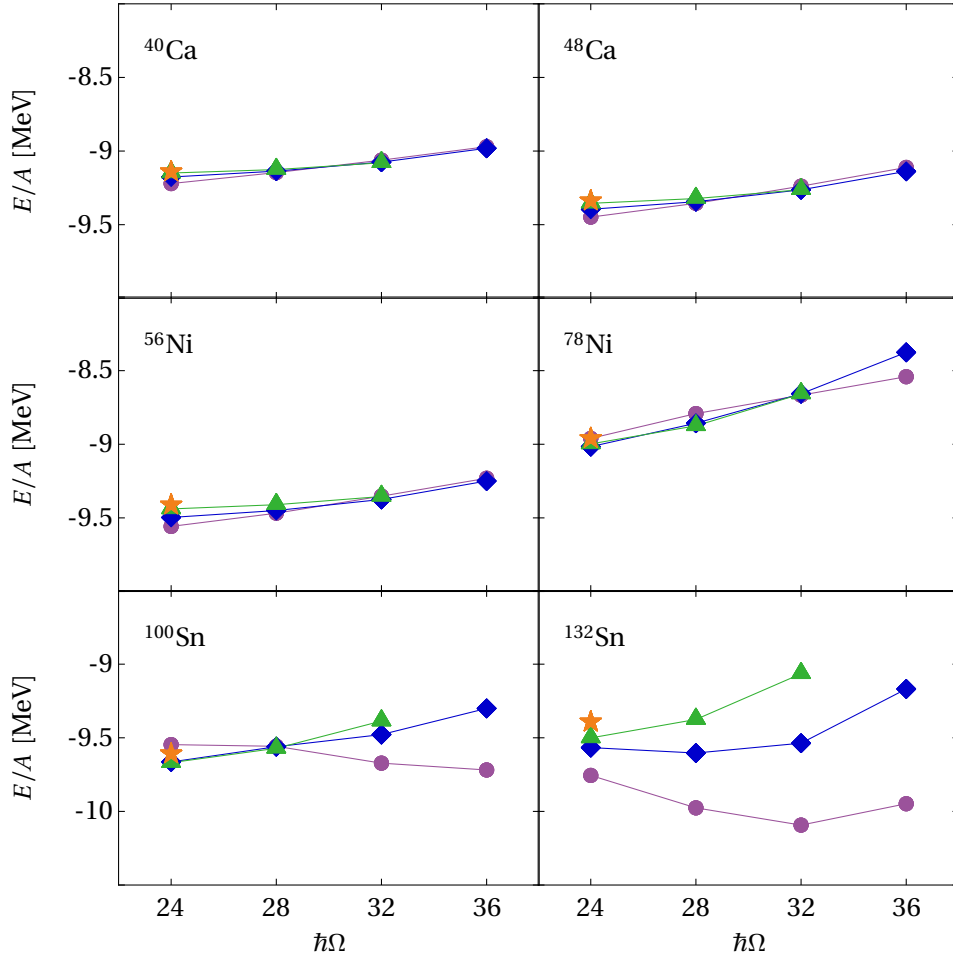


Figure 9.10 – Dependence of the CCSD ground-state energies on the HO frequency for the NN+3N-full Hamiltonian, and for the different parameters $E_{3\max} = 12$ (\bullet), 14 (\blacklozenge), 16 (\blacktriangle), and 18 (\star). CCSD uses a HF single-particle basis and is performed at $e_{\max} = 12$ and using the NO2B approximation.

of the many-body approach for fixed SRG flow parameter and for a given Hamiltonian of about 3% up to ^{100}Sn , which is determined mainly by the CR-CC(2,3) triples correction on top of the energy obtained from CCSD [136]. For the heavy tin isotopes the accuracy amounts to about 4% due to the somewhat slower convergence with respect to e_{\max} (cf. Figure 9.7). Based on this we study in the following the ground-state energies of nuclei with closed sub-shells spanning the range from ^{16}O up to ^{132}Sn using SRG-evolved chiral NN+3N-Hamiltonians that have been fixed entirely in two-, three- and four-body systems. We use the two SRG flow parameters $\alpha = 0.04$ and 0.08fm^4 to investigate the SRG flow-parameters dependence, and, therefore, indirectly the relevance of SRG-induced multi-nucleon contributions.

We summarize all results in Figure 9.11, where panels (a) and (c) show the ground-state energies obtained with CR-CC(2,3) in comparison to experiment for the NN+3N-induced and NN+3N-full Hamiltonian, respectively. Panels (b) and (d) show the size of the respective triples corrections beyond the CCSD level, which we also adopt as residual uncertainty

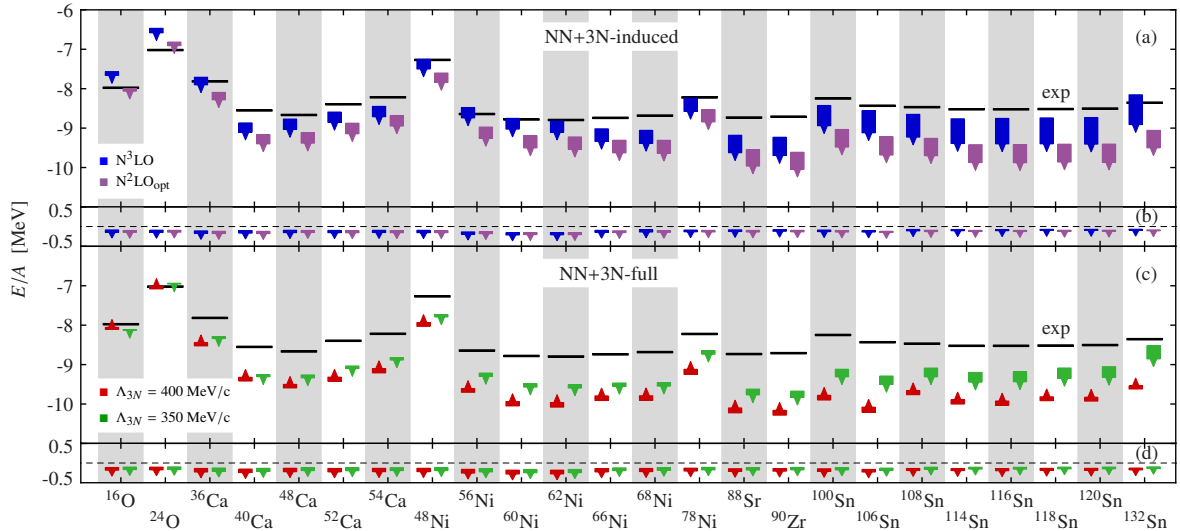


Figure 9.11 – CR-CC(2,3) ground-state energies per nucleon obtained with the (a) NN+3N-induced Hamiltonian using the $N^3\text{LO}$ and $N^2\text{LO}_{\text{opt}}$ chiral NN interactions, respectively, and the NN+3N-full Hamiltonian with momentum cutoff $\Lambda_{3N} = 400\text{ MeV}/c$ and $\Lambda_{3N} = 350\text{ MeV}/c$ using a HF basis. The span of the bars denotes the spread of the energies from $\alpha = 0.04\text{ fm}^4$ to $\alpha = 0.08\text{ fm}^4$, while the tip points in the direction of smaller flow parameters. In panels (b) and (d) we show the respective contributions of the CR-CC(2,3) triples corrections. Further parameters are $\hbar\Omega = 24\text{ MeV}$, and $E_{3\text{max}} = 18$ for the 3N interactions in NO2B approximation and for their full inclusion in CCSD $E_{3\text{max}} = 12$. Experimental energies are denoted as black bars [144]. (published in [136])

of the many-body method. Evidently, the triples corrections per nucleon remain rather constant over the whole mass range and contribute between 0.1 and 0.2 MeV per nucleon.

We proceed with the more detailed discussion considering the NN+3N-induced results depicted in panel (a). We concentrate first on the blue bars corresponding to calculations using the standard initial $N^3\text{LO}$ chiral NN interaction, which we introduced in Section 1.1. The span of the bars represents the difference between the results from $\alpha = 0.04\text{ fm}^4$ to $\alpha = 0.08\text{ fm}^4$, and the tip points towards smaller SRG flow parameters. For the light oxygen isotopes we observe only a slight dependence on the SRG flow parameter, which is at the same order of magnitude as the triples correction, i.e., the overall uncertainty of the calculations. Hence, this complies with our findings before that SRG-induced four- and multi-nucleon contributions originating from the initial NN interaction are irrelevant for ground-state energies (cf. Section 6.1 and 8 or Refs. [42, 43, 34]). In contrast, with increasing mass number we find a strong increase of the SRG flow-parameter dependence. The discussions in the previous subsections show that none of the remaining uncertainties can explain this increased flow-parameter dependence. Therefore, we conclude that in the heavy-mass regime the contributions of SRG-induced four- and multi-nucleon forces originating from the initial NN interaction grow and become significant. We confirm this observation by the results shown as violet bars, which correspond to the use of an alternative

chiral NN interaction, the so-called optimized chiral NN interaction N^2LO_{opt} introduced in Ref. [146]. In addition, the direction of the α dependence indicates an attractive character of the SRG-induced beyond-3N interactions, while we have found the SRG-induced 3N contribution to be repulsive, e.g., see Section 6.1 or Refs. [42, 145, 40].

We proceed with the energies computed with included initial chiral 3N interaction to the Hamiltonian containing the N^3LO NN interaction shown in Figure 9.11(c). We start with the results obtained with the 3N interaction with $\Lambda_{3N} = 400 \text{ MeV}/c$ that are depicted as red bars. We have found already before that the contributions of induced four- and multi-nucleon contributions are suppressed when we use this 3N interaction in calcium isotopes, see Section 6.3 and Refs [43, 46]. Now we can confirm this even for the heavy-mass regime, i.e., throughout the tin isotopic chain. This is striking due to the significant flow-parameter dependence in the NN+3N-induced Hamiltonian results. This can be explained by a cancellation of the attractive SRG-induced four- and multi-nucleon forces originating from the initial NN interaction with repulsive SRG-induced four- and multi-nucleon forces originating from the initial 3N interaction. We study this further based on the results obtained with the 3N interaction with the further reduced cutoff $\Lambda_{3N} = 350 \text{ MeV}/c$ shown as green bars. For nuclei up to ^{78}Ni the α dependence remains comparable to the one obtained with the $\Lambda_{3N} = 400 \text{ MeV}/c$ interaction, but the direction of the α dependence is reversed. For the heavier nuclei the effective weakening of the 3N interaction due to the further lowered cutoff Λ_{3N} also the repulsive SRG-induced 4N contributions from the initial 3N interaction is weakened (cf. Section 6.3). Accordingly, the attractive 4N contributions induced by the initial NN interaction prevail and lead to an reversed and increased flow-parameter dependence of ground-state energies of the tin isotopes indicating net attractive four- and multi-nucleon forces.

Exploiting the cancellation of the different SRG-induced contributions for the NN+3N-full Hamiltonian with $\Lambda_{3N} = 400 \text{ MeV}/c$ we take the opportunity to compare the ground-state energies to experiment. The latter are indicated in Figure 9.11 as black bars. For both oxygen isotopes we find very good agreement with experiment. For all remaining nuclei, i.e., over the whole mass range from ^{36}Ca up to ^{132}Sn , we find a remarkable qualitative agreement of our results with the experimental binding-energy systematics. We note once more that the low-energy constants of the applied chiral Hamiltonian have been determined in the few-nucleon sector. Overall, we find deviations from experiment of about 1 MeV per nucleon overbinding for all studied nuclei beyond ^{36}Ca . Altogether, this highlights the predictive power of chiral Hamiltonians even in the heavy-mass regime. Nevertheless, for more rigorous and quantitative statements or analyses one has to include consistently the sub-leading 3N interaction from N^3LO and also the leading 4N interaction that emerge at this order of the chiral power counting. In particular our findings that SRG-induced 4N interaction originating from the initial NN interaction, which have been found to be negligible in light nuclei, can be amplified by combinatorics may indicate relevant contributions of initial chiral 4N interactions in the medium- and heavy-mass regime. Note that these effects have been found to contribute a few hundred keV to the binding energy of ^4He in Ref. [170].

Finally, we note that charge radii computed with the Hartree-Fock reference state are systematically too small compared to experiment [171] with increasing deviations reaching from 0.3 fm to 1.0 fm from ^{16}O to ^{132}Sn . These discrepancies are larger than the effects expected from beyond-Hartree-Fock correlations or the consistent SRG evolution of the radii [109], and pose one challenge for future investigations from first principles already in light nuclei, which may require improvements of the initial chiral Hamiltonians.

In conclusion, we have presented first precise ab-initio calculations of heavy nuclei based on SRG-evolved chiral NN+3N Hamiltonians which allow for the direct validation of chiral Hamiltonians by means of ground-state energies of closed-shell nuclei in this mass regime. For this a careful uncertainty analysis is mandatory, and has been enabled by various technical developments we discuss throughout this work, such as the SRG transformation in sufficiently large model spaces (cf. Section 3 and 5), the normal-ordering of 3N matrix elements with large $E_{3\text{max}}$ (cf. Sections 2.3 and 8), and the extension of the coupled-cluster approach to heavy nuclei with the inclusion of 3N interactions that is discussed in detail in Ref. [96].

Part III

Three-Nucleon Forces in Ab-Initio Nuclear Reactions

INTRODUCTION TO PART III

Aggregates of neutrons and protons exhibit not only bound states, which have been the focus of the discussion so far, but also unbound resonances and scattering states. These states are of particular importance in different aspects: on the one hand nuclear scatterings and reactions are a standard tool for experimental nuclear physics, e.g., to populate and study properties of nuclear states that are not accessible by radioactive decays. On the other hand properties of atomic nuclei and their consequences in nuclear reactions are crucial to understand the formation of the lightest elements few minutes after the Big Bang and also to explain the abundance and production of heavier elements [6]. It is evident that nuclear theory should also provide the capabilities to describe scattering states and resonances of atomic nuclei and, thus, nuclear reactions.

Thus, the goal is to arrive at a unified ab-initio framework capable to describe structural properties as well as reactions of nuclei and, in view of the previous discussion in this thesis, capable to include chiral 3N interactions. This defines the topic of the third part of this thesis, which is organized as follows: We start with general aspects of many-body scattering to identify the quantities we need to compute later on and to fix the notation in Section 10. In Section 11 we introduce the formalism of the resonating group method combined with the no-core shell model (NCSM/RGM) that constitutes a nuclear scattering technique. In particular, we present in detail the necessary steps to extend the formalism to 3N interactions and highlight how this can be achieved also for targets beyond the lightest nuclei. After discussing the R matrix theory that is used to solve the NCSM/RGM equations in Section 12, we apply the extended formalism to nucleon- ^4He scattering and study the effects of chiral 3N interactions on phase shifts, differential cross sections and analyzing powers in Section 13. Finally, in Section 14 we introduce the so-called no-core shell model with continuum (NCSMC) that combines the NCSM and NCSM/RGM to an ab-initio approach capable to describe bound and continuum states on equal footing. Since the NCSM/RGM Hamiltonian kernels are one component also of the NCSMC equations the former developments for the NCSM/RGM facilitate the extension of NCSMC to include 3N interactions. Finally, we employ the NCSMC with explicit 3N interactions for first ab-initio investigations of the impact of the continuum and of the 3N interactions on the spectrum of ^9Be .

SECTION 10

Generalities on Many-Body Scattering

We begin our investigations of the theoretical formalism for nuclear scatterings and reactions with a brief overview of general prerequisites for the theoretical description of collisions involving many-nucleon systems. Ultimately, we aim at a unified ab-initio theory for the description of bound and continuum states, as motivated in the introduction. Before we describe the steps towards such a theory throughout the next sections, here we define the necessary notation, give the expressions for scattering states and their connection to scattering phase shifts, cross sections and polarization observables.

For the theoretical description of nuclear reactions the main focus is on A -nucleon systems that consist of different sub-clusters of nucleons. For a given energy E the particles may form all kinds of energetically allowed partitions p with $A = \sum_i A_{p,i}$, where $A_{p,i}$ denotes the mass number of the i -th sub-cluster of the partition p . An illustration of the different possible partitions is shown in Figure 10.1. In addition, the sub-clusters may exist in any of their excited states so that the total energy amounts to E . To keep track of all this information we introduce the concept of channels: we define a particular channel ν by specifying the partition p of the A nucleons into sub-clusters and, in addition, by listing their intrinsic energies and the good quantum numbers assigned to the internal states of all sub-clusters, respectively. Each channel has a so-called threshold energy $E_\nu = \sum_i E_{A_{p(\nu),i}}$ given by the sum of the intrinsic energies of all nucleon sub-clusters $E_{A_{p(\nu),i}}$. A channel is said to be open if its threshold energy E_ν is smaller than the total energy E of the system, and it is closed if $E_\nu \geq E$. To account for all these degrees of freedom adequately one needs to use a many-body basis which is sufficiently flexible. The most general basis states de-

scribing all these degrees of freedom may be written as

$$|\Phi\rangle = \hat{\mathcal{A}}_p |\phi_{1\nu}\rangle \otimes |\phi_{2\nu}\rangle \otimes |\vec{r}\rangle \quad (10.1)$$

$$+ \hat{\mathcal{A}}_{p'} |\phi_{1\nu'}\rangle \otimes |\phi_{2\nu'}\rangle \otimes |\phi_{3\nu'}\rangle \otimes |\vec{r}, \vec{r}'\rangle \quad (10.2)$$

$$+ \hat{\mathcal{A}}_{p''} |\phi_{1\nu''}\rangle \otimes |\phi_{2\nu''}\rangle \otimes |\phi_{3\nu''}\rangle \otimes |\phi_{4\nu''}\rangle \otimes |\vec{r}, \vec{r}', \vec{r}''\rangle \quad (10.3)$$

⋮

$$+ |\phi_\lambda\rangle, \quad (10.4)$$

where states $|\phi_{i\nu}\rangle$ are the intrinsic states of sub-cluster i and the channel index ν contains the relevant quantum numbers of *all* sub-clusters, we state more explicitly which quantum numbers it includes in different contexts below. The operators $\hat{\mathcal{A}}_p$ are the inter-cluster antisymmetrizers that ensure the antisymmetry of the basis state $|\Phi\rangle$ also for nucleon exchanges between different clusters, and the states $|\vec{r}, \vec{r}', \dots\rangle$ describe the relative distances between the nuclear clusters. In the last line we have singled-out square integrable A -body states, which are sometimes referred to as distortion states [172]. They help to handle the so-called specific distortion, which is related to the attractive character of the nuclear interaction at the long range and, therefore, the clusters tend to deform to make the best use of the attraction. Stated differently, this induces correlations in the A -body many-body states which can be described most efficiently by the inclusion of the distortion states. We come back to this in Section 14. In practical calculations it is, however, not feasible to take all terms shown in Eqs. (10.1)-(10.4) into account. Instead, we have to restrict the number of channels to a subset of the most important ones for the considered energy range. We can check if the selection is reasonable via the explicit investigation of the convergence of scattering observables with respect to the number of included channels. At high energies the number of relevant channels with significant contributions may become quite large. Finally, an important formal requirement of channels is that they are stable, i.e., that they do not decay into different sub-clusters for any finite time t . This is important for the mathematical description of the scattering process, for which we investigate so-called scattering states for times $t \rightarrow \pm\infty$, as discussed below. In fact, scattering experiments are quite often done involving unstable particles with respect to the definition above, a prominent example being scattering experiments involving the unstable neutron. However, in practice an infinite long lifetime means that the lifetime of the sub-clusters in a channel needs to be much larger compared to the actual collision time. Then it is sufficient to detect the sub-clusters before they are subject to decay. Scattering theory is usually adapted to this perspective. For instance, for the description of nuclear collisions with neutrons one usually neglects the weak interaction in the Hamiltonian, because the scattering process is dominated by the strong interaction. Thus, in the calculations the neutron is actually stable.

The nuclear Hamiltonian we use to describe the nuclear collisions is given by

$$\hat{H} = \hat{T}_{\text{int}} + \hat{V}^{\text{NN}} + \hat{V}^{\text{3N}}, \quad (10.5)$$

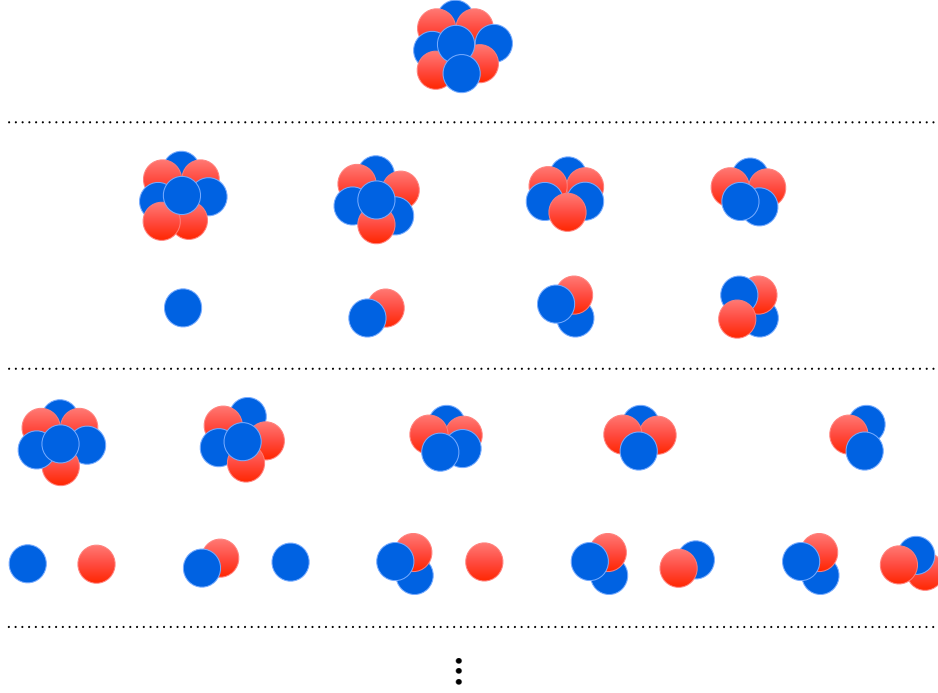


Figure 10.1 – Illustration of the possible partitions of an $A = 9$ system. Partitions that can be obtained by means of inter-cluster antisymmetrizers are not shown. The vertical ellipsis denotes partitions with four or more nucleon sub-clusters.

i.e., it is identical to the Hamiltonians investigated in the nuclear structure calculations discussed in Part II, in particular we account for 3N interactions explicitly. Accordingly, we will be able to study effects of the initial chiral 3N interactions by comparing results obtained with the NN+3N-full Hamiltonian to those from the NN+3N-induced Hamiltonian in the context of scattering observables (for the definitions of the Hamiltonians see Section. 3).

To be able to draw such conclusions we are required to investigate nuclear collisions in an ab-initio fashion. We present two possible approaches for this in Sections 11 and 14. Both of them rely on the usual approach to describe the scattering process as boundary-value problem, that is, only the states of the A -body system for long times before and after the actual scattering process need to be investigated. Stated differently, we need to determine the asymptotic states of the system for times $t \rightarrow \pm\infty$. Thus, the complicated details and structure of the collision present at intermediate times need not to be considered explicitly. In the following we restrict ourselves to channels with partitions involving two sub-clusters, i.e., to those depicted in the second row of Figure 10.1, and allow different channels in terms of excitations of the sub-clusters. We outline the general steps leading to the outgoing scattering state, which defines the phase shifts and differential and total cross sections or polarization observables. We assume that the incident particles can be described by a plane wave propagation in z -direction. We have to define an ansatz for the asymptotic scattering state $|\Psi_{vM_1M_2M_{T_1}M_{T_2}}^+(t \rightarrow \infty)\rangle$. Here and in the following, we adopt the notation in which all quantum numbers defining the considered channel are collected the

index ν . If particular quantum numbers are important in the context of a specific equation we may denote them explicitly, while they may be implicitly contained in ν in a different context. The M_i and M_{T_i} are the projection quantum numbers of the total intrinsic angular momenta \vec{I}_i and isospins \vec{T}_i for each of the two sub-clusters, respectively. The stationary scattering state can be expressed as superposition of partial-wave states as follows [173]

$$\begin{aligned}
 & |\Psi_{\nu M_1 M_2 M_{T_1} M_{T_2}}^+ \rangle \\
 &= i(2\pi)^{-\frac{3}{2}} \frac{\sqrt{\pi}}{k} \sum_{J\pi} \sum_{s l} \sum_T C_\nu^{-1} \sqrt{(2l+1)} e^{i\sigma_l} \\
 & \left(\begin{array}{cc|c} I_1 & I_2 & s \\ M_1 & M_2 & M_s \end{array} \right) \left(\begin{array}{cc|c} s & l & J \\ M_s & 0 & M \end{array} \right) \left(\begin{array}{cc|c} T_1 & T_2 & T \\ M_{T_1} & M_{T_2} & M_T \end{array} \right) |\Psi_\nu^{JM\pi TM_T}\rangle, \tag{10.6}
 \end{aligned}$$

with $M_T = M_{T_1} + M_{T_2}$, $M = M_1 + M_2$ and the Coulomb phase shift σ_l . In writing Eq. (10.6) we used the context-dependent meaning of the index ν : on the left-hand side it includes $\nu = \{E_1, I_1^{\pi_1}, T_1; E_2, I_2^{\pi_2}, T_2\}$, while on the right-hand side it is given as $\nu = \{E_1, I_1^{\pi_1}, T_1; E_2, I_2^{\pi_2}, T_2; s l\}$, where l is the orbital angular momentum quantum number of the relative motion of the two clusters. The Clebsch-Gordan coefficients take care of the angular-momentum coupling of \vec{I}_1 and \vec{I}_2 to the so-called channel spin \vec{s} . In addition, also the isospins of the sub-clusters, \vec{T}_1 and \vec{T}_2 , are coupled to the total isospin \vec{T} . This is convenient because the partial-wave states $|\Psi_\nu^{JM\pi TM_T}\rangle$ reflect the basic symmetries of the used Hamiltonian which make the total relative orbital momentum J and its projection as well as the total parity to good quantum numbers. In addition, we also assume the isospin to be a good quantum number, which is an approximation but typically very well fulfilled. The partial-wave states themselves are the quantities we need to calculate. They constitute the interface for the scattering formalisms we introduce in the next sections. The ansatz for these partial wave states can get quite complicated as we have seen in Eqs. (10.1)-(10.4). However, for collisions where the restriction to the partition with two sub-clusters is sufficient, they may be written as an expansion over basis states given by Eq. (10.1) in the generic angular-momentum coupled form

$$|\Psi_{\nu_0}^{JM\pi TM_T}\rangle = \sum_\nu \int dr r^2 \frac{u_{\nu(\nu_0)}(r)}{r} \hat{\mathcal{A}}_p [(|\phi_{1\nu}\rangle \otimes |\phi_{2\nu}\rangle)^s \otimes |r l m\rangle]^{JM\pi TM_T}, \tag{10.7}$$

where ν_0 indicates the channel of the incident particles. The expansion coefficients $u_{\nu(\nu_0)}(r)$ are the relative-motion wave functions that need to be calculated. Inserting these with help of Eq. (10.7) in Eq. (10.6) fully determines the scattering state. We will come back to this ansatz in more detail in the next Section about the NCSM/RGM approach.

Apart from that, we can construct the general form of the asymptotic scattering state following some general arguments: first of all, the whole formalism is developed under the requirement that all potentials tend to zero faster than $\frac{1}{r}$ for $r \rightarrow \infty$. The sole exception is a point-Coulomb interaction $V_C = \frac{Z_{1\nu_1} Z_{2\nu} e^2}{r}$ between the sub-clusters. If we switch off all other interactions and keep only this point-Coulomb interaction, we are essentially left with Coulomb scattering. Under these circumstances no coupling of the interaction to

the angular momenta of the sub-clusters exists, so that the asymptotic wave function³ is simply given by the product of the relative-motion wave function $\psi_C^+(\vec{r})$ from Coulomb scattering and the wave functions of the sub-clusters with the identical orbital quantum numbers as the incident wave function, i.e.,

$$\Psi_{\nu M_1 M_2 M_{T_1} M_{T_2}}^+(\{\vec{\xi}_i\}, \{\vec{\eta}_i\}, \vec{r}) \xrightarrow{r \rightarrow \infty} \psi_C^+(\vec{r}) \phi_{\nu I_1 M_1 T_1 M_{T_1}}(\{\vec{\xi}_i\}) \phi_{\nu I_2 M_2 T_2 M_{T_2}}(\{\vec{\eta}_i\}), \quad (10.8)$$

where the sets of coordinates $\{\vec{\xi}_i\}$ and $\{\vec{\eta}_i\}$ denote the Jacobi coordinates used for the description of the respective sub-clusters. We list convenient Jacobi coordinates for binary-cluster scattering in Appendix B. The relative-motion wave function $\psi_C^+(\vec{r})$ is known from Coulomb scattering and has the asymptotic form

$$\psi_C^+(\vec{r}) \xrightarrow{|r-z| \rightarrow \infty} (2\pi)^{-\frac{3}{2}} \left(e^{i(kz + \eta \ln(k(r-z)))} + f_C(\Omega) \frac{e^{i(kr - \eta \ln(2kr))}}{r} \right) \quad (10.9)$$

with the Coulomb scattering amplitude $f_C(\Omega)$ depending on the solid angle Ω and the Sommerfeld parameter η . We not discuss the details of Coulomb scattering here, a detailed discussion can be found, e.g., in Ref. [174]. If we now switch on again the nuclear and higher-order electromagnetic interactions, the radial dependence of the asymptotic wave function still needs to coincide with the form of the outgoing spherical wave from Coulomb scattering due to the fact that the point-Coulomb potential is the only interaction present at $r \rightarrow \infty$. However, now the angular momenta of the sub-clusters may have changed due to interaction effects. Therefore, the asymptotic behavior of the scattering wave function reads

$$\begin{aligned} \Psi_{\nu M_1 M_{T_1} M_2 M_{T_2}}^+(\{\vec{\xi}_i\}, \{\vec{\eta}_i\}, \vec{r}) &\xrightarrow{r \rightarrow \infty} \psi_C^+(\vec{r}) \phi_{\nu I_1 M_1 M_{T_1}}(\{\vec{\xi}_i\}) \phi_{\nu I_2 M_2 M_{T_2}}(\{\vec{\eta}_i\}) \\ &+ (2\pi)^{-\frac{3}{2}} \sum_{\nu'} \sum_{M'_1 M'_2 M'_{T_1} M'_{T_2}} \frac{e^{i(k_{\nu'} r - \eta_{\nu'} \ln(2k_{\nu'} r))}}{r} f_{\nu' M'_1 M'_2 M'_{T_1} M'_{T_2}}^{(\nu M_1 M_2 M_{T_1} M_{T_2})}(\Omega) \phi_{\nu' I'_1 M'_1 M'_{T_1}}(\{\vec{\xi}_i\}) \phi_{\nu' I'_2 M'_2 M'_{T_2}}(\{\vec{\eta}_i\}), \end{aligned} \quad (10.10)$$

where we introduce for each possible outgoing channel the complex scattering amplitudes $f_{\nu' M'_1 M'_2 M'_{T_1} M'_{T_2}}^{(\nu M_1 M_2 M_{T_1} M_{T_2})}(\Omega)$ at which the upper indices denote the angular quantum numbers of the incident particles. Equating the asymptotic limit of the scattering state (10.6) converted in coordinate-space representation with the asymptotic form (10.10) yields the scattering amplitudes [173]

³We switch to coordinate representation here to be consistent with most of the scattering literature.

$$\begin{aligned}
 & f_{\nu' M'_1 M'_2 M'_T M'_1 M'_2}^{(\nu M_1 M_2 M_T M_T)}(\Omega) \\
 &= i \frac{\sqrt{\pi}}{k} \sum_{J\pi} \sum_T \sum_{sl} \sum_{s'l'} \sqrt{2l+1} e^{i(\sigma_l + \sigma_{l'})} \\
 & \quad \begin{pmatrix} I_1 & I_2 & | & s \\ M_1 & M_2 & | & M_s \end{pmatrix} \begin{pmatrix} s & l & | & J \\ M_s & 0 & | & M \end{pmatrix} \begin{pmatrix} I'_1 & I'_2 & | & s' \\ M'_1 & M'_2 & | & M_{s'} \end{pmatrix} \begin{pmatrix} s' & l' & | & J \\ M_{s'} & M - M_{s'} & | & M \end{pmatrix} \\
 & \quad \begin{pmatrix} T_1 & T_2 & | & T \\ M_{T_1} & M_{T_2} & | & M_T \end{pmatrix} \begin{pmatrix} T'_1 & T'_2 & | & T \\ M'_{T_1} & M'_{T_2} & | & M_T \end{pmatrix} \\
 & \quad (\delta_{\nu',\nu} \delta_{s',s} \delta_{l',l} - U_{\nu' s' l', \nu s l}^{J\pi T}) Y_{l'}^{M_s - M_{s'}}(\Omega), \tag{10.11}
 \end{aligned}$$

where $U_{\nu' s' l', \nu s l}^{J\pi T}$ is the so-called scattering matrix element. It is the central object for the determination of the relative-motion wave functions as well as for the subsequent calculation of the scattering observables. We give the explicit expression in Section 12 on the R -matrix theory.

For completeness we also give the expressions for the scattering observables that we study in the following. All of them are deduced from the scattering amplitudes and can be found in Refs. [173, 175]. The differential elastic cross section is given by

$$\frac{d\sigma_{\text{el.}}}{d\Omega} = \frac{1}{(2I_1+1)(2I_2+1)} \sum_{M_1 M_2} \sum_{M'_1 M'_2} \left| f_C(\Omega) \delta_{M_1, M'_1} \delta_{M_2, M'_2} + f_{\nu' M'_1 M'_2 M'_T M'_1 M'_2}^{(\nu M_1 M_2 M_T M_T)}(\Omega) \right|^2, \tag{10.12}$$

with solid angle Ω . Note that the energy dependence of the differential cross section is absorbed in the scattering matrix elements entering the scattering amplitude $f_{\nu' M'_1 M'_2 M'_T M'_1 M'_2}^{(\nu M_1 M_2 M_T M_T)}(\Omega)$ in Eq. (10.11). The inelastic or reaction cross sections can be obtained from

$$\frac{d\sigma_{\nu \rightarrow \nu'}}{d\Omega} = \frac{1}{(2I_1+1)(2I_2+1)} \sum_{M_1 M_2} \sum_{M'_1 M'_2} \left| f_{\nu' M'_1 M'_2 M'_T M'_1 M'_2}^{(\nu M_1 M_2 M_T M_T)}(\Omega) \right|^2. \tag{10.13}$$

In addition, also polarization observables can be computed from the scattering amplitudes or differential cross sections. For a summary of their definition see, e.g., Ref. [176]. For the example of polarized spin one-half particles scattering off a unpolarized target and unpolarized ejectiles, i.e., the reaction $A(\vec{a}, b)B$, the differential cross section can be written as

$$\left(\frac{d\sigma}{d\Omega} \right) = \left(\frac{d\sigma}{d\Omega} \right)_{\text{unpol.}} \left[1 + \sum_i p_i A_i \right], \tag{10.14}$$

with $\left(\frac{d\sigma}{d\Omega} \right)_{\text{unpol.}}$ denoting the cross section for unpolarized projectiles, p_i indicating the component of the polarization vector of the incident particles, where $i \in \{x, y, z\}$, and A_i as the so-called analyzing powers that describe how the reaction is influenced by the individual polarization components. To compute for example the analyzing power for spin one-

half nucleons scattering off a nucleus with vanishing spin one can exploit that in this case the scattering amplitude can be written in terms of the non-spin-flip amplitude $a(E, \Theta)$ and the spin-flip amplitude $b(E, \Theta)$ as [177, 178]

$$f = a(E, \Theta)\mathbb{1} + ib(E, \Theta)\vec{e}_n \cdot \vec{\sigma} \quad (10.15)$$

in matrix notation, where $\mathbb{1}$ denotes the unit matrix, $\vec{\sigma}$ is the vector of Pauli matrices, and \vec{e}_n denotes the unit vector perpendicular to the scattering plane. The analyzing power A_y is then given by [177, 178]

$$A_y(\Theta) = \frac{2\text{Im}(a(E, \Theta)b(E, \Theta)^*)}{|a|^2 + |b|^2}. \quad (10.16)$$

Alternatively it can be computed directly as trace over the scattering amplitude by [178]

$$A_y = \frac{\text{Tr}(f\sigma_y f^\dagger)}{\text{Tr}(f f^\dagger)}. \quad (10.17)$$

SECTION 11

The No-Core Shell Model / Resonating Group Method

The combination of the no-core shell model with the resonating-group method (NCSM/RGM) is an ab-initio technique for the description of nuclear collisions, which has been introduced in Refs. [47] and [48]. It is a microscopic cluster technique using RGM-inspired basis states (10.1). The clusters occurring in each reaction channel are described via eigenstates obtained from the NCSM. Both the interactions between the sub-clusters and the interactions used within the NCSM to obtain the cluster eigenstates are given by realistic Hamiltonians. The NCSM/RGM approach has been successfully applied in various binary-cluster collisions such as nucleon-nucleus scatterings [47, 48, 179], for deuterons scattering off nuclei [180], for the radiative capture reaction ${}^7\text{Be}(p,\gamma){}^8\text{B}$ [181] and ${}^3\text{H}(d,n){}^4\text{He}$, and ${}^3\text{He}(d,p){}^4\text{He}$ fusion reactions [182]. Recently, the NCSM/RGM formalism has been extended to partitions involving three sub-clusters [183]. All these studies were performed using realistic SRG-transformed Hamiltonians at the NN-only level for a particular SRG flow parameter. Thus, neither SRG-induced 3N interactions nor initial 3N contributions have been studied in the NCSM/RGM approach so far.

Throughout this section we generalize the NCSM/RGM formalism to explicitly include 3N Hamiltonians allowing for studies of 3N-force effects on scattering observables from first principles. This brings us in the position to apply the chiral NN+3N Hamiltonians not only in nuclear structure as discussed in Part II, but also in ab-initio predictions of nuclear-reaction observables. At the same time, tests of the chiral NN+3N interactions in the context of nuclear collisions become possible and may reveal valuable information about the quality of modern nuclear forces. The formalism as described in this section allows these investigations also beyond the lightest nuclei. We note that the extension of the NCSM/RGM formalism to include 3N interactions resulted in a collaborative publication recently in Ref. [51], where we presented the first ab-initio study of nucleon- ${}^4\text{He}$ elastic scattering including 3N interactions. In this paper two alternatives for the treatment of the additional terms from 3N interactions are discussed — one using precom-

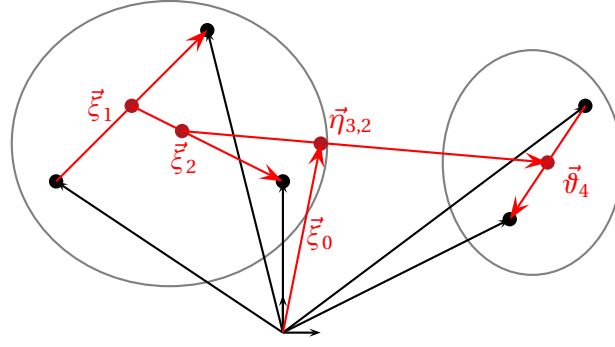


Figure 11.1 – Description of two nucleon sub-clusters by Jacobi coordinates $\vec{\xi}_0, \vec{\xi}_1, \vec{\xi}_2, \vec{\vartheta}_4$ and $\vec{\eta}_{3,2}$, exemplarily for an $A = 5$ system. Black dots denote the nucleons, red dots represent the centers of mass of different sub-systems used for the construction of the Jacobi coordinates. For the mathematical definition of the Jacobi coordinates see Appendix B.

puted coupled densities applicable mainly to targets up to $A = 4$ and one using uncoupled densities computed on-the-fly applicable also to heavier targets. Since we have developed the latter approach we will focus mainly on this variant here, however we will highlight the differences where interesting. We start with the discussion of generalities on the NCSM/RGM formalism following Refs. [47, 48] and [51]. Then, we discuss the derivations of the norm and Hamiltonian kernels in Section 11.2. We summarize the results for all kernels in Section 11.2.4 and discuss the differences compared to the alternative approach mentioned above. Finally, we give the details about the implementation of the kernels in Section 11.2.5.

11.1 General Formalism

The general idea of the binary-cluster NCSM/RGM approach is based on the division of the intrinsic A -body Hilbert space \mathcal{H}_A into three parts

$$\mathcal{H}_A = \mathcal{H}_{A-a} \otimes \mathcal{H}_a \otimes \mathcal{H}_{\text{rel}}. \quad (11.1)$$

Where the $(A - a)$ -body target and the a -body projectile are described within the Hilbert spaces \mathcal{H}_{A-a} and \mathcal{H}_a , respectively. Here we restrict ourselves to the case of binary-cluster systems, however note that NCSM/RGM approach was also successfully formulated and applied for three-cluster systems [183]. The remaining degree of freedom, namely the relative motion of the two nuclear clusters, is considered within the Hilbert space \mathcal{H}_{rel} . Because scattering processes as well as the properties of the nuclei themselves must conform translational invariance, we can safely omit the center-of-mass degrees of freedom of the A -body system from the outset. This means, the center of mass of the A -body system is not considered explicitly, which is accomplished by Jacobi coordinates as shown in Figure 11.1, where $\vec{\xi}_0$ points to the center of mass of the A -body systems and is thus omitted as explained above. Stated differently, the Hilbert spaces in Eq. (11.1) are intended for the

description of intrinsic degrees of freedom of the A -body system only.

For the description of this A -nucleon system by means of the single partition made of two sub-clusters we need a suitable many-body basis. One possible choice are the RGM inspired states [172, 184, 185, 186]

$$|\Phi\rangle = |\Psi_{A-a} E_1 I_1^{\pi_1} T_1\rangle \otimes |\Psi_a E_2 I_2^{\pi_2} T_2\rangle \otimes |rlm\rangle, \quad (11.2)$$

where $|\Psi_{A-a} E_1 I_1^{\pi_1} T_1\rangle$ and $|\Psi_a E_2 I_2^{\pi_2} T_2\rangle$ are translational invariant eigenstates of the target and projectile obtained from the ab-initio (IT-)NCSM with E_i as energy, $I_i^{\pi_i}$ as angular momentum and parity, and T_i as isospin quantum numbers. The state $|rlm\rangle$ describes the relative degree of freedom of the two clusters with quantum numbers for the relative distance r of the two clusters and the corresponding relative orbital angular momentum l and its projection m . In order to reflect the basic symmetries of the nuclear Hamiltonian already in the underlying basis, it is convenient to switch to angular-momentum-coupled basis states. Hence, starting from Eq. (11.2) and coupling the angular momenta of the NCSM eigenstates to the channel spin \hat{s} , and the latter with the orbital angular momentum \hat{l} to the total angular momentum \hat{J} and analogously coupling the isospins to total isospin \hat{T} , we obtain the binary-cluster channel states

$$|\Phi_{\nu r}^{JM\pi TM_T}\rangle = \left[(|\Psi_{A-a} E_1 I_1^{\pi_1} T_1\rangle \otimes |\Psi_a E_2 I_2^{\pi_2} T_2\rangle)^{sT} \otimes |rl\rangle \right]^{JM\pi TM_T}, \quad (11.3)$$

which will span the NCSM/RGM A -body model space. Analogously to Section 10 we collect all discrete quantum numbers in the channel index $\nu = \{A-a, E_1, I_1^{\pi_1}, T_1; a, E_2, I_2^{\pi_2}, T_2; sl\}$ and denote the continuous dependence on r as explicit index. Note that we omit the projection quantum numbers M and M_T for brevity in the following.

We use the binary-cluster channel basis $\{|\Phi_{\nu r}^{J\pi T}\rangle\}$ to expand the partial-wave scattering state on the right-hand side of Eq. (10.6) in analogy to Eq. (10.7)

$$|\Psi^{J\pi T}\rangle = \sum_{\nu} \int dr r^2 \frac{g_{\nu}^{J\pi T}(r)}{r} \hat{\mathcal{A}}_{\nu} |\Phi_{\nu r}^{J\pi T}\rangle, \quad (11.4)$$

where the sum over ν runs over all considered channels and the radial integral accounts for all relative distances in the binary system. The relative-motion wave functions are given by $\frac{g_{\nu}^{J\pi T}(r)}{r} = \langle \Phi_{\nu r}^{J\pi T} | \Psi_{\nu_0}^{J\pi T} \rangle$, i.e., they constitute the overlap between the binary-cluster channel states and the partial-wave scattering state. Of course $|\Psi^{J\pi T}\rangle$ must be fully antisymmetric with respect to particle exchange. The NCSM eigenstates of the projectile and target fulfill this for nucleons within the clusters, and we enforce the antisymmetry with respect to nucleon exchanges between different clusters using the inter-cluster antisymmetrizer

$$\hat{\mathcal{A}}_{\nu} = \sqrt{\frac{(A-a)!a!}{A!}} \sum_i \text{sgn}(\mathcal{P}_i) \mathcal{P}_i \quad (11.5)$$

where the summation covers all permutations \mathcal{P}_i of nucleons belonging to different clusters. To obtain the relative-motion wave functions $g_{\nu}^{J\pi T}(r)$, which are the unknowns in

expansion (11.4), we multiply the stationary many-body Schrödinger equation $\hat{H}|\Psi^{J\pi T}\rangle = E|\Psi^{J\pi T}\rangle$ from the left by $\langle\Phi_{v'r'}^{J\pi T}|\hat{\mathcal{A}}_{v'}$ and obtain

$$\sum_v \int drr^2 [\mathcal{H}_{v'v}^{J\pi T}(r', r) - E \mathcal{N}_{v'v}^{J\pi T}(r', r)] \frac{g_v^{J\pi T}(r)}{r} = 0 \quad (11.6)$$

with the so-called Hamiltonian kernel

$$\mathcal{H}_{v'v}^{J\pi T}(r', r) = \langle\Phi_{v'r'}^{J\pi T}|\hat{\mathcal{A}}_{v'}\hat{H}\hat{\mathcal{A}}_v|\Phi_{vr}^{J\pi T}\rangle \quad (11.7)$$

and norm kernel

$$\mathcal{N}_{v'v}^{J\pi T}(r', r) = \langle\Phi_{v'r'}^{J\pi T}|\hat{\mathcal{A}}_{v'}\hat{\mathcal{A}}_v|\Phi_{vr}^{J\pi T}\rangle. \quad (11.8)$$

The total energy in the center-of-mass frame is denoted by E and the intrinsic microscopic Hamiltonian \hat{H} is decomposed as

$$\hat{H} = \hat{T}_{\text{rel}} + \hat{\mathcal{V}}_{\text{rel}} + \hat{V}_C(\hat{r}) + \hat{H}_{A-a} + \hat{H}_a. \quad (11.9)$$

Here, \hat{T}_{rel} is the kinetic energy of the relative motion of the two clusters, and \hat{H}_{A-a} and \hat{H}_a are the intrinsic Hamiltonians of the target and projectile, respectively, including NN and 3N interactions. In addition we have added and subtracted the average Coulomb interaction between the clusters $\hat{V}_C(\hat{r}) = \frac{Z_{1v}Z_{2v}e^2}{\hat{r}}$ with nuclear charge numbers Z_{1v} and Z_{2v} of the clusters. The subtracted potential $\hat{V}_C(\hat{r})$ is absorbed in the inter-cluster potential $\hat{\mathcal{V}}_{\text{rel}}$, which in addition includes all nuclear interactions between nucleons belonging to different clusters and is given by

$$\begin{aligned} \hat{\mathcal{V}}_{\text{rel}} = & \sum_{i=1}^{A-a} \sum_{j=A-a+1}^A \frac{e^2(1 + \hat{\tau}_{3,i})(1 + \hat{\tau}_{3,j})}{4|\hat{r}_i - \hat{r}_j|} - \frac{1}{(A-a)a} \hat{V}_C(\hat{r}) + \hat{V}_{ij}^{\text{NN}} \\ & + \sum_{i<j=1}^{A-a} \sum_{k=A-a+1}^A \hat{V}_{ijk}^{3\text{N}} + \sum_{i=1}^{A-a} \sum_{j<k=A-a+1}^A \hat{V}_{ijk}^{3\text{N}}, \end{aligned} \quad (11.10)$$

where $\hat{\tau}_{3,i}$ denotes the three-component of the isospin operator. The subtraction of the average Coulomb potential cancels the leading $\frac{1}{r}$ contribution of the point Coulomb interaction and, thus, leads to an $\frac{1}{r^2}$ behavior of the overall Coulomb contribution in $\hat{\mathcal{V}}_{\text{rel}}$ [48] resulting in a localized $\hat{\mathcal{V}}_{\text{rel}}$, which is important for the description of the asymptotic scattering states by Coulomb functions, i.e., to obtain well-defined phase shifts (see Section 12). As before, we denote the NN interaction as \hat{V}^{NN} and the 3N force as $\hat{V}^{3\text{N}}$. We present the derivation of explicit formulas for the norm and Hamiltonian kernels as well as details of their implementation in the next subsection. The extension of the formalism to 3N interactions will give rise to two new contributions in addition to the well-known NN kernels, however also for the NN kernels we will introduce a new computational scheme compared to the one in Refs. [47, 48].

Having computed the kernels (11.7) and (11.8), our remaining task is to solve Eq. (11.6).

It is important to note that the relative-motion wave functions $g_v^{J\pi T}(r)$ are not usual Schrödinger wave functions because of the nonorthogonality of the basis. Nevertheless, they obey the same asymptotic boundary conditions as Schrödinger wave functions, since the nonorthogonality is of short range, i.e., typically the norm kernel $\mathcal{N}_{v'v}^{J\pi T}(r, r')$ practically vanishes for relative distances larger than 3 fm as discussed in detail in Ref. [48]. But the radial motion wave functions $g_v^{J\pi T}(r)$ are affected at small distances by this nonorthogonality, and consequently one has to be careful when using these wave functions for calculations of observables, e.g., transition matrix elements. To avoid this complication we introduce the orthogonalized version of the NCSM/RGM equations (11.6) by multiplying with the inverse square root of the norm kernel $\mathcal{N}^{-\frac{1}{2}}$ from the left and inserting a identity matrix in terms of $\mathcal{N}^{-\frac{1}{2}}\mathcal{N}^{\frac{1}{2}}$. We obtain

$$\sum_v \int dr r^2 \left[\mathbb{H}_{v'v}^{J\pi T}(r, r') - E \delta_{v'v} \frac{\delta(r-r')}{r'r} \right] \frac{\chi_v^{J\pi T}(r)}{r} = 0. \quad (11.11)$$

where the Hermitian nonlocal orthogonalized Hamiltonian kernel is given as

$$\mathbb{H}_{v'v}^{J\pi T}(r', r) = \sum_{\gamma'} \int dy' y'^2 \sum_{\gamma} \int dy y^2 \mathcal{N}_{v'\gamma'}^{-\frac{1}{2}}(r', y') \mathcal{H}_{\gamma'\gamma}^{J\pi T}(y', y) \mathcal{N}_{\gamma v}^{-\frac{1}{2}}(y, r) \quad (11.12)$$

and the new unknowns $\chi_v^{J\pi T}(r)$ are related to the original relative-motion wave functions by

$$\frac{\chi_v^{J\pi T}(r)}{r} = \sum_{\gamma} \int dy y^2 \mathcal{N}_{v\gamma}^{\frac{1}{2}}(r, y) \frac{g_{\gamma}^{J\pi T}(y)}{y}, \quad (11.13)$$

and accordingly

$$\frac{g_v^{J\pi T}(r)}{r} = \sum_{\gamma} \int dy y^2 \mathcal{N}_{v\gamma}^{-\frac{1}{2}}(r, y) \frac{\chi_{\gamma}^{J\pi T}(y)}{y}. \quad (11.14)$$

In addition, the orthogonalized channel states $|\xi_{vr}^{J\pi T}\rangle$ are given in terms of the original ones of Eq. (11.3) by

$$|\xi_{vr}^{J\pi T}\rangle = \sum_{\gamma} \int dy y^2 \mathcal{N}_{v\gamma}^{-\frac{1}{2}}(r, y) \hat{\mathcal{A}}_{\gamma} |\Phi_{\gamma y}^{J\pi T}\rangle. \quad (11.15)$$

For the calculation of the square roots of the norm kernel and also for the derivation of the kernel formulas in the next section we define the HO channel states by

$$\begin{aligned} |\Phi_{vr}^{J\pi T}\rangle &= \sum_n^{N_{\max}} \left[(|\Psi_{A-a} E_1 I_1^{\pi_1} T_1\rangle \otimes |\Psi_a E_2 I_2^{\pi_2} T_2\rangle)^{sT} \otimes |nl\rangle \right]^{J\pi T} R_{nl}(r, b) \\ &\doteq \sum_n^{N_{\max}} R_{nl}(r, b) |\Phi_{vn,b}^{J\pi T}\rangle, \end{aligned} \quad (11.16)$$

where we expand the state describing the relative motion of the nuclear clusters $|rlm\rangle$ in

a set of HO eigenstates $|nlm\rangle$ yielding the HO radial wave functions as expansion coefficients $\langle nl'm'|rlm\rangle = R_{nl}(r)\delta_{l'l}\delta_{m'm}$. The truncation N_{\max} of this expansion is performed consistently with the truncation of the HO model space used in the NCSM calculations of the sub-cluster eigenstates. Of course, the convergence of this expansion needs to be checked, however, it is valid as long as the involved operators are localized. We introduced in Eq. (11.16) the notation $|\Phi_{v_n,b}^{J\pi T}\rangle$ for the binary-cluster channel states using an HO eigenstate for the description of the relative motion. Here $b = \sqrt{\hbar/\mu\Omega} = \sqrt{A/A-1}b_0$ represents the HO length with $b_0 = \sqrt{\hbar/m_N\Omega}$ and the reduced mass $\mu = \frac{A-1}{A}m_N$. We will drop the HO length b as label in the HO channel states in the following for brevity.

The (inverse) square roots of the norm kernel matrix can be computed using the relation of the coordinate-space norm kernel to the norm kernel within the truncated HO model space

$$\mathcal{N}_{v'v}^{J\pi T}(r',r) = \delta_{v'v} \left[\frac{\delta(r'-r)}{r'r} - \sum_n R_{nl}(r')R_{nl}(r) \right] + \sum_{n'n}^{N_{\max}} R_{n'l'}(r')\Lambda_{v'n'v_n}^{J\pi T} R_{nl}(r). \quad (11.17)$$

The second term is the convolution of the HO model-space norm kernel whose matrix elements are denoted by $\Lambda_{v'n'v_n}^{J\pi T} = \langle \Phi_{v'n'}^{J\pi T} | \mathcal{A}^2 | \Phi_{v_n}^{J\pi T} \rangle$ and the first term is a correction due the finite size of the HO model space.

The (inverse) square roots of the norm kernel in the HO model space are then computed as usual by diagonalizing the HO norm kernel matrix and then using the eigenvalues $\lambda_{\Gamma}^{\pm\frac{1}{2}}$ and eigenvectors $|\varphi_{\Gamma}^{J\pi T}\rangle$ to obtain their spectral representation

$$\Lambda_{v'n'v_n}^{\pm\frac{1}{2}} = \sum_{\Gamma} \langle \Phi_{v'n'}^{J\pi T} | \varphi_{\Gamma}^{J\pi T} \rangle \lambda_{\Gamma}^{\pm\frac{1}{2}} \langle \varphi_{\Gamma}^{J\pi T} | \Phi_{v_n}^{J\pi T} \rangle. \quad (11.18)$$

Then the (inverse) square roots are in analogy to Eq. (11.17) given by

$$\mathcal{N}_{v'v}^{\pm\frac{1}{2}}(r',r) = \delta_{v'v} \left[\frac{\delta(r'-r)}{r'r} - \sum_n R_{nl}(r')R_{nl}(r) \right] + \sum_{n'n} R_{n'l'}(r')\Lambda_{v'n'v_n}^{\pm\frac{1}{2}} R_{nl}(r), \quad (11.19)$$

where one has to exclude the Pauli-forbidden states with $\lambda_{\Gamma}=0$ for the inverse operation to be well-defined [48]. Inserting this last equation and Eq. (11.12) in Eq. (11.11) we can cast the system of coupled differential equations into the form

$$\left[-\frac{\hbar^2}{2\mu} \frac{\partial^2}{\partial r'^2} + \frac{\hbar^2 l(l+1)}{r'^2} + \bar{V}_C(r') - (E - E_{v'}^{J_1^{\pi_1} T_1}) \right] \frac{\chi_{v'}^{J\pi T}(r')}{r'} + \sum_v \int dr r^2 W_{v'v}^{J\pi T}(r',r) \frac{\chi_v^{J\pi T}(r)}{r} = 0 \quad (11.20)$$

where all nonlocal terms are collected in the potential $W_{v'v}^{J\pi T}(r',r)$ and $E_{v'}^{J_1^{\pi_1} T_1}$ denotes the energy eigenvalue of the target within channel v' .

Having developed the general formalism to arrive at Eq. (11.20), the path towards scattering observables is a two-step process: first we need to compute the norm and Hamiltonian kernels, which is the computationally most demanding task. We discuss the corre-

sponding details in the next subsection. The second step is the actual solution of Eq. (11.20) for which we utilize the technique of the R -matrix formalism, as discussed in Section 12.

11.2 The Norm and Hamiltonian Kernels

In this section we present the derivation of the norm and Hamiltonian kernels including NN+3N interactions, and afterwards give details about their implementation. From now on we restrict ourselves to the single-nucleon projectiles, i.e., $a = 1$. All calculations addressed later on have been done in the single-nucleon formalism. Of course this leads to some simplifications, however, the generalizations to $a \geq 1$ are straight forward and can be found for the case of NN interactions in Ref. [180].

11.2.1 Derivation of the Kernels

As first consequence of the restriction to single-nucleon projectiles we can simplify the inter-cluster antisymmetrizer to

$$\mathcal{A} = \frac{1}{\sqrt{A}} \left(1 - \sum_{i=1}^{A-1} \hat{T}_{i,A} \right), \quad (11.21)$$

where we dropped the index ν for brevity. Hence, the squared antisymmetrizer which we will employ for the derivation of the kernels is given as

$$\begin{aligned} \mathcal{A}^2 &= \frac{1}{A} \left(1 - \sum_{i=1}^{A-1} \hat{T}_{i,A} \right) \left(1 - \sum_{i'=1}^{A-1} \hat{T}_{i',A} \right) \\ &= \frac{1}{A} \left(1 - 2 \sum_{i=1}^{A-1} \hat{T}_{i,A} + \sum_{i=1}^{A-1} \sum_{i'=1}^{A-1} \hat{T}_{i,A} \hat{T}_{i',A} \right) \\ &= \frac{1}{A} \left(1 - 2 \sum_{i=1}^{A-1} \hat{T}_{i,A} + \sum_{i=1}^{A-1} \hat{T}_{i,A} \hat{T}_{i,A} + \sum_{i'=1}^{A-1} \sum_{i \neq i'}^{A-1} \hat{T}_{i,A} \hat{T}_{i',A} \right) \\ &= \frac{1}{A} \left(1 - 2 \sum_{i=1}^{A-1} \hat{T}_{i,A} + (A-1) + \sum_{i'=1}^{A-1} \hat{T}_{i',A} \sum_{i \neq i'}^{A-1} \hat{T}_{i',i} \right) \\ &= \frac{1}{A} \left(1 - 2 \sum_{i=1}^{A-1} \hat{T}_{i,A} + (A-1) + (2-A) \sum_{i'=1}^{A-1} \hat{T}_{i',A} \right) \\ &= 1 - \sum_{i=1}^{A-1} \hat{T}_{i,A}. \end{aligned} \quad (11.22)$$

To facilitate the kernel derivation we note that the binary-cluster channel states in the single-nucleon formalism simplify to

$$|\Phi_{\nu r}^{J\pi T}\rangle = \left[\left(|\Psi_{A-a} E_1 I_1^{\pi_1} T_1\rangle \otimes |\Psi_1 \frac{1}{2} \frac{1}{2}\rangle \right)^{sT} \otimes |rl\rangle \right]^{J\pi T}. \quad (11.23)$$

Furthermore, for all terms in the kernels that originate from transpositions (see Eq. (11.22)) as well as for computing the matrix elements $\langle \Phi_{\nu' r'}^{J\pi T} | \mathcal{V}_{\text{rel}} | \Phi_{\nu r}^{J\pi T} \rangle$ we use the expansion (11.16)

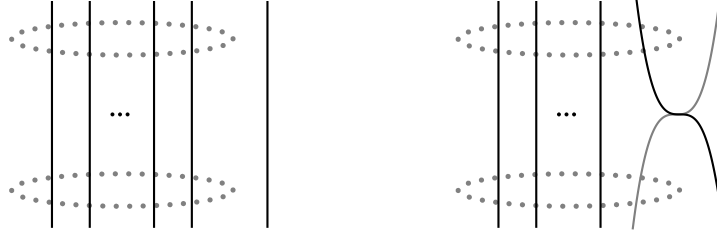


Figure 11.2 – Pictorial illustration of the direct (left) and exchange (right) contributions to the norm kernel. The dotted circled line emphasizes the $(A - 1)$ -nucleon cluster, i.e., the target. The separated line represents the projectile, here for the special case of the single-nucleon formalism. The lower ends of the lines represent the initial, the upper ends the final states, respectively.

in HO channel states. The HO channel states in the single-nucleon projectile formalism are given by

$$|\Phi_{v_n}^{J\pi T}\rangle = \left[(|\Psi_{A-a} E_1 I_1^{\pi_1} T_1\rangle \otimes |\Psi_1 \frac{1}{2} \frac{1}{2}\rangle)^{sT} \otimes |nl\rangle \right]^{J\pi T}. \quad (11.24)$$

We use Eqs. (11.22), (11.23) and (11.16) to convert the integral kernels into a more convenient form for the subsequent derivations. We find for the norm kernel

$$\mathcal{N}_{v'v}^{J\pi T}(r', r) = \langle \Phi_{v'r'}^{J\pi T} | \hat{\mathcal{A}}^2 | \Phi_{vr}^{J\pi T} \rangle = \langle \Phi_{v'r'}^{J\pi T} | (1 - \sum_{i=1}^{A-1} \hat{T}_{i,A}) | \Phi_{vr}^{J\pi T} \rangle \quad (11.25)$$

$$= \delta_{v'v} \frac{\delta(r' - r)}{r'r} - (A-1) \sum_{n'n} R_{n'l'}(r') R_{nl}(r) \langle \Phi_{v'n'}^{J\pi T} | \hat{T}_{A-1,A} | \Phi_{vn}^{J\pi T} \rangle \quad (11.26)$$

$$\doteq \delta_{v'v} \frac{\delta(r' - r)}{r'r} + \mathcal{N}_{v'v}^{\text{exchange}}(r', r), \quad (11.27)$$

where we exploit the fact that the $(A - 1)$ nucleons are treated as indistinguishable particles and consequently all transpositions of the projectile with any nucleon within the target yield identical contributions. The last line represents the typical decomposition of the norm kernel into a direct contribution, which stems from the identical permutation contained in $\hat{\mathcal{A}}$, and a so-called exchange term, $\mathcal{N}_{v'v}^{\text{exchange}}(r', r)$, which collects all other contributions. A pictorial illustration of the norm kernel is shown in Figure 11.2. The lines represent the nucleons, where their lower end correspond to the initial states and the upper ends to the final states. The lines that are encircled by the dashed circled line represent the target nucleons, whereas the separated single line denotes the single projectile nucleon. The exchange part of the norm kernel is represented by the right diagram that highlights the exchange of one nucleon from the target with the projectile one.

More involved due the presence of the nuclear interactions, but using similar arguments we can rewrite the Hamiltonian kernel. First we make use of the commutator of the inter-cluster antisymmetrizer with the A -body Hamiltonian $[\hat{\mathcal{A}}, \hat{H}] = 0$ and then distinguish between terms where eigenvalue relations are applicable and terms where the

inter-cluster potential \mathcal{V}_{rel} contributes. The latter are further split into terms including NN interactions denoted by $\mathcal{V}_{v'v}^{\text{NN}}(r', r)$, and into terms including 3N interactions denoted by $\mathcal{V}_{v'v}^{\text{3N}}(r', r)$. We obtain

$$\begin{aligned} \mathcal{H}_{v'v}^{J\pi T}(r', r) &= \langle \Phi_{v'r'}^{J\pi T} | \hat{H} \hat{\mathcal{Q}}^2 | \Phi_{vr}^{J\pi T} \rangle = \langle \Phi_{v'r'}^{J\pi T} | \hat{H} (1 - \sum_{i=1}^{A-1} \hat{T}_{i,A}) | \Phi_{vr}^{J\pi T} \rangle \\ &= \langle \Phi_{v'r'}^{J\pi T} | (\hat{T}_{\text{rel}} + \bar{V}_C(\hat{r}) + \hat{H}_{A-1} + \mathcal{V}_{\text{rel}}) (1 - \sum_{i=1}^{A-1} \hat{T}_{i,A}) | \Phi_{vr}^{J\pi T} \rangle \\ &= (T_{\text{rel}} + \bar{V}_C(r') + E_{v'}^{I_1^{\pi_1} T_1'}) N_{v'v}^{J\pi T}(r', r) + \mathcal{V}_{v'v}^{\text{NN}}(r', r) + \mathcal{V}_{v'v}^{\text{3N}}(r', r), \end{aligned} \quad (11.28)$$

where $E_{v'}^{I_1^{\pi_1} T_1}$ is the eigenenergy of the target eigenstate and we also used the eigenvalue relation for the average Coulomb potential. In addition, we use the coordinate space representation of the relative kinetic energy of the sub-clusters

$$T_{\text{rel}} = -\frac{\hbar^2}{2\mu} \frac{1}{r'} \frac{\partial^2}{\partial r'^2} r' + \frac{\hbar^2 l'(l'+1)}{2\mu r'^2}. \quad (11.29)$$

We note that the Hamiltonian kernel as defined in Eq. (11.28) is non-Hermitian. For the solution of the radial equation we use the Hermetized Hamiltonian kernel

$$\bar{\mathcal{H}}_{v'v}^{J\pi T}(r', r) = \langle \Phi_{v'r'}^{J\pi T} | \hat{\mathcal{Q}} \hat{H} \hat{\mathcal{Q}} | \Phi_{vr}^{J\pi T} \rangle = \langle \Phi_{v'r'}^{J\pi T} | H - \frac{1}{2} \sum_i (\hat{T}_{iA} \hat{H} + \hat{H} \hat{T}_{iA}) | \Phi_{vr}^{J\pi T} \rangle, \quad (11.30)$$

which in practice can be obtained by adding of Eq. (11.28) to itself with exchanged bra and ket states [48]. Note that the total contribution of the average Coulomb potential to the Hermitian Hamiltonian kernel is given by [48]

$$\frac{1}{2} \delta_{v'v} (\bar{V}_C(r') + \bar{V}_C(r)) \left[\frac{\delta(r' - r)}{r'r} - \sum_n R_{nl}(r') R_{nl}(r) \right], \quad (11.31)$$

and follows from the fact that the subtracted average Coulomb part is hidden in the interaction kernel, which is expanded in the HO basis.

For further investigations of the part of the Hamiltonian kernel containing the two-body interaction part,

$$\mathcal{V}_{v'v}^{\text{NN}}(r', r) = \langle \Phi_{v'r'}^{J\pi T} | \sum_{j=1}^{A-1} \hat{V}_{jA} (1 - \sum_{i=1}^{A-1} \hat{T}_{i,A}) | \Phi_{vr}^{J\pi T} \rangle, \quad (11.32)$$

we split this expression into three parts:

(i) first term

$$\begin{aligned}
 & \langle \Phi_{v'r'}^{J\pi T} | \sum_{j=1}^{A-1} \hat{V}_{jA} | \Phi_{vr}^{J\pi T} \rangle \\
 &= (A-1) \langle \Phi_{v'r'}^{J\pi T} | \hat{V}_{A-1A} | \Phi_{vr}^{J\pi T} \rangle \\
 &= (A-1) \sum_{n'n} R_{n'l'}(r') R_{nl}(r) \langle \Phi_{v'n'}^{J\pi T} | \hat{V}_{A-1A} | \Phi_{vn}^{J\pi T} \rangle
 \end{aligned} \tag{11.33}$$

(ii) second term for $j = i$

$$\begin{aligned}
 & - \langle \Phi_{v'r'}^{J\pi T} | \sum_{i=1}^{A-1} \hat{V}_{iA} \sum_{j=1}^{A-1} \hat{T}_{j,A} \delta_{j,i} | \Phi_{vr}^{J\pi T} \rangle \\
 &= - \langle \Phi_{v'r'}^{J\pi T} | \sum_{i=1}^{A-1} \hat{V}_{iA} \hat{T}_{i,A} | \Phi_{vr}^{J\pi T} \rangle \\
 &= -(A-1) \sum_{n'n} R_{n'l'}(r') R_{nl}(r) \langle \Phi_{v'n'}^{J\pi T} | \hat{V}_{A-1A} \hat{T}_{A-1,A} | \Phi_{vn}^{J\pi T} \rangle
 \end{aligned} \tag{11.34}$$

(iii) second term for $j \neq i$

$$\begin{aligned}
 & - \langle \Phi_{v'r'}^{J\pi T} | \sum_{i=1}^{A-1} \hat{V}_{iA} \sum_{j=1, j \neq i}^{A-1} \hat{T}_{j,A} | \Phi_{vr}^{J\pi T} \rangle \\
 &= -(A-1) \langle \Phi_{v'r'}^{J\pi T} | \sum_{i=1}^{A-2} \hat{V}_{iA} \hat{T}_{A-1,A} | \Phi_{vr}^{J\pi T} \rangle \\
 &= -(A-1)(A-2) \sum_{n'n} R_{n'l'}(r') R_{nl}(r) \langle \Phi_{v'n'}^{J\pi T} | \hat{V}_{A-2A} \hat{T}_{A-1,A} | \Phi_{vn}^{J\pi T} \rangle.
 \end{aligned} \tag{11.35}$$

The contributions are collected into a direct NN potential kernel given by Eqs. (11.33) and (11.34)

$$\gamma_{v'v}^{\text{NN, direct}}(r', r) = (A-1) \sum_{n'n} R_{n'l'}(r') R_{nl}(r) \langle \Phi_{v'n'}^{J\pi T} | \hat{V}_{A-1A} (1 - \hat{T}_{A-1,A}) | \Phi_{vn}^{J\pi T} \rangle, \tag{11.36}$$

and an exchange NN potential kernel defined by Eq. (11.35)

$$\gamma_{v'v}^{\text{NN, exchange}}(r', r) = -(A-1)(A-2) \sum_{n'n} R_{n'l'}(r') R_{nl}(r) \langle \Phi_{v'n'}^{J\pi T} | \hat{V}_{A-2A} \hat{T}_{A-1,A} | \Phi_{vn} \rangle. \tag{11.37}$$

A diagrammatic illustration of the NN potential kernel can be found in Figure 11.3. The general pattern is the same as for the norm kernel, the additional red dashed line connects the interacting nucleons.

Analogously we consider the contribution of the 3N interaction to the potential kernel. As a consequence of the single-nucleon projectile only the first term of the 3N interaction in Eq (11.10) contributes, and yields

$$\langle \Phi_{v'r'}^{J\pi T} | \sum_{j < k} \hat{V}_{jkA} \mathcal{E}^2 | \Phi_{vr}^{J\pi T} \rangle = \langle \Phi_{v'r'}^{J\pi T} | \sum_{j < k} \hat{V}_{jkA} [1 - \sum_{i=1}^{A-1} \hat{T}_{iA}] | \Phi_{vr}^{J\pi T} \rangle, \tag{11.38}$$

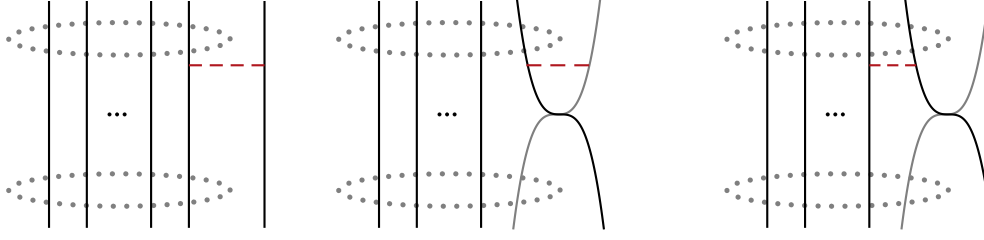


Figure 11.3 – Pictorial illustration of the direct (first two) and exchange (right) contributions to the NN interaction kernel. The red-dashed line connects the interacting nucleons. The remaining illustrations are identical to Figure 11.2

which we split into four parts:

(i) first term

$$\begin{aligned}
 & \langle \Phi_{v'r'}^{J\pi T} | \sum_{i < j} \hat{V}_{ijA} | \Phi_{vr}^{J\pi T} \rangle \\
 &= \frac{(A-1)(A-2)}{2} \langle \Phi_{v'r'}^{J\pi T} | \hat{V}_{A-2A-1A} | \Phi_{vr}^{J\pi T} \rangle \\
 &= \frac{(A-1)(A-2)}{2} \sum_{n'n} R_{n'l'}(r') R_{nl}(r) \langle \Phi_{v'n'}^{J\pi T} | \hat{V}_{A-2A-1A} | \Phi_{vn}^{J\pi T} \rangle
 \end{aligned} \tag{11.39}$$

where we again used the internal symmetry of the target state and, therefore, obtain identical contributions leading to the prefactor $\frac{(A-2)(A-1)}{2}$, equal to the number of nucleon-pairs in the target. In the second term of Eq. (11.38) we distinguish the following three cases

(ii) $i \neq j \wedge i \neq k$

$$\begin{aligned}
 & -\langle \Phi_{v'r'}^{J\pi T} | \sum_{j < k} \hat{V}_{j k A} \sum_{i=1, i \neq j, k}^{A-1} \hat{T}_{iA} | \Phi_{vr}^{J\pi T} \rangle \\
 &= -(A-1) \langle \Phi_{v'r'}^{J\pi T} | \sum_{j < k}^{A-2} \hat{V}_{j k A} \hat{T}_{A-1A} | \Phi_{vr}^{J\pi T} \rangle \\
 &= -\frac{(A-1)(A-2)(A-3)}{2} \sum_{n'n} R_{n'l'}(r') R_{nl}(r) \langle \Phi_{v'n'}^{J\pi T} | \hat{V}_{A-3A-2A} \hat{T}_{A-1A} | \Phi_{vn}^{J\pi T} \rangle,
 \end{aligned} \tag{11.40}$$

(iii) $i = j$

$$\begin{aligned}
 & -\langle \Phi_{v'r'}^{J\pi T} | \sum_{j < k} \hat{V}_{j k A} \hat{T}_{jA} | \Phi_{vr}^{J\pi T} \rangle \\
 &= -\frac{(A-1)(A-2)}{2} \langle \Phi_{v'r'}^{J\pi T} | \hat{V}_{A-2A-1A} \hat{T}_{A-2A} | \Phi_{vr}^{J\pi T} \rangle \\
 &= -\frac{(A-1)(A-2)}{2} \sum_{n'n} R_{n'l'}(r') R_{nl}(r) \langle \Phi_{v'n'}^{J\pi T} | \hat{V}_{A-2A-1A} \hat{T}_{A-2A} | \Phi_{vn}^{J\pi T} \rangle,
 \end{aligned} \tag{11.41}$$

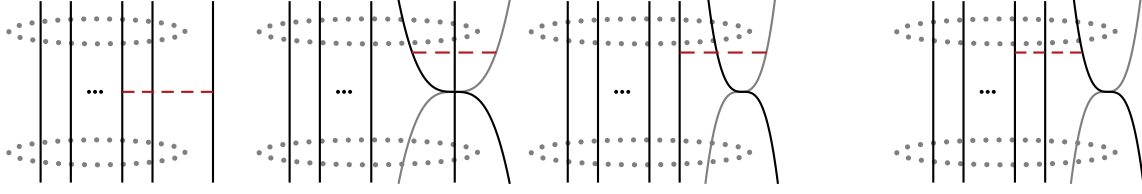


Figure 11.4 – Pictorial illustration of the direct (first three) and exchange (right) contributions to the 3N interaction kernel. The remaining illustrations are identical to Figure 11.3

(iv) $i = k$

$$\begin{aligned}
 & -\langle \Phi_{v'r'}^{J\pi T} | \sum_{j < k}^{A-1} \hat{V}_{jkA} \hat{T}_{jA} | \Phi_{vr}^{J\pi T} \rangle \\
 & = -\frac{(A-1)(A-2)}{2} \langle \Phi_{v'r'}^{J\pi T} | \hat{V}_{A-1A-2A} \hat{T}_{A-1A} | \Phi_{vr}^{J\pi T} \rangle \\
 & = -\frac{(A-1)(A-2)}{2} \sum_{n'n} R_{n'l'}(r') R_{nl}(r) \langle \Phi_{v'n'}^{J\pi T} | \hat{V}_{A-1A-2A} \hat{T}_{A-1A} | \Phi_{vn}^{J\pi T} \rangle.
 \end{aligned} \tag{11.42}$$

We collect the contributions of Eqs. (11.39), (11.41), and (11.42) in the direct 3N potential kernel

$$\gamma_{v'v}^{3N, \text{direct}}(r', r) = (A-1) \sum_{n'n} R_{n'l'}(r') R_{nl}(r) \langle \Phi_{v'n'}^{J\pi T} | \hat{V}_{A-2,A-1,A} (1 - \hat{T}_{A-1,A} - \hat{T}_{A-2,A}) | \Phi_{vn}^{J\pi T} \rangle, \tag{11.43}$$

and Eq.(11.40) represents the exchange 3N potential kernel

$$\gamma_{v'v}^{3N, \text{exchange}}(r', r) = -\frac{(A-1)(A-2)}{2} \sum_{n'n} R_{n'l'}(r') R_{nl}(r) \langle \Phi_{v'n'}^{J\pi T} | \hat{V}_{A-1,A-2,A} \hat{T}_{A-1,A} | \Phi_{vn}^{J\pi T} \rangle. \tag{11.44}$$

The diagrams corresponding to the 3N potential kernel can be found in Figure 11.4.

11.2.2 Slater Determinant Channel States and Translational Invariant Kernels

All presented kernels have one common structure which needs to be evaluated, namely matrix elements of a translational invariant operator \hat{O} with respect to the HO binary-channel states $\langle \Phi_{v'n'}^{J\pi T} | \hat{O} | \Phi_{vn}^{J\pi T} \rangle$. The basis states $|\Phi_{vn}^{J\pi T}\rangle$ as defined in the previous section are translational invariant. This implies that in particular the target eigenstates can be obtained by diagonalization using an NCSM model space spanned by HO Jacobi-coordinate basis states, as described in Section 4.1. However, the properties of the HO allow to recover the translational invariant kernels in spite of using an NCSM model space spanned by standard HO Slater determinant basis states that include center-of-mass degrees of freedom. We will exploit this because of two reasons: the computation of target eigenstates beyond the lightest nuclei can be done much more efficiently using the HO Slater determinant basis because its antisymmetrization is straight forward, while the antisym-

metrization becomes inefficient for the Jacobi HO basis for $A > 4$ due to the demanding computation of the coefficients of fractional parentage. Furthermore, also the computation and derivation of the kernel formulas is simpler when using the HO Slater determinant basis, because we can make use of second-quantization techniques. We briefly review the recipe to obtain the translational invariant kernels from those computed with respect to HO Slater determinants. Afterwards we use the latter for the derivation of the norm and Hamiltonian kernels.

The so-called Slater determinant channel states in the single-nucleon projectile formalism read

$$|\Phi_{vn}^{\mathcal{J}\pi T}\rangle_{\text{SD}} = |\Psi_{A-a} E_1 I_1^{\pi_1} T_1\rangle |N_{cm}^{A-1}=0, L_{cm}^{A-1}=0\rangle \otimes |\Psi_1 \frac{1}{2} \frac{1}{2}\rangle \otimes |\frac{I_A}{\sqrt{A}} \ell\rangle \quad (11.45)$$

$$= |\Psi_{A-a} E_1 I_1^{\pi_1} T_1\rangle |N_{cm}^{A-1}=0, L_{cm}^{A-1}=0\rangle \otimes |\Psi_1 \frac{1}{2} \frac{1}{2}\rangle \otimes |\frac{I_A}{\sqrt{A}} \ell\rangle, \quad (11.46)$$

with the factorization of the Slater determinant NCSM target eigenstate denoted by the subscript SD is given by

$$|\Psi_{A-a} I_1^{\pi_1} M_1 T_1 M_{T_1}\rangle_{\text{SD}} = |\Psi_{A-a} I_1^{\pi_1} M_1 T_1 M_{T_1}\rangle |N_{cm}^{A-1}=0, L_{cm}^{A-1}=0, M_L^{A-1}=0\rangle, \quad (11.47)$$

which is a consequence of the N_{max} -truncation scheme as discussed in Section 4.1. We note that the couplings shown in Eqs. (11.45) and (11.46) are equivalent due to the fact that the center-of-mass part of the target eigenstate is forced to be in its HO ground state. To arrive at the translational-invariant kernels from those obtained with respect to the states (11.45) we need a link between the two different bases. Therefore, we start from the states (11.46) and transform the center-of-mass coordinates \vec{r}_A and $\vec{R}_{cm}^{A-1} = \frac{1}{\sqrt{A-1}} \sum_{i=1}^{A-1} \vec{r}_i$ of the target and projectile, by means of an orthogonal transformation into the center-of-mass coordinate of the A -body system

$$\vec{\xi}_0 = \sqrt{\frac{A-1}{A}} \vec{R}_{cm}^{A-1} + \frac{\vec{r}_A}{\sqrt{A}} \quad (11.48)$$

and the relative coordinate between the two sub-clusters

$$\vec{\eta}_{A-1} = \sqrt{\frac{1}{A}} \vec{R}_{cm}^{A-1} - \sqrt{\frac{A-1}{A}} \vec{r}_A. \quad (11.49)$$

This transformation of the underlying coordinate system is accomplished using so-called generalized Harmonic-Oscillator Brackets (HOBs) denoted by $\langle\langle \dots | \dots \rangle\rangle_d$ (see [94, 187] for

details) with parameter $d = \frac{1}{A-1}$, yielding

$$\begin{aligned}
 |\Phi_{vn}^{\mathcal{J}\pi T}\rangle_{\text{SD}} &= \sum_{nl(\vec{\eta})} \sum_{\mathcal{N}\mathcal{L}(\vec{\xi}_0)} \langle \langle nl(\vec{\eta}), \mathcal{N}\mathcal{L}(\vec{\xi}_0); \ell | 00, nl(\vec{r}_A) \rangle \rangle \frac{1}{A-1} \\
 &\times |\Psi_{A-a} E_1 I_1^{\pi_1} T_1\rangle \otimes |\Psi_1 \frac{1}{2} \frac{1}{2}\rangle |nl(\vec{\eta})\rangle \otimes |\mathcal{N}\mathcal{L}(\vec{\xi}_0)\rangle. \quad (11.50)
 \end{aligned}$$

The vectors in the parenthesis after the orbital angular momentum quantum numbers indicate the coordinates used to define the orbital angular-momentum operators.

In a second step, we recouple the angular momenta with help of $6j$ -symbols and obtain

$$\begin{aligned}
 |\Phi_{vn}^{\mathcal{J}\pi T}\rangle_{\text{SD}} &= \sum_{nl(\vec{\eta})} \sum_{\mathcal{N}\mathcal{L}(\vec{\xi}_0)} \sum_J \langle \langle nl(\vec{\eta}), \mathcal{N}\mathcal{L}(\vec{\xi}_0); \ell | 00, nl(\vec{r}_A) \rangle \rangle \frac{1}{A-1} \hat{f}\hat{\ell}(-1)^{s+l(\vec{\eta})+\mathcal{L}(\vec{\xi}_0)+\mathcal{J}} \\
 &\times \left\{ \begin{array}{ccc} s & l(\vec{\eta}) & J \\ \mathcal{L}(\vec{\xi}_0) & \mathcal{J} & \ell \end{array} \right\} |\Psi_{A-a} E_1 I_1^{\pi_1} T_1\rangle \otimes |\Psi_1 \frac{1}{2} \frac{1}{2}\rangle |nl(\vec{\eta})\rangle \otimes |\mathcal{N}\mathcal{L}(\vec{\xi}_0)\rangle \\
 &= \sum_{nl(\vec{\eta})} \sum_{\mathcal{N}\mathcal{L}(\vec{\xi}_0)} \sum_J \langle \langle nl(\vec{\eta}), \mathcal{N}\mathcal{L}(\vec{\xi}_0); \ell | 00, nl(\vec{r}_A) \rangle \rangle \frac{1}{A-1} \hat{f}\hat{\ell}(-1)^{s+l(\vec{\eta})+\mathcal{L}(\vec{\xi}_0)+\mathcal{J}} \\
 &\times \left\{ \begin{array}{ccc} s & l(\vec{\eta}) & J \\ \mathcal{L}(\vec{\xi}_0) & \mathcal{J} & \ell \end{array} \right\} |\Phi_{vn}^{J\pi T}\rangle_{\mathcal{N}\mathcal{L}(\vec{\xi}_0)}, \quad (11.51)
 \end{aligned}$$

where we recognize the translational invariant channel states in the last line. With help of Eq. (11.51) we can relate the translational invariant kernels to those obtained with respect to the Slater determinant channel basis via

$$\begin{aligned}
 {}_{\text{SD}} \langle \Phi_{v'n'}^{\mathcal{J}\pi T} | \hat{O} | \Phi_{vn}^{\mathcal{J}\pi T} \rangle_{\text{SD}} &= \\
 &\sum_{nl(\vec{\eta})} \sum_{n'l'(\vec{\eta})} \sum_J \sum_{\mathcal{N}\mathcal{L}(\vec{\xi}_0)} \\
 &\times \langle \langle nl(\vec{\eta}), \mathcal{N}\mathcal{L}(\vec{\xi}_0); \ell | 00, n'l'(\vec{r}_A) \rangle \rangle \frac{1}{A-1} \langle \langle n'l'(\vec{\eta}), \mathcal{N}\mathcal{L}(\vec{\xi}_0); \ell | 00, n'l'(\vec{r}_A) \rangle \rangle \frac{1}{A-1} \\
 &\times (-1)^{s+s'+l(\vec{\eta})+l'(\vec{\eta})+2\mathcal{J}} \hat{f}^2 \hat{\ell} \hat{\ell}' \left\{ \begin{array}{ccc} s & l(\vec{\eta}) & J \\ \mathcal{L}(\vec{\xi}_0) & \mathcal{J} & \ell(\vec{r}_A) \end{array} \right\} \left\{ \begin{array}{ccc} s' & l'(\vec{\eta}) & J \\ \mathcal{L}(\vec{\xi}_0) & \mathcal{J} & \ell'(\vec{r}_A) \end{array} \right\} \\
 &\times \langle \Phi_{v'n'}^{J\pi T} | \hat{O} | \Phi_{vn}^{J\pi T} \rangle. \quad (11.52)
 \end{aligned}$$

It is evident that inverting this relation, which can be managed by a matrix inversion, allows to obtain the translational invariant kernel matrix elements from those computed in the Slater determinant channel basis. This is convenient as both, the derivation of the kernel formulas and their actual computation is done more easily starting from the Slater

determinant channel states. Note that all partial-wave states of the Slater-determinant channel basis do contribute to each partial wave of the translational invariant basis. This strategy to recover the translational invariant kernels can be applied also to projectiles with $a > 1$ as described for instance in Ref. [48].

11.2.3 Integration Kernels in the Slater Determinant Channel Basis

Having the ability to transform the Slater determinant basis kernels into the translational invariant ones, the remaining task is then to derive the kernel formulas that are suitable for implementation. Foremost, we once more change the angular-momentum couplings of the SD channel basis according to

$$|\Phi_{vn}^{\mathcal{J}\pi T}\rangle_{\text{SD}} = \sum_j (-1)^{I_1 + \mathcal{J} + j} \hat{s} \hat{j} \begin{Bmatrix} I_1 & \frac{1}{2} & s \\ \ell & \mathcal{J} & j \end{Bmatrix} |\epsilon_{vn}^{\mathcal{J}\pi T}\rangle_{\text{SD}} \quad (11.53)$$

with the states

$$|\epsilon_{vn}^{\mathcal{J}\pi T}\rangle_{\text{SD}} = |\Psi_{A-a} E_1 I_1^{\pi_1} T_1\rangle_{\text{SD}} \otimes |\Psi_1 \frac{1}{2} \frac{1}{2}\rangle |n\ell(\vec{r}_A)\rangle, \quad (11.54)$$

which sets the starting point for the different derivations in the following.

We begin with the investigation of the norm kernel

$$\begin{aligned} {}_{\text{SD}} \langle \epsilon_{v'n'}^{\mathcal{J}\pi T} | \hat{T}_{A-1,A} | \epsilon_{vn}^{\mathcal{J}\pi T} \rangle_{\text{SD}} = \\ \sum_{M_1 m_j} \sum_{M_{T_1} m_t} \sum_{M'_1 m'_j} \sum_{M'_{T_1} m'_t} \begin{pmatrix} I_1 & j \\ M_1 & m_j \end{pmatrix} \begin{pmatrix} T_1 & \frac{1}{2} \\ M_{T_1} & m_t \end{pmatrix} \begin{pmatrix} I'_1 & j' \\ M'_1 & m'_j \end{pmatrix} \begin{pmatrix} T'_1 & \frac{1}{2} \\ M'_{T_1} & m'_t \end{pmatrix} \\ \times {}_{\text{SD}} \langle \Psi_{A-1} E'_1 I_1^{\pi'_1} M'_1 T'_1 M'_{T_1} | \langle n'\ell'j'm_j \frac{1}{2} m_t | \hat{T}_{A-1,A} | \Psi_{A-1} E_1 I_1^{\pi_1} M_1 T_1 M_{T_1} \rangle_{\text{SD}} | n\ell j m_j \frac{1}{2} m_t \rangle, \end{aligned} \quad (11.55)$$

by decoupling the angular momenta \vec{I}_i of the target and the projectile \vec{j} as well as their isospins. In the following, we omit the isospin quantum numbers in the single-particle states of the projectile, and the parity of the target states π_1 and π'_1 for brevity.

Thus, we are left with

$$\begin{aligned}
 & {}_{\text{SD}}\langle\Psi_{A-1}E'_1I'_1M'_1T'_1M_{T'_1}|\langle n'\ell'j'm_jm_t|\hat{T}_{A-1,A}|\Psi_{A-1}E_1I_1M_1T_1M_{T_1}\rangle_{\text{SD}}|n\ell jm_jm_t\rangle \\
 &= \sum_{\alpha_1\dots\alpha_A}\sum_{\alpha'_1\dots\alpha'_A} {}_{\text{SD}}\langle\Psi_{A-1}E'_1I'_1M'_1T'_1M_{T'_1}|\langle n'\ell'j'm_jm_t|\alpha'_1\dots\alpha'_A\rangle \\
 &\quad \times \langle\alpha'_1\dots\alpha'_A|\hat{T}_{A-1,A}|\alpha_1\dots\alpha_A\rangle\langle\alpha_1\dots\alpha_A|\Psi_{A-1}E_1I_1M_1T_1M_{T_1}\rangle_{\text{SD}}|n\ell jm_jm_t\rangle \\
 &= \sum_{\alpha_1\dots\alpha_A}\sum_{\alpha'_{A-1}\alpha'_A} {}_{\text{SD}}\langle\Psi_{A-1}E'_1I'_1M'_1T'_1M_{T'_1}|\langle n'\ell'j'm_jm_t|\alpha_1\dots\alpha_{A-2}\alpha'_{A-1}\alpha'_A\rangle \\
 &\quad \times \langle\alpha'_{A-1}\alpha'_A|\alpha_A\alpha_{A-1}\rangle\langle\alpha_1\dots\alpha_A|\Psi_{A-1}E_1I_1M_1T_1M_{T_1}\rangle_{\text{SD}}|n\ell jm_jm_t\rangle \\
 &= \frac{1}{(A-1)!}\sum_{\alpha_1\dots\alpha_A} {}_{\text{SD}}\langle\Psi_{A-1}E'_1I'_1M'_1T'_1M_{T'_1}|\alpha_1\dots\alpha_{A-2}\alpha_A\rangle_a\langle n'\ell'j'm_jm_t|\alpha_{A-1}\rangle \\
 &\quad \times {}_a\langle\alpha_1\dots\alpha_{A-1}|\Psi_{A-1}E_1I_1M_1T_1M_{T_1}\rangle_{\text{SD}}\langle\alpha_A|n\ell jm_jm_t\rangle \\
 &= \frac{1}{(A-1)!}\sum_{\alpha_1\dots\alpha_{A-2}} {}_{\text{SD}}\langle\Psi_{A-1}E'_1I'_1M'_1T'_1M_{T'_1}|\hat{a}^\dagger_{n\ell jm_jm_t}|\alpha_1\dots\alpha_{A-2}\rangle_a \\
 &\quad \times {}_a\langle\alpha_1\dots\alpha_{A-2}|\hat{a}_{n'\ell'j'm'_jm'_t}|\Psi_{A-1}E_1I_1M_1T_1M_{T_1}\rangle_{\text{SD}} \\
 &= \frac{1}{A-1} {}_{\text{SD}}\langle\Psi_{A-1}E'_1I'_1M'_1T'_1M_{T'_1}|\hat{a}^\dagger_{n\ell jm_jm_t}\hat{a}_{n'\ell'j'm'_jm'_t}|\Psi_{A-1}E_1I_1M_1T_1M_{T_1}\rangle_{\text{SD}}. \tag{11.56}
 \end{aligned}$$

We started by inserting the A -body identity operators consisting of product states of HO $l s$ -coupled single-particle states $|\alpha_i\rangle$

$$\hat{\mathbb{1}} = \sum_{\alpha_1\dots\alpha_A} |\alpha_1\dots\alpha_A\rangle\langle\alpha_1\dots\alpha_A| \tag{11.57}$$

on both sides of the transposition operator. We have explicitly performed the transposition, used the orthogonality relations of the HO single-particle states and made use of the antisymmetry of the target eigenstates which automatically projects the $(A-1)$ -portion of the HO product states on $(A-1)$ -body Slater determinants. Then we have introduced the creation and annihilation operators \hat{a}^\dagger and \hat{a} , respectively, with respect to HO single-particle states, which leads to the one-body density matrix. The final step was then to use the identity

$$\frac{1}{(A-2)!} = \sum_{\alpha_1\dots\alpha_{A-2}} |\alpha_1\dots\alpha_{A-2}\rangle_a {}_a\langle\alpha_1\dots\alpha_{A-2}|. \tag{11.58}$$

We continue with the derivation of the NN interaction kernels which is done with respect to the states $|\Psi_{A-1}E_1I_1M_1T_1M_{T_1}\rangle_{\text{SD}}|n\ell jm_jm_t\rangle$, too. The angular-momentum couplings can be accounted afterwards and are identical to those in Eq. (11.55). As we will see, it is useful to stick to the splitting into the direct and exchange NN kernels for the derivation. We start with the direct contributions and follow essentially the same procedure as

described above

$$\begin{aligned}
 & \langle \Psi'_{A-1} E'_1 I'_1 M'_1 T'_1 M'_T | \langle n' \ell' j' m'_j m'_t | \hat{V}_{A-1A} (1 - \hat{T}_{A-1,A}) | \Psi_{A-1} E_1 I_1 M_1 T_1 M_T \rangle | n \ell j m_j m_t \rangle \\
 &= \sum_{\alpha_1 \alpha_2 \dots \alpha_A} \sum_{\alpha'_{A-1} \alpha'_A} \langle \Psi_{A-1} E_1 I_1 M_1 T_1 M_T | \langle n' \ell' j' m'_j m'_t | \alpha_1 \alpha_2 \dots \alpha_A \rangle \\
 & \quad \times \langle \alpha_1 \alpha_2 \dots \alpha_A | \hat{V}_{A-1A} (1 - \hat{T}_{A-1,A}) | \alpha_1 \alpha_2 \dots \alpha_A \rangle \\
 & \quad \times \langle \alpha_1 \alpha_2 \dots \alpha_{A-2} \alpha'_{A-1} \alpha'_A | \Psi_{A-1} E_1 I_1 M_1 T_1 M_T \rangle | n \ell j m_j m_t \rangle \\
 &= \sum_{\alpha_1 \alpha_2 \dots \alpha_A} \sum_{\alpha'_{A-1} \alpha'_A} \langle \Psi'_{A-1} E'_1 I'_1 M'_1 T'_1 M'_T | \alpha_1 \alpha_2 \dots \alpha_{A-1} \rangle \delta_{n' \ell' j' m'_j m'_t, \alpha_A} \\
 & \quad \times \langle \alpha_1 \alpha_2 \dots \alpha_A | \hat{V}_{A-1A} (1 - \hat{T}_{A-1,A}) | \alpha_1 \alpha_2 \dots \alpha_{A-2} \alpha'_{A-1} \alpha'_A \rangle \\
 & \quad \times \langle \alpha_1 \alpha_2 \dots \alpha_{A-2} \alpha'_{A-1} | \Psi_{A-1} E_1 I_1 M_1 T_1 M_T \rangle \delta_{\alpha'_A, n \ell j m_j m_t} \\
 &= \frac{1}{(A-1)!} \sum_{\alpha_1 \alpha_2 \dots \alpha_{A-1}} \sum_{\alpha'_{A-1}} \langle \Psi'_{A-1} E'_1 I'_1 M'_1 T'_1 M'_T | \alpha_1 \alpha_2 \dots \alpha_{A-1} \rangle_a \\
 & \quad \times \langle \alpha_{A-1} n' \ell' j' m'_j m'_t | \hat{V}_{A-1A} (1 - \hat{T}_{A-1,A}) | \alpha'_{A-1} n \ell j m_j m_t \rangle \\
 & \quad \times {}_a \langle \alpha_1 \alpha_2 \dots \alpha_{A-2} \alpha'_{A-1} | \Psi_{A-1} E_1 I_1 M_1 T_1 M_T \rangle \\
 &= \frac{1}{(A-1)!} \sum_{\alpha_1 \alpha_2 \dots \alpha_{A-2}} \sum_{\alpha_{A-1}} \sum_{\alpha'_{A-1}} \\
 & \quad \times \langle \Psi'_{A-1} E'_1 I'_1 M'_1 T'_1 M'_T | \hat{a}_{\alpha_{A-1}}^\dagger | \alpha_1 \alpha_2 \dots \alpha_{A-2} \rangle_a {}_a \langle \alpha_1 \alpha_2 \dots \alpha_{A-2} | \hat{a}_{\alpha'_{A-1}} | \Psi_{A-1} E_1 I_1 M_1 T_1 M_T \rangle \\
 & \quad \times \langle \alpha_{A-1} n' \ell' j' m'_j m'_t | \hat{V}_{A-1A} (1 - \hat{T}_{A-1,A}) | \alpha'_{A-1} n \ell j m_j m_t \rangle \\
 &= \frac{1}{A-1} \sum_{\alpha_{A-1}} \sum_{\alpha'_{A-1}} \\
 & \quad \times \langle \Psi'_{A-1} E'_1 I'_1 M'_1 T'_1 M'_T | \hat{a}_{\alpha_{A-1}}^\dagger \hat{a}_{\alpha'_{A-1}} | \Psi_{A-1} E_1 I_1 M_1 T_1 M_T \rangle \\
 & \quad \times \langle \alpha_{A-1} n' \ell' j' m'_j m'_t | \hat{V}_{A-1A} (| \alpha'_{A-1} n \ell j m_j m_t \rangle - | n \ell j m_j m_t \alpha'_{A-1} \rangle) \\
 &= \frac{1}{A-1} \sum_{\alpha_{A-1}} \sum_{\alpha'_{A-1}} \\
 & \quad \times \langle \Psi'_{A-1} E'_1 I'_1 M'_1 T'_1 M'_T | \hat{a}_{\alpha_{A-1}}^\dagger \hat{a}_{\alpha'_{A-1}} | \Psi_{A-1} E_1 I_1 M_1 T_1 M_T \rangle \\
 & \quad \times {}_a \langle \alpha_{A-1} n' \ell' j' m'_j m'_t | \hat{V} | \alpha'_{A-1} n \ell j m_j m_t \rangle_a. \tag{11.59}
 \end{aligned}$$

In the last step used that the antisymmetrizer is idempotent and

$$\begin{aligned}
 & \langle \alpha_{A-1} n' \ell' j' m'_j m'_t | \hat{V} (| \alpha'_{A-1} n \ell j m_j m_t \rangle - | n \ell j m_j m_t \alpha'_{A-1} \rangle) \\
 &= \sqrt{2} \langle \alpha_{A-1} n' \ell' j' m'_j m'_t | \mathcal{A} \hat{V} | \alpha'_{A-1} n \ell j m_j m_t \rangle_a \\
 &= {}_a \langle \alpha_{A-1} n' \ell' j' m'_j m'_t | \hat{V} | \alpha'_{A-1} n \ell j m_j m_t \rangle_a \tag{11.60}
 \end{aligned}$$

to arrive at the antisymmetric two-body states.

Also the derivation of the exchange NN kernel follows the same lines, however the identification of antisymmetric two-body states is less obvious

$$\begin{aligned}
 & {}_{\text{SD}} \langle \Psi'_{A-1} E'_1 I'_1 M'_1 T'_1 M'_{T_1} | \langle n' \ell' j' m'_j m'_t | \hat{V}_{A-2A} \hat{T}_{A-1,A} | \Psi_{A-1} E_1 I_1 M_1 T_1 M_{T_1} \rangle_{\text{SD}} | n \ell j m_j m_t \rangle \\
 &= \sum_{\alpha_1 \dots \alpha_A} \sum_{\alpha'_{A-2} \alpha'_{A-1}} \sum_{\alpha'_A} {}_{\text{SD}} \langle \Psi'_{A-1} E'_1 I'_1 M'_1 T'_1 M'_{T_1} | \langle n' \ell' j' m'_j m'_t | \alpha_1 \dots \alpha_A \rangle \\
 &\quad \times \langle \alpha_1 \dots \alpha_A | \hat{V}_{A-2A} \hat{T}_{A-1,A} | \alpha_1 \dots \alpha_{A-3} \alpha'_{A-2} \alpha'_{A-1} \alpha'_A \rangle \\
 &\quad \times \langle \alpha_1 \dots \alpha_{A-3} \alpha'_{A-2} \alpha'_{A-1} \alpha'_A | \Psi_{A-1} E_1 I_1 M_1 T_1 M_{T_1} \rangle_{\text{SD}} | n \ell j m_j m_t \rangle \\
 &= \sum_{\alpha_1 \dots \alpha_A} \sum_{\alpha'_{A-2} \alpha'_{A-1}} \sum_{\alpha'_A} {}_{\text{SD}} \langle \Psi'_{A-1} E'_1 I'_1 M'_1 T'_1 M'_{T_1} | \alpha_1 \dots \alpha_{A-1} \rangle \delta_{n' \ell' j' m'_j m'_t, \alpha_A} \\
 &\quad \times \langle \alpha_{A-2} \alpha_{A-1} \alpha_A | \hat{V}_{A-2A} | \alpha'_{A-2} \alpha'_{A-1} \alpha'_A \rangle \delta_{\alpha'_A, n \ell j m_j m_t} \\
 &\quad \times \langle \alpha_1 \dots \alpha_{A-3} \alpha'_{A-2} \alpha'_{A-1} | \Psi_{A-1} E_1 I_1 M_1 T_1 M_{T_1} \rangle_{\text{SD}} \\
 &= \sum_{\alpha_1 \dots \alpha_{A-1}} \sum_{\alpha'_{A-2} \alpha'_{A-1}} {}_{\text{SD}} \langle \Psi'_{A-1} E'_1 I'_1 M'_1 T'_1 M'_{T_1} | \alpha_1 \dots \alpha_{A-1} \rangle \\
 &\quad \times \langle \alpha_{A-2} \alpha_{A-1} n' \ell' j' m'_j m'_t | \hat{V}_{A-2A} | \alpha'_{A-2} n \ell j m_j m_t \alpha'_{A-1} \rangle \\
 &\quad \times \langle \alpha_1 \dots \alpha_{A-3} \alpha'_{A-2} \alpha'_{A-1} | \Psi_{A-1} E_1 I_1 M_1 T_1 M_{T_1} \rangle_{\text{SD}} \delta_{\alpha_{A-1}, n \ell j m_j m_t} \\
 &= \sum_{\alpha_1 \dots \alpha_{A-2}} \sum_{\alpha'_{A-2} \alpha'_{A-1}} {}_{\text{SD}} \langle \Psi'_{A-1} E'_1 I'_1 M'_1 T'_1 M'_{T_1} | \alpha_1 \dots n \ell j m_j m_t \rangle \\
 &\quad \times \langle \alpha_{A-2} n' \ell' j' m'_j m'_t | \hat{V}_{A-2A} | \alpha'_{A-2} \alpha'_{A-1} \rangle \langle \alpha_1 \dots \alpha_{A-3} \alpha'_{A-2} \alpha'_{A-1} | \Psi_{A-1} E_1 I_1 M_1 T_1 M_{T_1} \rangle_{\text{SD}} \\
 &= \frac{1}{(A-1)!} \sum_{\alpha_1 \dots \alpha_{A-2}} \sum_{\alpha'_{A-2} \alpha'_{A-1}} \\
 &\quad \times {}_{\text{SD}} \langle \Psi'_{A-1} E'_1 I'_1 M'_1 T'_1 M'_{T_1} | \hat{a}_{n \ell j m_j m_t}^\dagger \hat{a}_{\alpha_{A-2}}^\dagger | \alpha_1 \dots \alpha_{A-3} \rangle_a \\
 &\quad \times {}_a \langle \alpha_1 \dots \alpha_{A-3} | \hat{a}_{\alpha'_{A-2}} \hat{a}_{\alpha'_{A-1}} | \Psi_{A-1} E_1 I_1 M_1 T_1 M_{T_1} \rangle_{\text{SD}} \\
 &\quad \times \langle \alpha_{A-2} n' \ell' j' m'_j m'_t | \hat{V}_{A-2A} | \alpha'_{A-2} \alpha'_{A-1} \rangle \\
 &= \frac{1}{2(A-1)(A-2)} \sum_{\alpha_{A-2}} \sum_{\alpha'_{A-2} \alpha'_{A-1}} \\
 &\quad \times {}_{\text{SD}} \langle \Psi'_{A-1} E'_1 I'_1 M'_1 T'_1 M'_{T_1} | \hat{a}_{n \ell j m_j m_t}^\dagger \hat{a}_{\alpha_{A-2}}^\dagger \hat{a}_{\alpha'_{A-2}} \hat{a}_{\alpha'_{A-1}} | \Psi_{A-1} E_1 I_1 M_1 T_1 M_{T_1} \rangle_{\text{SD}} \\
 &\quad \times {}_a \langle \alpha_{A-2} n' \ell' j' m'_j m'_t | \hat{V}_{A-2A} | \alpha'_{A-2} \alpha'_{A-1} \rangle_a .
 \end{aligned} \tag{11.61}$$

The trick to end up with antisymmetric two-body states is to rename two indices which are summed, and introduce the factor $\frac{1}{2}$. We show the similar step in detail in the case of the 3N exchange kernel.

Now we come to the derivation of the kernels involving the 3N interactions. Again we consider the terms contributing to the direct kernels together, because this facilitates the use of 3N matrix elements with respect to antisymmetric 3N states. We obtain for the direct

3N contribution

$$\begin{aligned}
 & {}_{\text{SD}} \langle \Psi'_{A-1} E'_1 I'_1 M'_1 T'_1 M'_T | \langle n' \ell' j' m'_j m'_t | \hat{V}_{A-2A-1A} (1 - \hat{T}_{A-1,A} - \hat{T}_{A-2,A}) | \Psi_{A-1} E_1 I_1 M_1 T_1 M_T \rangle_{\text{SD}} | n \ell j m_j m_t \rangle \\
 &= \sum_{\alpha_1 \dots \alpha_A} \sum_{\alpha'_{A-2}} \sum_{\alpha'_{A-1}} \sum_{\alpha'_A} \\
 & \quad \times {}_{\text{SD}} \langle \Psi'_{A-1} E'_1 I'_1 M'_1 T'_1 M'_T | \langle n' \ell' j' m'_j m'_t | \alpha_1 \dots \alpha_A \rangle \\
 & \quad \times \langle \alpha_1 \dots \alpha_A | \hat{V}_{A-2A-1A} (1 - \hat{T}_{A-1,A} - \hat{T}_{A-2,A}) | \alpha_1 \dots \alpha_{A-3} \alpha'_{A-2} \alpha'_{A-1} \alpha'_A \rangle \\
 & \quad \times \langle \alpha_1 \dots \alpha_{A-3} \alpha'_{A-2} \alpha'_{A-1} \alpha'_A | \Psi_{A-1} E_1 I_1 M_1 T_1 M_T \rangle_{\text{SD}} | n \ell j m_j m_t \rangle \\
 &= \sum_{\alpha_1 \dots \alpha_A} \sum_{\alpha'_{A-2}} \sum_{\alpha'_{A-1}} \sum_{\alpha'_A} \\
 & \quad \times {}_{\text{SD}} \langle \Psi'_{A-1} E'_1 I'_1 M'_1 T'_1 M'_T | \alpha_1 \dots \alpha_{A-1} \rangle \delta_{\alpha_A, n' \ell' j' m'_j m'_t} \\
 & \quad \times \langle \alpha_{A-2} \alpha_{A-1} \alpha_A | \hat{V} (1 - \hat{T}_{A-1,A} - \hat{T}_{A-2,A}) | \alpha'_{A-2} \alpha'_{A-1} \alpha'_A \rangle \\
 & \quad \times \langle \alpha_1 \dots \alpha_{A-3} \alpha'_{A-2} \alpha'_{A-1} | \Psi_{A-1} E_1 I_1 M_1 T_1 M_T \rangle_{\text{SD}} \delta_{\alpha'_A, n \ell j m_j m_t} \\
 &= \frac{1}{(A-1)!} \sum_{\alpha_1 \dots \alpha_{A-1}} \sum_{\alpha'_{A-2}} \sum_{\alpha'_{A-1}} \\
 & \quad \times {}_{\text{SD}} \langle \Psi'_{A-1} E'_1 I'_1 M'_1 T'_1 M'_T | \alpha_1 \dots \alpha_{A-1} \rangle_a \\
 & \quad \times \langle \alpha_{A-2} \alpha_{A-1} n' \ell' j' m'_j m'_t | \hat{V} (1 - \hat{T}_{A-1,A} - \hat{T}_{A-2,A}) | \alpha'_{A-2} \alpha'_{A-1} n \ell j m_j m_t \rangle \\
 & \quad \times {}_a \langle \alpha_1 \dots \alpha_{A-3} \alpha'_{A-2} \alpha'_{A-1} | \Psi_{A-1} E_1 I_1 M_1 T_1 M_T \rangle_{\text{SD}} \\
 &= \frac{1}{(A-1)!} \sum_{\alpha_1 \dots \alpha_{A-1}} \sum_{\alpha'_{A-2}} \sum_{\alpha'_{A-1}} \\
 & \quad \times {}_{\text{SD}} \langle \Psi'_{A-1} E'_1 I'_1 M'_1 T'_1 M'_T | \hat{a}_{\alpha_{A-1}}^\dagger \hat{a}_{\alpha_{A-2}}^\dagger | \alpha_1 \dots \alpha_{A-3} \rangle_a \\
 & \quad \times {}_a \langle \alpha_1 \dots \alpha_{A-3} | \hat{a}_{\alpha'_{A-2}} \hat{a}_{\alpha'_{A-1}} | \Psi_{A-1} E_1 I_1 M_1 T_1 M_T \rangle_{\text{SD}} \\
 & \quad \times \langle \alpha_{A-2} \alpha_{A-1} n' \ell' j' m'_j m'_t | \hat{V} (1 - \hat{T}_{A-1,A} - \hat{T}_{A-2,A}) | \alpha'_{A-2} \alpha'_{A-1} n \ell j m_j m_t \rangle \\
 &= \frac{1}{(A-1)(A-2)} \sum_{\alpha_{A-2}} \sum_{\alpha_{A-1}} \sum_{\alpha'_{A-2}} \sum_{\alpha'_{A-1}} \\
 & \quad \times {}_{\text{SD}} \langle \Psi'_{A-1} E'_1 I'_1 M'_1 T'_1 M'_T | \hat{a}_{\alpha_{A-1}}^\dagger \hat{a}_{\alpha_{A-2}}^\dagger \hat{a}_{\alpha'_{A-2}} \hat{a}_{\alpha'_{A-1}} | \Psi_{A-1} E_1 I_1 M_1 T_1 M_T \rangle_{\text{SD}} \\
 & \quad \times \langle \alpha_{A-2} \alpha_{A-1} n' \ell' j' m'_j m'_t | \hat{V} (| \alpha'_{A-2} \alpha'_{A-1} n \ell j m_j m_t \rangle - | \alpha'_{A-2} n \ell j m_j m_t \alpha'_{A-1} \rangle \\
 & \quad - | n \ell j m_j m_t \alpha'_{A-1} \alpha'_{A-2} \rangle) \\
 &= \frac{1}{(A-1)(A-2)} \sum_{\alpha_{A-2}} \sum_{\alpha_{A-1}} \sum_{\alpha'_{A-2}} \sum_{\alpha'_{A-1}} \\
 & \quad \times \frac{1}{2} \left[{}_{\text{SD}} \langle \Psi'_{A-1} E'_1 I'_1 M'_1 T'_1 M'_T | \hat{a}_{\alpha_{A-1}}^\dagger \hat{a}_{\alpha_{A-2}}^\dagger \hat{a}_{\alpha'_{A-2}} \hat{a}_{\alpha'_{A-1}} | \Psi_{A-1} E_1 I_1 M_1 T_1 M_T \rangle_{\text{SD}} \right. \\
 & \quad \times \langle \alpha_{A-2} \alpha_{A-1} n' \ell' j' m'_j m'_t | \hat{V} (| \alpha'_{A-2} \alpha'_{A-1} n \ell j m_j m_t \rangle - | \alpha'_{A-2} n \ell j m_j m_t \alpha'_{A-1} \rangle \\
 & \quad - | n \ell j m_j m_t \alpha'_{A-1} \alpha'_{A-2} \rangle) \\
 & \quad \left. + \langle \Psi'_{A-1} E'_1 I'_1 M'_1 T'_1 M'_T | \hat{a}_{\alpha_{A-1}}^\dagger \hat{a}_{\alpha_{A-2}}^\dagger \hat{a}_{\alpha'_{A-1}} \hat{a}_{\alpha'_{A-2}} | \Psi_{A-1} E_1 I_1 M_1 T_1 M_T \rangle_{\text{SD}} \right. \\
 & \quad \times \langle \alpha_{A-2} \alpha_{A-1} n' \ell' j' m'_j m'_t | \hat{V} (| \alpha'_{A-1} \alpha'_{A-2} n \ell j m_j m_t \rangle - | \alpha'_{A-1} n \ell j m_j m_t \alpha'_{A-2} \rangle \\
 & \quad \left. - | n \ell j m_j m_t \alpha'_{A-2} \alpha'_{A-1} \rangle) \right]
 \end{aligned}$$

$$\begin{aligned}
 &= \frac{1}{2(A-1)(A-2)} \sum_{\alpha_{A-2}} \sum_{\alpha_{A-1}} \sum_{\alpha'_{A-2}} \sum_{\alpha'_{A-1}} \\
 &\quad \times_{\text{SD}} \langle \Psi'_{A-1} E'_1 I'_1 M'_1 T'_1 M'_{T_1} | \hat{a}_{\alpha_{A-1}}^\dagger \hat{a}_{\alpha_{A-2}}^\dagger \hat{a}_{\alpha'_{A-2}} \hat{a}_{\alpha'_{A-1}} | \Psi_{A-1} E_1 I_1 M_1 T_1 M_{T_1} \rangle_{\text{SD}} \\
 &\quad \times \langle \alpha_{A-2} \alpha_{A-1} n' \ell' j' m'_j m'_t | \hat{V} (| \alpha'_{A-2} \alpha'_{A-1} n \ell j m_j m_t \rangle - | \alpha'_{A-2} n \ell j m_j m_t \alpha'_{A-1} \rangle \\
 &\quad - | n \ell j m_j m_t \alpha'_{A-1} \alpha'_{A-2} \rangle - | \alpha'_{A-1} \alpha'_{A-2} n \ell j m_j m_t \rangle + | \alpha'_{A-1} n \ell j m_j m_t \alpha'_{A-2} \rangle \\
 &\quad + | n \ell j m_j m_t \alpha'_{A-2} \alpha'_{A-1} \rangle) \\
 &= \frac{1}{2(A-1)(A-2)} \sum_{\alpha_{A-2}} \sum_{\alpha_{A-1}} \sum_{\alpha'_{A-2}} \sum_{\alpha'_{A-1}} \\
 &\quad \times_{\text{SD}} \langle \Psi'_{A-1} E'_1 I'_1 M'_1 T'_1 M'_{T_1} | \hat{a}_{\alpha_{A-1}}^\dagger \hat{a}_{\alpha_{A-2}}^\dagger \hat{a}_{\alpha'_{A-2}} \hat{a}_{\alpha'_{A-1}} | \Psi_{A-1} E_1 I_1 M_1 T_1 M_{T_1} \rangle_{\text{SD}} \\
 &\quad \times \langle \alpha_{A-2} \alpha_{A-1} n' \ell' j' m'_j m'_t | \hat{V} | \alpha'_{A-2} \alpha'_{A-1} n \ell j m_j m_t \rangle_a \sqrt{6} \\
 &= \frac{1}{2(A-1)(A-2)} \sum_{\alpha_{A-2}} \sum_{\alpha_{A-1}} \sum_{\alpha'_{A-2}} \sum_{\alpha'_{A-1}} \\
 &\quad \times_{\text{SD}} \langle \Psi'_{A-1} E'_1 I'_1 M'_1 T'_1 M'_{T_1} | \hat{a}_{\alpha_{A-1}}^\dagger \hat{a}_{\alpha_{A-2}}^\dagger \hat{a}_{\alpha'_{A-2}} \hat{a}_{\alpha'_{A-1}} | \Psi_{A-1} E_1 I_1 M_1 T_1 M_{T_1} \rangle_{\text{SD}} \\
 &\quad \times_a \langle \alpha_{A-2} \alpha_{A-1} n' \ell' j' m'_j m'_t | \hat{V} | \alpha'_{A-2} \alpha'_{A-1} n \ell j m_j m_t \rangle_a
 \end{aligned} \tag{11.62}$$

Finally, the derivation of the exchange 3N kernel reads

$$\begin{aligned}
 & {}_{\text{SD}} \langle \Psi'_{A-1} E'_1 I'_1 M'_1 T'_1 M'_T | \langle n' \ell' j' m'_j m'_t | \hat{V}_{A-3A-2A} \hat{T}_{A-1,A} | \Psi_{A-1} E_1 I_1 M_1 T_1 M_T \rangle_{\text{SD}} | n \ell j m_j \frac{1}{2} m_t \rangle \\
 &= \sum_{\alpha_1 \dots \alpha_A} \sum_{\alpha'_{A-3} \dots \alpha'_A} \\
 & \quad \times {}_{\text{SD}} \langle \Psi'_{A-1} E'_1 I'_1 M'_1 T'_1 M'_T | \langle n' \ell' j' m'_j m'_t | \alpha_1 \dots \alpha_A \rangle \langle \alpha_1 \dots \alpha_A | \hat{V}_{A-3A-2A} \hat{T}_{A-1,A} \\
 & \quad \times | \alpha_1 \dots \alpha_{A-4} \alpha'_{A-3} \dots \alpha'_A \rangle \langle \alpha_1 \dots \alpha_{A-4} \alpha'_{A-3} \dots \alpha'_A | \Psi_{A-1} E_1 I_1 M_1 T_1 M_T \rangle_{\text{SD}} | n \ell j m_j m_t \rangle \\
 &= \sum_{\alpha_1 \dots \alpha_A} \sum_{\alpha'_{A-3} \dots \alpha'_A} \\
 & \quad \times {}_{\text{SD}} \langle \Psi'_{A-1} E'_1 I'_1 M'_1 T'_1 M'_T | \alpha_1 \dots \alpha_{A-1} \rangle \delta_{n' \ell' j' m'_j m'_t, \alpha_A} \\
 & \quad \times \langle \alpha_{A-3} \alpha_{A-2} \alpha_{A-1} \alpha_A | \hat{V}_{A-3A-2A} | \alpha'_{A-3} \alpha'_{A-2} \alpha'_A \alpha'_{A-1} \rangle \delta_{\alpha_{A-1}, \alpha'_A} \\
 & \quad \times \langle \alpha_1 \dots \alpha_{A-4} \alpha'_{A-3} \dots \alpha'_{A-1} | \Psi_{A-1} E_1 I_1 M_1 T_1 M_T \rangle_{\text{SD}} \delta_{n \ell j m_j m_t, \alpha'_A} \\
 &= \sum_{\alpha_1 \dots \alpha_{A-2}} \sum_{\alpha'_{A-3} \dots \alpha'_{A-1}} \\
 & \quad \times {}_{\text{SD}} \langle \Psi'_{A-1} E'_1 I'_1 M'_1 T'_1 M'_T | \alpha_1 \dots \alpha_{A-2} n \ell j m_j m_t \rangle \\
 & \quad \times \langle \alpha_{A-3} \alpha_{A-2} n' \ell' j' m'_j m'_t | \hat{V}_{A-3A-2A} | \alpha'_{A-3} \alpha'_{A-2} \alpha'_{A-1} \rangle \\
 & \quad \times \langle \alpha_1 \dots \alpha_{A-4} \alpha'_{A-3} \dots \alpha'_{A-1} | \Psi_{A-1} E_1 I_1 M_1 T_1 M_T \rangle_{\text{SD}} \\
 &= \frac{1}{(A-1)!} \sum_{\alpha_1 \dots \alpha_{A-2}} \sum_{\alpha'_{A-3} \dots \alpha'_{A-1}} \\
 & \quad \times {}_{\text{SD}} \langle \Psi'_{A-1} E'_1 I'_1 M'_1 T'_1 M'_T | \alpha_1 \dots \alpha_{A-2} n \ell j m_j m_t \rangle_a \langle \alpha_1 \dots \alpha_{A-4} \alpha'_{A-3} \dots \alpha'_{A-1} | \Psi_{A-1} E_1 I_1 M_1 T_1 M_T \rangle_{\text{SD}} \\
 & \quad \times \langle \alpha_{A-3} \alpha_{A-2} n' \ell' j' m'_j m'_t | \hat{V}_{A-3A-2A} | \alpha'_{A-3} \alpha'_{A-2} \alpha'_{A-1} \rangle \\
 &= \frac{1}{(A-1)!} \sum_{\alpha_1 \dots \alpha_{A-2}} \sum_{\alpha'_{A-3} \dots \alpha'_{A-1}} \\
 & \quad \times {}_{\text{SD}} \langle \Psi'_{A-1} E'_1 I'_1 M'_1 T'_1 M'_T | \hat{a}_{n \ell j m_j m_t}^\dagger \hat{a}_{\alpha_{A-2}}^\dagger \hat{a}_{\alpha_{A-3}}^\dagger | \alpha_1 \dots \alpha_{A-4} \rangle_a \\
 & \quad \times {}_a \langle \alpha_1 \dots \alpha_{A-4} | \hat{a}_{\alpha'_{A-3}} \hat{a}_{\alpha'_{A-2}} \hat{a}_{\alpha'_{A-1}} | \Psi_{A-1} E_1 I_1 M_1 T_1 M_T \rangle_{\text{SD}} \\
 & \quad \times \langle \alpha_{A-3} \alpha_{A-2} n' \ell' j' m'_j m'_t | \hat{V}_{A-3A-2A} | \alpha'_{A-3} \alpha'_{A-2} \alpha'_{A-1} \rangle \\
 &= \frac{1}{(A-1)(A-2)(A-3)} \sum_{\alpha_{A-3}} \sum_{\alpha_{A-2}} \sum_{\alpha'_{A-3}} \sum_{\alpha'_{A-2}} \sum_{\alpha'_{A-1}} \\
 & \quad \times {}_{\text{SD}} \langle \Psi'_{A-1} E'_1 I'_1 M'_1 T'_1 M'_T | \hat{a}_{n \ell j m_j m_t}^\dagger \hat{a}_{\alpha_{A-2}}^\dagger \hat{a}_{\alpha_{A-3}}^\dagger \hat{a}_{\alpha'_{A-3}} \hat{a}_{\alpha'_{A-2}} \hat{a}_{\alpha'_{A-1}} | \Psi_{A-1} E_1 I_1 M_1 T_1 M_T \rangle_{\text{SD}} \\
 & \quad \times \langle \alpha_{A-3} \alpha_{A-2} n' \ell' j' m'_j m'_t | \hat{V}_{A-3A-2A} | \alpha'_{A-3} \alpha'_{A-2} \alpha'_{A-1} \rangle
 \end{aligned}$$

$$\begin{aligned}
 &= \frac{1}{6(A-1)(A-2)(A-3)} \sum_{\alpha_{A-3}} \sum_{\alpha_{A-2}} \sum_{\alpha'_{A-3}} \sum_{\alpha'_{A-2}} \sum_{\alpha'_{A-1}} \\
 &\quad \times \langle \alpha_{A-3} \alpha_{A-2} n' \ell' j' m'_j m'_t | \hat{V}_{A-3A-2A} \cdot_{\text{SD}} \langle \Psi'_{A-1} E'_1 I'_1 M'_1 T'_1 M'_1 | \\
 &\quad \times \left(\hat{a}_{nljm_j m_t}^\dagger \hat{a}_{\alpha_{A-2}}^\dagger \hat{a}_{\alpha_{A-3}}^\dagger \hat{a}_{\alpha'_{A-3}} \hat{a}_{\alpha'_{A-2}} \hat{a}_{\alpha'_{A-1}} | \Psi_{A-1} E_1 I_1 M_1 T_1 M_{T_1} \rangle_{\text{SD}} | \alpha'_{A-3} \alpha'_{A-2} \alpha'_{A-1} \rangle \right. \\
 &+ \hat{a}_{nljm_j m_t}^\dagger \hat{a}_{\alpha_{A-2}}^\dagger \hat{a}_{\alpha_{A-3}}^\dagger \hat{a}_{\alpha'_{A-1}} \hat{a}_{\alpha'_{A-3}} \hat{a}_{\alpha'_{A-2}} | \Psi_{A-1} E_1 I_1 M_1 T_1 M_{T_1} \rangle_{\text{SD}} | \alpha'_{A-1} \alpha'_{A-3} \alpha'_{A-2} \rangle \\
 &+ \hat{a}_{nljm_j m_t}^\dagger \hat{a}_{\alpha_{A-2}}^\dagger \hat{a}_{\alpha_{A-3}}^\dagger \hat{a}_{\alpha'_{A-2}} \hat{a}_{\alpha'_{A-1}} \hat{a}_{\alpha'_{A-3}} | \Psi_{A-1} E_1 I_1 M_1 T_1 M_{T_1} \rangle_{\text{SD}} | \alpha'_{A-2} \alpha'_{A-1} \alpha'_{A-3} \rangle \\
 &+ \hat{a}_{nljm_j m_t}^\dagger \hat{a}_{\alpha_{A-2}}^\dagger \hat{a}_{\alpha_{A-3}}^\dagger \hat{a}_{\alpha'_{A-2}} \hat{a}_{\alpha'_{A-3}} \hat{a}_{\alpha'_{A-1}} | \Psi_{A-1} E_1 I_1 M_1 T_1 M_{T_1} \rangle_{\text{SD}} | \alpha'_{A-2} \alpha'_{A-3} \alpha'_{A-1} \rangle \\
 &+ \hat{a}_{nljm_j m_t}^\dagger \hat{a}_{\alpha_{A-2}}^\dagger \hat{a}_{\alpha_{A-3}}^\dagger \hat{a}_{\alpha'_{A-1}} \hat{a}_{\alpha'_{A-2}} \hat{a}_{\alpha'_{A-3}} | \Psi_{A-1} E_1 I_1 M_1 T_1 M_{T_1} \rangle_{\text{SD}} | \alpha'_{A-1} \alpha'_{A-2} \alpha'_{A-3} \rangle \\
 &\left. + \hat{a}_{nljm_j m_t}^\dagger \hat{a}_{\alpha_{A-2}}^\dagger \hat{a}_{\alpha_{A-3}}^\dagger \hat{a}_{\alpha'_{A-3}} \hat{a}_{\alpha'_{A-1}} \hat{a}_{\alpha'_{A-2}} | \Psi_{A-1} E_1 I_1 M_1 T_1 M_{T_1} \rangle_{\text{SD}} | \alpha'_{A-3} \alpha'_{A-1} \alpha'_{A-2} \rangle \right) \\
 &= \frac{1}{6(A-1)(A-2)(A-3)} \sum_{\alpha_{A-3}} \sum_{\alpha_{A-2}} \sum_{\alpha'_{A-3}} \sum_{\alpha'_{A-2}} \sum_{\alpha'_{A-1}} \\
 &\quad \times_{\text{SD}} \langle \Psi'_{A-1} E'_1 I'_1 M'_1 T'_1 M'_1 | \hat{a}_{nljm_j m_t}^\dagger \hat{a}_{\alpha_{A-2}}^\dagger \hat{a}_{\alpha_{A-3}}^\dagger \hat{a}_{\alpha'_{A-3}} \hat{a}_{\alpha'_{A-2}} \hat{a}_{\alpha'_{A-1}} | \Psi_{A-1} E_1 I_1 M_1 T_1 M_{T_1} \rangle_{\text{SD}} \\
 &\quad \times \langle \alpha_{A-3} \alpha_{A-2} n' \ell' j' m'_j m'_t | \hat{V}_{A-3A-2A} \\
 &\quad \times \left(| \alpha'_{A-3} \alpha'_{A-2} \alpha'_{A-1} \rangle + | \alpha'_{A-1} \alpha'_{A-3} \alpha'_{A-2} \rangle + | \alpha'_{A-2} \alpha'_{A-1} \alpha'_{A-3} \rangle - | \alpha'_{A-2} \alpha'_{A-3} \alpha'_{A-1} \rangle \right. \\
 &\quad \left. - | \alpha'_{A-1} \alpha'_{A-2} \alpha'_{A-3} \rangle - | \alpha'_{A-3} \alpha'_{A-1} \alpha'_{A-2} \rangle \right) \\
 &= \frac{1}{\sqrt{6}(A-1)(A-2)(A-3)} \sum_{\alpha_{A-3}} \sum_{\alpha_{A-2}} \sum_{\alpha'_{A-3}} \sum_{\alpha'_{A-2}} \sum_{\alpha'_{A-1}} \\
 &\quad \times_{\text{SD}} \langle \Psi'_{A-1} E'_1 I'_1 M'_1 T'_1 M'_1 | \hat{a}_{nljm_j m_t}^\dagger \hat{a}_{\alpha_{A-2}}^\dagger \hat{a}_{\alpha_{A-3}}^\dagger \hat{a}_{\alpha'_{A-3}} \hat{a}_{\alpha'_{A-2}} \hat{a}_{\alpha'_{A-1}} | \Psi_{A-1} E_1 I_1 M_1 T_1 M_{T_1} \rangle_{\text{SD}} \\
 &\quad \times \langle \alpha_{A-3} \alpha_{A-2} n' \ell' j' m'_j \frac{1}{2} m'_t | \hat{V}_{A-3A-2A} | \alpha'_{A-3} \alpha'_{A-2} \alpha'_{A-1} \rangle_a \\
 &= \frac{1}{6(A-1)(A-2)(A-3)} \sum_{\alpha_{A-3}} \sum_{\alpha_{A-2}} \sum_{\alpha'_{A-3}} \sum_{\alpha'_{A-2}} \sum_{\alpha'_{A-1}} \\
 &\quad \times_{\text{SD}} \langle \Psi'_{A-1} E'_1 I'_1 M'_1 T'_1 M'_1 | \hat{a}_{nljm_j m_t}^\dagger \hat{a}_{\alpha_{A-2}}^\dagger \hat{a}_{\alpha_{A-3}}^\dagger \hat{a}_{\alpha'_{A-3}} \hat{a}_{\alpha'_{A-2}} \hat{a}_{\alpha'_{A-1}} | \Psi_{A-1} E_1 I_1 M_1 T_1 M_{T_1} \rangle_{\text{SD}} \\
 &\quad \times_a \langle \alpha_{A-3} \alpha_{A-2} n' \ell' j' m'_j \frac{1}{2} m'_t | \hat{V}_{A-3A-2A} | \alpha'_{A-3} \alpha'_{A-2} \alpha'_{A-1} \rangle_a \tag{11.63}
 \end{aligned}$$

This derivation is quite elaborate because we want to end up with 3N matrix elements with respect to antisymmetric 3N states. We have used similar tricks already before in the derivations of the exchange NN and direct 3N kernels. Here, we distinguish six terms where we renamed the primed indices of the HO single-particle states in the six different combinations that are possible by their permutations and introduced a factor $\frac{1}{6}$. Due to the anti-commutation relations of the fermionic annihilation operators we can recast them into their original order in each term, while generating the appropriate signs that lead us to the antisymmetric 3N state in the ket. Then we can use the idempotence of the antisymmetrizer and exploit that it does commute with the 3N interaction to obtain the antisymmetric 3N state in the bra.

This completes the derivation of the necessary kernels for NN+3N Hamiltonians. We

will give a summary of the results in the next subsection and confront our formulas with those obtained using a different strategy, namely using coupled densities as, e.g., in Ref. [48].

11.2.4 Summary of Kernels — Coupled vs. Uncoupled Densities

In this section we give a summary of the kernel formulas which are the starting point for our implementations and discuss their general structure. Afterwards, we give a short review of an alternative approach where the kernel formulas are manipulated further before implementation, which is mainly followed by Quaglioni, Navrátil and Hupin, see, e.g., [51, 48].

We start by summarizing the norm and Hamiltonian kernels with respect to states (11.54) as derived in the previous subsection. Here we switch the notation and replace the α as label of ℓs -coupled HO single-particle states, which was convenient for the derivations of the formulas, by the labels a, b, \dots to be consistent with the notation in Part I and II. Then, the expressions for the different kernels read:

norm kernel

$$\begin{aligned} \langle \epsilon_{\nu'n'}^{\mathcal{J}\pi T} | \hat{T}_{A-1,A} | \epsilon_{\nu n}^{\mathcal{J}\pi T} \rangle = \\ \sum_{M_1 m_j} \sum_{M_{T_1} m_t} \sum_{M'_1 m'_j} \sum_{M'_{T_1} m'_t} \begin{pmatrix} I_1 & j \\ M_1 & m_j \end{pmatrix} \begin{pmatrix} \mathcal{J} \\ \mathcal{M} \end{pmatrix} \begin{pmatrix} T_1 & \frac{1}{2} \\ M_{T_1} & m_t \end{pmatrix} \begin{pmatrix} T \\ M_T \end{pmatrix} \begin{pmatrix} I'_1 & j' \\ M'_1 & m'_j \end{pmatrix} \begin{pmatrix} \mathcal{J} \\ \mathcal{M} \end{pmatrix} \begin{pmatrix} T'_1 & \frac{1}{2} \\ M'_{T_1} & m'_t \end{pmatrix} \begin{pmatrix} T \\ M_T \end{pmatrix} \\ \times \frac{1}{A-1} \text{sd} \langle \Psi_{A-1} E'_1 I'_1 M'_1 T'_1 M'_{T_1} | \hat{a}_{n\ell j m_j m_t}^\dagger \hat{a}_{n'\ell' j' m'_j m'_t} | \Psi_{A-1} E_1 I_1 M_1 T_1 M_{T_1} \rangle_{\text{SD}} \end{aligned} \quad (11.64)$$

Direct NN interaction kernel

$$\begin{aligned} \langle \epsilon_{\nu'n'}^{\mathcal{J}\pi T} | \hat{V}_{A-1,A} (1 - \hat{T}_{A-1,A}) | \epsilon_{\nu n}^{\mathcal{J}\pi T} \rangle = \\ \sum_{M_1 m_j} \sum_{M_{T_1} m_t} \sum_{M'_1 m'_j} \sum_{M'_{T_1} m'_t} \begin{pmatrix} I_1 & j \\ M_1 & m_j \end{pmatrix} \begin{pmatrix} \mathcal{J} \\ \mathcal{M} \end{pmatrix} \begin{pmatrix} T_1 & \frac{1}{2} \\ M_{T_1} & m_t \end{pmatrix} \begin{pmatrix} T \\ M_T \end{pmatrix} \begin{pmatrix} I'_1 & j' \\ M'_1 & m'_j \end{pmatrix} \begin{pmatrix} \mathcal{J} \\ \mathcal{M} \end{pmatrix} \begin{pmatrix} T'_1 & \frac{1}{2} \\ M'_{T_1} & m'_t \end{pmatrix} \begin{pmatrix} T \\ M_T \end{pmatrix} \\ \times \frac{1}{A-1} \sum_{ab} \text{sd} \langle \Psi'_{A-1} E'_1 I'_1 M'_1 T'_1 M'_{T_1} | \hat{a}_a^\dagger \hat{a}_b | \Psi_{A-1} E_1 I_1 M_1 T_1 M_{T_1} \rangle_{\text{SD}} \\ \times {}_a \langle a n' \ell' j' m'_j m'_t | \hat{V} | b n \ell j m_j m_t \rangle_a \end{aligned} \quad (11.65)$$

Exchange NN interaction kernel

$$\begin{aligned}
 & \langle \epsilon_{v'n'}^{\mathcal{J}\pi T} | \hat{V}_{A-2A} \hat{T}_{A-1,A} | \epsilon_{vn}^{\mathcal{J}\pi T} \rangle = \\
 & \sum_{M_1 m_j} \sum_{M_{T_1} m_t} \sum_{M'_1 m'_j} \sum_{M'_{T_1} m'_t} \begin{pmatrix} I_1 & j \\ M_1 & m_j \end{pmatrix} \begin{pmatrix} \mathcal{J} \\ \mathcal{M} \end{pmatrix} \begin{pmatrix} T_1 & \frac{1}{2} \\ M_{T_1} & m_t \end{pmatrix} \begin{pmatrix} T \\ M_T \end{pmatrix} \begin{pmatrix} I'_1 & j' \\ M'_1 & m'_j \end{pmatrix} \begin{pmatrix} \mathcal{J} \\ \mathcal{M} \end{pmatrix} \begin{pmatrix} T'_1 & \frac{1}{2} \\ M'_{T_1} & m'_t \end{pmatrix} \begin{pmatrix} T \\ M_T \end{pmatrix} \\
 & \times \frac{1}{2(A-1)(A-2)} \sum_a \sum_{c d} \\
 & \times_{\text{SD}} \langle \Psi'_{A-1} E'_1 I'_1 M'_1 T'_1 M'_{T_1} | \hat{a}_{nlj m_j m_t}^\dagger \hat{a}_a^\dagger \hat{a}_c \hat{a}_d | \Psi_{A-1} E_1 I_1 M_1 T_1 M_{T_1} \rangle_{\text{SD}} \\
 & \times_a \langle a n' \ell' j' m'_j m'_t | \hat{V}_{A-2A} | c d \rangle_a
 \end{aligned} \tag{11.66}$$

Direct 3N interaction kernel

$$\begin{aligned}
 & \langle \epsilon_{v'n'}^{\mathcal{J}\pi T} | \hat{V}_{A-2A-1A} (1 - \hat{T}_{A-1,A} - \hat{T}_{A-2,A}) | \epsilon_{vn}^{\mathcal{J}\pi T} \rangle = \\
 & \sum_{M_1 m_j} \sum_{M_{T_1} m_t} \sum_{M'_1 m'_j} \sum_{M'_{T_1} m'_t} \begin{pmatrix} I_1 & j \\ M_1 & m_j \end{pmatrix} \begin{pmatrix} \mathcal{J} \\ \mathcal{M} \end{pmatrix} \begin{pmatrix} T_1 & \frac{1}{2} \\ M_{T_1} & m_t \end{pmatrix} \begin{pmatrix} T \\ M_T \end{pmatrix} \begin{pmatrix} I'_1 & j' \\ M'_1 & m'_j \end{pmatrix} \begin{pmatrix} \mathcal{J} \\ \mathcal{M} \end{pmatrix} \begin{pmatrix} T'_1 & \frac{1}{2} \\ M'_{T_1} & m'_t \end{pmatrix} \begin{pmatrix} T \\ M_T \end{pmatrix} \\
 & \times \frac{1}{2(A-1)(A-2)} \sum_{abde} \\
 & \times_{\text{SD}} \langle \Psi'_{A-1} E'_1 I'_1 M'_1 T'_1 M'_{T_1} | \hat{a}_a^\dagger \hat{a}_b^\dagger \hat{a}_d \hat{a}_e | \Psi_{A-1} E_1 I_1 M_1 T_1 M_{T_1} \rangle_{\text{SD}} \\
 & \times_a \langle b a n' \ell' j' m'_j m'_t | \hat{V} | d e n \ell j m_j m_t \rangle_a
 \end{aligned} \tag{11.67}$$

Exchange 3N interaction kernel

$$\begin{aligned}
 & \langle \epsilon_{v'n'}^{\mathcal{J}\pi T} | \hat{V}_{A-3A-2A} \hat{T}_{A-1,A} | \epsilon_{vn}^{\mathcal{J}\pi T} \rangle = \\
 & \sum_{M_1 m_j} \sum_{M_{T_1} m_t} \sum_{M'_1 m'_j} \sum_{M'_{T_1} m'_t} \begin{pmatrix} I_1 & j \\ M_1 & m_j \end{pmatrix} \begin{pmatrix} \mathcal{J} \\ \mathcal{M} \end{pmatrix} \begin{pmatrix} T_1 & \frac{1}{2} \\ M_{T_1} & m_t \end{pmatrix} \begin{pmatrix} T \\ M_T \end{pmatrix} \begin{pmatrix} I'_1 & j' \\ M'_1 & m'_j \end{pmatrix} \begin{pmatrix} \mathcal{J} \\ \mathcal{M} \end{pmatrix} \begin{pmatrix} T'_1 & \frac{1}{2} \\ M'_{T_1} & m'_t \end{pmatrix} \begin{pmatrix} T \\ M_T \end{pmatrix} \\
 & \times \frac{1}{6(A-1)(A-2)(A-3)} \sum_{abcdef} \\
 & \times_{\text{SD}} \langle \Psi'_{A-1} E'_1 I'_1 M'_1 T'_1 M'_{T_1} | \hat{a}_{nlj m_j m_t}^\dagger \hat{a}_b^\dagger \hat{a}_a^\dagger \hat{a}_d \hat{a}_e \hat{a}_f | \Psi_{A-1} E_1 I_1 M_1 T_1 M_{T_1} \rangle_{\text{SD}} \\
 & \times_a \langle a b n' \ell' j' m'_j m'_t | \hat{V}_{A-3A-2A} | d e f \rangle_a
 \end{aligned} \tag{11.68}$$

Before entering the final step of solving the radial equation, the kernels listed above undergo the following manipulations: First, they are transformed with help of Eq. (11.54) to yield the kernels with respect to the Slater determinant channel basis. These are converted into the translational invariant kernels with help of the inversion of Eq. (11.52). Finally, the Hamiltonian kernels enter the radial Schrödinger Equation (11.11) directly, while the norm kernel enters in form of its inverse square root. The steps towards the solution of the radial equation are discussed in Section 12.

All kernels (11.64) - (11.68) have a common structure: they consist of sums over four Clebsch-Gordan coefficients that accomplish the angular-momentum and isospin decoupling of the target and projectile for the bra and ket states, respectively. It is important to note that the total isospin quantum number M_T is known from the proton and neutron content of the A -body system under consideration, and all terms with non-vanishing Clebsch-Gordan coefficients contribute to the kernel matrix element. A second generic feature of the kernels is their dependence on density matrices. The norm and direct NN kernels depend on a one-body density matrix, the exchange and direct 3N kernels on a two-body density matrix and the exchange 3N kernel on a three-body density matrix, all of them with respect to the NCSM target eigenstates given as superposition of Slater determinants. The occurrence of a three-body density matrix in the 3N kernels highlights the increased computational cost compared to calculations considering only NN interactions. Actually, the handling of the three-body density poses the main challenge for the computational realization, because its storage in memory for reasonably-large model spaces is problematic. Therefore, we have developed an efficient on-the-fly calculation of the densities, which will be explained in more detail in the next subsection. The next critical objects in the kernels are the interaction matrix elements with respect to m -scheme states. As we have discussed in Section 2.2.1 the storage in fast memory of 3N matrix elements in the m -scheme becomes challenging beyond $E_{3\max} = 11$. Thus, we make use of the 3N matrix elements in the $\mathcal{J}T$ -coupled scheme and the corresponding on-the-fly decoupling (see Section 2.2.1 or Ref. [44]) that yields the necessary m -scheme matrix elements. Moreover, it is evident that the projection quantum numbers of the target eigenstates need to be treated explicitly including consistent relative phases. Technically, NCSM eigenvectors with different projections stem from independent diagonalizations of the Hamiltonian matrix since the projection quantum numbers are defined beforehand to reduce the many-body basis dimension. However, different diagonalizations may yield different relative phases. To overcome this problem and also to avoid additional diagonalizations we can generalize the well-known raising and lowering operators for the angular momentum \hat{j}_{\pm} and isospin \hat{T}_{\pm} to operators acting in A -body space, using for example

$$\begin{aligned}
 \hat{j}_+^{(A-1)} |\Psi_{A-1} E_1 I_1 M_1 T_1 M_{T_1}\rangle_{\text{SD}} \\
 &= \sum_m^A \hat{1} \otimes \dots \otimes \hat{1} \otimes \underbrace{\hat{j}_+}_{m\text{-th space}} \otimes \hat{1} \dots \otimes \hat{1} \sum_i C_i |\Phi_i, M_1\rangle_a \\
 &= \sum_i C_i \sum_m \sqrt{\hbar^2(j_{i_m} - m_{i_m})(j_{i_m} + m_{i_m} + 1)} |\Phi_i, M_1 + 1\rangle_a,
 \end{aligned} \tag{11.69}$$

where we denote HO Slater determinants with sum of all projection quantum numbers equal to M_1 by $|\Phi_i, M_1\rangle_a$. The single-particle raising operator is denoted by \hat{j}_+ , and the angular momentum and its projection quantum number are denoted by j_{n_i} and m_{n_i} , respectively. Hence, we can generate all necessary inputs from a single NCSM run, which generates an eigenvector with specific projection quantum numbers, and obtain all other input vectors with necessary projection quantum numbers using the raising and lowering

operators and a subsequent renormalization of the vectors.

The formulas as discussed so far have been used in our calculations and are implemented as described in the next subsection. In the literature, however, also a different strategy to handle the kernels exists, that is to manipulate the formulas given above such that angular momentum coupled densities are introduced. This has been done in the original NCSM/RGM kernels for NN-only calculations [48] and is also an option when 3N interactions are present as discussed in our collaborative paper [51]. In order to introduce angular-momentum coupled densities in Eq. (11.68), one can introduce the $\mathcal{J}T$ -coupled 3N matrix elements and exploit the Wigner-Eckart theorem [188] to obtain reduced density matrices in angular momentum and isospin. After this, one can evaluate all summations of projection quantum numbers in exchange for summations over quantum numbers from intermediate angular-momentum couplings. As a consequence of using the Wigner-Eckart theorem for the isospin one cannot include the isospin dependence of the NN interaction exactly. Instead one adopts an averaging procedure to account for the isospin symmetry breaking approximately, for details see Ref. [51]. In contrast, our approach treats the isospin dependence of the nuclear interaction without approximation. We assess the quality of the averaging procedure in the case of p-⁴He scattering on the level of phase shifts as discussed in Section 13. Here, we want to discuss this alternative treatment of the NCSM/RGM kernels for the 3N exchange kernel, i.e., the one including the three-body density, exemplarily. The corresponding formula with angular-momentum coupled densities reads

$$\begin{aligned}
 & \langle \epsilon_{v'n'}^{\mathcal{J}\pi T} | \hat{V}_{A-3A-2A} \hat{T}_{A-1,A} | \epsilon_{vn}^{\mathcal{J}\pi T} \rangle = \\
 & \frac{1}{6(A-1)(A-2)(A-3)} \sum_{\bar{a}\bar{b}\bar{d}\bar{e}\bar{f}} \sum_{J_{ab}T_{ab}} \sum_{J_0T_0} \sum_{J_{de}T_{de}} \sum_{J_gT_g} \sum_{K\tau} \\
 & \hat{J}_0 \hat{T}_0 \hat{J}_g \hat{T}_g \hat{K} \hat{\tau} (-1)^{j+j'+J_{ab}+K-J_g+I_1+\mathcal{J}+1+T_{ab}+\tau-T_g+T_1+T} \\
 & \left\{ \begin{matrix} I_1 & K & I'_1 \\ j' & \mathcal{J} & j \end{matrix} \right\} \left\{ \begin{matrix} j' & K & j \\ J_g & J_{ab} & J_0 \end{matrix} \right\} \left\{ \begin{matrix} T_1 & \tau & T'_1 \\ \frac{1}{2} & \tau & \frac{1}{2} \end{matrix} \right\} \\
 & \left\{ \begin{matrix} j' & \mathcal{J} & j \\ J_g & J_{ab} & J_0 \end{matrix} \right\} \left\{ \begin{matrix} \frac{1}{2} & T & \frac{1}{2} \\ T_g & T_{ab} & T_0 \end{matrix} \right\} \\
 & {}_{\text{SD}} \langle \Psi'_{A-1} E'_1 I'_1 T'_1 \| \left[\left((\hat{a}_{\bar{a}}^\dagger \hat{a}_{\bar{b}}^\dagger)^{J_{ab}T_{ab}} \hat{a}_{n\ell j}^\dagger \right)^{J_g T_g} \left((\hat{a}_{\bar{d}} \hat{a}_{\bar{e}})^{J_{de}T_{de}} \hat{a}_{\bar{f}} \right)^{J_0 T_0} \right]^{K\tau} \| \Psi_{A-1} E_1 I_1 T_1 \rangle_{\text{SD}} \\
 & {}_a \langle ((\bar{a}\bar{b})J_{ab} T_{ab}, n'\ell'j') J_0 T_0 | \hat{V}^{3N} | ((\bar{d}\bar{e})J_{de} T_{de}, \bar{f}) J_0 T_0 \rangle_a, \tag{11.70}
 \end{aligned}$$

with time-reversed annihilation operators $\hat{a}_{\bar{a}} = (-1)^{j_a - m_{j_a} + \frac{1}{2} - m_{t_a}} \hat{a}_{n_a \ell_a j_a - m_{j_a} - m_{t_a}}$. Moreover, as already introduced in Section 2.3, the HO single-particle indices \bar{a}, \bar{b}, \dots denote sets of HO single-particle quantum numbers without projection quantum numbers, i.e., HO single-particle orbitals $\bar{a} = \{n_a, \ell_a, j_a\}$. The three vertical bars in the coupled-density matrix element indicates their reduced character. Although the angular-momentum coupling reduces the memory needs to store the reduced density in memory, it still remains prohibitive. To overcome this problem one inserts an identity in terms of $(A-4)$ -body eigenstates in between of the creation and annihilation operators, and arrives at the following

form which can be employed in calculations

$$\begin{aligned}
 & \text{SD} \langle \epsilon_{\nu' n'}^{\mathcal{J} \pi T} | \hat{T}_{A-1, A} \hat{V}_{A-3, A-2, A-1}^{3N} | \epsilon_{\nu n}^{\mathcal{J} \pi T} \rangle_{\text{SD}} \\
 &= \frac{1}{6(A-1)(A-2)(A-3)} \sum_{\bar{a} \bar{b} \bar{d} \bar{e} \bar{f}} \sum_{J_{ab} T_{ab}} \sum_{J_0 T_0} \sum_{J_{de} T_{de}} \sum_{J_g T_g} \sum_{\beta} \\
 & \times \hat{J}_0 \hat{T}_0 \hat{J}_g \hat{T}_g \begin{Bmatrix} I_{\beta} & J_g & I'_1 \\ J_0 & J_{ab} & j' \\ I_1 & j & J \end{Bmatrix} \begin{Bmatrix} T_{\beta} & T_g & T'_1 \\ T_0 & T_{ab} & \frac{1}{2} \\ T_1 & \frac{1}{2} & T \end{Bmatrix} \\
 & \times {}_a \langle ((\bar{a} \bar{b}) J_{ab} T_{ab}, n' \ell' j' \frac{1}{2}) J_0 T_0 | \hat{V}^{3N} | ((\bar{d} \bar{e}) J_{de} T_{de}, \bar{f}) J_0 T_0 \rangle_a \\
 & \times_{\text{SD}} \langle \Psi_{A-1} \alpha'_1 I'_1 \pi'_1 T'_1 | | | \left((\hat{a}_a^{\dagger} \hat{a}_b^{\dagger})^{J_{ab} T_{ab}} \hat{a}_{n \ell j \frac{1}{2}}^{\dagger} \right)^{J_g T_g} | | | \Psi_{A-4} E_{\beta} I_{\beta}^{\pi_{\beta}} T_{\beta} \rangle_{\text{SD}} \\
 & \times_{\text{SD}} \langle \Psi_{A-1} \alpha_1 I_1 T_1 | | | \left((\hat{a}_{\bar{d}}^{\dagger} \hat{a}_{\bar{e}}^{\dagger})^{J_{de} T_{de}} \hat{a}_{\bar{f}}^{\dagger} \right)^{J_0 T_0} | | | \Psi_{A-4} E_{\beta} I_{\beta}^{\pi_{\beta}} T_{\beta} \rangle_{\text{SD}}. \tag{11.71}
 \end{aligned}$$

In this form, the explicit treatment of the three-body density matrix can be avoided by breaking it down into matrix elements of three coupled creation or annihilation operators, which are easily manageable in memory. Unfortunately, this procedure is limited to light systems, because one needs a sufficiently complete set of $(A-4)$ -body eigenstates to make the splitting of the three-body density accurate. This is of course a nontrivial task and, thus, this approach is at the moment limited to $A=4$ targets in the single-nucleon formalism. Nevertheless, in collaboration with Hupin, Navrátil and Quaglioni we made use of this approach to cross-check the NCSM/RGM kernels and phase shifts in the case of nucleon- ^4He elastic scattering, which resulted in a joint publication which will be the focus of Section 13. In our approach, i.e., utilizing Eqs. (11.64)-(11.68), the principal limitation to light targets is absent, which is the reason why reactions involving heavier targets with explicit 3N interactions are now accessible. We will discuss first results for scattering involving heavier targets in Section 14 in context of the no-core shell model with continuum approach, where also the NCSM/RGM kernels enter, for the example of ^9Be in terms of neutron- ^8Be scattering.

Another formal difference to our approach is the direct use of the 3N matrix elements in the $\mathcal{J} T$ -coupled scheme. Therefore, the step of angular-momentum decoupling can be avoided, however in exchange one needs to consider sums of $\mathcal{J} T$ -coupled 3N matrix elements including appropriate $6j$ -symbols if a matrix element not contained in the standard storage scheme is required. This is the identical complication that we encounter during the calculation of 3N matrix elements in the NO2B approximation discussed in Section 2.3 or in Ref. [96].

11.2.5 Implementation Details

The aim of this section is to give more details on the actual evaluation of Eqs. (11.64)-(11.68) that leads to a hybrid MPI/OpenMP parallel implementation. As mentioned above, we have to pay special attention to the three-body density matrix that occurs in the 3N exchange kernel, because of its memory needs. Our approach is to compute the three-body

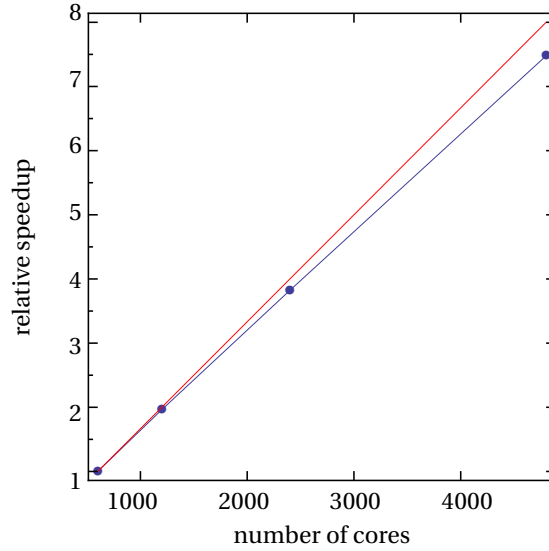


Figure 11.5 – Scaling of the NCSM/RGM kernel calculation. Shown is the speed-up (●) as function of CPU cores relative to a calculation on 25 nodes each with 24 cores. The red line marks ideal scaling.

density matrix elements, and likewise all other density matrix elements in the NCSM/RGM kernels, on the fly. This has the advantages that no additional memory to store the densities is needed, and we have the possibility to treat the isospin dependence of the nuclear interaction without further approximations.

First of all, from Eqs. (11.64)-(11.68) it is evident that we need to consider those combinations of projection quantum numbers which lead to non-vanishing contributions only, i.e., those terms where all four Clebsch-Gordan coefficients are non-zero. Once we have decided which channels shall be taken into account this information is simply given by the corresponding triangular relations. This is due the fact that we know the total projection of the isospin determined by the number of protons and neutrons in the A -body system beforehand, and that we can choose an arbitrary value for the projection quantum number of the total angular momentum $M_{\mathcal{J}}$, because the kernels are independent of this quantity. In practice, we split the calculation of the kernels into different runs for each contributing combination of projection quantum numbers. In a subsequent step all partial contributions are added and yield the final results for the NCSM/RGM kernels.

For the implementation of the single contributions of a specific set of projection quantum numbers we exploit the fact that the NCSM target eigenstates are implicitly given as expansion in terms of HO $(A-1)$ -body Slater determinants $|\phi_n\rangle$ within the NCSM model space

$$|\Psi_{A-1} E_1 I_1 M_1 T_1 M_{T_1}\rangle_{\text{SD}} = \sum_i^{|\phi_i, M_1\rangle_a \in \mathcal{M}_{\text{NCSM}}} C_i |\phi_i, M_1\rangle_a. \quad (11.72)$$

We can pull the two summations from the expansions of the target states in the bra and ket in front of the summations over the HO single-particle states in Eqs. (11.68) - (11.64). In

this way we guarantee that each term within these two summations contributes independently to the respective total kernel matrix elements. This means, we obtain an expression ideally suited for parallel computation with good scaling. To this end we developed an hybrid OpenMP/MPI parallel code for the kernel computations. The scaling behavior of our NCSM/RGM kernel implementation is illustrated in Figure 11.5. Furthermore, within each of these terms the sums over HO single-particle states are restricted to those combinations that can connect the SD in the ket with the SD in the bra state with help of the creation and annihilation operators. To identify the contributing combinations we can make use of the algorithms for the computation of many-body matrix elements of the NN or 3N interaction, e.g., during the setup of the many-body Hamilton matrix in the NCSM. Here, we adopt the routines that have been developed originally for this step within the IT-NCSM framework. Generally, the corresponding procedure is known as Slater-Condon rules, for reference see, e.g., [126, 127, 189].

Besides the three-body density matrix, also the storage of the m -scheme three-body matrix elements is prohibitive. Here, we benefit again, as before in the NCSM calculations, from the $\mathcal{J}T$ -coupled scheme of the 3N matrix elements in combination with the corresponding storage scheme tailored to the effective decoupling into the m -scheme as discussed in detail in Section 2.2.1. In terms of computing time the production of the direct and exchange 3N kernels are most expensive. In the future, one option for possible improvements in this direction might be the processing of the decoupling of the 3N matrix elements on graphics processing units (GPUs), which are currently available on modern super-computers. We have tested a first version of this GPU decoupling routine (cf. Section 2.2.3 or Ref. [95], which can eventually be used in the NCSM/RGM kernel production runs, too.

We conclude the remarks on our implementation of the kernel formulas by outlining the general program flow: After the definition of the NCSM target eigenstates we want to take into account, we determine the allowed combinations of projection quantum numbers with help of the triangular relations of the Clebsch-Gordan coefficients. Each of these combinations is then handled in a separate hybrid OpenMP/MPI parallelized job. These jobs start with reading the necessary NN and 3N interaction matrix elements in the $\mathcal{J}T$ -coupled scheme as well as the two necessary target eigenvectors. This data is subsequently broadcasted to all nodes using the built-in routines of the MPI library. The loops over the SD components of the target eigenvectors are parallelized via MPI over different nodes and using OpenMP within each node. At the end of these loops each node reduces the contributions to the five NCSM/RGM kernels of the different OpenMP threads, respectively. After that the contributions from different nodes are accumulated using again collective MPI-library routines. Finally, the transformation into the SD channel basis (11.53) is performed and the kernels are written to disk. Once all jobs dealing with the different sets of projection quantum numbers have finished, all contributions are read-in, summed in the appropriate way and a file with the NCSM/RGM kernel in SD channel basis for the given set of considered target eigenstates is generated.

Finally, this file is read-in again, the translational invariant kernels are computed and

the radial Eq. (11.20) is solved with the techniques discussed in the next section.

SECTION 12

The *R*-Matrix Theory

The *R*-matrix theory was introduced in the late 1940s by Wigner and Eisenbud [190, 191, 192] and was primarily formulated to describe resonances in nuclear reactions. In the mean time, the *R*-matrix formalism has evolved into a well-established tool to describe scattering in nuclear physics involving nucleons and nuclei [193], or in quantum chemistry involving electrons, atoms and molecules [174]. Two variants of the *R*-matrix theory have been developed [173]: one is the so-called phenomenological *R*-matrix approach, which is mainly used in nuclear physics. Here the parameters of the *R*-matrix are determined from experimental data and then the *R*-matrix can be used to analyze, e.g., radiative-capture cross-sections at low energies as it is of interest in astrophysics. We will not discuss these aspects of the *R*-matrix theory in further detail here, however, thorough review articles including examples of its applications can be found in Refs. [193, 194, 173]. In the following, we will focus on the second variant, which initially has been used in atomic physics and is generally known as calculable *R*-matrix approach. It constitutes an elegant path towards accurate solutions to the radial Schrödinger equation at positive energies as they typically emerge in scattering problems, however, also solutions for bound states are accessible as they are relevant, e.g., for capture cross-sections. It has been introduced for nuclear problems, but subsequently was developed further particularly for electron scattering off atoms and molecules to describe excitation or ionization processes. In the context of nuclear physics, it has proven to be applicable in particular for coupled-channel scatterings and microscopic cluster techniques, which is also the application we focus on.

12.1 Calculation of the *R*-Matrix for Single-Channel Problems

Throughout this subsection we focus on the solution of the radial Schrödinger equation, where we consider a single channel only. We will generalize the formalism to multi-channel problems in the next subsection. For now, we aim at the solution of a radial Schrödinger

equation in coordinate-space representation that can be cast in the form

$$\left(-\frac{\hbar^2}{2\mu} \frac{\partial^2}{\partial r^2} + \frac{\hbar^2 l(l+1)}{r^2} + V(r) - E \right) u_l(r) = 0 \quad (12.1)$$

with $u(0) = 0$ as additional constraint at the origin. The relative orbital angular momentum quantum number l denotes the arbitrary partial wave considered and the spherical harmonic describing the orbital part of the wave function has been separated already. In addition we require the potential to fulfill the asymptotic property

$$V(r) \xrightarrow{r \rightarrow \infty} \frac{Z_1 Z_2 e^2}{r} + \mathcal{O}\left(\frac{1}{r^2}\right), \quad (12.2)$$

i.e., at large relative distances r the particles interact only via the Coulomb force. The asymptotic property is automatically fulfilled for the centrifugal barrier. Moreover, we note that also non-local potentials, e.g., in the form

$$V(r)u_l(r) = U(r)u_l(r) + \int_0^\infty dr W(r', r)u_l(r') \quad (12.3)$$

as in the case of the NCSM/RGM equations, can be handled as long as they are localized. Finally, we assume the potentials to be real, so that the phase shifts are real and the scattering matrix is unitary.

The basic principle of R -matrix theory is the splitting of the configuration space into two parts, an internal and an external region, which are connected at the so-called channel radius a . The external interaction is approximated just by the Coulomb interaction, hence in practice we have to ensure that the channel radius is chosen large enough to obtain accurate results. Stated differently, this means that all extracted physical observables should be independent of the actual choice for the channel radius. The remaining task is to find the solutions of the radial Schrödinger equation in the internal and external regions for given energy E respectively, and to ensure that the continuity conditions at the channel radius are fulfilled, i.e., $u_l^{\text{int}}(a) = u_l^{\text{ext}}(a)$ and $u_l'^{\text{int}}(a) = u_l'^{\text{ext}}(a)$.

Let us start with the solutions u_l^{ext} in the external region, where the radial Schrödinger equation simplifies to the Coulomb wave equation

$$\left(\frac{\partial^2}{\partial r^2} - \frac{l(l+1)}{r^2} - \frac{2k\eta}{r} + k^2 \right) u_l^{\text{int}}(r) = 0, \quad (12.4)$$

where we introduced the dimensionless Sommerfeld parameter $\eta = \frac{Z_1 Z_2 e^2}{\hbar v}$ with relative velocity $v = \frac{\hbar k}{\mu}$, and the wavenumber $k = \frac{\sqrt{2\mu E}}{\hbar}$. In the context of nuclear reactions $\eta \geq 0$ holds. Solutions for positive energies are the regular and irregular Coulomb functions $F_l(\eta, kr)$ and $G_l(\eta, kr)$, respectively. Accordingly, general solutions are given by linear combinations of these two functions. We employ the ansatz

$$u_l^{\text{ext}}(r) = C_l (I_l(\eta, kr) - U_l O_l(\eta, kr)) \quad (12.5)$$

using the combinations

$$I_l(\eta, kr) = G_l(\eta, kr) - iF_l(\eta, kr) \quad (12.6)$$

and

$$O_l(\eta, kr) = G_l(\eta, kr) + iF_l(\eta, kr) = I_l^*(\eta, kr). \quad (12.7)$$

These choices are particular convenient because their asymptotics correspond to incoming

$$I_l(\eta, kr) \xrightarrow{kr \rightarrow \infty} e^{-i(kr - \frac{1}{2}l\pi - \eta \ln 2x + \sigma_l)} \quad (12.8)$$

and outgoing

$$O_l(\eta, kr) \xrightarrow{kr \rightarrow \infty} e^{i(kr - \frac{1}{2}l\pi - \eta \ln 2x + \sigma_l)} \quad (12.9)$$

waves. For vanishing Sommerfeld parameter the Coulomb functions are reduced to spherical Bessel and von-Neumann functions $F_l(0, kr) = kr j_l(kr)$ and $G_l(0, kr) = kr n_l(kr)$, respectively. Bound-state solutions, i.e., at negative energies, are given by Whittaker functions $W_{-\eta_B, l+\frac{1}{2}}(2\kappa_B r)$, with $\kappa_B = \frac{\sqrt{-2\mu E}}{\hbar}$ and $\eta_B = \frac{\text{sgn}(Z_1 Z_2)}{a_B \kappa_B}$, which are singular at $r = 0$.

Clearly, the nontrivial task is to determine the wave function $u_l^{\text{int}}(r)$ in the internal region, where we have to consider the more complicated nuclear interaction. We make use of an expansion of the internal wave function for partial wave l in terms of a finite basis of N square-integrable basis functions $\varphi_j(r)$

$$u_l^{\text{int}}(r) = \sum_{j=1}^N c_j \varphi_j(r), \quad (12.10)$$

which need to be linearly independent and must vanish at the origin. However, they are not necessarily orthogonal and they are not required to meet any special conditions at the channel radius a . Of course this method relies on suitably chosen basis functions that allow a good matching to the external wave function at the channel radius, and at the same time the number of functions N needs to be computationally manageable. For all results we will discuss we have used Lagrange functions [195] in the expansion (12.10) and we will give more details on this choice in Section 12.3. However, we note that other choices are discussed in the literature as well, e.g., sine functions [173] and basis functions with Gaussian behavior [196, 173].

Having our ansätze for the wave functions in the internal and external domain, we can define the so-called R -matrix at energy E by

$$u_l(a) = R_l(E)[a u_l'(a) - B u_l(a)], \quad (12.11)$$

with a dimensionless parameter B . For the single-channel problem considered through-

out this subsection the R -matrix is just a number, i.e., a matrix of dimension one. This will differ in the multi-channel case discussed in the next subsection. In the following, the strategy will be to solve for the R -matrix using information from the internal region and then to obtain the scattering matrix U_l .

The investigation of the radial Schrödinger equation (12.1) over the internal region $[0, a]$ reveals that the differential operator composed of the first three terms, i.e., the Hamiltonian for partial wave l , is not Hermitian as can be seen by explicit evaluation of matrix elements of the kinetic energy operator. This can be fixed using the surface operator originally introduced by Bloch

$$\mathcal{L}(B) = \frac{\hbar^2}{2\mu} \delta(r-a) \left(\frac{d}{dr} - \frac{B}{r} \right), \quad (12.12)$$

sometimes also referred to as Bloch operator. It turns out that the sum of the Hamiltonian for partial wave l and the Bloch operator is Hermitian in $[0, a]$ as discussed in detail in Ref. [197]. We utilize this to approximate the Schrödinger equation (12.1) by the so-called Bloch-Schrödinger equation

$$\left(-\frac{\hbar^2}{2\mu} \frac{\partial^2}{\partial r^2} + \frac{\hbar^2 l(l+1)}{r^2} + V(r) + \mathcal{L}(B) - E \right) u_l^{\text{int}}(r) = \mathcal{L}(B) u_l^{\text{ext}}(r), \quad (12.13)$$

where the external wave function is approximated by Eq. (12.5). It is evident from explicitly inserting the Bloch operator that Eq. (12.13) is equivalent to the radial Schrödinger equation plus the continuity condition $u_l^{\text{int}}(a) = u_l^{\text{ext}}(a)$. This means, solutions of the Bloch-Schrödinger equation automatically fulfill the continuity of the derivative of the wave function, which is a useful side effect of the Bloch operator.

To obtain a formal solution of Eq. (12.13) is always possible with help of a Green's function $G(r, r')$ by

$$\left(-\frac{\hbar^2}{2\mu} \frac{\partial^2}{\partial r^2} + \frac{\hbar^2 l(l+1)}{r^2} + V(r) + \mathcal{L}(B) - E \right) G(r, r') = \delta(r-r') \quad \text{and} \quad G(0, r) = 0. \quad (12.14)$$

We use the generic solution expressed in terms of the Green's function to solve for the R -matrix by comparing

$$\begin{aligned} u_l(a) &= \int_0^a G_l(a, r') \mathcal{L}(B) u_l^{\text{ext}}(r') dr' \\ &= \int_0^a G_l(a, r') \frac{\hbar^2}{2\mu} \delta(r'-a) \left(\frac{\partial}{\partial r'} - \frac{B}{r'} \right) u_l^{\text{ext}}(r') dr' \\ &= G_l(a, a) \frac{\hbar^2}{2\mu a} (a u_l^{\text{ext}}(a) - B u_l^{\text{ext}}(a)) \end{aligned} \quad (12.15)$$

to Eq. (12.11) and obtain $R_l(E) = G_l(a, a) \frac{\hbar^2}{2\mu a}$. Without the knowledge of the Green's function beforehand this expression for the R -matrix is of no practical gain, however, it reveals the general structure of the R -matrix and we will aim at its representation in terms of the

set of basis functions $\varphi_j(r)$ in the following. Therefore, we rewrite the Bloch-Schrödinger equation (12.13) using the expansion (12.10) for the internal wave function on the left-hand side and in addition we project the whole equation on the basis function $\varphi_i(r)$ by multiplication from the left and integration over r . This yields

$$\begin{aligned} \int_0^a dr \varphi_i(r) \left(-\frac{\hbar^2}{2\mu} \frac{\partial^2}{\partial r^2} + \frac{\hbar^2 l(l+1)}{r^2} + V(r) + \mathcal{L}(B) - E \right) \sum_{j=1}^N c_j \varphi_j(r) \\ = \int_0^a dr \varphi_i(r) \frac{\hbar^2}{2\mu} \delta(r-a) \left(\frac{\partial}{\partial r} - \frac{B}{r} \right) u_l^{\text{ext}}(r) \\ = \frac{\hbar^2}{2\mu a} \varphi_i(a) (a u_l^{\prime \text{ext}}(a) - B u_l^{\text{ext}}(a)) \end{aligned} \quad (12.16)$$

or equivalently

$$\begin{aligned} \sum_{j=1}^N \underbrace{\left(\int_0^a dr \varphi_i(r) \left(-\frac{\hbar^2}{2\mu} \frac{\partial^2}{\partial r^2} + \frac{\hbar^2 l(l+1)}{r^2} + V(r) + \mathcal{L}(B) - E \right) \varphi_j(r) \right)}_{\equiv C_{ij}(E, B)} c_j \\ = \frac{\hbar^2}{2\mu a} \varphi_i(a) (a u_l^{\prime \text{ext}}(a) - B u_l^{\text{ext}}(a)), \end{aligned} \quad (12.17)$$

where we have introduced the matrix $C(E, B)$ defined by its matrix elements $C_{ij}(E, B)$ in the last expression. In the following we use the notation $C_{ij} = C_{ij}(E, B)$ for matrix elements for brevity. Owing to the fact that the right-hand side is given in terms of the known external wave function, we can solve for the coefficients c_j using the inverse matrix $C(E, B)^{-1}$

$$c_k = \sum_{i,j=1}^N (C^{-1})_{ki} C_{ij} c_j = \sum_{i=1}^N (C^{-1})_{ki} \frac{\hbar^2}{2\mu a} \varphi_i(a) (a u_l^{\prime \text{ext}}(a) - B u_l^{\text{ext}}(a)). \quad (12.18)$$

By inserting these coefficients in the expansion of the internal wave function we can identify the R -matrix

$$u_l^{\text{int}}(a) = \sum_{j=1}^N \sum_{i=1}^N (C^{-1})_{ji} \frac{\hbar^2}{2\mu a} \varphi_i(a) (a u_l^{\prime \text{ext}}(a) - B u_l^{\text{ext}}(a)) \varphi_j(a) \quad (12.19)$$

$$\Rightarrow R_l(E, B) = \sum_{i,j=1}^N \frac{\hbar^2}{2\mu a} \varphi_i(a) (C^{-1})_{ij} \varphi_j(a). \quad (12.20)$$

This is the desired representation of the R -matrix over a finite basis as one can use it in actual calculations. Finally, we obtain for the internal wave function

$$u_l^{\text{int}}(r) = \frac{\hbar^2}{2\mu a} \frac{u_l^{\text{ext}}(a)}{R_l(E, B)} \sum_{i,j=1}^N (C^{-1})_{ij} \varphi_i(a) \varphi_j(r). \quad (12.21)$$

If we assume the basis functions $\varphi_j(r)$ to be orthonormal, we can further manipulate the expression for the R -matrix. By diagonalizing the matrix $C(0, B)$ we obtain its eigenvectors \vec{v}_{nl} and the corresponding eigenvalues E_{nl} , where l labels the considered partial

wave. We can use the eigenvectors and eigenvalues to bring the matrix $C(E, B)$ in its spectral decomposition

$$C(E, B) = \sum_{n=1}^N \vec{v}_{nl} E_{nl} \vec{v}_{nl}^\top - \sum_{n=1}^N \vec{v}_{nl} \vec{v}_{nl}^\top E, \quad (12.22)$$

which can be used to obtain the inverse matrix

$$C(E, B)^{-1} = \sum_{n=1}^N \vec{v}_{nl} (E_{nl} - E)^{-1} \vec{v}_{nl}^\top. \quad (12.23)$$

Note that the dependence on B on the right-hand side is implicit in the eigenvectors. We introduce this in Eq. (12.20) and receive

$$\begin{aligned} R_l(E, B) &= \sum_{n=1}^N \frac{\sum_{i=1}^N \frac{\hbar^2}{2\mu a} v_{nl,i} \varphi_i(r) \sum_{j=1}^N v_{nl,j} \varphi_j(r)}{E_{nl} - E} \\ &= \sum_{n=1}^N \frac{\gamma_{nl}^2}{E_{nl} - E}, \end{aligned} \quad (12.24)$$

where we define the so-called reduced width amplitudes

$$\gamma_{nl} = \sqrt{\frac{\hbar^2}{2\mu a}} \sum_{i=1}^N v_{nl,i} \varphi_i(r)$$

and with $v_{nl,i}$ as the i -th component of eigenvector \vec{v}_{nl} [173].

For solutions with positive energies the final step is the determination of the scattering the scattering matrix U_l . From the continuity condition for the wave function at $r = a$ and the defining relation for the R -matrix (12.11) we obtain

$$C_l(I_l(ka) - U_l O_l(ka)) = u_l^{\text{int}}(a) = R_l(E, B)(a u_l'(a) - B u_l(a)) \quad (12.25)$$

which we can solve for the scattering matrix by introducing once more the external wave function at the channel radius in the right-hand side

$$\begin{aligned} I_l(ka) - U_l O_l(ka) &= R_l(E, B) \left(ka(I_l'(ka) - U_l O_l'(ka)) - B(I_l - U_l O_l(ka)) \right) \\ \Rightarrow U_l &= \frac{I_l(ka) \left(1 - R_l(E, B) \left(ka \frac{I_l'(ka)}{I_l(ka)} - B \right) \right)}{O_l(ka) \left(1 - R_l(E, B) \left(ka \frac{O_l'(ka)}{O_l(ka)} - B \right) \right)} \end{aligned} \quad (12.26)$$

$$= e^{2i\phi_l} \frac{1 - R_l(E, B) \left(ka \frac{I_l'(ka)}{I_l(ka)} - B \right)}{1 - R_l(E, B) \left(ka \frac{O_l'(ka)}{O_l(ka)} - B \right)}, \quad (12.27)$$

where $\phi_l(ka) = -\arctan\left(\frac{F_l(ka)}{G_l(ka)}\right)$ holds. We further simplify this expression by defining

$$L_l = ka \frac{O_l'(ka)}{O_l(ka)} = S_l(ka) + iP_l(ka), \quad (12.28)$$

with the so-called shift factor S_l and the penetration factor P_l . In practice they can be computed by

$$P_l(E) = \frac{ka}{F_l(ka)^2 + G_l(ka)^2}, \quad (12.29)$$

$$S_l(E) = P_l(E)(F_l(ka)F_l'(ka) + G_l(ka)G_l'(ka)). \quad (12.30)$$

Inserting Eqs. (12.29) and (12.30) with help of definition (12.28) in Eq. (12.27) yields the final result for the scattering matrix

$$U_l(E) = e^{2i\delta_l(E)} = e^{2i\phi_l} \frac{1 - (S_l(E) - B)R_l(E, B) + iP_l(E)R_l(E, B)}{1 - (S_l(E) - B)R_l(E, B) - iP_l(E)R_l(E, B)}. \quad (12.31)$$

As we have discussed in Section 10 the scattering matrix elements fully determine the scattering amplitude as evident from Eq. (10.11). Therefore, knowing the scattering matrix U_l we are able to compute the scattering observables we are interested in such as cross-sections or polarization observables. Note that it can be shown that the scattering matrix (12.31) is independent of the boundary parameter B [173]. The scattering phase shifts can be computed by

$$\delta_l = \phi_l + \arctan\left(\frac{P_l(E)R_l(E, B)}{1 - (S_l(E) - B)R_l(E, B)}\right). \quad (12.32)$$

An important feature of the R -matrix theory for the development of a unified theory of nuclear structure and reactions is its ability to solve Eq. (12.13) also for the bound states of the system, i.e., to obtain the solutions of the radial Schrödinger equation at negative energies. Following Ref. [198] we make a convenient choice of the boundary parameter B such that the right-hand side of Eq. (12.17) vanishes, i.e., we choose

$$B = 2\kappa_B a \frac{W'_{\eta, l+1/2}(2\kappa_B a)}{W_{\eta, l+1/2}(2\kappa_B a)}. \quad (12.33)$$

Due to the Dirac delta function in the Bloch operator this cancels the right-hand side and we are left with the solution of

$$\sum_{j=1}^N C_{ij}(0, B)\varphi_j(r) c_j = E_B c_i, \quad (12.34)$$

with matrix C as defined in Eq. (12.17). This resembles a standard eigenvalue problem, however, the boundary parameter B depends on the binding energy E_B . Therefore, we solve Eq. (12.34) using an iterative procedure starting with $B = 0$ corresponding to $E_B = 0$. At convergence of the binding energies we solve the eigenvalue problem and calculate the coefficients c_j , which in turn yield the internal wave function.

12.2 The Calculable R -Matrix in Multi-Channel Scattering

In the previous subsection we presented a brief summary of necessary steps towards the determination of the scattering matrix and phase shifts for single-channel problems. Now, we aim at the generalization of this approach to multi-channel scattering problems, as needed in the NCSM/RGM approach discussed in Section 11 and the NCSMC formalism in Section 14. The generalization to more than one channel does not change the general features of the R -matrix and also its derivations follows the same strategy as in the single-channel case.

The first generalization towards a multi-channel scattering theory is obviously the emergence of additional channels labelled by ν in the expansion of the partial wave states

$$|\Psi^{JM\pi T}\rangle = \sum_{\nu} \int dr r^2 \frac{u_{\nu}(r)}{r} \hat{\mathcal{A}}_p [(|\phi_{1\nu}\rangle \otimes |\phi_{2\nu}\rangle)^{ST} \otimes |rlm\rangle]^{JM\pi TM_T}, \quad (12.35)$$

where restrict ourselves to binary-cluster channels. With help of this expansion we have to solve the set of radial Schrödinger equations

$$\sum_{\nu'} \left[\left(-\frac{\hbar^2}{2\mu_{\nu}} \frac{\partial^2}{\partial r^2} + \frac{\hbar^2 l_{\nu}(l_{\nu}+1)}{r^2} + E_{\nu} - E \right) \delta_{\nu',\nu} + V_{\nu',\nu}(r) \right] u_{\nu'}(r) = 0 \quad (12.36)$$

As before, we require the potentials to fulfill the asymptotic behavior

$$V_{\nu',\nu}(r) \xrightarrow{r \rightarrow \infty} \frac{Z_{1\nu} Z_{2\nu} e^2}{r} \delta_{\nu',\nu} \quad (12.37)$$

so that we are allowed to make use of the external wave functions from pure Coulomb scattering. Hence, we have

$$u_{\nu(v_0)}^{\text{ext}}(r) = \nu_{\nu}^{-\frac{1}{2}} (I_{\nu}(k_{\nu} r) \delta_{\nu, v_0} - U_{\nu v_0} O_{\nu}(k_{\nu} r)) \quad (12.38)$$

for open channels, i.e., $E > E_{\nu}$, where we ensure that incoming flux can only occur a chosen entrance channel labelled by v_0 . For closed channels with $E < E_{\nu}$ we adopt

$$u_{\nu(v_0)}^{\text{ext}}(r) = A_{\nu v_0} W_{-\eta_{\nu}, l + \frac{1}{2}}(2\kappa_{\nu} r). \quad (12.39)$$

The definition of the multi-channel R -matrix is given by

$$u_{\nu}(a) = \sum_{\nu'} \sqrt{\frac{\mu_{\nu}}{\mu_{\nu'}}} R_{\nu',\nu}(E) (a u'_{\nu'}(a) - B_{\nu'} u_{\nu'}(a)), \quad (12.40)$$

where $R_{\nu',\nu}$ are now matrix elements of the symmetric R -matrix after which the whole approach is named. The dimension of the R -matrix is always equal to the number of included channels independent of the energy. Following the same arguments as in the single-channel case, we define for the multi-channel formalism a set of Bloch operators as

in Eq. (12.12) but with an additional channel index

$$\mathcal{L}_\nu = \frac{\hbar^2}{2\mu_\nu} \delta(r-a) \left(\frac{d}{dr} - \frac{B_\nu}{r} \right), \quad (12.41)$$

and where the boundary parameters B_ν are chosen as zero or as in Eq. (12.33) for open and closed channels, respectively [173].

Accordingly, the set of Bloch-Schrödinger equations is given by

$$\sum_{\nu'} \left[\left(-\frac{\hbar^2}{2\mu_{\nu'}} \frac{\partial^2}{\partial r^2} + \frac{\hbar^2 l_\nu(l_\nu+1)}{r^2} + \mathcal{L}_{\nu'} + E_\nu - E \right) \delta_{\nu',\nu} + V_{\nu'\nu}(r) \right] u_{\nu'}^{\text{int}}(r) = \mathcal{L}_\nu u_\nu^{\text{ext}}(r) \quad (12.42)$$

with the additional conditions $u_\nu^{\text{ext}}(a) = u_\nu^{\text{int}}(a)$. We skip the formal solution in terms of a Green's function here and investigate immediately the practically relevant spectral decomposition of the Green's functions with help of an expansion of the internal wave functions over the basis functions $\varphi_j(r)$, i.e.,

$$u_\nu^{\text{int}}(r) = \sum_{j=1}^N c_{\nu j} \varphi_j(r). \quad (12.43)$$

We insert this expansion for u_ν^{int} in the ν -th Bloch-Schrödinger equation and project it on the basis function $\varphi_i(r)$ yielding

$$\begin{aligned} \sum_{\nu'} \sum_{j=1}^N \underbrace{\left[\int dr \varphi_i(r) \left(\left(-\frac{\hbar^2}{2\mu_{\nu'}} \frac{\partial^2}{\partial r^2} + \frac{\hbar^2 l_\nu(l_\nu+1)}{r^2} + \mathcal{L}_{\nu'} + E_\nu - E \right) \delta_{\nu',\nu} + V_{\nu'\nu} \right) \varphi_j(r) \right]}_{\equiv C_{\nu i, \nu' j}(E, B_\nu)} c_{\nu' j} \\ = \varphi_i(a) \frac{\hbar^2}{2\mu_\nu a} (a u_\nu^{\text{ext}}(a) - B_\nu u_\nu^{\text{ext}}(a)), \end{aligned} \quad (12.44)$$

where we define the expression inside the brackets as matrix elements $C_{\nu i, \nu' j}(E, B_\nu)$. By multiplication with the inverse matrix C^{-1} from the left we solve for the expansion coefficients $c_{\nu j}$ and obtain for the internal wave function evaluated at the channel radius

$$u_\nu^{\text{int}}(a) = \sum_{\nu'} \sum_{j=1}^N \sum_{i=1}^N \varphi_j(a) (C^{-1})_{\nu j, \nu' i} \varphi_i(a) \frac{\hbar^2}{2\mu_\nu a} (a u_{\nu'}^{\text{ext}} - B_{\nu'} u_{\nu'}^{\text{ext}}(a)). \quad (12.45)$$

By comparison to Eq. (12.40) we read off the R -matrix elements as

$$R_{\nu'\nu} = \frac{\hbar^2}{2\sqrt{\mu_\nu \mu_{\nu'}} a} \sum_{j=1}^N \sum_{i=1}^N \varphi_j(a) (C^{-1})_{\nu j, \nu' i} \varphi_i(a). \quad (12.46)$$

As in the single-channel formalism, diagonalizing the matrix $C(E, B_\nu)$ at zero energy allows for the calculation of its inverse matrix using the spectral decomposition with respect to

the eigenvectors $\vec{v}_{n,\nu}$ of $C(0, B_\nu)$

$$C^{-1} = \sum_n \vec{v}_{n,\nu} \frac{1}{E_{n,\nu} - E} \vec{v}_{n,\nu}^\top, \quad (12.47)$$

where the number of summands is determined by the number of included channels times the number of considered basis functions N . The $E_{n,\nu}$ are the eigenvalues of $C(0, B_\nu)$. Finally, we can convert the R -matrix elements into the familiar form

$$R_{\nu\nu'} = \sum_n \frac{\gamma_{n\nu} \gamma_{n\nu'}}{E_{n,\nu} - E} \quad (12.48)$$

with the reduced-width amplitudes $\gamma_{n\nu} = \sqrt{\frac{\hbar^2}{2\mu_\nu a}} \sum_{i=1}^N v_{n,\nu i} \varphi_i(a)$.

Finally, we deduce the scattering matrix from

$$\begin{aligned} \sum_{\nu'} v_\nu^{-\frac{1}{2}} (I_\nu(k_\nu a) \delta_{\nu,\nu'} - U_{\nu\nu'} O_\nu(k_\nu a)) \\ = \sum_{\nu'} \sqrt{\frac{\mu_\nu}{\mu_{\nu'}}} v_{\nu'}^{-\frac{1}{2}} R_{\nu'\nu} \left[k_{\nu'} a (I_{\nu'}(k_{\nu'} a) \delta_{\nu'\nu} - U_{\nu\nu'} O_{\nu'}(k_{\nu'} a) \right. \\ \left. - B_{\nu'} (I_{\nu'}(k_{\nu'} a) \delta_{\nu'\nu} - U_{\nu\nu'} O_{\nu'}(k_{\nu'} a)) \right], \end{aligned} \quad (12.49)$$

where we used the continuity of the wave function at the channel radius and the definition of the multi-channel R -matrix. We isolate all terms that contain scattering matrix elements $U_{\nu\nu'}$ on the left-hand side and collect all other terms on the right-hand side, and we make use of $\sqrt{\frac{\mu_\nu}{\mu_{\nu'}}} = \sqrt{\frac{v_{\nu'}}{v_\nu}}$ to identify the structure of the equation as

$$\sum_{\nu'} Z_{\nu\nu'} U_{\nu'\nu_0} = Z_{\nu\nu_0}^*. \quad (12.50)$$

In terms of matrices we then obtain the scattering matrix U by multiplication with the inverse of matrix Z from the left

$$U = Z^{-1} Z^*, \quad (12.51)$$

where the elements of the matrix Z are given by

$$Z_{\nu\nu'} = \frac{1}{\sqrt{k_{\nu'} a}} (O_\nu(k_\nu a) \delta_{\nu'\nu} - k_{\nu'} a R_{\nu\nu'} O_{\nu'}(k_{\nu'} a) - B_{\nu'} R_{\nu\nu'} O_{\nu'}(k_{\nu'} a)). \quad (12.52)$$

From diagonalizing the U matrix using a matrix S obtained from the eigenvectors of U we can extract the eigenphase shifts δ_n from with help of

$$S^\top U S = e^{2i\delta}, \quad (12.53)$$

where δ is a diagonal matrix with the eigenphase shifts as diagonal entries.

The treatment of bound states is exactly analogous as described at the end of the previ-

ous section for the single channel case. The only difference induced by the multi-channel problem is the fact that the scattering matrix U_l is now really a matrix while it was a simple coefficient in the single-channel case. For the iterative solution of Eq. (12.44) we start with $B_\nu = 0$ for all channels.

12.3 R-Matrix Theory on a Lagrange Mesh

So far we have discussed the solution of the radial Schrödinger equation using the R -matrix theory which is based on the generic expansion of the internal wave function over N basis functions $\varphi_j(r)$,

$$u_\nu^{\text{int}}(r) = \sum_{j=1}^N c_{\nu j} \varphi_j(r). \quad (12.54)$$

Up to now we did not specify the basis functions and, actually, various choices are possible and discussed in the literature, see, e.g., Refs. [173, 199, 195]. We stress again, that neither the functions are required to meet any boundary conditions at the channel radius nor they need to be orthogonal. However, of course the quality of the matching of the internal and external wave functions and, thus, the accuracy of the obtained phase shifts depend on the conformity of the functions with the problem. For example, it is known that choosing sine functions does not lead to accurate results because the derivatives of all basis functions vanish at the channel radius as discussed in detail in [173]. Another common choice are Gaussian functions, which one the one hand often leads to analytically solvable integrals but on the other hand they contain parameters that need to be adapted to the considered system [173, 196]. In the following we will give the details about the Lagrange basis functions, which we use to obtain the results of Sections 13 and 14. For an overview of Lagrange functions corresponding to different kinds of meshes see Ref. [195].

We employ a set of N functions $\varphi_i(r)$ which are associated with a mesh of points ax_i on the internal region $[0, a]$ such that the so-called Lagrange conditions

$$\varphi_i(ax_j) = (a\lambda_i)^{-\frac{1}{2}} \delta_{i,j}, \quad (12.55)$$

hold. Hence, all functions vanish at all these mesh points except one, where the coefficients λ_i are given by the weights of a Gauss quadrature

$$\int_0^1 f(r) dr \approx \sum_{i=1}^N \lambda_i f(r_i). \quad (12.56)$$

Functions fulfilling these conditions are so-called Lagrange functions, and various sets of functions with corresponding meshes are possible [195]. In the following we adopt Lagrange functions constructed from Legendre polynomials and the mesh points are fixed by the roots of the Legendre polynomials. This choice originally has been applied to the R -matrix theory by Malegat in Ref. [200], and was further developed to include multiple channels [201] and to handle non-local interactions by Hesse et al. in Ref. [202]. Both ex-

tensions are important for the applications throughout the next sections. Thus, we adopt the N Lagrange functions of Ref. [202]

$$\varphi_i(r) = (-1)^{N+i} \left(\frac{r}{ax_i} \right) \sqrt{ax_i(1-x_i)} \frac{P_N(2\frac{r}{a} - 1)}{r - ax_i}, \quad (12.57)$$

with the Legendre polynomials of order N and where the x_i are the roots of the shifted Legendre polynomial, i.e., they fulfill

$$P_N(2x_i - 1) = 0. \quad (12.58)$$

The weights λ_i of Eq. (12.55) correspond to a Gauss-Legendre quadrature in the interval $[0, 1]$. The Lagrange functions are continuous and indefinitely differentiable over the complete interval, however they are not orthogonal due to the prefactor $\frac{r}{ax_i}$. However, all integrals which will be evaluated using the Gauss-Legendre quadrature approximation such that the basis functions become approximately orthogonal in the sense

$$\int_0^a \varphi_i(r) \varphi_j(r) \approx \delta_{i,j}, \quad (12.59)$$

which still leads to accurate results as found in Ref. [199]. The introduction of the regularization via the prefactor $\frac{r}{ax_i}$ offers the possibility to retain the exact matrix elements of singular potentials in spite of using the Gauss quadrature approximation. In the following this is important to treat the singularities at $r = 0$ in the Coulomb and centrifugal barrier potential [203].

We employ the Lagrange mesh technique to calculate the matrix elements $C_{vi,v'j}$ in Eq. (12.44) defined as

$$C_{vi,v'j} = \int dr \varphi_i(r) \left(\left(-\frac{\hbar^2}{2\mu_v} \frac{\partial^2}{\partial r^2} + \frac{\hbar^2 l_v(l_v + 1)}{r^2} + \mathcal{L}_v + E_v - E \right) \delta_{v,v'} + V_{v'v} \right) \varphi_j(r). \quad (12.60)$$

The first term corresponds to the matrix elements of the kinetic energy $T_{ij}^{(v)}$, which are diagonal in the channel index. Following Ref. [204], together with the matrix elements for the Bloch operator $\mathcal{L}_{ij}^{(v)}$ and using the Lagrange functions (12.57), they are exactly given by

$$T_{ii}^{(v)} + \mathcal{L}_{ii}^{(v)}(0) = \frac{1}{6a^2 x_i(1-x_i)} \left[4N(N+1) + 3 + \frac{1-6x_i}{x_i(1-x_i)} \right], \quad (12.61)$$

and for non-diagonal matrix elements by

$$T_{ij}^{(v)} + \mathcal{L}_{ij}^{(v)}(0) = \frac{(-1)^{i+j}}{2a^2 \sqrt{x_i x_j (1-x_i)(1-x_j)}} \left[N(N+1) + 1 + \frac{x_i + x_j - 2x_i x_j}{(x_i - x_j)^2} - \frac{1}{1-x_i} - \frac{1}{1-x_j} \right] \quad (12.62)$$

The next term constitutes the centrifugal barrier which has a singularity at $r = 0$. As mentioned above and discussed in more detail in Ref. [199] the regularization of the Lagrange functions ensures the exact evaluation of this term using the Gauss quadrature, i.e., one

obtains

$$\int_0^a \varphi_i(r) \frac{\hbar^2 l_v(l_v + 1)}{r^2} \varphi_j(r) dr = \frac{\hbar^2 l_v(l_v + 1)}{a^2 x_i^2} \delta_{i,j}. \quad (12.63)$$

This allows the accurate treatment of the centrifugal term also for non-zero relative orbital angular momenta l_v [199, 203]. The contributions to matrix elements of the Bloch operator for nonzero B_v can be computed by

$$\varphi_i(r) \frac{\delta(r-a)}{r} \varphi_j(r) = \frac{(-1)^{i+j}}{a^2 \sqrt{x_i x_j (1-x_i)(1-x_j)}} \quad (12.64)$$

given in Ref. [204]. We split the matrix elements of the potential part in two parts: The matrix elements containing the local interaction become

$$U_{ij} = \int_0^a \varphi_i(r) U(r) \varphi_j(r) dr \approx U(ax_i) \delta_{i,j}. \quad (12.65)$$

The second part handles the non-local contributions to the potentials, which have been treated in the *R*-matrix on a Lagrange mesh formalism first in Ref. [202]. The corresponding matrix elements are given by

$$W_{ij} = \int_0^a \int_0^a \varphi_i(r) W(r, r') \varphi_j(r') dr dr' \approx a \sqrt{\lambda_i \lambda_j} W(ax_i, ax_j), \quad (12.66)$$

where again the Gauss quadrature has been used. Finally, the last two contributions are simply given by Eq. (12.59). Altogether, we can compute the matrix elements C_{v_i, v'_j} just from the knowledge of the potentials at the mesh points, i.e., in particular analytic evaluations of integrals are avoided and thus the simplicity of a mesh calculation is retained. In spite of the Gauss quadrature the matrix $C(E, B_v)$ remains symmetric due to the exact treatment of the kinetic part. Having computed the matrix $C(E, B_v)$ we can obtain the *R*-matrix as explained after Eq. (12.17) in the previous subsection. We note that so-called forbidden states, i.e., non-vanishing radial wave functions that are solutions to the RGM equations for all energies, are removed by dropping those eigenvectors with eigenvalues close to zero in the spectral decomposition of $C(E, B_v)$. Their numbers increases with larger numbers of used basis function N , i.e., with increasing accuracy [202]. For further details about this procedure see Refs. [205, 172].

The accuracy of the *R*-matrix on a Lagrange mesh method has been benchmarked in different scenarios: the comparison in case of an analytically solvable problem [201], as well as the comparison to calculations using alternative basis functions [199, 173] and also benchmarks of the Lagrange mesh against exact calculations with Lagrange functions [203, 199] did prove its very good accuracy. At the same time it is very efficient thanks to the significantly simplified computation of the integral terms. Compared to finite-difference methods already few basis functions, i.e., few mesh points, yield already accurate results [202]. For our results presented in Sections 13 and 14 we typically use 40

basis functions. Furthermore, as can be seen from Eq. (12.54) another advantage is the knowledge of the wave function not only at the mesh points, but over the complete interval $(0, a)$ such that subsequent calculations of matrix elements with respect to the wave function may be obtained exactly.

SECTION 13

Nucleon- ^4He Scattering

As first application of the extended NCSM/RGM formalism, capable to explicitly include 3N interactions, we study nucleons scattering off a ^4He target. Although this constitutes one of the simplest scattering systems, it exhibits interesting features that allow to analyze consequences of 3N interactions for scattering observables. In earlier studies of the NCSM/RGM formalism with NN interactions [47, 48] the spin-orbit splitting between the $^2P_{3/2}$ and $^2P_{1/2}$ resonances has been found too small. Consequently, we expect the inclusion of 3N interactions to enlarge this splitting. This has been first investigated by means of Green's function Monte Carlo (GFMC) calculations in Ref. [206], using the local Argonne V18 potential [8] and the phenomenological Urbana IX and Illinois2 3N interactions [39]. The nucleon- ^4He scattering discussed in the following constitutes the first investigation with chiral NN+3N Hamiltonians and also their first application to scattering observables for systems with $A > 4$ without approximation. This emphasizes that the extension of the NCSM/RGM formalism to explicit 3N interactions paves the way for ab-initio calculations of a wealth of scattering observables based on chiral NN+3N interactions.

Another favorable property of the nucleon- ^4He system is the presence of only a single open binary-cluster channel up to fairly high energies beyond 15 MeV, due to the tightly bound ^4He target. This makes it an ideal benchmark system for scattering calculations in general and, in particular, for the two alternative approaches for the inclusion of the 3N interaction into the NCSM/RGM formalism discussed in Section 11.2.4.

In the first subsection we present a comprehensive convergence analysis of the different truncations involved in the NCSM/RGM approach, including the convergence with respect to the number of included channels, here given by the number of excited states of ^4He . In addition, the dependence on the SRG flow parameter and the different possibilities to treat the isospin are investigated in this section. Afterwards, in Section 13.2, we concentrate on the 3N interaction effects on scattering phase shifts with special attention to the distinction of effects originating from the SRG-induced 3N and from the initial chiral 3N interaction on the P -wave spin-orbit splitting mentioned above. Finally, we investigate the sensitivity of differential cross sections and analyzing powers to the inclusion of 3N

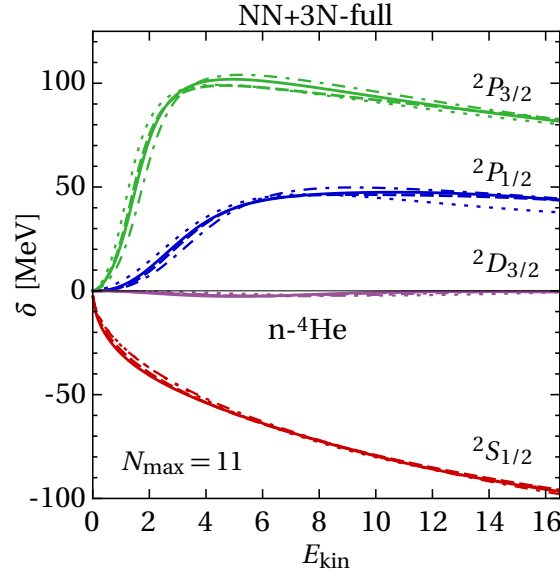


Figure 13.1 – Convergence of the ${}^2S_{1/2}$, ${}^2P_{1/2}$, ${}^2P_{3/2}$ and ${}^2D_{3/2}$ partial-wave phase shifts with respect to the model-space size, for $N_{\max} = 7$ (.....), 9 (---), 11 (---), and 13 (—) from single-channel calculations including the ground-state of ${}^4\text{He}$. The NN+3N-full Hamiltonian is applied at SRG flow-parameter $\alpha = 0.0625 \text{ fm}^4$ with $E_{3\max} = 14$ and $\hbar\Omega = 20 \text{ MeV}$. (published in [51])

interactions in Section 13.3. The findings of this section have resulted in the collaborative publication Ref. [51].

13.1 Convergence Studies of Scattering Phase Shifts

This section is dedicated to a comprehensive analysis of all relevant parameter variations of the NCSM/RGM with explicit 3N interactions. We concentrate on the effects on scattering phase shifts, from which all other scattering observables can be deduced. Moreover, we focus on the ${}^2S_{1/2}$, ${}^2P_{1/2}$, ${}^2P_{3/2}$ and ${}^2D_{3/2}$ phase shifts (${}^{2s+1}l_J$), because all remaining phase shifts are very small, although they are not always negligible as discussed in Section 13.3. The NCSM/RGM equations (11.20) are solved using the calculable R -matrix method on a Lagrange mesh described in Section 12. To expand the wave function in the internal region we use 40 lattice points, and the internal and external regions are matched at the channel radius of 18 fm. Beyond the channel radius the clusters interact via the average Coulomb force only. We have checked explicitly the independence of all following results from these parameters. We apply the identical SRG-transformed Hamiltonians as in Part II, in particular the standard initial chiral 3N interaction at N²LO with cutoff momentum $\Lambda_{3N} = 500 \text{ MeV}/c$.

13.1.1 Dependence on the Model-Space Truncation N_{\max}

First, we explore the convergence of elastic neutron- ${}^4\text{He}$ (n - ${}^4\text{He}$) phase shifts with respect to the HO model-space truncation parameter N_{\max} . The same HO model-space size is used consistently in both, the expansion of the localized parts of the NCSM/RGM kernels

(cf. Eqs. (11.43) and 11.44), and the NCSM when computing the eigenstates of the ${}^4\text{He}$ target that enter expansion (11.4). We use the chiral NN+3N-full Hamiltonian evolved to SRG flow-parameter $\alpha = 0.0625\text{fm}^4$ and the HO frequency $\hbar\Omega = 20\text{MeV}$. In Figure 13.1 we show the (first four) elastic scattering phase shifts for $N_{\text{max}} = 7, 9, 11$, and 13 obtained from a single-channel calculation including the ground state (g.s.) of ${}^4\text{He}$ only. All phase shifts exhibit a good rate of convergence: while the steps from $N_{\text{max}} = 7$ through 9 to 11 are visible, the phase shifts for $N_{\text{max}} = 11$ and $N_{\text{max}} = 13$ are practically identical. The only exception is the ${}^2P_{3/2}$ phase shift between 4 and 10 MeV, where we find a difference of about 5 deg or less. Moreover, this convergence behavior is similar to the one obtained in Ref. [121] with the NCSM/RGM approach using NN-only Hamiltonians at the same SRG flow parameter. Accordingly, we perform some of the following convergence studies using the smaller $N_{\text{max}} = 11$ to cope with the large-scale calculations.

Finally, we list in Table 13.1 the energies of the first seven ${}^4\text{He}$ eigenstates, which we utilize in the calculations later on. We note that the ground-state energy is well converged with respect to N_{max} . For $\alpha = 0.0625\text{fm}^4$ the change between the energies for $N_{\text{max}} = 10$ to $N_{\text{max}} = 12$ is below 0.2%, and for $\alpha = 0.08$ and 0.04fm^4 below 0.1% and below 0.7%, respectively.

13.1.2 Dependence on $E_{3\text{max}}$

Next we study the dependence of the phase shifts on different truncations $E_{3\text{max}}$ of the 3N matrix elements. Recall that calculations for a specific N_{max} in principle require 3N matrix elements up to $E_{3\text{max}} = 2 \cdot N_{\text{max}}$ for a complete calculation, but typically only matrix element sets with much smaller $E_{3\text{max}}$ are manageable. Hence, the $E_{3\text{max}}$ truncation is not consistent with the NCSM/RGM model space, similarly as for the coupled-cluster approach discussed in Part II, and could lead to spurious effects. In Figure 13.2 we present the n- ${}^4\text{He}$ phase shifts computed at $N_{\text{max}} = 11$ and using $E_{3\text{max}} = 10, 12$ and 14 for the NN+3N-induced (left panel) and the NN+3N-full Hamiltonian (right panel). For both Hamiltonians we find the $E_{3\text{max}} = 12$ and 14 results agree very well, i.e., they are practically on top of each other. From analogous studies for different combinations of α , $\hbar\Omega$ and N_{max} we confirm that the $E_{3\text{max}}$ truncation leads to less uncertainties than other parameters such as the NCSM/RGM model space truncation. For all calculations presented in the following we adopt $E_{3\text{max}} = 14$.

Table 13.1 – Energies of the first seven eigenstates of ${}^4\text{He}$ in MeV at $N_{\text{max}} = 12$ (13 for negative parity) for the three SRG flow parameters and computed with the NN+3N-full Hamiltonian at $\hbar\Omega = 20\text{MeV}$. The experimental energies are listed in the last row.

α [fm ⁴]	g.s.	0 ⁺ 0	0 ⁻ 0	2 ⁻ 0	2 ⁻ 1	1 ⁻ 1	1 ⁻ 0
0.04	-28.36	-5.37	-6.38	-5.24	-3.86	-3.58	-2.73
0.0625	-28.44	-5.62	-6.51	-5.39	-4.03	-3.77	-2.95
0.08	-28.46	-5.70	-6.55	-5.44	-4.09	-3.84	-3.03
exp. [81]	-28.29	-8.08	-7.28	-6.45	-4.99	-4.65	-4.04

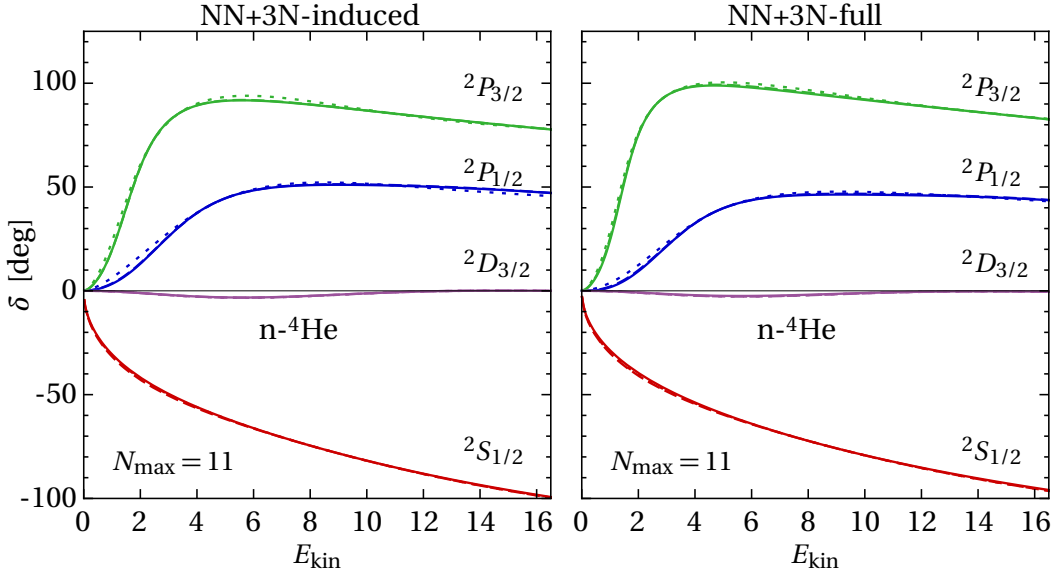


Figure 13.2 – Phase shifts $^2S_{1/2}$, $^2P_{1/2}$, $^2P_{3/2}$ and $^2D_{3/2}$ for $E_{3\text{max}} = 10$ (.....), 12 (---) and 14 (—) from single-channel calculations including the ground-state of ^4He for the NN+3N-induced (left-hand panel) and the NN+3N-full (right-hand panel) Hamiltonians. Remaining parameters are $N_{\text{max}} = 11$, $\alpha = 0.0625 \text{ fm}^4$, $E_{3\text{max}} = 14$, and $\hbar\Omega = 20 \text{ MeV}$. (published in [51])

13.1.3 Dependence on the HO Frequency

We proceed with the sensitivity of the n- ^4He (g.s.) phase shifts to the HO frequency $\hbar\Omega$ by varying the frequency from 16 through 20 to 24 MeV, and again we use $N_{\text{max}} = 11$ and $\alpha = 0.0625 \text{ fm}^4$. The phase shifts for the larger two frequencies are practically identical with only marginal deviations around the $^2P_{1/2}$ and $^2P_{3/2}$ resonance positions. For the lower frequency $\hbar\Omega = 16 \text{ MeV}$ the observed deviations are slightly enhanced. However, from our discussions in Sections 5 and 9 we know that here the finite SRG model space and also the $E_{3\text{max}}$ parameter can affect the frequency dependence. Nevertheless, overall we find only minor dependence on the HO frequency and stick to $\hbar\Omega = 20 \text{ MeV}$ in the following.

13.1.4 Dependence on the Number of Excitations of the ^4He Target

As discussed in Section 10, for scattering calculations involving many-body systems typically only a subset of a priori most relevant channels can be included in the calculation. To make sure the selection provides accurate results one needs to study the convergence with respect to the considered channels. Due to the single open channel of the nucleon- ^4He system up to fairly high energies, we adopt here the NCSM/RGM model space characterized by expansion (11.4) in terms of binary-cluster channel states that are, for the single-nucleon projectile formalism, given by Eq. (11.24). Consequently, we need to study the convergence with respect to the NCSM/RGM model-space size by including more and more channels, i.e., excited states of ^4He , into our investigations. Each included channel increases the computational cost for the Norm and Hamiltonian kernels. In Figure 13.4 we present the convergence of the n- ^4He phase shifts with respect to the number of excited

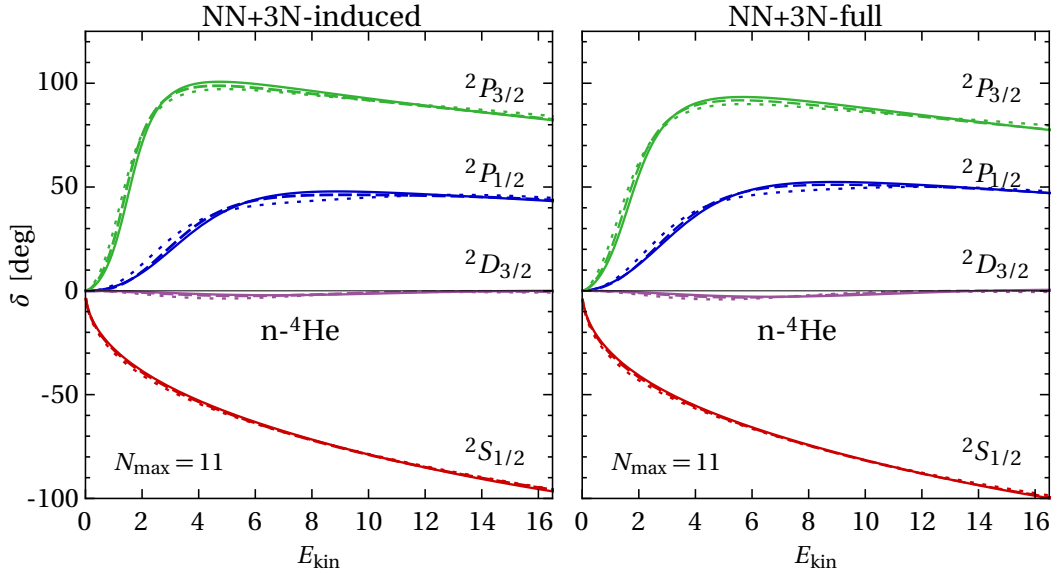


Figure 13.3 – Dependence of the ${}^2S_{1/2}$, ${}^2P_{1/2}$, ${}^2P_{3/2}$ and ${}^2D_{3/2}$ n - ${}^4\text{He}$ phase shifts on the HO frequency for $\hbar\Omega = 16\text{ MeV}$ (.....), $\hbar\Omega = 20\text{ MeV}$ (---) and $\hbar\Omega = 24\text{ MeV}$ (—) from single-channel calculations including the ground-state of ${}^4\text{He}$ for the NN+3N-induced (left-hand panel) and the NN+3N-full (right-hand panel) Hamiltonians. Remaining parameters are $N_{\text{max}} = 11$, $\alpha = 0.0625\text{ fm}^4$ and $E_{3\text{max}} = 14$. (published in [51])

states of the ${}^4\text{He}$ target up to the first seven states ($I_1^{\pi_1} T_1 = \text{g.s.}, 0^+0, 0^-0, 2^-0, 2^-1, 1^-1, 1^-0$). Their energies obtained from the NCSM are listed in Table 13.1. We use the largest model space $N_{\text{max}} = 13$ and the NN+3N-full Hamiltonian evolved to $\alpha = 0.0625\text{ fm}^4$ and $\hbar\Omega = 20\text{ MeV}$. The crucial role of the excited states is evident in particular from the resonant P wave phase shifts: the ${}^2P_{1/2}$ phase shift is enhanced by the inclusion of the negative parity states at energies beyond its resonance position with strongest effects by the 1^- states. The ${}^2P_{3/2}$ phase shift near the resonance energy is strongly influenced by the 2^-0 state and further enhanced by the additional states. In contrast, the phase shift corresponding to the Pauli blocked ${}^2S_{1/2}$ partial wave is mostly insensitive to the polarization effects triggered by inclusion of more channels. The rather slow convergence of the NCSM/RGM with respect to the number of excited states is consistent with Refs. [47, 48] for NN-only Hamiltonians. However, the changes in the phase shifts obtained with six or seven states are acceptably small. Hence, we adopt the inclusion of seven excited states for our studies of the 3N interaction effects and their comparison to experiment in Section 13.2. One reason for the large number of ${}^4\text{He}$ states necessary to reach convergence is connected with the fact that correlations of the A -body system are more conveniently described if the so-called A -body distortion functions (see last line of Eq. (10.4)) considered in the basis. These are not included in the NCSM/RGM model space. However, it is possible to extend the NCSM/RGM approach to account for such contributions. This is the topic of Section 14 and leads to the no-core shell model with continuum approach.

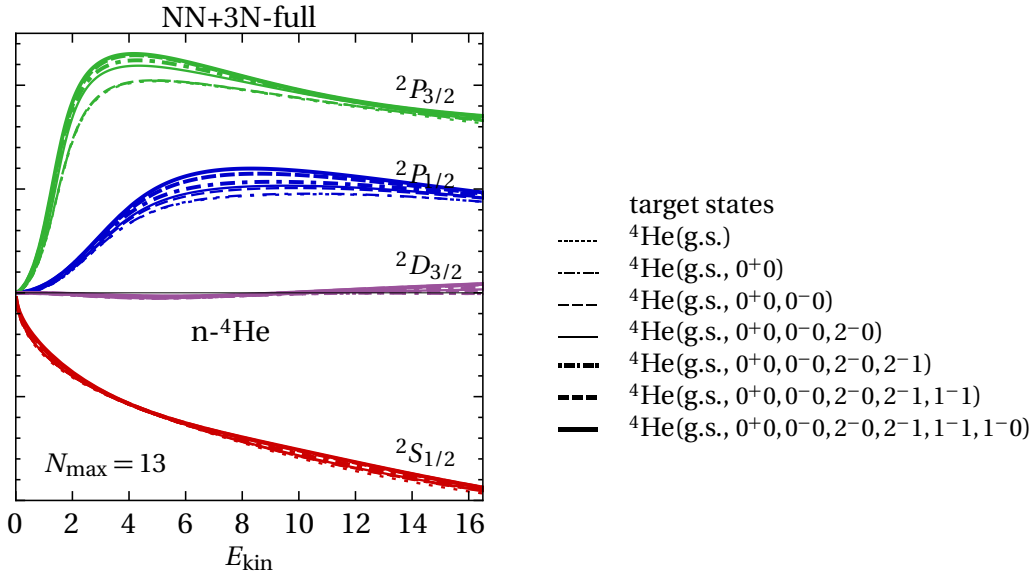


Figure 13.4 – Dependence of the $^2S_{1/2}$, $^2P_{1/2}$, $^2P_{3/2}$ and $^2D_{3/2}$ n-⁴He phase shifts on the NCSM/RGM model space via the successive inclusion of excited states of ⁴He in corresponding multi-channel calculations. Remaining parameters are $N_{\max} = 13$, $\alpha = 0.0625 \text{ fm}^4$ and $E_{3\max} = 14$. (published in [51])

13.1.5 Relevance of Discarded SRG-Induced Multi-Nucleon Forces

Now we study the SRG flow-parameter dependence of the low-energy n-⁴He phase shifts to assess the role of discarded SRG-induced multi-nucleon contributions. In Part II we have emphasized that a reliable assessment the α dependence requires convergence with respect to the model-space size of the approach, see, e.g., Section 6. In addition, we stress that even if no SRG-induced multi-nucleon forces would have been neglected, significant artificial dependencies on the SRG flow parameter can arise from inconsistent truncations are used as, e.g., the $E_{3\max}$ in the NCSM/RGM. Furthermore, the α dependence carried by the NCSM input vectors for the ⁴He target is translated into the NCSM/RGM kernels, too. We investigate this point for SRG flow parameters $\alpha = 0.0625$ and 0.08 fm^4 using the largest accessible model space, i.e., including seven states of ⁴He at $N_{\max} = 13$ and $E_{3\max} = 14$. The results are shown in the left- and right-hand panel of Figure 13.5 for the NN+3N-induced and NN+3N-full Hamiltonian, respectively. The $^2S_{1/2}$ and $^2D_{3/2}$ phase shifts, which we have found well converged with respect to all truncations discussed throughout the previous subsections, are on top of each other. That is, the discarded SRG-induced multi-nucleon interactions are irrelevant for these partial waves. For the $^2P_{1/2}$ and $^2P_{3/2}$ phase shifts the dependence is visible and slightly larger for the NN+3N-full Hamiltonian, but overall very small. Note that these partial waves have shown the largest sensitivities to the truncations studied before, such that our statement above applies and the slight α dependence could be artificial. To confirm the latter point we additionally study the third SRG flow parameter $\alpha = 0.04 \text{ fm}^4$ with the NN+3N-full Hamiltonian and include only four excited states of ⁴He by dropping the 1^- states. The resulting phase shifts are depicted in Figure 13.6. The $^2S_{1/2}$ and $^2D_{3/2}$ phase shifts are again practically identical for all three flow

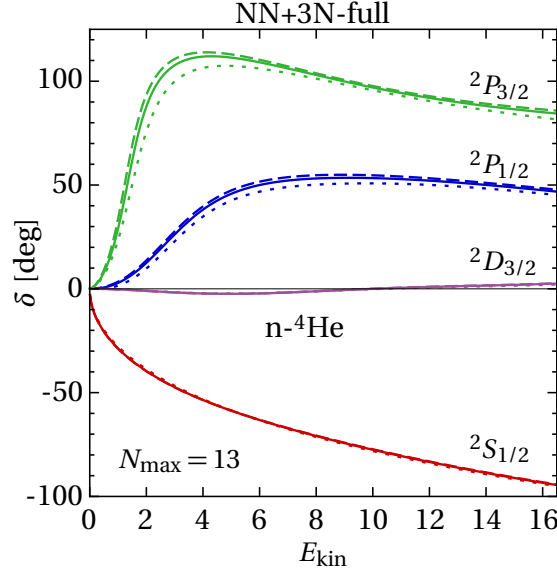


Figure 13.6 – Dependence of the ${}^2S_{1/2}$, ${}^2P_{1/2}$, ${}^2P_{3/2}$ and ${}^2D_{3/2}$ n - ${}^4\text{He}$ phase shifts on the SRG flow parameter for the NN+3N-full Hamiltonians including five eigenstates of ${}^4\text{He}$ ($I_1^{\pi_1} T_1 = g.s., 0^+0, 0^-0, 2^-0, 2^-1$). Shown are results for $\alpha = 0.08$ (---), 0.0625 fm^4 (—), and 0.04 fm^4 (.....). Remaining parameters are $N_{\text{max}} = 13$, $E_{3\text{max}} = 14$, and $\hbar\Omega = 20 \text{ MeV}$. (published in [51])

eraged initial interaction developed in [207]. As a result the total 3N interaction, i.e., the SRG-induced and the transformed chiral contribution, is isospin averaged and Eqs. (11.68) and (11.71) are equivalent. However, the NN interaction, resulting from SRG transformation in two-body space, includes charge dependence effects of both, the nuclear interaction and the proton-proton Coulomb interaction. Thus, for the NN kernels computed with reduced density matrices in spirit of Eq. (11.71), see Ref. [48] for details, the isospin averaged NN interaction is used. In particular, the $T = 1$ matrix elements are obtained via

$$\langle \hat{V}_{T=1}^{\text{NN}} \rangle = c_{pn} \langle \hat{V}_{T=1}^{\text{pn}} \rangle + c_{pp} \langle \hat{V}_{T=1}^{\text{pp}} \rangle + c_{nn} \langle \hat{V}_{T=1}^{\text{nn}} \rangle \quad (13.1)$$

with

$$c_{pn} = \frac{\frac{1}{2}(Z_p N_T + N_p Z_T)}{Z_p Z_T + N_p N_T + \frac{1}{2}(Z_p N_T + N_p Z_T)}, \quad (13.2)$$

$$c_{pn} = \frac{Z_p N_T}{Z_p Z_T + N_p N_T + \frac{1}{2}(Z_p N_T + N_p Z_T)}, \quad (13.3)$$

$$c_{pn} = \frac{N_p N_T}{Z_p Z_T + N_p N_T + \frac{1}{2}(Z_p N_T + N_p Z_T)}, \quad (13.4)$$

with Z_p, N_p and Z_T, N_T as number of protons and neutrons in the projectile and target, respectively [51]. Because our implementation of the NN kernels (11.65) and (11.66) does not rely on this averaging we are in the position to validate the averaging procedure. We compare both approaches in Figure 13.7 using the phase shifts for the four lowest partial waves of proton- ${}^4\text{He}$ scattering, where the effects of the isospin averaging are enhanced due to the relevance of the inter-cluster Coulomb interaction. The calculations include the first four excited states of ${}^4\text{He}$, i.e., in particular the 2^-1 state with non-vanishing isospin, and we employ the NN+3N-full Hamiltonian at $\alpha = 0.0625 \text{ fm}^4$ with $E_{3\text{max}} = 14$. The calculations

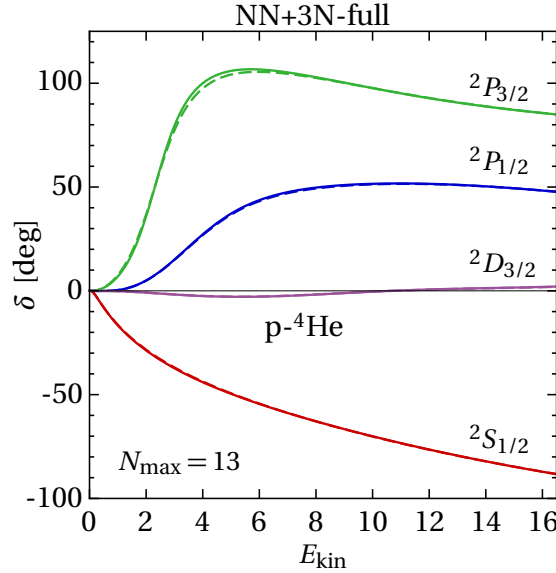


Figure 13.7 – Comparison of the two approaches to treat the isospin in the potential kernels for the example of $p\text{-}^4\text{He}$ scattering phase shifts including 5 eigenstates of ^4He . The isospin dependence is treated exactly in kernels with uncoupled densities (11.65) and (11.66) (—), or using the averaging (13.1) and kernels using reduced coupled densities (11.71) (---). For further details see text. Remaining parameters are $N_{\max} = 13$, $E_{3\max} = 14$, and $\hbar\Omega = 20$ MeV. (published in [51])

with and without isospin averaging are shown as dashed and solid lines, respectively. We find the isospin averaging (13.1) very accurate and slight differences occur only in the $^2P_{3/2}$ phase shift. Thus, the isospin averaging used throughout the initial NCSM/RGM calculations [47, 48] appears reliable as long as the isospin violation of the included target states is small.

13.2 Three-Nucleon Force Effects on Scattering Phase Shifts

Having completed the comprehensive uncertainty analysis of all truncations involved in the NCSM/RGM formalism including 3N interactions in the previous subsection, we now focus on the 3N force effects on the scattering phase shifts. Therefore, we apply the largest NCSM/RGM model space considered before, i.e., including the seven states of ^4He ($I_1^{\pi_1} T_1 = g.s., 0^+0, 0^-0, 2^-0, 2^-1, 1^-1, 1^-0$) at $N_{\max} = 13$ with $\hbar\Omega = 20$ MeV and using the truncation $E_{3\max} = 14$ for the 3N matrix elements. In addition, we adopt $\alpha = 0.0625 \text{ fm}^4$ throughout.

We show in Figure 13.8 the comparison between the scattering phase shifts obtained with the NN-only, the NN+3N-induced, and the NN+3N-full Hamiltonians. First we focus on the $^2S_{1/2}$ and $^2D_{3/2}$ partial waves that we find almost insensitive to the inclusion of 3N interactions. The $^2D_{3/2}$ phase shift is practically identical for all three Hamiltonians. For the $^2S_{1/2}$ phase shift we find small changes if the SRG-induced 3N components are included, and additional slightly smaller changes of opposite sign once the chiral 3N interaction is included. These findings are consistent with the Green's function Monte Carlo results presented in Ref. [206] obtained for the AV18 [8] NN interaction along with

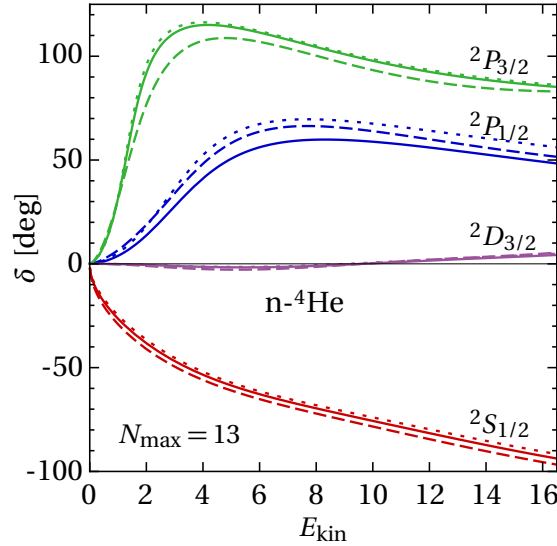


Figure 13.8 – Comparison of the n-⁴He $^2S_{1/2}$, $^2P_{1/2}$, $^2P_{3/2}$ and $^2D_{3/2}$ phase shifts for the NN-only (.....), NN+3N-induced (---) and NN+3N-full (—) Hamiltonians including seven eigenstates of ⁴He and at $N_{\max} = 13$. Remaining parameters are $E_{3\max} = 14$ and $\hbar\Omega = 20$ MeV. (published in [51])

the UIX or IL2 3N interaction models [39]. We find stronger effects of 3N interactions in the P wave phase shifts. As can be seen by comparison to the NN+3N-induced results, both are overestimated by the NN-only Hamiltonian for energies around their respective resonance position and also beyond. Therefore, the inclusion of SRG-induced 3N interactions is crucial to reveal and eliminate the artificial enhancement of the NN-only phase shifts. While the effect of the SRG-induced 3N interactions is quite similar for both P wave phase shifts, they are pushed apart by the chiral 3N interaction. The $^2P_{1/2}$ resonance is slightly broadened and overall its phase shift is further reduced by the chiral 3N interaction. In contrast, the $^2P_{3/2}$ phase shift is increased and ends up almost on top of the NN-only result, which is accidental. Again our results are similar to those obtained in Ref. [206] with the GFMC. In summary, we have found the inclusion of 3N interactions important on the one hand to avoid artificial results caused by discarded SRG-induced 3N contributions and on the other hand to include the additional operators structures of the chiral 3N interaction. Both contributions yield sizable effects in the P wave phase shifts and in particular the splitting between the P wave resonances.

Finally, we explore if the inclusion of the initial chiral 3N interaction helps to improve the agreement with experimental phase shifts. For that we compare in Figure 13.9 the phase shifts obtained from the NN+3N-induced and NN+3N-full Hamiltonians to experimental phase shifts from an accurate phenomenological R matrix analysis of the ⁵He data [208]. We start with the discussion of the n-⁴He case shown in the left-hand panel. We find very good agreement with the experimental phase shifts for the $^2S_{1/2}$, $^2P_{1/2}$ and $^2D_{3/2}$ phase shifts. For the $^2P_{1/2}$ clearly the chiral 3N interaction is responsible for the improved agreement compared to the NN+3N-induced results. However, we also note slightly larger deviations from experiment compared to the NN+3N-induced calculations

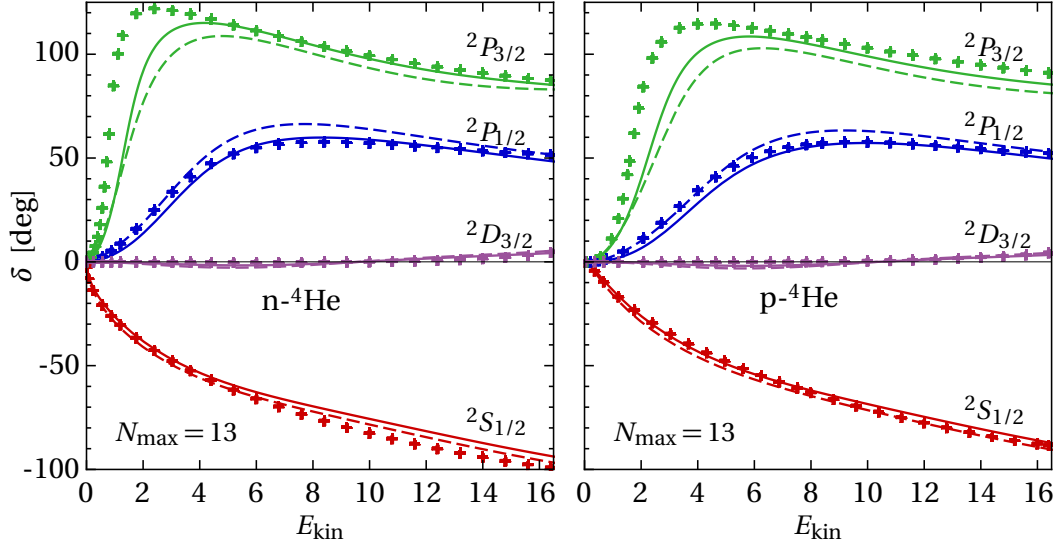


Figure 13.9 – Comparison of the $n\text{-}^4\text{He}$ (left-hand panel) and $p\text{-}^4\text{He}$ (right-hand panel) scattering phase shifts for partial wave $^2S_{1/2}$, $^2P_{1/2}$, $^2P_{3/2}$ and $^2D_{3/2}$ obtained with the NN+3N-induced (---) and NN+3N-full (—) Hamiltonians to experimental phase shifts (+) obtained from R -matrix analysis [208]. The calculations include seven eigenstates of ^4He and use $N_{\text{max}} = 13$. Remaining parameters are $E_{3\text{max}} = 14$ and $\hbar\Omega = 20$ MeV. (published in [51])

for the $^2P_{1/2}$ phase shift below its resonance energy and for the $^2S_{1/2}$ phase shift at large energies. The $^2P_{3/2}$ phase shift is clearly enhanced by the chiral 3N interaction leading to quite good agreement with experiment beyond 4 MeV energy in the center-of-mass frame. As mentioned before, a particularly interesting feature in $n\text{-}^4\text{He}$ scattering is the spin-orbit splitting between the P waves. When we compare the difference of the resonance positions of both P wave phase shifts obtained with the NN+3N-induced Hamiltonian to the splitting resulting from the additional inclusion of the chiral 3N, the latter indeed increases the difference. However, the enhancement of the $^2P_{3/2}$ phase shift remains too small for energies around its resonance centroid and below. Consequently, a clear discrepancy to the experimental resonance energy at 0.78 MeV remains. However, we are not in the position to blame this on the initial chiral Hamiltonian because one possible explanation is of course connected to the still limited NCSM/RGM model space. As evident from Table 13.1 we have included ^4He states up to excitation energies of 24 MeV. However, the deuteron- ^3H channels opens experimentally at 17.63 MeV and the coupling to this channel is likely to impact the results and would yield a more complete picture. In order to include this channel it is required to extend the NCSM/RGM formalism for two-nucleon projectiles to include 3N interactions. Another possibility to overcome the limited convergence of the NCSM/RGM approach is the use of the no-core shell model with continuum, discussed in Section 14, that includes low-lying ^5He states into the basis expansion. Work in both directions is currently underway [209].

The discussion of the $p\text{-}^4\text{He}$ phase shifts, shown in the right-hand panel of Figure 13.9, is qualitatively identical. We find the $^2S_{1/2}$ and $^2D_{3/2}$ in good agreement with experiment

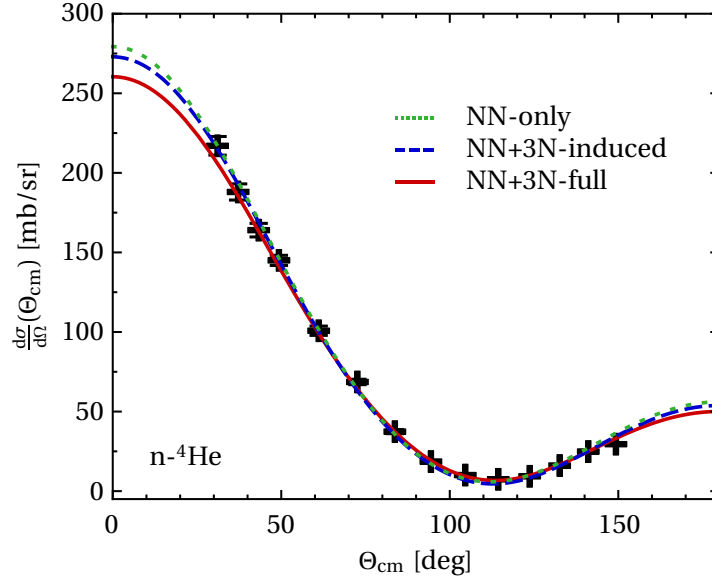


Figure 13.10 – Differential cross section for neutron-⁴He elastic scattering at incident neutron energy of 17.6 MeV obtained with the three types of Hamiltonians compared to experiment. The NCSM/RGM calculations include the first seven low-lying states of ⁴He $I_1^{\pi_1} T_1 =$ (g.s., $0^+0, 0^-0, 2^-0, 2^-1, 1^-1, 1^-0$). Remaining parameters are $N_{\max} = 13$, $E_{3\max} = 14$, $\alpha = 0.0625 \text{ fm}^4$, and $\hbar\Omega = 20 \text{ MeV}$. The experimental data is taken from Ref. [210]. (published in [51])

and they are, as in the n-⁴He case, not very sensitive to the inclusion of the initial chiral 3N interaction. For the $^2P_{1/2}$ phase shift the NN+3N-full Hamiltonian is responsible for the good agreement with experiment at large energies, but near the resonance around 3.2 MeV we observe small deviations from experiment and the NN+3N-induced Hamiltonian yields the better agreement with experiment. For the $^2P_{3/2}$ partial wave the NN+3N-full Hamiltonian leads to better agreement with experiment than the NN+3N-induced Hamiltonian for all studied energies. In line with the n-⁴He discussion above, we still find rather large differences to experiment in the $^2P_{3/2}$ phase shift below 6 MeV such that the experimental resonance position at 1.69 MeV [147] is clearly not reproduced. As before this may be related to missing deuteron-³He contributions.

Altogether, the agreement with experiment for the nucleon-⁴He phase shifts is very promising, confirms the validity of chiral NN+3N Hamiltonians also in ab-initio studies of nuclear reactions, and motivates the investigation of further scattering observables.

13.3 Cross Sections and Analyzing Powers

Now we focus on elastic scattering observables of the nucleon-⁴He system. Given the discussion in the last subsection it is clear that we should investigate energies beyond the P wave resonances for such studies. That is, we focus on energies where the phase shifts are in good agreement with experiment. In Ref. [179] it has been demonstrated that the NCSM/RGM approach with NN-only interactions is able to provide sensible descriptions of angular differential cross sections and analyzing powers even when including only two

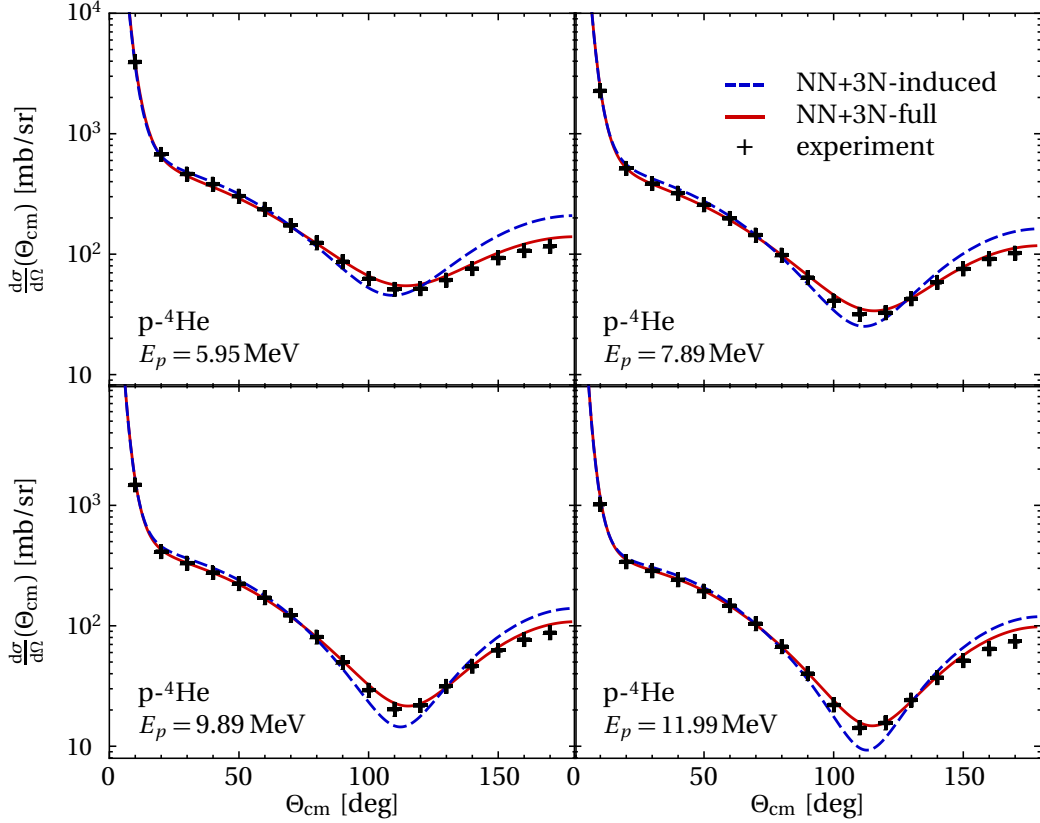


Figure 13.11 – Differential cross section for proton- ^4He elastic scattering at different proton energies E_p obtained with the NN+3N-induced and NN+3N-full Hamiltonians compared to experimental data of Ref. [211]. Note that the 2% uncertainty of the data is hidden by the plot markers. The remaining parameters are identical to Figure 13.10. (published in [51])

excited states of ^4He . Note, however, that this is related to the artificial enhancement of the NN-only phase shifts due to the omission of SRG-induced 3N interactions. In the following we discuss differential cross sections and analyzing powers computed with the chiral NN+3N Hamiltonians and with the set of parameters used in the previous Section, i.e., in particular including the first seven states of ^4He .

We begin with the investigation of the differential cross section at incident neutron energy of 17.6 MeV shown in Figure 13.10 for the NN-only (green-dotted line), the NN+3N-induced (blue-dashed line), and the NN+3N-full Hamiltonian (solid-red line) in comparison to the experimental data of Drogg et al. [210] (crosses). At all angles we find good agreement with experiment. Between 45 and 135 degrees all three Hamiltonians yield practically the identical results. Strikingly, in particular the inclusion of the 3N interaction does not affect the differential cross section for these angles, which might be expected due to the limited effects also in the phase shifts at the corresponding center-of-mass frame energy of 14.08 MeV. However, at smaller angles the inclusion of both, the SRG-induced 3N and the initial 3N interaction slightly reduces the differential cross section, leading to a marginal underestimation of the data point at 30 degrees. Also at large angles the inclusion of both 3N interactions leads to a minor decrease of the differential cross section. In

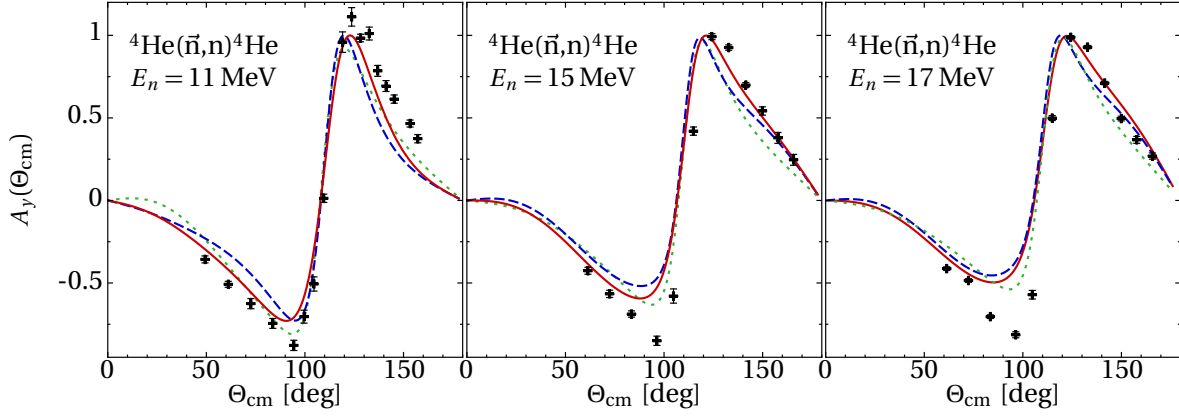


Figure 13.12 – Analyzing power A_y for neutron-⁴He elastic scattering at incident neutron energies 11 (left-hand panel), 15 (middle panel), and 17 MeV (right-hand panel) obtained for the NN+3N-induced (---) and NN+3N-full (—) Hamiltonians compared to experimental data (+) of Refs.[212, 210, 213]. The NCSM/RGM calculations include the first seven low-lying states of ⁴He $I_1^{\pi_1} T_1 = (\text{g.s.}, 0^+0, 0^-0, 2^-0, 2^-1, 1^-1, 1^-0)$. Remaining parameters are identical to Figure 13.10. (published in [51])

addition, we show in Figure 13.11 the p-⁴He differential cross section the incident proton energies of 5.95, 7.89, 9.89, and 11.99 MeV for the NN+3N-induced and NN+3N-full Hamiltonians compared to experiment. By comparison of the results for these two Hamiltonians we study the impact of the initial chiral 3N interaction. For angles below 90 degrees both results are on top of each other and, as above for the n-⁴He cross section, we find no effect of the initial 3N interaction. However, this changes at larger angles beyond 90 degrees, where the latter clearly yields additional contributions that yield good agreement of the differential cross sections with experiment essentially for all angles, although a slight overestimation for large angles remains.

We proceed with the discussion of the analyzing power A_y , which is more complicated. We start again with neutron-⁴He scattering and present the A_y at incident neutron energies 11, 15 and 17 MeV for the three types of Hamiltonians compared to experiment in Figure 13.12. Near the minimum around 95 degrees the NN-only Hamiltonian leads to results closer to experiment than the NN+3N-induced Hamiltonian, which is due to the accidentally better agreement of the $^2P_{3/2}$ phase shift with experiment for the NN-only Hamiltonian than for NN+3N-induced Hamiltonian, as evident from a comparison of Figures 13.8 and 13.9. However, for 15 and 17 MeV at large angles the NN+3N-induced Hamiltonian leads to better agreement with experiment. Finally, the inclusion of the initial 3N interaction improves the agreement with experiment at 11 and 15 MeV for small and large angles compared to the NN+3N-induced Hamiltonian, while both yield similar values for A_y between 100 and 125 degrees. For the 17 MeV results the NN+3N-full Hamiltonian overall improves the experimental agreement, with the exception of the largest angles measured. Altogether, the deviations from experiment are clearly larger for the A_y than for the differential cross section discussed above. One reason is that this polarization observable is more sensitive to the spin-orbit components of the nuclear interaction [214] and to non-

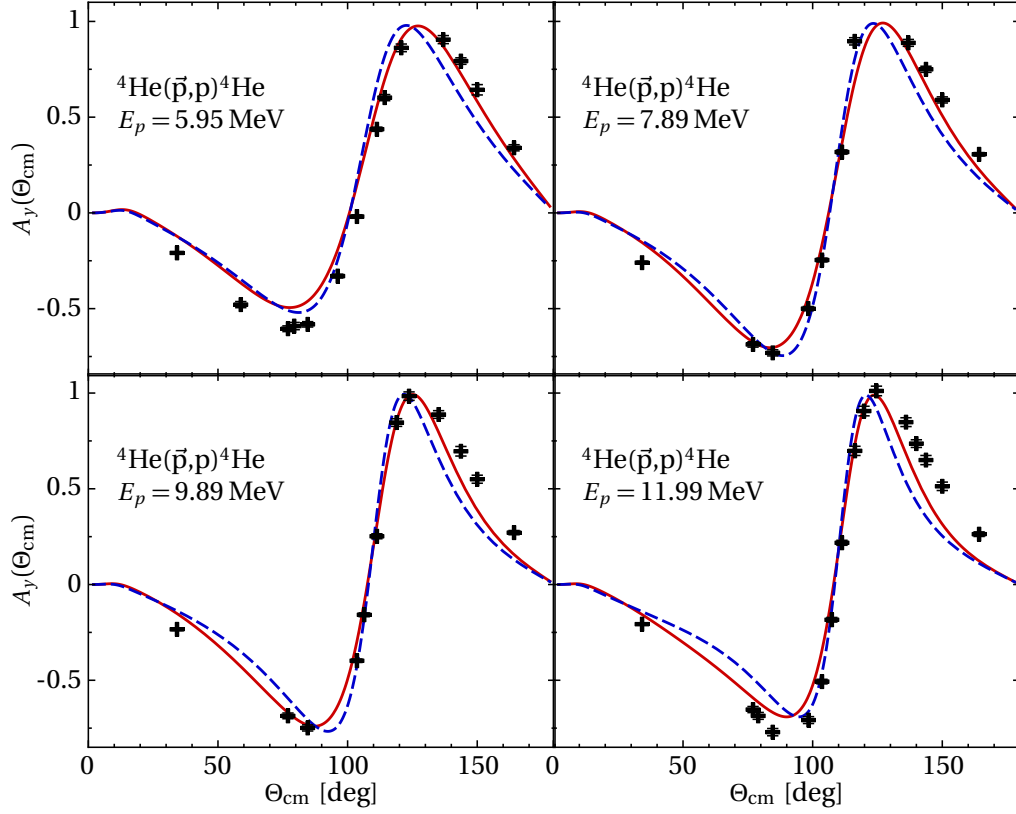


Figure 13.13 – Analyzing power A_y for proton- ^4He elastic scattering for different incident proton energies E_p obtained for the NN+3N-induced (---) and NN+3N-full (—) Hamiltonians compared to experimental data (+) of Ref. [211]. The NCSM/RGM calculations include the first seven low-lying states of ^4He $I_1^{\pi_1} T_1 = (\text{g.s.}, 0^+0, 0^-0, 2^-0, 2^-1, 1^-1, 1^-0)$. Remaining parameters are identical to Figure 13.10. (published in [51])

convergence with respect to model-space size. For instance, the small deviations of the phase shifts from experiment present in Figure 13.9 at $E_{\text{kin}} = 8.8\text{MeV}$ corresponding to 11 MeV neutron energy are amplified in the A_y . A second reason for the deviations is related to the fact that the A_y at energies above 11 MeV is sensitive to partial waves up to at least $J = \frac{11}{2}$ before convergence is reached. However, for the discussed results at 15 and 17 MeV we have limited this expansion to partial waves with $J \leq \frac{7}{2}$ because we found phase shifts corresponding to higher partial waves at these energies to be biased by the $E_{3\text{max}}$ truncation. However, for the lower energy of 11 MeV we include partial waves up to $J = \frac{11}{2}$, and this is also the case for the A_y of p- ^4He shown in Figure 13.13 where we study again the four incident proton energies below 12 MeV. Overall, for all four energies the NN+3N-full Hamiltonian improves the agreement with experiment compared to the NN+3N-induced results except for the minimum near 90 degrees for 5.95 MeV incident proton energy and the peak at 110 degrees for the 7.89 MeV case. However, at small angles below the minimum discrepancies between the A_y and experiment remain for all energies also for the NN+3N-full Hamiltonian. The experimental data around the minimum is best reproduced at $E_p = 7.89$ and 9.89 MeV. For angles larger than 135 degrees we find devi-

ations from experiment for the NN+3N-induced Hamiltonian for all considered energies and for the NN+3N-full Hamiltonian for the larger energies 9.89 and 11.99 MeV that are in line with the overestimation of the differential cross section, respectively.

In conclusion, the chiral 3N interaction is vital for the study of nucleon-⁴He scattering resulting in a good description of n-⁴He and p-⁴He scattering phase shifts away from the ²P_{3/2} resonance. For the ²P_{3/2} phase shift convergence with respect to the NCSM/RGM model space size is not yet reached in spite of including seven states of the ⁴He target. This can be improved by also including the deuteron-triton channel and by using the no-core shell model with continuum approach, which will be the focus of the next section. In addition, we have found remarkably good agreement of differential cross sections with experiment over a wide incident energy range, in particular for p-⁴He scattering due to the included chiral 3N interaction. For the analyzing powers we find larger deviations at certain energies and angles.

Altogether, these findings give confidence in further developments of more sophisticated ab-initio approaches to nuclear reactions and applications to scattering involving heavier target nuclei. Furthermore, our results pave the way towards detailed benchmarks and sensitivity studies of the chiral nuclear forces also in the domain of scattering observables for light nuclei similar to the studies in Sections 6 and 7 for nuclear structure.

SECTION 14

No-Core Shell Model with Continuum

The extension of the NCSM/RGM formalism to include 3N interactions discussed in Section 11 in combination with the R -matrix theory for solving the radial Schrödinger equation constitutes a major step towards the ab-initio description of bound- and scattering states based on chiral NN+3N Hamiltonians. In the previous section we found encouraging results for nucleon- ^4He scattering including chiral 3N interactions. In order to converge the calculations with respect to the NCSM/RGM model space we included up to six excited states of the ^4He target, but in particular for the P -wave phase shifts full convergence was not yet reached. The same issue has been found also in calculations for $^7\text{Be}(p,\gamma)^8\text{B}$ with NN interactions, and it becomes even more apparent when the sub-clusters are weakly bound, e.g., for deuteron projectiles where the inclusion of numerous excited pseudo-states of the deuteron is required [180, 182]. Even though, this poses no formal problems, the calculations become much more complex due to many coupled channels, and the computational cost for the norm and Hamiltonian kernels increases significantly. The origin of this rather slow convergence is connected to a lack of correlations in the A -body states of the NCSM/RGM channel basis due to their cluster structure. The correlations within the $(A - a)$ -body target and the a -body projectile clusters are well described by the representation as NCSM eigenstates, however, the inter-cluster correlations are not taken into account and, thus, need to be covered by the inclusion of more eigenstates of the projectile and the target into the calculation. This is similar to the NCSM, where the superposition of Slater determinants covers the A -body correlations, while a single Slater determinant carries no information about correlations of the system.

To improve on this issue of the NCSM/RGM approach Baroni, Navrátil and Quaglioni recently proposed the ab-initio no-core shell model with continuum (NCSMC)[49, 50]. The basic idea is to augment the partial-wave scattering state of the NCSM/RGM formalism (11.4) by a superposition of NCSM eigenstates of the A -body system. Based on the discussion above, the motivation for this choice of basis states is evident: the NCSM eigenstates have the ability to describe the short-range correlations of the systems properly, while they do not exhibit the correct asymptotic behavior to describe weakly-bound

or even scattering states, because they are expanded in a finite HO basis. However, the weakly-bound or scattering states are well-described by the cluster states adopted from the NCSM/RGM approach. In this way one obtains a symbiotic basis, where the advantages of both parts remedy the drawbacks of each other. In combination with the R -matrix theory the NCSMC treats bound- and scattering states on equal footing suitable for the ab-initio predictions of structural and scattering observables within a unified framework.

So far, the NCSMC has been successfully applied to the unbound ${}^7\text{He}$ nucleus with NN-only Hamiltonians [50, 49]. In this section, we aim at the application of the NCSMC formalism including explicit 3N interactions. As demonstrated in the next subsection, the extension of the NCSM/RGM kernels to include 3N interactions discussed in Section 11 constitutes a major step towards the extension of the NCSMC formalism to 3N interactions. In the next subsection we outline the general formalism of the NCSMC. Afterwards, we present first results for NCSMC with explicit 3N interactions for the neutron- ${}^8\text{Be}$ system. The results presented in the following are achieved in collaboration with Petr Navrátil (TRIMUF).

14.1 Formalism

We start with a brief overview of the NCSMC approach following Ref. [49], where further details about the formalism for NN interactions can be found. In particular, we highlight which quantities are affected by the extension of the formalism to 3N interactions.

The ansatz for the eigenstates of the A -body system in the NCSMC formalism reads

$$|\Psi^{J\pi T}\rangle = \sum_{\lambda} c_{\lambda} |\Psi_A E_{\lambda} J^{\pi} T\rangle + \sum_{\nu} \int dr r^2 \frac{\chi_{\nu}(r)}{r} |\xi_{\nu r}^{J\pi T}\rangle, \quad (14.1)$$

where the first term is a superposition of NCSM eigenstates of the A -body system (cf. Section 4.1), and the second term represents the expansion in binary-cluster channel states analogous to Eq. (11.4). We have dropped the projection quantum numbers M and M_T and the superscript $J\pi T$ at the relative motion wave function $\chi_{\nu}(r)$ for brevity. Note that we wrote the expansion in terms of the orthogonalized NCSM/RGM channel states (11.15), which are related to the non-orthogonalized channel states by

$$|\xi_{\nu r}^{J\pi T}\rangle = \sum_{\nu'} \int dr' r'^2 \mathcal{N}_{\nu'\nu}^{-\frac{1}{2}}(r', r) \hat{\mathcal{A}}_{\nu'} |\Phi_{\nu' r'}^{J\pi T}\rangle, \quad (14.2)$$

with the inverse of the square root of the norm kernel as given in Eq. (11.19), and the unknowns of this expansion are the coefficients c_{λ} and the relative wave functions $\chi_{\nu}(r)$.

It is evident, that the basis states (14.1) are well-suited to describe bound and scattering states. The appropriate treatment of correlations of the A -body system, which are problematic in the NCSM/RGM cluster basis, is accomplished by the NCSM eigenstates. Thus, if the existence of nucleon sub-clusters is relevant for the description of the A -nucleon system this ansatz improves the model-space convergence compared to both, the NCSM and NCSM/RGM approach.

To derive the conditional equations for the coefficients c_λ and the relative wave functions $\chi_\nu(r)$ we insert ansatz (14.1) in the time-independent Schrödinger equation $\hat{H}|\Psi^{J^\pi T}\rangle = E|\Psi^{J^\pi T}\rangle$. In addition, multiplication from the left by another NCSM eigenstate $\langle\Psi_A E_{\lambda'} J^\pi T|$ leads to

$$\sum_\lambda (H_{\text{NCSM}})_{\lambda'\lambda} c_\lambda + \sum_\nu \int dr r^2 h_{\lambda'\nu}(r) \frac{\chi_\nu(r)}{r} = E \sum_\lambda \delta_{\lambda'\lambda} c_\lambda + \sum_\nu \int dr r^2 g_{\lambda'\nu}(r) \frac{\chi_\nu(r)}{r} \quad (14.3)$$

with the definitions

$$(H_{\text{NCSM}})_{\lambda'\lambda} = \langle\Psi_A E_{\lambda'} J^\pi T|\hat{H}|\Psi_A E_\lambda J^\pi T\rangle = E_\lambda \delta_{\lambda'\lambda}, \quad (14.4)$$

$$h_{\lambda'\nu}(r) = \langle\Psi_A E_{\lambda'} J^\pi T|\hat{H}|\xi_{\nu r}^{J^\pi T}\rangle \quad (14.5)$$

$$= \sum_{\nu'} \int dr' r'^2 \langle\Psi_A E_{\lambda'} J^\pi T|\hat{H} \cdot \hat{\mathcal{A}}_{\nu'} |\Phi_{\nu' r'}^{J^\pi T}\rangle \mathcal{N}_{\nu' \nu}^{-\frac{1}{2}}(r', r), \quad (14.6)$$

$$g_{\lambda'\nu}(r) = \langle\Psi_A E_{\lambda'} J^\pi T|\xi_{\nu r}^{J^\pi T}\rangle \quad (14.7)$$

$$= \sum_{\nu'} \int dr' r'^2 \langle\Psi_A E_{\lambda'} J^\pi T|\hat{\mathcal{A}}_{\nu'} |\Phi_{\nu' r'}^{J^\pi T}\rangle \mathcal{N}_{\nu' \nu}^{-\frac{1}{2}}(r', r). \quad (14.8)$$

In Eqs. (14.6) and (14.8) we have inserted Eq. (14.2) to express the functions $h_{\lambda'\nu}(r)$ and $g_{\lambda'\nu}(r)$ in terms of the non-orthogonalized channel states, because this is more convenient regarding the implementation. Multiplication from the left by an orthogonalized channel state $\langle\xi_{\nu' r'}^{J^\pi T}|$ leads to

$$\sum_\lambda h_{\lambda\nu'} c_\lambda + \sum_\nu \int dr r^2 \mathcal{H}(r', r) \frac{\chi_\nu(r)}{r} = E \sum_\lambda g_{\lambda\nu'}(r) c_\lambda + \sum_\nu \int dr r^2 \frac{\delta(r' - r) \delta_{\nu' \nu}}{r' r} \frac{\chi_\nu(r)}{r}, \quad (14.9)$$

with

$$\begin{aligned} \mathcal{H}(r', r) &= \langle\xi_{\nu' r'}^{J^\pi T}|\hat{H}|\xi_{\nu r}^{J^\pi T}\rangle \\ &= \sum_{\gamma\gamma'} \int dy y^2 \int dy' y'^2 \mathcal{N}_{\gamma\nu'}^{-\frac{1}{2}}(y, r') \langle\Phi_{\gamma y}^{J^\pi T}|\hat{\mathcal{A}}_\gamma \hat{H} \cdot \hat{\mathcal{A}}_{\gamma'} |\Phi_{\gamma' y'}^{J^\pi T}\rangle \mathcal{N}_{\gamma' \nu}^{-\frac{1}{2}}(y', r), \end{aligned} \quad (14.10)$$

which is exactly the NCSM/RGM Hamiltonian kernel with respect to the orthogonalized basis (11.12). The latter contains with $\langle\Phi_{\gamma y}^{J^\pi T}|\hat{\mathcal{A}}_\gamma \hat{H} \cdot \hat{\mathcal{A}}_{\gamma'} |\Phi_{\gamma' y'}^{J^\pi T}\rangle$ the Hamiltonian kernel for which we have derived the explicit formulas for the inclusion of 3N interactions and discussed implementation strategies in Section 11. The remaining quantity that needs to be generalized to 3N interactions is the coupling form factor $h_{\lambda'\nu}(r)$ of Eq. (14.6), which has been completed by Petr Navrátil. With help of above definitions we can cast the NCSMC Eqs. (14.3) and (14.9) in a more compact form by means of matrix notation

$$\begin{pmatrix} H_{\text{NCSM}} & h \\ h & \mathcal{H} \end{pmatrix} \begin{pmatrix} c \\ \chi(r)/r \end{pmatrix} = E \begin{pmatrix} \mathbb{1} & g \\ g & \mathbb{1} \end{pmatrix} \begin{pmatrix} c \\ \chi(r)/r \end{pmatrix}. \quad (14.11)$$

Of course, the NCSMC basis in terms of states (14.1) is over-complete, which is manifested by the presence of the norm matrix

$$N = \begin{pmatrix} \mathbb{1} & g \\ g & \mathbb{1} \end{pmatrix} \quad (14.12)$$

on the right-hand side of Eq. (14.11). In practice it is more convenient to work with the orthogonalized NCSMC equations that can be obtained analogously as in the NCSM/RGM approach by multiplications with appropriate (inverse) square roots of N . For the details of the orthogonalization procedure we refer to Ref. [50]. Finally, the orthogonalized NCSMC equations become

$$\tilde{H} \begin{pmatrix} \bar{c} \\ \bar{\chi}(r)/r \end{pmatrix} = E \begin{pmatrix} \bar{c} \\ \bar{\chi}(r)/r \end{pmatrix}, \quad (14.13)$$

with the orthogonalized Hamiltonian matrix

$$\tilde{H} = N^{-\frac{1}{2}} \begin{pmatrix} H_{\text{NCSM}} & h \\ h & \mathcal{H} \end{pmatrix} N^{-\frac{1}{2}} \quad \text{and} \quad \begin{pmatrix} \bar{c} \\ \bar{\chi}/r \end{pmatrix} = N^{\frac{1}{2}} \begin{pmatrix} c \\ \chi/r \end{pmatrix}. \quad (14.14)$$

The solution of the orthogonalized NCSMC equations is achieved by the R -matrix method on a Lagrange mesh presented in Section 12 that yields the bound- as well as scattering-state solutions.

Finally, we note that the application of the NCSMC formalism extended to 3N interactions beyond the lightest systems, i.e., beyond ${}^4\text{He}$ targets relies on the computation of the NCSM/RGM kernels using our approach based on the on-the-fly computation of the involved density matrices, see Eqs. (11.64)–(11.68), while it is prohibitive in the alternative strategy using coupled densities (cf. Section 11.2.4).

14.2 Ab-Initio Description of ${}^9\text{Be}$ via n- ${}^8\text{Be}$ Scattering

As first application of the NCSMC with explicit 3N interactions we focus on the excitation spectrum of ${}^9\text{Be}$. This system is interesting because only its ground state is bound while all excited states are above the n- ${}^8\text{Be}$ energy threshold located experimentally at 1.665 MeV [215, 148]. Therefore, it is appealing to study the impact of the continuum on the excited-state resonances with particular focus on the effects of chiral 3N interactions. In addition, ${}^9\text{Be}$ is of interest for astrophysics, because it provides seed material for the production of ${}^{12}\text{C}$ via the $(\alpha n){}^9\text{Be}(\alpha, n){}^{12}\text{C}$ reaction as alternative to the triple- α reaction [216].

We aim at the description of the low-energy resonances up to about 10 MeV above the n- ${}^8\text{Be}$ threshold. Hence, all excited states of ${}^9\text{Be}$ in this energy range may significantly contribute in the NCSMC expansion (14.1). We include the four positive-parity states $\frac{1}{2}^+$, $\frac{5}{2}^+$, $\frac{3}{2}^+$, $\frac{9}{2}^+$, and the six negative-parity states $\frac{3}{2}^-$, $\frac{5}{2}^-$, $\frac{1}{2}^-$, $\frac{3}{2}^-$, $\frac{7}{2}^-$, and $\frac{5}{2}^-$ as these are the lowest-energy states computed with the (IT-)NCSM. The selection of these states is also

consistent with the experimental energy levels which show a gap of about 3 MeV between the second $\frac{5}{2}^-$ state that we still include and the next experimentally known resonance at 11.2 MeV [148], which is also found near this energy in NCSM calculations. Similar arguments lead to the selection of channels that we include into the NCSM/RGM part of the NCSMC expansion. First of all, we restrict ourselves to channels with projectiles consisting of single neutron projectiles and ${}^8\text{Be}$ targets. For the ${}^8\text{Be}$ target we take its 0^+ ground state and the 2^+ excited state into account. The next excitation of ${}^8\text{Be}$ is a broad 4^+ state around 11 MeV that is beyond the targeted energy range.

The solution of the NCSMC equations is achieved by the R -matrix theory on a Lagrange mesh using a channel radius of 18 fm and 40 mesh points. We study the NN+3N-induced and NN+3N-full Hamiltonians, where for the latter we employ the reduced cutoff momentum $\Lambda_{3N} = 400 \text{ MeV}/c$. This choice is motivated by the observation that the $\Lambda_{3N} = 500 \text{ MeV}/c$ Hamiltonian overbinds the n - ${}^8\text{Be}$ threshold by about 800 keV in IT-NCSM calculations at $N_{\text{max}} = 12$, which is not the case with the reduced-cutoff 3N interaction. In the following, we study the convergence with respect to different truncations present in the NCSMC calculations and the dependence on the SRG flow parameter for phase shifts and eigenphase shifts of the n - ${}^8\text{Be}$ system. Finally, we extract the resonance centroids and corresponding widths and investigate the continuum as well as 3N-force effects on the spectrum of ${}^9\text{Be}$ in Section 14.2.5.

14.2.1 Monitoring the IT-NCSM Inputs in the NCSMC

The NCSMC relies on a set of NCSM eigenstates for ${}^8\text{Be}$ and ${}^9\text{Be}$. Their computation quickly becomes demanding when large model spaces are considered and, accordingly, we compute the required eigenstates with the IT-NCSM for $N_{\text{max}} > 7$. We emphasize that this does not only reduce the computational cost for the input vectors, but also and equally important the computation of the NCSM/RGM kernels and NCSMC coupling form factors is significantly simplified because much less Slater determinants are included in the superposition of the eigenstates in Eq. (11.72). Also the energy eigenvalues enter the NCSMC equations, namely in H_{NCSM} for ${}^9\text{Be}$, and to determine whether a channel is open or closed for ${}^8\text{Be}$. The extrapolation to vanishing importance thresholds is performed for these energies as discussed in Section 4.2. However, for the computation of the NCSM/RGM kernels and NCSMC coupling form factor we use the eigenvectors from the IT-NCSM at the smallest importance threshold $\kappa_{\text{min}} = 3 \cdot 10^{-5}$ and $C_{\text{min}} = 10^{-4}$. That is, we waive the extrapolation to vanishing importance thresholds for the computed phase shifts and scattering observables, as this would significantly complicate the calculations. Instead we assess the quality of the importance truncation by direct comparison to phase shifts computed with full NCSM vectors in the largest feasible model space.

In a first step we investigate n - ${}^8\text{Be}$ scattering in the NCSM/RGM formalism only, where the IT-NCSM vectors enter in the norm and Hamiltonian kernels, which are also a component of the NCSMC approach later on. We show the phase shifts and eigenphase shifts at $N_{\text{max}} = 8$ (9 for negative parity) in Figure 14.1 computed from IT-NCSM vectors as dashed

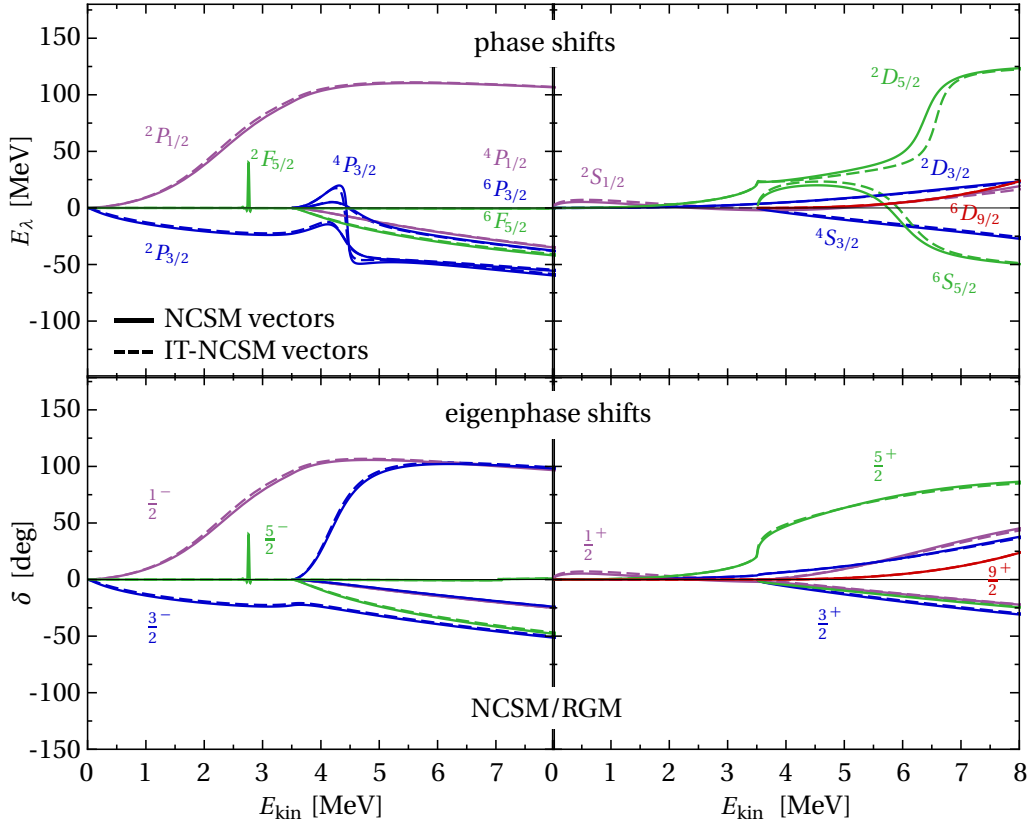


Figure 14.1 – NCSM/RGM n - ${}^8\text{Be}$ phase shifts (upper panels) and eigenphase shifts (lower panels) at $N_{\text{max}} = 8$ for negative parity (left-hand panels) and $N_{\text{max}} = 9$ for positive parity (right-hand panels). Compared are results using NCSM vectors (—) to results based on IT-NCSM vectors (---). Remaining parameters are $\hbar\Omega = 20\text{MeV}$, $\alpha = 0.0625\text{fm}^4$ and $E_{3\text{max}} = 14$. Same colors correspond to identical angular momenta.

lines, and from NCSM vectors as solid lines, and both as function of the kinetic energy E_{kin} in the center-of-mass frame. Note that the phase shifts are extracted from the diagonal entries of the scattering matrix before it is diagonalized. Hence, they correspond to particular partial waves with well defined quantum numbers. This is useful to identify which partial wave is responsible for a resonance present in the eigenphase shifts. The latter are relevant to determine resonance energies and corresponding widths, i.e., they are important for comparisons of energy levels against experiment (cf. Section 14.2.4). Note that we include in Figure 14.1 only those (eigen)phase shifts that are significantly different from zero. In addition, the eigenphase shifts and phase shifts below about 3.5 MeV are identical, because at these low energies only a single open channel, defined by the ${}^8\text{Be}$ ground state, exists.

First, we concentrate on the negative-parity results shown in the left-hand panels of Figure 14.1. The phase shifts and eigenphase shifts resulting from NCSM/RGM calculations based on IT-NCSM and NCSM vectors are practically on top of each other. Thus, configurations discarded by the importance truncation yield negligible contributions to the (eigen)phase shifts. The spike in the ${}^2F_{5/2}$ partial wave slightly below 3 MeV is not an

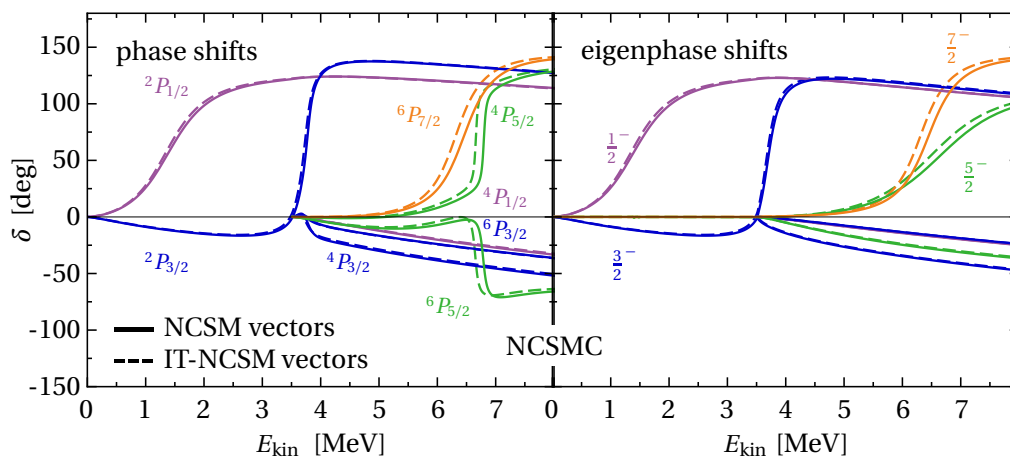


Figure 14.2 – NCSMC $n\text{-}{}^8\text{Be}$ negative-parity phase shifts (left-hand panel) and eigenphase shifts (right-hand panel) at $N_{\text{max}} = 8$. Compared are results using NCSM vectors (—) to results based on IT-NCSM vectors (---). Remaining parameters are $\hbar\Omega = 20\text{ MeV}$, $\alpha = 0.0625\text{ fm}^4$, and $E_{3\text{max}} = 14$. Same colors correspond to identical angular momenta.

artifact but corresponds to a narrow resonance which is not fully resolved by the energy grid used here. Note that it is also present in the calculations based on the IT-NCSM vectors, where it is again not fully resolved and can be seen slightly below its position from the calculation with NCSM vectors. For the positive-parity results shown in the right-hand panels of Figure 14.1 the general conclusion is the same: we find good agreement between the NCSM/RGM (eigen)phase shifts of $n\text{-}{}^8\text{Be}$ based on the NCSM and IT-NCSM vectors. An interesting detail is that the ${}^2D_{5/2}$ and ${}^6S_{5/2}$ phase shifts show deviations near their resonance energies, however, after the diagonalization of the scattering matrix both $\frac{5}{2}^+$ eigenphase shifts are again in excellent agreement.

For NCSMC calculations we show the impact of using the IT-NCSM instead of NCSM vectors in Figure 14.2 again for both, phase shifts and eigenphase shifts at $N_{\text{max}} = 8$. We note that here the ${}^8\text{Be}$ and additionally the ${}^9\text{Be}$ vectors enter in the NCSMC coupling form factor. However, given the large computational cost of the calculations involving the full NCSM vectors we restrict ourselves to negative parities. Again we find most phase shifts and eigenphase shifts computed with IT-NCSM or NCSM on top of each other. The sole exception are the $\frac{7}{2}^-$ and $\frac{5}{2}^-$ resonances, where we find slight differences of about 100 keV for the resonance positions, respectively.

Overall we have found good agreement for NCSM/RGM or NCSMC (eigen)phase shifts with NCSM and IT-NCSM eigenstates of ${}^8\text{Be}$ and ${}^9\text{Be}$. This gives confidence in the application of IT-NCSM vectors for larger model spaces. In the following, we use NCSM input vectors for $N_{\text{max}} = 6$ and 7, and beyond we resort to IT-NCSM vectors.

14.2.2 Model-Space Convergence

Next we discuss the convergence of the $n\text{-}{}^8\text{Be}$ phase shifts and eigenphase shifts with respect to the model-space truncation N_{max} . The results are summarized in Figure 14.3. We

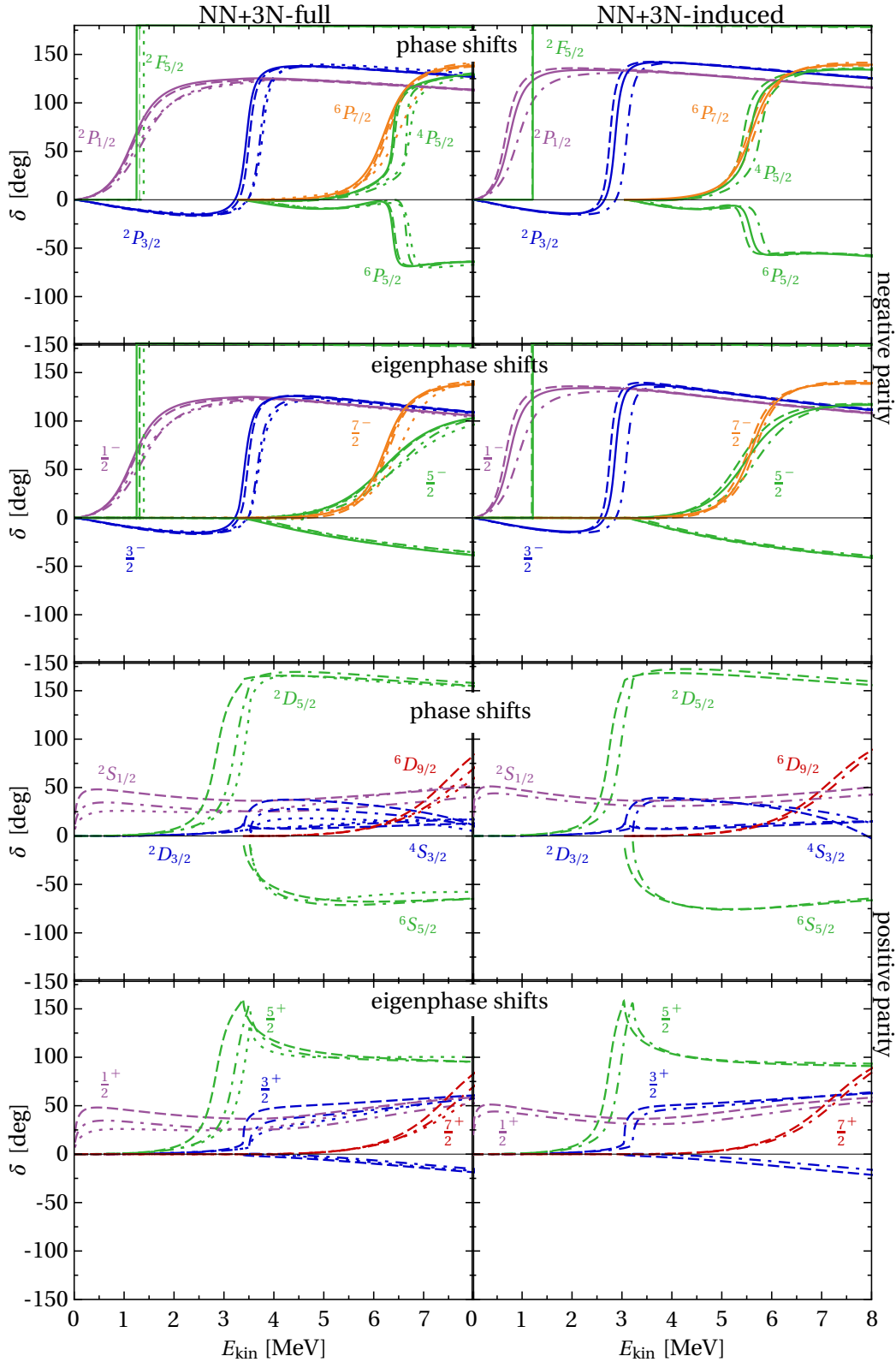


Figure 14.3 – NCSMC n - ${}^8\text{Be}$ (eigen)phase shifts for positive (negative) parity for $N_{\text{max}} = 6(7)$ (.....), 8 (9) (----), 10 (11) (---), 12 (13) (—) using IT-NCSM vectors for $N_{\text{max}} > 7$. The left- and right-hand columns show the results for the NN+3N-induced and NN+3N-full Hamiltonian, respectively. Remaining parameters are $\hbar\Omega = 20$ MeV, $\alpha = 0.0625$ fm 4 , and $E_{3\text{max}} = 14$. Same colors correspond to identical angular momenta.

start with the negative-parity phase shifts and eigenphase shifts shown in the first two rows, respectively. The left-hand panels show the results for the NN+3N-full Hamiltonian, and the right-hand panels for the NN+3N-induced Hamiltonian. We note that the (eigen)phase shifts are most sensitive to the model-space size near their resonance positions. For the NN+3N-full Hamiltonian we find minor changes for the step $N_{\text{max}} = 6$ to 8, followed by a larger effect to $N_{\text{max}} = 10$, and finally a minor change to the $N_{\text{max}} = 12$ results. The only exception is the $\frac{7}{2}^-$ (eigen)phase shift, where the results for the three largest model spaces are almost on top of each other. The findings are similar for the NN+3N-induced Hamiltonian, however, the differences between $N_{\text{max}} = 10$ and 12 are slightly larger than in the NN+3N-full results. Note that for the ${}^2F_{5/2}$ resonance the $N_{\text{max}} = 10$ and 12 results are perfectly on top of each other. An interesting detail is visible in the $\frac{5}{2}^-$ results: although the ${}^4P_{5/2}$ and ${}^6P_{5/2}$ phase shifts both show a large change going from $N_{\text{max}} = 8$ to 10, only the resonant eigenphase shift shows this behavior while the non-resonant one is rather insensitive to the different model-space sizes. Altogether, the N_{max} convergence for the negative-parity phase shifts is acceptable and similar to the one found in Ref [50, 49] with NN-only Hamiltonians for ${}^7\text{He}$. Although there will be further contributions from larger model spaces we do not expect that an $N_{\text{max}} = 14$ calculations would significantly change the present results.

The convergence behavior of the (eigen)phase shifts for the positive-parity partial waves are shown in the lowest two rows of Figure 14.3. Again, the (eigen)phase shifts are most sensitive to the growing model space near their resonance positions. However, an exception is the ${}^2S_{1/2}$ phase shift and the corresponding $\frac{1}{2}^+$ eigenphase shift that is affected at all energies. As before the convergence pattern is similar for the NN+3N-induced and NN+3N-full Hamiltonians. However, the N_{max} dependence of the individual phase shifts is stronger than for the negative-parity partial waves and the large changes between the $N_{\text{max}} = 9$ and 11 phase shifts show that the calculation is not yet converged. Nevertheless, we use the $N_{\text{max}} = 11$ results for the following investigations of the positive parity spectrum.

14.2.3 Dependence on the SRG Flow Parameter

Although we are in the domain of light nuclei and we are using the 3N interaction with the reduced cutoff $\Lambda_{3\text{N}} = 400\text{MeV}/c$, which reduces the flow-parameter dependence of energies (cf. Section 6.3), possible non-convergences or inconsistent truncations, e.g., $E_{3\text{max}}$, can lead to dependencies on the SRG flow parameter. Hence, we study the n - ${}^8\text{Be}$ (eigen)phase shifts for the different SRG flow parameters $\alpha = 0.04, 0.0625, \text{ and } 0.08\text{fm}^4$ for the NN+3N-full Hamiltonian in Figure 14.4. All (eigen)phase shifts for negative-parity partial waves shown in the left-hand panels reveal only negligible differences for $\alpha = 0.0625$ and 0.08fm^4 , since they are almost on top of each other. However, the latter deviate from the $\alpha = 0.04\text{fm}^4$ (eigen)phase shifts at least near resonance energies. As discussed in Part II further evolved Hamiltonians exhibit an improved rate of convergence with respect to model-space size. Accordingly, the (eigen)phase shifts for $\alpha = 0.04\text{fm}^4$ are expected to converge slower than those for larger flow parameters. Indeed, the direction of the deviations

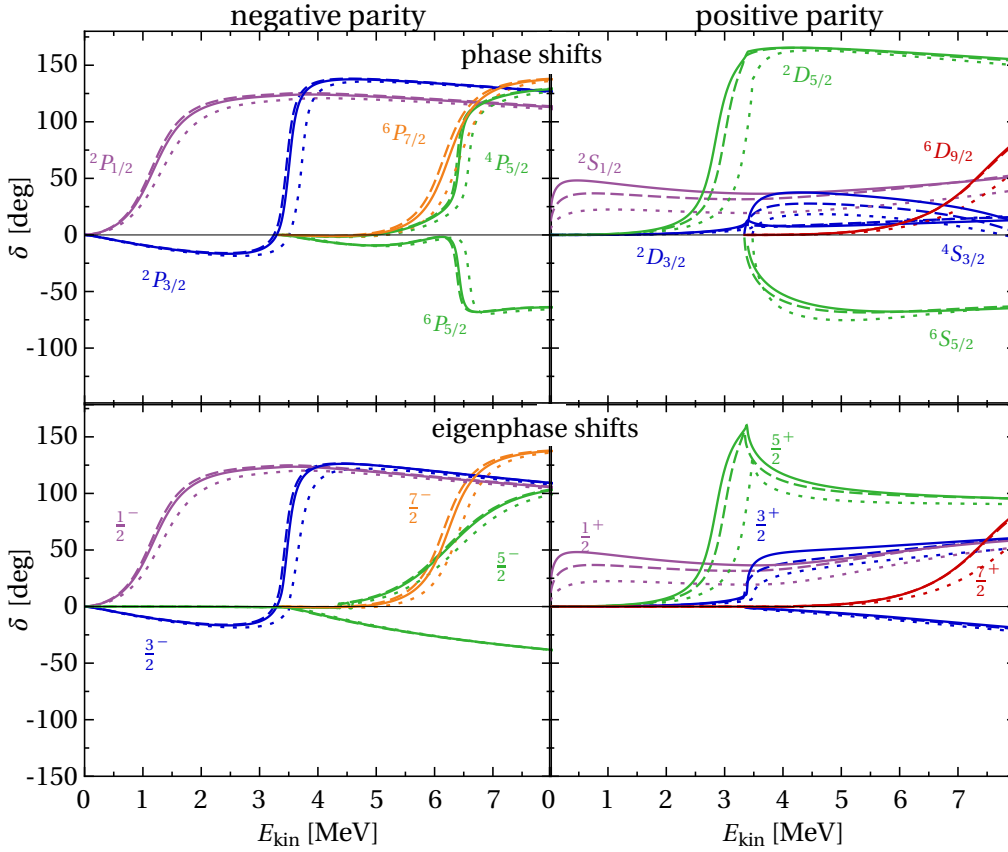


Figure 14.4 – SRG parameter dependence of the NCSMC n - ${}^8\text{Be}$ phase shifts (upper panels) and eigenphase shifts (lower panels) for $\alpha = 0.04$ (.....), 0.0625 (—), and 0.08 fm^4 (---) for the NN+3N-full Hamiltonian. Remaining parameters are $N_{\text{max}} = 10$ (11) for the negative (positive) parity partial waves, $\hbar\Omega = 20 \text{ MeV}$ and $E_{3\text{max}} = 14$.

is consistent with the convergence pattern with respect to N_{max} shown in Figure 14.3.

The right-hand panels of Figure 14.4 show the (eigen)phase shifts for the positive-parity partial waves for the same set of flow parameters. The overall conclusions are identical, however, the differences between $\alpha = 0.08$ and 0.0625 fm^4 and also between $\alpha = 0.0625$ and 0.04 fm^4 are larger compared to the negative-parity results. Again, this may be related to the somewhat slower rate of convergence we found for the positive-parity partial waves in Figure 14.3. Note that the $\frac{1}{2}^+$ resonance shows a dependence on the SRG parameter also for energies beyond its resonance position, however, for all flow parameters its resonance position remains rather stable, in particular above the threshold.

As argued above some contributions to the α dependence could also originate from the $E_{3\text{max}}$ truncation. For all calculations presented here we use $E_{3\text{max}} = 14$, which is currently the largest we can manage in the NCSMC. For the NCSM/RGM kernels, which are one ingredient to the NCSMC equations, almost no dependence on $E_{3\text{max}}$ for the somewhat lighter system n - ${}^4\text{He}$ (cf. Figure 13.2). Due to the small differences between phase shifts for $\alpha = 0.0625$ and 0.08 fm^4 , and since the larger differences for $\alpha = 0.04 \text{ fm}^4$ are likely due to a reduced rate of convergence, we stick to $\alpha = 0.0625 \text{ fm}^4$ for our discussion in the following.

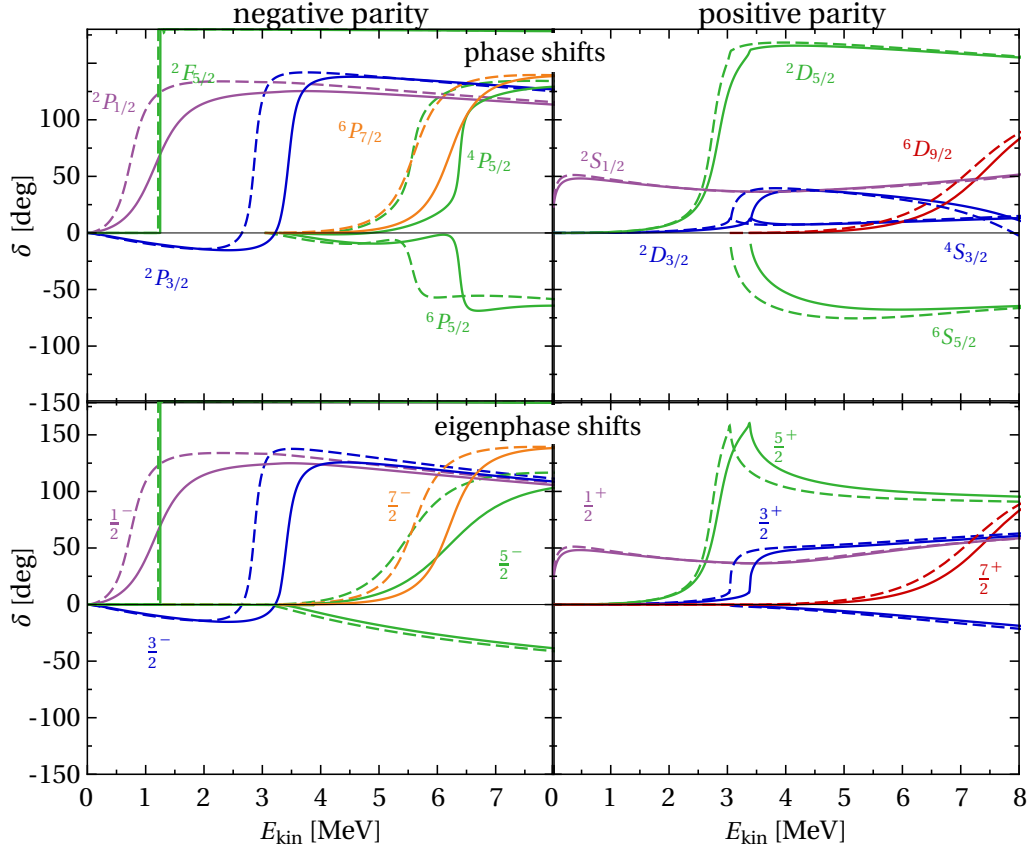


Figure 14.5 – n - ${}^8\text{Be}$ NCSMC (eigen)phase shifts for the NN+3N-induced (---) vs. the NN+3N-full (—) Hamiltonians at $\alpha = 0.0625\text{fm}^4$ and $N_{\text{max}} = 12$ using IT-NCSM vectors. The remaining parameters are $\hbar\Omega = 20\text{MeV}$ and $E_{3\text{max}} = 14$.

14.2.4 3N-force Effects on n - ${}^8\text{Be}$ Scattering Phase Shifts

In this section we aim at disentangling the effects of the SRG-induced 3N interactions on the (eigen)phase shifts from the effects originating from the initial chiral 3N interaction. Therefore, we compare the (eigen)phase shifts for the NN+3N-induced and NN+3N-full Hamiltonians in the left- and right-hand panels of Figure 14.5 for positive- and negative-parity partial waves, respectively. For all partial waves we find some sensitivity to the inclusion of the initial chiral 3N interactions, except for the narrow ${}^2F_{5/2}$ resonance which is practically identical for both Hamiltonians. In general, we observe larger effects of the chiral 3N interactions for the negative-parity than for the positive-parity partial waves, particularly near resonance energies. We note that the initial chiral 3N interaction always moves the resonance energy of all eigenphase shifts to larger energies relative to the n - ${}^8\text{Be}$ threshold. The non-resonant $\frac{5}{2}^-$ or $\frac{3}{2}^+$ eigenphase shifts are basically unaffected. This is also true for all remaining non-resonant phase shifts that we do not show here. For negative parity, the largest effect caused by the initial chiral 3N interaction is found in the rather broad $\frac{5}{2}^-$ resonance around 6 MeV. All other negative-parity partial-wave phase shifts encounter roughly the same shift of their resonance position due to the initial 3N interaction. In addition, the chiral 3N interaction yields almost identical resonance positions for the

$\frac{1}{2}^-$ and $\frac{5}{2}^-$ eigenphase shifts. The largest effect on its resonance energy for positive parity emerges for the $\frac{3}{2}^+$ phase shift. The resonant $\frac{5}{2}^+$ eigenphase shift is affected beyond its resonance energy, mainly regarding the position of its kink. This kink is due to the fact that the $\frac{5}{2}^+$ resonance is bound with respect to the second excited state of ${}^8\text{Be}$, which we consider in the NCSMC ansatz. The changed position of the kink complies with the effect on the excitation energy of the 2^+ state of ${}^8\text{Be}$ caused by the initial 3N interaction. Finally, the $\frac{1}{2}^+$ eigenphase shift is only slightly enhanced by the initial chiral 3N interaction and its resonance position is practically identical for both Hamiltonians, i.e., the $\frac{1}{2}^+$ state remains slightly unbound in excellent agreement with experiment.

14.2.5 Impact of the Continuum on the ${}^9\text{Be}$ Spectrum

For a more direct comparison of the impact of the continuum and the 3N interactions on the ${}^9\text{Be}$ resonances we extract the energies of the resonance centroids E_R and corresponding widths Γ from the eigenphase shifts shown above. As in the initial NCSMC publications [50, 49] we extract the centroids from the maximum of the derivative of the eigenphase shifts with respect to the kinetic energy, i.e., E_R is defined by the inflection point of the eigenphase shifts. The width follows from

$$\Gamma = 2 / \left(\frac{d\delta(E_{\text{kin}})}{dE_{\text{kin}}} \right) \Big|_{E_{\text{kin}}=E_R} \quad (14.15)$$

with eigenphase shifts δ in units of radians. Although there exist other possibilities to extract resonance energies and widths, this constitutes a generally accepted approach safely applicable to sharp resonances [217]. For the following qualitative discussions we adopt the described procedure for all resonances. In addition to resonances the NCSMC approach also yields bound-state energies on equal footing. They follow with help of R -matrix theory with bound-state boundary conditions (cf. Section 12.1). For all NN+3N Hamiltonians considered here, only one bound state is found, namely the $\frac{3}{2}^-$ ground state of ${}^9\text{Be}$.

The influence of the continuum on the ${}^9\text{Be}$ spectrum can be seen in Figure 14.6 by comparison of the ${}^9\text{Be}$ energies relative to the n- ${}^8\text{Be}$ threshold for the IT-NCSM and the NCSMC. The left-hand panel shows the negative-parity states, and the positive-parity results are shown in the right-hand panel. In each panel, the first two columns contain the negative (positive) parity results from IT-NCSM at $N_{\text{max}} = 6$ (7) and 12 (11), respectively. Columns four and five show the corresponding results for NCSMC, and in the middle we include the experimental energies. First, we concentrate on the left-hand panel showing the spectrum for the negative-parity states. By comparing the IT-NCSM and NCSMC results at equal N_{max} we find for all states significant contributions of the additional continuum degrees of freedom in the NCSMC. The sole exception is the $\frac{7}{2}^-$ state, where the effects stay below 0.5 MeV. The NCSMC reduces the energy differences to the threshold compared to the IT-NCSM for all states and for both N_{max} , respectively. As a consequence, the agreement with the experimental energies relative to the n- ${}^8\text{Be}$ threshold is generally improved, and we

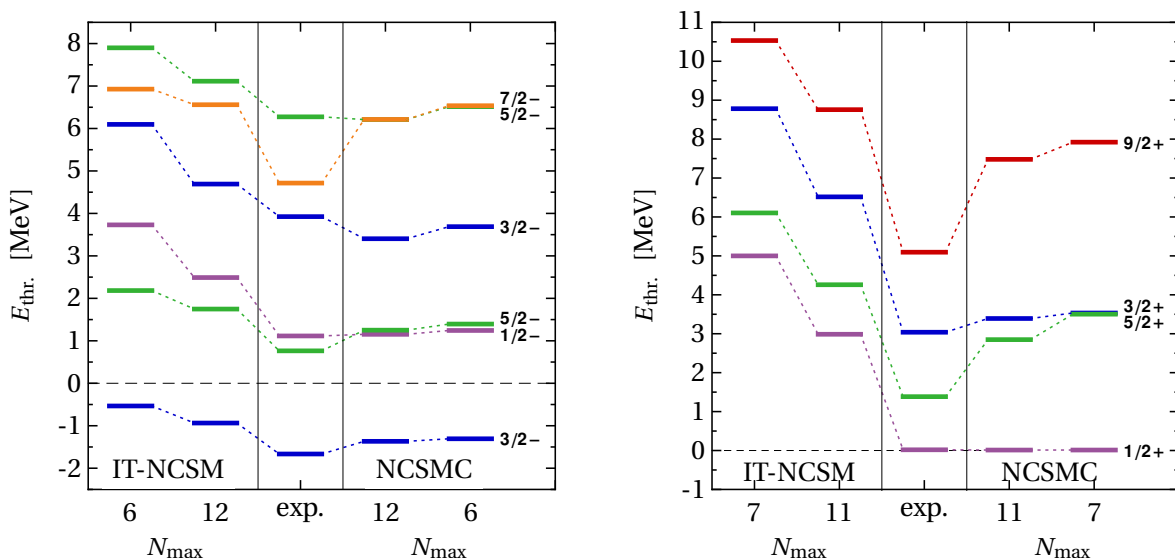


Figure 14.6 – Negative (left-hand panel) and positive (right-hand panel) parity spectrum of ${}^9\text{Be}$ relative to the n - ${}^8\text{Be}$ threshold (---) at $N_{\text{max}} = 6$ (7) and 12 (11) for IT-NCSM (first two columns) and NCSMC (last two columns) compared to experiment [148]. Remaining parameters are $\hbar\Omega = 20$ MeV and $\alpha = 0.0625 \text{ fm}^4$. For further explanations see text.

find excellent agreement for the $\frac{1}{2}^-$ and second $\frac{5}{2}^-$ resonances at $N_{\text{max}} = 12$. Note that also the energy of the $\frac{3}{2}^-$ ground state is lowered by about 0.5 MeV due to continuum contributions and the agreement with experiment is improved. Next we compare the changes for $N_{\text{max}} = 6$ to 12 for both methods, respectively. For the NCSMC energies we find only small effects from the increased model-space size that are slightly larger for the higher-excited states but still remain below 0.5 MeV. Thus, the NCSMC calculations seem to be well converged with respect to N_{max} as already observed for the eigenphase shifts in the previous subsection. This is different for the IT-NCSM energies, where we find significantly larger effects hinting at less converged calculations. This is of course not unexpected due to the fact that all excited states of ${}^9\text{Be}$ are resonances and the IT-NCSM with its basis of A -body HO Slater determinants is not designed for a proper description of continuum states.

The discussion of the positive-parity states of ${}^9\text{Be}$ in context of the right-hand panel of Figure 14.6 is similar: we find even more dramatic effects of the continuum as evident from comparing the energies for fixed N_{max} between the two approaches. Again, the NCSMC reduces all energy differences relative to the n - ${}^8\text{Be}$ threshold compared to the IT-NCSM, leading to improved agreement with experiment. The agreement is particularly striking for the S -wave dominated $\frac{1}{2}^+$ state, which for $N_{\text{max}} = 7$ is shifted by about 5 MeV right on top of its experimental position slightly above the threshold, and remains practically constant for the step to $N_{\text{max}} = 11$ in the NCSMC. Also the $\frac{3}{2}^+$ resonance dominated by the ${}^4S_{\frac{3}{2}}$ partial wave is found in good agreement with experiment, while the discrepancies remain larger for the $\frac{5}{2}^+$ and $\frac{9}{2}^+$ resonances. Note that one might expect contributions from the broad 4^+ state of ${}^8\text{Be}$ that might improve the $\frac{9}{2}^+$ resonance of ${}^9\text{Be}$. As for the negative parities, the NCSMC energies are much less affected by increasing the model space from $N_{\text{max}} = 7$ to 11

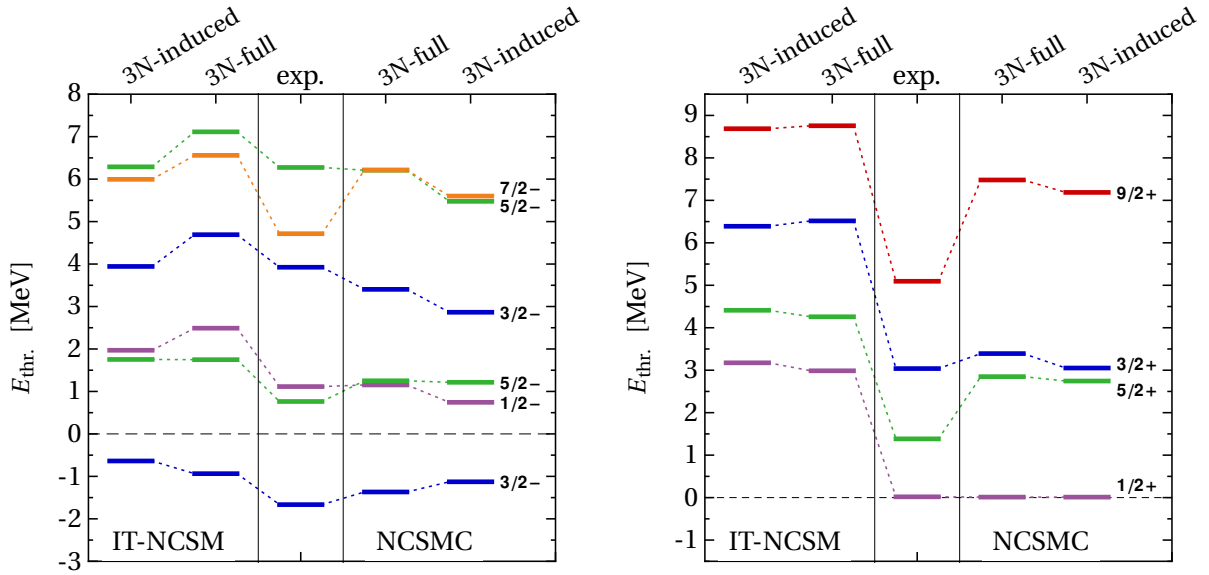


Figure 14.7 – Negative (left-hand panel) and positive (right-hand panel) parity spectrum of ${}^9\text{Be}$ relative to the $n-{}^8\text{Be}$ threshold (---) at $N_{\text{max}} = 12$ and 11 , respectively. Shown are from IT-NCSM (first two columns) and NCSMC (last two columns) results and experiment (middle columns) [148]. The first and last columns contain the energies for the NN+3N-induced and the second and fourth column for the NN+3N-full Hamiltonian, respectively. Remaining parameters are $\hbar\Omega = 20\text{ MeV}$ and $\alpha = 0.0625\text{ fm}^4$. For further explanations see text.

than the IT-NCSM energies, which exhibit significant changes.

We add a comment on excitation energies that can be read off Figure 14.6 by the energy differences to the ground-state. The excitation energy of the $\frac{5}{2}^-$ resonance and similarly all excitation energies of the positive-parity states relative to the $\frac{1}{2}^+$ state are in good agreement with experiment already at the level of IT-NCSM calculations. It seems as if the main issue of the IT-NCSM is to produce the correct threshold energy.

So far we have found significant effects due to the continuum in the ${}^9\text{Be}$ energy levels for the NN+3N-full Hamiltonian. In Figure 14.7 we go on with distinguishing effects caused by the SRG-induced 3N interaction from those originating from the initial chiral 3N interaction. Again the left hand-panel covers the negative-parity spectrum at $N_{\text{max}} = 12$, and the right-hand panel contains the energies of positive-parity states at $N_{\text{max}} = 11$. Within each panel the first two columns depict the results from the IT-NCSM while the two last columns cover the results from the NCSMC, and we include the experimental energy in the middle. Furthermore, the first column contains the results from the NN+3N-induced Hamiltonian and the second the energies for NN+3N-full. This is reversed for the columns corresponding to NCSMC (see column labels). In the negative-parity spectrum we find all states, except the first $\frac{5}{2}^-$ resonance, sensitive to the inclusion of the initial chiral 3N interaction with effects of roughly similar size for both, the IT-NCSM and the NCSMC. Except for the ground state the inclusion of the initial chiral 3N interaction increases the energy difference to the threshold. Since the IT-NCSM energy differences for the NN+3N-induced Hamiltonian are typically close to or above the experimental energies, the agree-

Table 14.1 – Resonance energies relative to the n - ${}^8\text{Be}$ threshold and corresponding width in MeV for NCSMC with the NN+3N-full Hamiltonian with $\Lambda_{3N} = 400\text{MeV}/c$ extracted as explained in the text in comparison to experiment [148]. For positive and negative parity the model-space truncation $N_{\text{max}} = 11$ and 12 is used, respectively.

${}^9\text{Be}$ states	NCSMC		experiment	
	E_R [MeV]	Γ [MeV]	E_R [MeV]	Γ [MeV]
$\frac{1}{2}^+$	0.012	0.09	0.019	0.22
$\frac{5}{2}^+$	3.39	0.17	1.38	0.28
$\frac{3}{2}^+$	2.85	0.41	3.03	0.74
$\frac{9}{2}^+$	7.48	2.25	5.09	1.33
$\frac{3}{2}^-$	-1.367	-	-1.66	-
$\frac{1}{2}^-$	1.15	0.95	1.11	1.08
$\frac{5}{2}^-$	1.25	0.02 keV	0.76	0.78 keV
$\frac{3}{2}^-$	3.4	0.26	3.92	1.33
$\frac{5}{2}^-$	6.21	2.22	6.27	1.0
$\frac{7}{2}^-$	6.21	0.84	4.71	1.21

ment with experiment becomes worse when the initial 3N interaction is included. In contrast, the NCSMC energy differences for the NN+3N-induced Hamiltonian are typically smaller than the experimental ones and, thus, the overall agreement with experiment is clearly improved due to the initial chiral 3N interaction. Note that this conclusion would have been opposite based on the IT-NCSM, which highlights the benefit from the NCSMC approach, i.e., the inclusion of continuum effects, for validations of the chiral Hamiltonians in ${}^9\text{Be}$. Exceptions are the $\frac{5}{2}^-$ resonance, which is not affected at all and the $\frac{7}{2}^-$ state for which the shift caused by the initial 3N interaction has the wrong sign, hinting again at possible deficiencies in the initial (3N) Hamiltonian.

The same study for the positive-parity spectrum, contained in the right-hand panel of Figure 14.7, reveals the positive-parity states to be rather insensitive to the initial 3N interaction compared to the energy shifts we observed for the negative-parity states. In particular, the $\frac{1}{2}^+$ state is practically unaffected and remains slightly above the threshold in excellent agreement with experiment. Note that this state has been found to be very weakly-bound in NN-only calculations [209].

Finally, we list the extracted resonance centroids and corresponding widths for the NCSMC calculations using the NN+3N-full Hamiltonian with $\Lambda_{3N} = 400\text{MeV}/c$ along with the experimental data in Table 14.1. As before the positive-parity states are treated in an $N_{\text{max}} = 11$ model space and the negative-parity states are computed at $N_{\text{max}} = 12$. We have discussed the resonance energies already above in context of Figures 14.6 and 14.7. Overall the widths extracted as described above are within the same order of magnitude as the experimental ones. Typically the computed widths are smaller than the experimental ones,

except for the $\frac{9}{2}^+$ and the $\frac{3}{2}^-$ resonances, which we find larger than experiment. Note that the narrow $\frac{5}{2}^-$ resonance with experimental width of 0.78 keV is also found very narrow in the NCSMC calculations.

In conclusion, NCSMC calculations are well converged already at moderate model-space sizes (here $N_{\max} = 6$ or 7) and, if continuum effects are important, yield results superior to IT-NCSM calculations that are performed in much larger model spaces. The sole exception for the negative-parity states of ${}^9\text{Be}$ is the $\frac{7}{2}^-$ state, which is rather insensitive to both, additional continuum degrees of freedom and to the larger model spaces. Although we cannot rule out the relevance of different cluster structures that are not captured by the single-nucleon binary-cluster ansatz used here, one might expect larger sensitivities to the IT-NCSM model-space size if such structures would be relevant. Therefore, the deviations from experiment are likely to be connected to deficiencies of the chiral NN+3N Hamiltonian.

SUMMARY AND OUTLOOK

We have discussed the building blocks for the inclusion of 3N interactions, as they emerge from chiral effective field theory, consistently in ab-initio calculations for different nuclear structure and reaction scenarios. This involved the development of an adapted storage scheme that turned out to be key for the practical management of 3N matrix elements, and the consistent transformation of the chiral NN+3N Hamiltonians by means of the SRG, followed by the application of the SRG-evolved Hamiltonians in nuclear structure calculations using the IT-NCSM and CC method. In applications to ground-state energies we found dependencies on the SRG flow parameter hinting at effects of discarded SRG-induced multi-nucleon interactions beyond the 3N level for nuclei within the upper p -shell and heavier. We traced back the origin of these SRG-induced interactions to the two-pion exchange contribution of the leading chiral 3N interaction, and we found a way around those by lowering the cutoff momentum of the 3N force. Applying the latter interactions by means of the normal-ordered two-body approximation, which we found to be accurate, for ab-initio predictions of binding energies for selected closed-shell nuclei up to ^{132}Sn , revealed remarkable agreement with the experimental binding energy systematics. Furthermore, we have studied the effects of chiral 3N interactions on nuclear energy spectra, where we found an improved agreement with experiment. However, a sensitivity study in the ^{12}C and ^{10}B spectra with respect to variations of low-energy constants of the 3N interaction also revealed discrepancies with experiment for certain states and hints at missing operator structures in the leading chiral 3N interaction. In Part III we have focussed on the ab-initio description of nuclear reactions. Therefore, we extended the NCSM/RGM formalism to include 3N interactions in particular for targets involving more than four nucleons. We applied this extended formalism to nucleon- ^4He scattering and found good agreement with experimental data for scattering phase shifts, cross sections and analyzing powers. We then moved on to the NCSMC approach that combines the NCSM and NCSM/RGM to an ab-initio framework suitable to describe nuclear bound and continuum states on equal footing. Our developments for the NCSM/RGM facilitate the extension of the NCSMC to 3N interactions, which we eventually apply to neutron- ^8Be scattering and explore the impact of the continuum on the ^9Be energy levels. The NCSMC approach shows superior convergence properties compared to both, IT-NCSM and the NCSM/RGM approach and the 3N interaction overall yields improved agreement with experiment.

Our results show that ab-initio nuclear theory using chiral NN+3N Hamiltonian is able to exploit the link to low-energy QCD via chiral EFT interactions, i.e., to arrive at predictions for binding energies up to the heavy-mass regime, for nuclear spectra throughout

the p - and lower sd -shell, and also for nuclear reaction observables. Nevertheless, there are several directions for further research. One of these concerns ab-initio predictions for open-shell nuclei in the medium-mass regime including 3N interactions. Promising techniques that recently became available are extensions of coupled-cluster theory, the in-medium similarity renormalization group [34] or the self-consistent Gorkov Green's function approach [31].

Another important challenge already in lighter nuclei is the investigation of nuclear structure observables other than energies, e.g., radii or electromagnetic transitions. This involves the inclusion of electromagnetic currents provided by chiral EFT to arrive at a consistent description. Furthermore, the corresponding operators need to be included consistently in the SRG evolution.

Concerning nuclear reactions next steps involve the inclusion of 3N interactions also in the two-nucleon projectile formalism of the NCSM/RGM and NCSMC approaches. Optimally also the extension of both methods to handle channels including three-body cluster systems with 3N interactions is interesting, but poses a formidable task. This will allow for further systematic studies of chiral interactions in nuclear reactions

Finally, it will be interesting to see how the next-generation chiral interactions alter the findings in the different aspects covered in this work. On the one hand this includes optimized fits of the low-energy constants to experimental data, see, e.g., Ref. [146] for first attempts in this direction. On the other hand also sub-leading 3N interactions, i.e., at $N^3\text{LO}$ will become available in the near future and can enter the framework presented in this work. Eventually it will be challenging how to handle chiral four-nucleon interactions that also emerge at $N^3\text{LO}$, and which one would have to take into account for consistency.

APPENDICES

APPENDIX A

High-Order Padé-Resummed Many-Body Perturbation Theory

In this appendix we present another nuclear structure many-body method based on standard Rayleigh-Schrödinger many-body perturbation theory (MBPT)[218] that complements the methods of Section 4. We discuss how the generalization of MBPT to degeneracies in combination with the evaluation of high-order contributions can serve for the ab-initio description of ground-states and excitation spectra of closed- and open-shell nuclei. We have published the formalism and results presented in the following in Ref. [219].

Low-order MBPT has been used for studies of systematics of ground-state properties of closed-shell nuclei throughout the nuclear chart [220, 103, 87], and for calculations focussing on infinite neutron and nuclear matter [84, 221], however, the quality of such low-order approximations often remains unclear. With the recursive formulation of MBPT we present in the following, it becomes possible to test this at least for light nuclei, and the application of a subsequent resummation of the perturbation series by means of Padé approximants [222] allows for very stable and converged energies in very good agreement with exact NCSM calculations.

We start with a brief overview of the necessary steps to formulate degenerate many-body perturbation theory (DMBPT) for high orders. The degeneracy concerns the unperturbed, i.e., zeroth-order, energy level and needs to be considered explicitly to allow for studies of excited states and open-shell nuclei. The non-degenerate case, which is suitable to describe ground states of closed-shell nuclei, follows as special case. The starting point for the formulation of DMBPT is the eigenvalue problem of the intrinsic Hamiltonian \hat{H} of Eq. (4.1), which is partitioned into an unperturbed part \hat{H}_0 and a perturbation \hat{W} and we introduce a auxiliary parameter λ , i.e.,

$$\hat{H} \xrightarrow{\text{partitioning}} \hat{H}_\lambda = \hat{H}_0 + \lambda \hat{W} = \hat{H}_0 + \lambda(\hat{H} - \hat{H}_0). \quad (\text{A.1})$$

Note that the original Hamiltonian is recovered for $\lambda = 1$. Basically, there are no further

formal restrictions on the partitioning, i.e., on the form of the unperturbed Hamiltonian \hat{H}_0 . However, the eigenvalue problem of the unperturbed Hamiltonian

$$\hat{H}_0 |\phi_n\rangle = \epsilon_n |\phi_n\rangle \quad (\text{A.2})$$

fixes the unperturbed states $\{|\phi_n\rangle\}$ that are used a basis for the subsequent perturbative expansion. Therefore, in practice we are interested in choosing the partitioning such that the unperturbed states are convenient from a computational and physical point of view. Typical choices for \hat{H}_0 adopted in the nuclear-structure context are single-particle Hamiltonians, e.g., of Hartree-Fock or harmonic oscillator type, such that the unperturbed states are given as Slater determinants of the corresponding single-particle states. Accordingly, the unperturbed energies are determined by the sum of single-particle energies of occupied states in $|\phi_n\rangle$. We concentrate mainly on unperturbed HO single-particle Hamiltonians, but all formulas are of general validity.

Since we are aiming at a general formulation, suitable to describe open-shell nuclei and also excited states, we need to take possible degeneracies of the unperturbed energy levels ϵ_n into account. We do so by introducing the degeneracy index d labeling the unperturbed states $|\phi_{nd}\rangle$, which span the g_n -dimensional degenerate subspace associated with ϵ_n . As a consequence we have to attach the degeneracy index also in the power-series for the perturbed energies and states, that is we set

$$E_{nd}(\lambda) = \epsilon_n + \lambda E_{nd}^{(1)} + \lambda^2 E_{nd}^{(2)} + \dots, \quad (\text{A.3})$$

$$|\Psi_{nd}(\lambda)\rangle = |\Psi_{nd}^{(0)}\rangle + \lambda |\Psi_{nd}^{(1)}\rangle + \lambda^2 |\Psi_{nd}^{(2)}\rangle + \dots, \quad (\text{A.4})$$

with $E_{nd}^{(0)} = \epsilon_n$. Furthermore, $E_{nd}^{(p)}$ and $|\Psi_{nd}^{(p)}\rangle$ denote the p -th order energy and states corrections, respectively, and, therefore, are the quantities we want to determine up to high orders p . We obtain the starting point for the derivation of these corrections by inserting Eqs. (A.3) and (A.4) together with the partitioned Hamiltonian (A.1) in the eigenvalue problem of the Hamiltonian \hat{H}_λ , and match same orders of λ to arrive at

$$\hat{W} |\Psi_{nd}^{(p-1)}\rangle + \hat{H}_0 |\Psi_{nd}^{(p)}\rangle = \sum_{j=0}^p E_{nd}^{(j)} |\Psi_{nd}^{(p-j)}\rangle. \quad (\text{A.5})$$

Before starting the actual derivation of the corrections, we need to fix another subtlety caused by degeneracy: as evident from the power-series ansatz and also from Eq. (A.5) we need an expression for the unperturbed state $|\Psi_{nd}^{(0)}\rangle$. However, we can choose arbitrary linear combinations of the g_n unperturbed Slater determinants $|\phi_{nd}\rangle$ corresponding to energy level ϵ_n , i.e.,

$$|\Psi_{nd}^{(0)}\rangle = \sum_{e=0}^{g_n-1} \chi_{nd,ne} |\Phi_{ne}\rangle. \quad (\text{A.6})$$

Inserting the latter expansion in Eq. (A.5) at $p = 1$ and multiplication by $\langle\Phi_{nd'}|$ yields the

eigenvalue equation of the perturbation \hat{W} in the n th degenerate subspace

$$\sum_{e=0}^{g_n-1} (\langle \Phi_{nd'} | W | \Phi_{ne} \rangle - E_{nd}^{(1)} \delta_{d'e}) \chi_{nd,ne} = 0. \quad (\text{A.7})$$

Thus, diagonalization yields the expansion coefficients $\chi_{nd,ne}$ of $|\Psi_{nd}^{(0)}\rangle$ and determines the first-order energy correction $E_{nd}^{(1)}$. Moreover, orthonormality of the unperturbed states $\langle \Psi_{nd}^{(0)} | \Psi_{nd'}^{(0)} \rangle = \delta_{dd'}$ holds, and choosing the intermediate normalization $\langle \Psi_{nd}^{(0)} | \Psi_{nd} \rangle = 1$ one can deduce $\langle \Psi_{nd}^{(0)} | \Psi_{nd}^{(p)} \rangle = \delta_{0p}$. These relations are important during the derivation of the perturbative corrections.

The p th order energy correction is obtained via multiplication of Eq. (A.5) by $\langle \Psi_{nd}^{(0)} |$ as

$$E_{nd}^{(p)} = \langle \Psi_{nd}^{(0)} | \hat{W} | \Psi_{nd}^{(p-1)} \rangle, \quad (\text{A.8})$$

and is identical to the form in non-degenerate MBPT [223]. For the derivation of the state corrections we start with expanding the p th order state correction in the unperturbed basis

$$|\Psi_{nd}^{(p)}\rangle = \sum_m^{m \neq n} \sum_e C_{nd,me}^{(p)} |\phi_{me}\rangle + \sum_e^{e \neq d} D_{nd,ne}^{(p)} |\Psi_{ne}^{(0)}\rangle, \quad (\text{A.9})$$

where we use the simple Slater determinants $|\phi_{me}\rangle$ in the subspaces orthogonal to the degenerate subspace n , and within the latter we use the unperturbed states (A.6). Accordingly, we have defined $C_{nd,me}^{(p)} = \langle \phi_{me} | \Psi_{nd}^{(p)} \rangle$ for $m \neq n$, and $D_{nd,ne}^{(p)} = \langle \Psi_{ne}^{(0)} | \Psi_{nd}^{(p)} \rangle$ for $e \neq d$. Thus, to complete the derivation we need the expression for these expansion coefficients. For coefficients C we multiply Eq. (A.5) by $\langle \phi_{me} |$ for $m \neq n$, and to determine the coefficient D we multiply Eq. (A.5) by $\langle \Psi_{ne}^{(0)} |$ for $e \neq d$. After some algebra we obtain the following expressions, which provide the complete information to evaluate the perturbation series (A.3) and (A.4): the energy corrections are given by

$$E_{nd}^{(p=1)} = \sum_{e=0}^{g_n-1} \sum_{e'=0}^{g_n-1} \chi_{nd,ne}^* \chi_{nd,ne'} \langle \Phi_{ne} | \hat{W} | \Phi_{ne'} \rangle, \quad (\text{A.10})$$

and

$$E_{nd}^{(p \geq 2)} = \sum_{m,e}^{m \neq n} \sum_{e'=0}^{g_n-1} \chi_{nd,ne'}^* \langle \Phi_{ne'} | \hat{W} | \Phi_{me} \rangle \cdot C_{nd,me}^{(p-1)}. \quad (\text{A.11})$$

The expressions for the C -coefficients read

$$C_{nd,me}^{(p=0)} = 0, \quad (\text{A.12})$$

$$C_{nd,me}^{(p=1)} = \frac{\langle \Phi_{me} | \hat{W} | \Phi_{nd} \rangle}{\epsilon_n - \epsilon_m}, \quad (\text{A.13})$$

and

$$C_{nd,me}^{(p \geq 2)} = \frac{1}{\epsilon_n - \epsilon_m} \left(\sum_{m',e'}^{m' \neq n} \langle \Phi_{me} | \hat{W} | \Phi_{m'e'} \rangle C_{nd,m'e'}^{(p-1)} + \sum_{e'}^{e' \neq d} \sum_{e''=0}^{g_n-1} \chi_{ne',ne''} \langle \Phi_{me} | \hat{W} | \Phi_{ne''} \rangle D_{nd,ne'}^{(p-1)} - \sum_{j=1}^{p-1} E_{nd}^{(j)} C_{nd,me}^{(p-j)} \right). \quad (\text{A.14})$$

For the D -coefficients we obtain

$$D_{nd,ne}^{(p=0)} = 0 \quad (\text{A.15})$$

and

$$D_{nd,ne}^{(p \geq 1)} = \frac{1}{E_{nd}^{(1)} - E_{ne}^{(1)}} \left(\sum_{m,e'}^{m \neq n} \sum_{e''=0}^{g_n-1} \chi_{ne,ne''}^* \langle \Phi_{ne''} | \hat{W} | \Phi_{me'} \rangle C_{nd,me'}^{(p)} - \sum_{j=1}^{p-1} E_{nd}^{(j+1)} D_{nd,ne}^{(p-j)} \right). \quad (\text{A.16})$$

For the practical implementation of Eqs. (A.10) - (A.16) and their efficient evaluation up to high orders p , it is mandatory to exploit their recursive structure: to compute the energy correction of p th order we need the state correction of $(p-1)$ th order (cf. Eq. (A.8)), however as evident from Eq. (A.11) only the coefficients $C_{nd,me}^{(p-1)}$ are required, which only implicitly depend on the coefficients $D_{nd,ne}^{(p-2)}$. The expansion coefficients $C_{nd,ne}^{(p \geq 2)}$ depend on C coefficients, D coefficients and energy corrections of lower orders, and the $D_{nd,ne}^{(p \geq 1)}$ depend on lower-order D coefficients and on C coefficients of same order. Thus, it becomes possible to construct the perturbation series order by order up to very high orders as follows: the zeroth-order energy is given by the unperturbed energy ϵ_n , the first-order correction follows from the diagonalization in the degenerate subspace, and for the second-order correction we need only the coefficients $C_{nd}^{(1)}$. For the energy corrections of order $p \geq 3$ we start with computing coefficients $D_{nd,ne}^{(p-2)}$ which include the known $C_{nd}^{(p-2)}$ and all lower-order D coefficients. Then the coefficients $D_{nd,ne}^{(p-2)}$ and the C coefficients up to $p-2$ input the computation of $C_{nd}^{(p-1)}$ which finally yield $E_{nd}^{(p)}$. Furthermore, we note that in the special case of no degeneracy of the targeted energy level the formulas presented above simplify to the recursive scheme for the non-degenerate case, which we published in Ref. [223]. Note in particular that the coefficients D are not defined in this case. Furthermore, we point out that the recursive structure of the expressions is less obvious in a diagrammatic approach or if the A -body matrix elements are broken down into two- or three-body matrix elements of the interactions involved.

Concerning the inclusion of the 3N interaction into the formalism, we emphasize that we did not make any assumptions about the interactions included in the Hamiltonian for the formalism presented above, which is consequently valid for 3N interactions, too. This is again due to the fact, that the formalism is formulated in terms of A -body Slater determinants so that the only complication when switching from NN to 3N interactions is due to the generalization of the Slater-Condon rules [126] that are used for the evaluation of

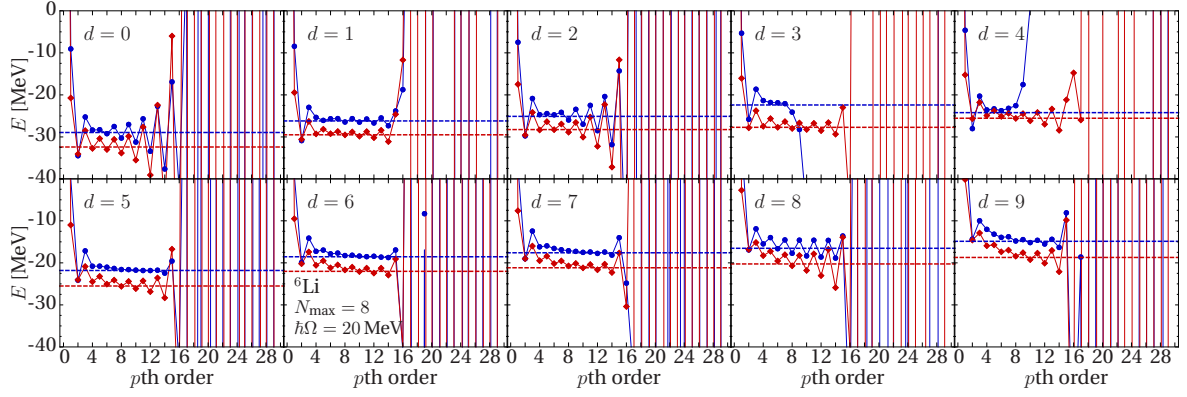


Figure A.1 – Energies from the DMBPT power series (A.3) truncated at order p for ${}^6\text{Li}$ and for the levels corresponding to the degenerate $n = 0$ subspace computed with the NN-only Hamiltonian. As unperturbed Hamiltonian the HO is used with $\hbar\Omega = 20\text{MeV}$ and the model space is truncated as in the NCSM at $N_{\text{max}} = 8$. Results are shown for SRG flow parameters $\alpha = 0.04\text{fm}^4$ (●) and 0.16fm^4 (◆), and the dashed lines correspond to the exact NCSM results obtained using the identical model space. (published in [219])

the A -body matrix elements like $\langle\Phi_{me}|\hat{W}|\Phi_{nd}\rangle$, analogously as in the NCSM for the computation of the Hamilton matrix elements in Eq. (4.2). Another computational similarity to the NCSM approach are the matrix-vector multiplications of the Hamilton matrix and the coefficient vectors, e.g., in Eqs. (A.14) or (A.16), and the coefficient vectors of previous orders need to be stored. This is similar to the operations in the Lanczos algorithm used for the matrix-diagonalization step in the NCSM. Accordingly, the limitations with respect to nucleon number and model-space size of the DMBPT approach are similar to those of NCSM at least when aiming at high-order corrections, e.g., of 30th order which we study in the following. Therefore, to go beyond the domain of the NCSM one has to invent alternatives for an efficient evaluation of the nested sums in the expressions above, or one needs to resort to low-orders.

In Figure A.1 we present results for ${}^6\text{Li}$ using DMBPT up to 30th order. We restrict ourselves to the NN-only Hamiltonian using the chiral two-nucleon interaction at N^3LO , see Section 1.1, as initial Hamiltonian, and do not consider 3N interaction for simplicity. The unperturbed Hamiltonian includes the kinetic energy and a one-body HO potential, and defines the unperturbed basis states $|\Phi_{nd}\rangle$ given as Slater determinants of HO single-particle states, i.e., they are identical to the basis states used in the NCSM. Therefore, we adopt the model-space truncation in terms of N_{max} , and use $N_{\text{max}} = 8$ with $\hbar\Omega = 20\text{MeV}$. Since we study ${}^6\text{Li}$, which is not consistent with an HO shell closure, we need to consider degeneracies, and we concentrate on the subspace with lowest unperturbed energy, i.e., $n = 0$, which consists of ten degenerate states $|\Phi_{0d}\rangle$. We assign the degeneracy index d in the order of ascending first-order energy corrections obtained by the diagonalization of the perturbation \hat{W} in the degenerate subspace. Results from an exact diagonalization via the NCSM are shown as dashed horizontal lines. Obviously, we find for all states a divergent perturbation series, in fact for both SRG parameters. We observe different patterns

of the partial sums as function of the perturbation order p : in some cases the agreement with the exact result seems to be reasonable but then the perturbative corrections become larger again and the series starts to diverge oscillatory (e.g. for $d = 5, 6, 7$), or the perturbation series exhibits an oscillatory pattern already at low orders and the amplitude of the oscillation increases with ascending order p (e.g. for $d = 0, 8$). In addition, we observe even monotonous divergence beyond $p \approx 8$ (e.g. for $d = 3$ and 4 for $\alpha = 0.04 \text{ fm}^4$). Also low-order corrections do not yield a reliable estimate: while the second and third-order results for $\alpha = 0.04 \text{ fm}^4$ are typically below and above the exact result, respectively, with increasing degeneracy index the second-order partial sum approaches the exact result and is above the exact result for $d = 9$. This is even more severe for $\alpha = 0.16 \text{ fm}^4$ results, where the step from second to third order typically enlarges the deviation from the exact result. Hence, in summary perturbation theory based on HO basis states does not provide controlled approximations of the exact energy eigenvalues. It is important to note that also the significantly softer Hamiltonian with $\alpha = 0.16 \text{ fm}^4$ does not improve this issue. Thus, the SRG can improve the convergence of many-body calculations with respect to model-space size, but it does not necessarily improve the convergence of the perturbation series. Nevertheless, such soft interactions are sometimes termed 'perturbative' see, e.g., Ref.[224], which might be misleading.

To overcome these convergence issues, which are consistent with our findings with non-degenerate MBPT for ^4He , ^{16}O , and ^{40}Ca presented in Ref. [223], we take advantage of resummations of the perturbation series by means of Padé approximants [225, 222]. The idea is to represent the energy $E_{nd}(\lambda)$ by means of a rational function

$$E(\lambda) = \frac{a_0 + \lambda a_1 + \lambda^2 a_2 \dots}{b_0 + \lambda b_1 + \lambda^2 b_2 \dots} \quad (\text{A.17})$$

instead of the simple power-series (A.3) of pure DMBPT. The truncation of the polynomials in the numerator at order L , and the one in the denominator at order M yields the definition of the Padé approximant

$$[L/M](\lambda) = \frac{a_0 + \lambda a_1 + \lambda^2 a_2 \dots + \lambda^L a_L}{b_0 + \lambda b_1 + \lambda^2 b_2 \dots + \lambda^M b_M}, \quad (\text{A.18})$$

which by construction is able to describe singularities [225, 222, 189]. The coefficients $\{a_i\}$, $\{b_j\}$ can be obtained from a set of coupled linear equations derived by matching same orders of λ for a Taylor expansion of Eq (A.18) and the perturbation series (A.3), i.e., they can be determined completely by information from the DMBPT calculation. An alternative possibility to compute the Padé approximants, equivalent to the solution of the above mentioned set of coupled equations, is the ratio of determinants that are constructed di-

rectly from the energy corrections $E^{(p)}$ of the DMBPT power series

$$[L/M](\lambda) = \frac{\begin{vmatrix} E^{(L-M+1)} & E^{(L-M+2)} & \dots & E^{(L+1)} \\ E^{(L-M+2)} & E^{(L-M+3)} & \dots & E^{(L+2)} \\ \vdots & \vdots & \ddots & \vdots \\ E^{(L)} & E^{(L+1)} & \dots & E^{(L+M)} \\ \sum_{p=0}^{L-M} E^{(p)} \lambda^{M+p} & \sum_{p=0}^{L-M+1} E^{(p)} \lambda^{M+p-1} & \dots & \sum_{p=0}^L E^{(p)} \lambda^p \end{vmatrix}}{\begin{vmatrix} E^{(L-M+1)} & E^{(L-M+2)} & \dots & E^{(L+1)} \\ E^{(L-M+2)} & E^{(L-M+3)} & \dots & E^{(L+2)} \\ \vdots & \vdots & \ddots & \vdots \\ E^{(L)} & E^{(L+1)} & \dots & E^{(L+M)} \\ \lambda^M & \lambda^{M-1} & \dots & 1, \end{vmatrix}}, \quad (\text{A.19})$$

with $E^{(p)} = 0$, where we have dropped the subscript nd for brevity. From this it follows that in order to compute the Padé approximant $[L/M](\lambda)$ we need the first $L + M$ energy corrections $E^{(p)}$ from DMBPT for the state under investigation. Its evaluation at the physical point, i.e., $[L/M](\lambda = 1)$ then provides the resummed energy. We note that the same information, namely the DMBPT energy corrections, enter the Padé approximant $[L/M]$ and the perturbation series at $p = L + M$. We note that an extensive convergence theory of Padé approximants does exist [225, 222], however, most theorems rely on the knowledge of the complete power series. Nevertheless, there is the so-called Padé conjecture [225] that can help to understand the results presented in the following. It essentially states that for a continuous function $E(\lambda)$ there is an infinite sub-sequence of diagonal Padé approximants $[L/L](\lambda)$ that converges uniformly against $E(\lambda)$ for $|\lambda| \leq 1$. The formal continuity requirement is always fulfilled for real λ in our applications, and, therefore, the Padé conjecture may motivate a convergent sequence in our results.

We can apply the concept of Padé approximants evaluated at the physical point again to the ten-fold degenerate subspace $n = 0$ of ${}^6\text{Li}$ for the NN-only Hamiltonian at SRG flow parameter $\alpha = 0.04 \text{ fm}^4$. The energy corrections presented in Figure A.1 constitute the sole input for the Padé approximants. We compute the diagonal $[L/L]$, the superdiagonal $[L/L + 1]$, and the subdiagonal $[L/L - 1]$ Padé approximants and plot the resulting energies in Figure A.2. Evidently, if we include only information from low-order DMBPT the agreement with the exact results, shown as horizontal dashed line, is not improved compared to the pure perturbative treatment. However, including information of higher-orders of DMBPT improves the agreement with the NCSM result and in particular beyond $L + M \approx 15$ we obtain an overall excellent agreement. This is remarkable since exactly the high-order energy corrections that caused the failure of the simple perturbation series are key for the accuracy of the Padé approximants. This complies with the above mentioned Padé conjecture, note, however, that we also find excellent agreement for the non-diagonal approximants. In principle, outliers are possible since the Padé conjecture covers only a sub-sequence of diagonal approximants, and in fact we observe slightly larger deviations for

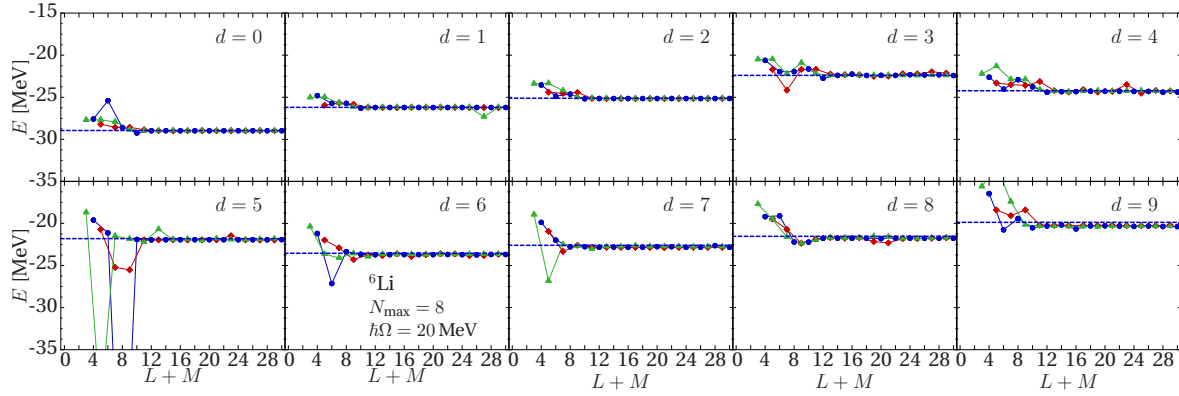


Figure A.2 – Energies obtained by means of Padé approximants for the ten states corresponding to the $n=0$ HO subspace of ${}^6\text{Li}$. Plotted are the diagonal $[L/L]$ (\bullet), the superdiagonal $[L/L+1]$ (\blacklozenge), and the subdiagonal $[L/L-1]$ (\blacktriangle) Padé approximants as well as the energies obtained by diagonalization in the NCSM ($-\cdot-\cdot-$). The model space is truncated at $N_{\max}=8$, and we use $\hbar\Omega=20\text{ MeV}$ and $\alpha=0.04\text{ fm}^4$. (published in [219])

some individual approximants, e.g., for off-diagonal approximants at $d=3,4,5$ or 8 . Given the clear divergences of the DMBPT power series, the recovery of such accurate results via Padé resummation, even for the monotonously divergent cases $d=3$ and 4 , is impressive. Nevertheless, we find that at least 10th order perturbation theory is mandatory to achieve accurate agreement with the NCSM results.

From the data shown in Figure A.2 we can extract an averaged result. Therefore, we average all approximants with $L+M \geq 15$, exclude those approximants which exhibit deviations larger than 0.5 MeV , and rebuild the average of the reduced set and adopt the standard deviation as uncertainty of the averaged approximants. We compile the energies in terms of the positive parity excitation spectrum of ${}^6\text{Li}$ in the left panel of Figure A.3, where the averaged Padé results are depicted in the third column. In addition, the first column shows the energy levels obtained from experiment, and the second column the NCSM results obtained in the same HO model space as the DMBPT energy corrections that input the Padé approximants. We find very good agreement of the energies extracted by means of the averaged Padé approximants with the exact NCSM results for the energetically lowest 5 states. Note that the standard deviation from the averaging process is depicted as orange band. For the remaining high-lying states we find small deviations from the corresponding exact results. In addition, we conduct the same type of calculations for the low-lying negative parity states of ${}^7\text{Li}$ and obtain the spectrum shown in the right panel of Figure A.2. We find again very good agreement with the NCSM energies for all states. In the fourth to last column of the respective spectra we include the results obtained from the partial sums of the DMBPT power series truncated at order $p=2,3,4$, and 8 , respectively. These low-order DMBPT results do not provide reliable approximations for the exact eigenvalues. The second-order excitation energies are too large for all investigated states, and their deviation from the NCSM energies seem to increase with increasing excitation. The inclusion of the third order correction typically lowers the excitation energies, thus

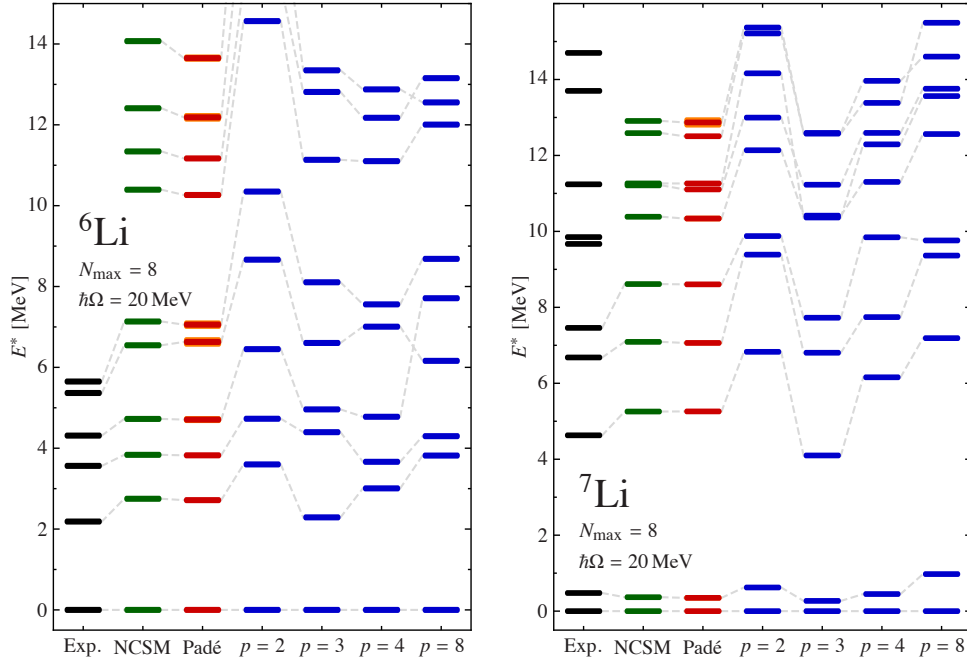


Figure A.3 – Low-lying excitation energies of ${}^6\text{Li}$ and ${}^7\text{Li}$ obtained in the $N_{\text{max}} = 8$ model space, at $\hbar\Omega = 20 \text{ MeV}$ and $\alpha = 0.04 \text{ fm}^4$. Shown are in each panel from the left the experimental energies, the NCSM results, the Padé resummed results as described in the text, and the results from the DMBPT power series truncated at $p = 2, 3, 4$, and 8 . Experimental results taken from Ref. [147]. (published in [219])

reducing the deviations from the exact results. However, generally the forth-order contributions are less coherent, and several level crossings occur in the step to $p = 8$. For even higher orders (not shown) the excitation spectra are completely destroyed due to the strong divergence of the DMBPT power series, cf. Figure A.1.

Overall, we state that DMBPT formulated by means of HO unperturbed basis states is typically divergent despite the use of very soft interactions, and low-order DMBPT results are not sufficient to obtain reliable approximations to the exact NCSM results. However, when we use the Padé resummation technique based on DMBPT information up to high orders, i.e., 15th - 30th order, we observe remarkably good agreement with the energies obtained in the identical model-space within the ab-initio NCSM.

Finally, the discrepancies between the Padé-resummed DMBPT and NCSM excitation energies from experiment hints at deficiencies of the SRG-evolved NN interaction. As mentioned above the inclusion of 3N interaction into the DMBPT framework is straightforward, however, before going in this direction, which requires the whole 3N matrix-element technology we have discussed in Section 2.2.3, another option is a change in the partitioning of the Hamiltonian (A.1) and correspondingly to a change of the unperturbed basis. A first step in this direction is the use of single-particle basis states obtained from a preceding Hartree-Fock calculation using the consistent nuclear Hamiltonian and model space. First results for the MBPT ground-state energy of ${}^{16}\text{O}$ using such a Hartree-Fock basis with $e_{\text{max}} = 8$ and the considerations of up to 2-particle-2-hole (2p2h) excitations of the Hartree-Fock ground state are shown in Figure A.4 as function of the perturbation order. The per-

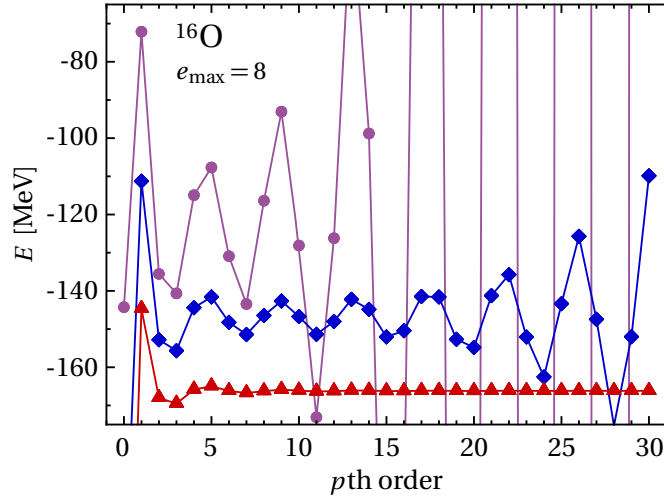


Figure A.4 – ^{16}O ground-state energy obtained from the MBPT power series truncated p th order computed with Hartree-Fock basis at model-space truncation $e_{\max} = 8$ allowing up to $2p2h$ -excitations. Shown are results obtained with the NN-only Hamiltonian at SRG flow parameters $\alpha = 0.02$ (\bullet), 0.04 (\blacklozenge), 0.08 fm^4 (\blacktriangle). Figure adapted from [226].

turbation series obtained for the Hamiltonians at $\alpha = 0.02$ (violet circles) and 0.04 fm^4 (blue diamonds) are both non-convergent and, therefore, fit in the usual picture we discussed above in context of Figure A.1 using the HO basis. However, we find the amplitude of the oscillatory pattern reduced for the softer Hamiltonian at $\alpha = 0.04 \text{ fm}^4$. Furthermore, for the further softened Hamiltonian at $\alpha = 0.08 \text{ fm}^4$ we find the perturbation series practically converged beyond eighth order without Padé resummation and even lower-order partial sums constitute a good approximation. Although we are using a severely truncated model-space with only $2p2h$ excitations, these results hint towards the improvement of the convergence of the perturbation series (A.3) for further SRG-transformed, i.e., softer Hamiltonians, in contrast to our findings based on the HO basis in Figure A.1. An analogous pattern has been found also in different small model spaces, and a more systematic and detailed investigation can be found in Ref. [226] and is subject to further research.

APPENDIX B

Binary-Cluster Jacobi Coordinates

We give suitable Jacobi coordinates for the description of binary-cluster scattering for the general case of an $(A - a)$ -body target and a -body projectile, where an average nucleon mass m is assumed. They can be also found in Ref. [48]. The coordinates are given in terms of the Cartesian single-particle coordinates $\{\vec{r}_i\}$.

The vector proportional to the center of mass of the A -nucleon system is given by

$$\vec{\xi}_0 = \frac{1}{\sqrt{A}} \sum_{i=1}^A \vec{r}_i. \quad (\text{B.1})$$

The Jacobi coordinates describing the $(A - a)$ target nucleons read

$$\vec{\xi}_1 = \frac{1}{\sqrt{2}} (\vec{r}_1 - \vec{r}_2) \quad (\text{B.2})$$

$$\vec{\xi}_k = \sqrt{\frac{k}{k+1}} \left(\frac{1}{k} \sum_{i=1}^k \vec{r}_i - \vec{r}_{k+1} \right) \quad \text{for } 2 \leq k \leq A - a - 1. \quad (\text{B.3})$$

The internal coordinates concerning the a -body projectile are given by

$$\vec{\vartheta}_{A-k} = \sqrt{\frac{k}{k+1}} \left(\frac{1}{k} \sum_{i=1}^k \vec{r}_{A-i+1} - \vec{r}_{A-k} \right) \quad \text{for } a - 1 \geq k \geq 2 \quad (\text{B.4})$$

$$\vec{\vartheta}_{A-1} = \frac{1}{\sqrt{2}} (\vec{r}_{A-1} - \vec{r}_A). \quad (\text{B.5})$$

Finally, the relative vector between the centers of mass of the two clusters reads

$$\vec{\eta}_{A-a,a} = \sqrt{\frac{(A-a)a}{A}} \left(\frac{1}{A-a} \sum_{i=1}^{A-a} \vec{r}_i - \frac{1}{a} \sum_{j=A-a+1}^A \vec{r}_j \right). \quad (\text{B.6})$$

For the special case of the single-nucleon projectile formalism these coordinates simplify to those depicted in Figure 11.1.

APPENDIX C

List of Publications

During this dissertation the following list of publications has been achieved:

Peer-Reviewed Journals

1. R. Roth, J. Langhammer, A. Calci, S. Binder, P. Navrátil
Similarity-Transformed Chiral NN+3N Interactions for the Ab Initio Description of ^{12}C and ^{16}O
Physical Review Letters **107**, 072501 (2011)
2. R. Roth, S. Binder, K. Vobig, A. Calci, J. Langhammer, P. Navrátil
Ab Initio Calculations of Medium-Mass Nuclei with Normal-Ordered Chiral NN+3N Interactions
Physical Review Letters **109**, 052501 (2012)
3. J. Langhammer, R. Roth, C. Stumpf
Spectra of Open-Shell Nuclei with Padé-Resummed Degenerate Perturbation Theory
Physical Review C **86**, 054315 (2012)
4. S. Binder, J. Langhammer, A. Calci, P. Navrátil, R. Roth
Ab Initio Calculations of Medium-Mass Nuclei with Explicit Chiral 3N Interactions
Physical Review C **87**, 021303(R) (2013) - Editors' Suggestion
5. G. Hupin, J. Langhammer, P. Navrátil, S. Quaglioni, A. Calci, R. Roth
Ab Initio Many-Body Calculations of Nucleon- ^4He Scattering with Three-Nucleon Forces
Physical Review C **88**, 054622 (2013)
6. H. Hergert, S. K. Bogner, S. Binder, A. Calci, J. Langhammer, R. Roth, A. Schwenk
In-Medium Similarity Renormalization Group with Chiral Two- Plus Three-Nucleon Interactions
Physical Review C **87**, 034307 (2013)

7. H. Hergert, S. Binder, A. Calci, J. Langhammer, R. Roth
Ab Initio Calculations of Even Oxygen Isotopes with Chiral Two- Plus Three- Nucleon Interactions
Physical Review Letters **110**, 242501 (2013)
8. S. Binder, P. Piecuch, A. Calci, J. Langhammer, P. Navrátil, R. Roth
Extension of coupled-cluster theory with a non-iterative treatment of connected triply excited clusters to three-body Hamiltonians
Physical Review C **88**, 054319 (2013)
9. R. Roth, A. Calci, J. Langhammer, S. Binder
Evolved Chiral NN+3N Hamiltonians for Ab Initio Nuclear Structure Calculations
submitted to Physical Review C
10. S. Binder, J. Langhammer, A. Calci, R. Roth
Ab Initio Path to Heavy Nuclei
submitted to Physical Review Letters
11. S. K. Bogner, H. Hergert, J. D. Holt, A. Schwenk, S. Binder, A. Calci, J. Langhammer, R. Roth
Nonperturbative shell-model interactions from the in-medium similarity renormalization group
submitted to Physical Review Letters

Peer-Reviewed Conference Proceedings

1. R. Roth, J. Langhammer, A. Calci, S. Binder, Petr Navrátil
Ab Initio Nuclear Structure Theory with Chiral NN+3N Interactions
Progress of Theoretical Physics Supplement **196**, 131 (2012)
2. R. Roth, J. Langhammer, S. Binder, A. Calci
New Horizons in Ab Initio Nuclear Structure Theory
Journal of Physics: Conference Series **403**, 012020 (2012)
3. R. Roth, J. Langhammer, A. Calci, S. Binder
From Chiral EFT Interactions to Ab Initio Nuclear Structure
Proceedings of Science (CD12) 015 (2013)
Proceedings of the 7th International Workshop on Chiral Dynamics, August 6 - 10, 2012, Jefferson Lab, Newport News, VA, USA
4. P. Maris, H. M. Aktulga, S. Binder, A. Calci, Ü. Catalyürek, J. Langhammer, E. Ng, E. Saule, R. Roth, J. Vary, C. Yang
No Core CI Calculations for Light Nuclei with Chiral 2- and 3-body Forces
Journal of Physics: Conference Series **454**, 012063 (2013)
Proceedings of the 24th IUPAP Conference on Computational Physics (IUPAP-CCP 2012), October 14 - 18, 2012, Kobe, Japan

-
5. R. Roth, A. Calci, J. Langhammer, S. Binder
Ab Initio Nuclear Structure Theory: From Few to Many
Proceedings of the 22nd European Conference on Few-Body Problems in Physics (EFB22), September 9-13, 2013, Krakow, Poland
 6. R. Roth, A. Calci, J. Langhammer, S. Binder
Towards New Horizons in Ab Initio Nuclear Structure Theory
Proceedings of the 25th International Nuclear Physics Conference 2013 (INPC2013), June 2 - 7, 2013, Firenze, Italy
 7. D. Oryspayev, H. Potter, P. Maris, M. Sosonkina, J. P. Vary, S. Binder, A. Calci, J. Langhammer, R. Roth
Leveraging GPUs in Ab Initio Nuclear Physics Calculations
IEEE 27th Parallel and Distributed Processing Symposium Workshops & PhD Forum (2013)
 8. G. Hupin, S. Quaglioni, J. Langhammer, P. Navrátil, A. Calci, R. Roth
Progress on Light-Ion Fusion Reactions with Three-Nucleon Forces
Proceedings of the 22nd European Conference on Few-Body Problems in Physics, Krakow, Poland, 9-13 September 2013
 9. S. Quaglioni, P. Navrátil, G. Hupin, J. Langhammer, C. Romero-Redondo, R. Roth
No-Core Shell Model Analysis of Light Nuclei
Few-Body Systems Volume 54, Issue 7-10, pp 877-884 (2013)

References

- [1] E. Rutherford; *The scattering of alpha and beta particles by matter and the structure of the atom*; Philosophical Magazine **21** (1911) 669.
- [2] *Nobel Lectures, Chemistry 1901-1921*; Elsevier Publishing Company, Amsterdam (1966).
- [3] J. Chadwick; *Possible Existence of a Neutron*; Nature **129** (1932) 312.
- [4] J. Chadwick; *The Existence of a Neutron*; Proceedings of the Royal Society of London **136** (1932) 692.
- [5] J. Chadwick; *The Neutron and Its Properties - Nobel Lectures, Physics 1922-1941*; Elsevier Publishing Company, Amsterdam (1965).
- [6] E. M. Burbidge, G. R. Burbidge, William A. Fowler, F. Hoyle; *Synthesis of the Elements in Stars*; Reviews of Modern Physics **29** (1957) 547.
- [7] H. Yukawa; *On the Interaction of Elementary Particles I*; Proceedings of the Physico-Mathematical Society of Japan. 3rd Series **17** (1935) 48.
- [8] R. B. Wiringa, V. G. J. Stoks, R. Schiavilla; *An Accurate Nucleon–Nucleon Potential with Charge–Independence Breaking*; Physical Review C **51** (1995) 38.
- [9] R. Machleidt; *High-precision, charge-dependent Bonn nucleon-nucleon potential*; Physical Review C **63** (2001) 024001.
- [10] S. Pastore, Steven C. Pieper, R. Schiavilla, R. B. Wiringa; *Quantum Monte Carlo calculations of electromagnetic moments and transitions in $A \leq 9$ nuclei with meson-exchange currents derived from chiral effective field theory*; Physical Review C **87** (2013) 035503.
- [11] D. J. Gross, F. Wilczek; *Ultraviolet Behavior of Non-Abelian Gauge Theories*; Physical Review Letters **30** (1973) 1343.
- [12] H. D. Politzer; *Reliable Perturbative Results for Strong Interactions?*; Physical Review Letters **30** (1973) 1346.
- [13] S. Weinberg; *Nuclear forces from chiral Lagrangians*; Physics Letters B **251** (1990) 288.

- [14] S. Weinberg; *Effective chiral Lagrangians for nucleon-pion interactions and nuclear forces*; Nuclear Physics B **363** (1991) 3.
- [15] S. Weinberg; *Three-body interactions among nucleons and pions*; Physics Letters B **295** (1992) 114.
- [16] U. van Kolck; *Few-nucleon forces from chiral Lagrangians*; Physical Review C **49** (1994) 2932.
- [17] R. Machleidt, D. R. Entem; *Chiral effective field theory and nuclear forces*; Physics Reports **503** (2011) 1.
- [18] E. Epelbaum, H.-W. Hammer, U.-G. Meißner; *Modern theory of nuclear forces*; Reviews of Modern Physics **81** (2009) 1773.
- [19] J. Carlson; *Alpha particle structure*; Physical Review C **38** (1988) 1879.
- [20] B. S. Pudliner, V. R. Pandharipande, J. Carlson, R. B. Wiringa; *Quantum Monte Carlo Calculations of $A \leq 6$ Nuclei*; Physical Review Letters **74** (1995) 4396.
- [21] B. S. Pudliner, V. R. Pandharipande, J. Carlson, *et al.*; *Quantum Monte Carlo calculations of nuclei with $A < 7$* ; Physical Review C **56** (1997) 1720.
- [22] B. Barrett, B. Mihaila, S. C. Pieper, R. B. Wiringa; *Ab initio calculations of light nuclei*; Nuclear Physics News **13** (2003) 17.
- [23] R. B. Wiringa, S. C. Pieper; *Evolution of Nuclear Spectra with Nuclear Forces*; Physical Review Letters **89** (2002) 182501.
- [24] S. C. Pieper, K. Varga, R. B. Wiringa; *Quantum Monte Carlo calculations of $A = 9, 10$ nuclei*; Physical Review C **66** (2002) 044310.
- [25] P. Navrátil, J. P. Vary, B. R. Barrett; *Properties of ^{12}C in the Ab Initio Nuclear Shell Model*; Physical Review Letters **84** (2000) 5728.
- [26] P. Navrátil, J. P. Vary, B. R. Barrett; *Large-basis ab initio no-core shell model and its application to ^{12}C* ; Physical Review C **62** (2000) 054311.
- [27] R. Roth, P. Navrátil; *Ab Initio Study of ^{40}Ca with an Importance-Truncated No-Core Shell Model*; Physical Review Letters **99** (2007) 092501.
- [28] R. Roth; *Importance Truncation for Large-Scale Configuration Interaction Approaches*; Physical Review C **79** (2009) 064324.
- [29] G. Hagen, T. Papenbrock, A. Ekström, *et al.*; *Coupled-cluster calculations of nucleonic matter*; Physical Review C **89** (2014) 014319.
- [30] A. Cipollone, C. Barbieri, P. Navrátil; *Isotopic Chains Around Oxygen from Evolved Chiral Two- and Three-Nucleon Interactions*; Physical Review Letters **111** (2013) 062501.

-
- [31] V. Soma, A. Cipollone, C. Barbieri, *et al.*; *Leading chiral three-nucleon forces along isotope chains in the calcium region*; arXiv: 1312.2068 (2013).
- [32] K. Tsukiyama, S. K. Bogner, A. Schwenk; *In-Medium Similarity Renormalization Group For Nuclei*; Physical Review Letters **106** (2011) 222502.
- [33] H. Hergert, S. K. Bogner, S. Binder, *et al.*; *In-medium similarity renormalization group with chiral two- plus three-nucleon interactions*; Physical Review C **87** (2013) 034307.
- [34] H. Hergert, S. Binder, A. Calci, *et al.*; *Ab Initio Calculations of Even Oxygen Isotopes with Chiral Two-Plus-Three-Nucleon Interactions*; Physical Review Letters **110** (2013) 242501.
- [35] D. Lee; *Lattice simulations for few- and many-body systems*; Progress in Particle and Nuclear Physics **63** (2009) 117.
- [36] E. Epelbaum, H. Krebs, D. Lee, U.-G. Meißner; *Ab Initio Calculation of the Hoyle State*; Physical Review Letters **106** (2011) 192501.
- [37] E. Caurier, P. Navrátil, W. E. Ormand, J. P. Vary; *Ab initio shell model for $A = 10$ nuclei*; Physical Review C **66** (2002) 024314.
- [38] D. R. Entem, R. Machleidt, H. Witala; *Chiral NN model an A_y puzzle*; Physical Review C **65** (2002) 064005.
- [39] S. C. Pieper, V. R. Pandharipande, R. B. Wiringa; *Realistic models of pion-exchange three-nucleon interactions*; Physical Review C **64** (2001) 014001.
- [40] E. D. Jurgenson, P. Navrátil, R. J. Furnstahl; *Evolving Nuclear Many-Body Forces with the Similarity Renormalization Group*; Physical Review C **83** (2011) 034301.
- [41] B. R. Barrett, P. Navrátil, J. P. Vary; *Ab initio no core shell model*; Progress in Particle and Nuclear Physics **69** (2013) 131.
- [42] R. Roth, J. Langhammer, A. Calci, *et al.*; *Similarity-Transformed Chiral NN+3N Interactions for the Ab Initio Description of ^{12}C and ^{16}O* ; Physical Review Letters **107** (2011) 072501.
- [43] R. Roth, S. Binder, K. Vobig, *et al.*; *Ab Initio Calculations of Medium-Mass Nuclei with Normal-Ordered Chiral NN+3N Interactions*; Physical Review Letters **109** (2012) 052501.
- [44] R. Roth, A. Calci, J. Langhammer, S. Binder; *Evolved Chiral NN+3N Hamiltonians for Ab Initio Nuclear Structure Calculations*; arXiv:1311.3563 (2013).
- [45] G. Hagen, T. Papenbrock, D. J. Dean, *et al.*; *Coupled-cluster theory for three-body Hamiltonians*; Physical Review C **76** (2007) 034302.
-

- [46] S. Binder, J. Langhammer, A. Calci, *et al.*; *Ab initio calculations of medium-mass nuclei with explicit chiral 3N interactions*; Physical Review C **87** (2013) 021303.
- [47] S. Quaglioni, P. Navrátil; *Ab Initio Many-Body Calculations of n - ^3H , n - ^4He , p - $^{3,4}\text{He}$, and n - ^{10}Be Scattering*; Physical Review Letters **101** (2008) 092501.
- [48] S. Quaglioni, P. Navrátil; *Ab initio many-body calculations of nucleon-nucleus scattering*; Physical Review C **79** (2009) 044606.
- [49] S. Baroni, P. Navrátil, S. Quaglioni; *Ab Initio Description of the Exotic Unbound ^7He Nucleus*; Physical Review Letters **110** (2013) 022505.
- [50] S. Baroni, P. Navrátil, S. Quaglioni; *Unified ab initio approach to bound and unbound states: No-core shell model with continuum and its application to ^7He* ; Physical Review C **87** (2013) 034326.
- [51] G. Hupin, J. Langhammer, P. Navrátil, *et al.*; *Ab initio many-body calculations of nucleon- ^4He scattering with three-nucleon forces*; Physical Review C **88** (2013) 054622.
- [52] S. K. Bogner, R. J. Furnstahl, R. J. Perry; *Similarity renormalization group for nucleon-nucleon interactions*; Physical Review C **75** (2007) 061001(R).
- [53] D. H. Politzer; *Asymptotic freedom: An approach to strong interactions*; Physics Reports **14** (1974) 129.
- [54] M. J. Savage; *Nuclear Forces from Lattice Quantum Chromodynamics*; arXiv:1309.4752 (2013).
- [55] S. Aoki, N. Ishii, K. Ishikawa, PACS-CS Collaboration; *Lattice quantum chromodynamics at the physical point and beyond*; Progress of Theoretical and Experimental Physics **01A102** (2012) 31.
- [56] S. R. Beane, P. F. Bedaque, K. Orginos, M. J. Savage; *Nucleon-Nucleon Scattering from Fully Dynamical Lattice QCD*; Physical Review Letters **97** (2006) 012001.
- [57] NPLQCD Collaboration, S. R. Beane, E. Chang, *et al.*; *Light nuclei and hypernuclei from quantum chromodynamics in the limit of $SU(3)$ flavor symmetry*; Physical Review D **87** (2013) 034506.
- [58] N. Ishii, S. Aoki, T. Hatsuda; *Nuclear Force from Lattice QCD*; Physical Review Letters **99** (2007) 022001.
- [59] K. Murano; *Nuclear Forces in the Odd Parity Sector and the LS Forces from Lattice QCD*; in *Few-Body Systems*; vol. 54; 1105–1108; Springer Vienna (2013).
- [60] Z. Fodor, C. Hoelbling; *Light hadron masses from lattice QCD*; Reviews of Modern Physics **84** (2012) 449.

-
- [61] L. Platter; *Few-Body Systems and the Pionless Effective Field Theory*; arXiv:0910.0031 (2009).
- [62] S. Weinberg; *Phenomenological Lagrangians*; *Physica A: Statistical Mechanics and its Applications* **96** (1979) 327.
- [63] E. Noether; *Invariante Variationsprobleme*; *Nachrichten von der Gesellschaft der Wissenschaften zu Göttingen, Mathematisch-Physikalische Klasse* (1918).
- [64] J. Goldstone; *Field theories with Superconductor solutions*; *Il Nuovo Cimento* **19** (1961) 154.
- [65] J. Goldstone, A. Salam, S. Weinberg; *Broken Symmetries*; *Physical Review* **127** (1962) 965.
- [66] E. Epelbaum; *Nuclear forces from chiral effective field theory: a primer*; Lectures given at the 2009 Joliot-Curie School, Lacanau, France, 27 September - 3 October (2009).
- [67] Tae-Sun Park, Dong-Pil Min, Mannque Rho; *Chiral Lagrangian approach to exchange vector currents in nuclei*; *Nuclear Physics A* **596** (1996) 515.
- [68] S. Pastore, R. Schiavilla, J. L. Goity; *Electromagnetic two-body currents of one- and two-pion range*; *Physical Review C* **78** (2008) 064002.
- [69] D. R. Entem, R. Machleidt; *Accurate nucleon–nucleon potential based upon chiral perturbation theory*; *Physics Letters B* **524** (2002) 93.
- [70] D. R. Entem, R. Machleidt; *Chiral two-pion exchange at fourth order and peripheral NN scattering*; *Physical Review C* **66** (2002) 014002.
- [71] D. R. Entem, R. Machleidt; *Accurate charge-dependent nucleon-nucleon potential at fourth order of chiral perturbation theory*; *Physical Review C* **68** (2003) 041001(R).
- [72] Jun-ichi Fujita, Hironari Miyazawa; *Pion Theory of Three-Body Forces*; *Progress of Theoretical Physics* **17** (1957) 360.
- [73] E. Epelbaum, A. Nogga, W. Glöckle, *et al.*; *Three-nucleon forces from chiral effective field theory*; *Physical Review C* **66** (2002) 064001.
- [74] Petr Navrátil; *Local three-nucleon interaction from chiral effective field theory*; *Few Body Systems* **41** (2007) 117.
- [75] E. Epelbaum, U.-G. Meißner, J. E. Palomar; *Isospin dependence of the three-nucleon force*; *Physical Review C* **71** (2005) 024001.
- [76] Doron Gazit, Sofia Quaglioni, Petr Navrátil; *Three-Nucleon Low-Energy Constants from the Consistency of Interactions and Currents in Chiral Effective Field Theory*; *Physical Review Letters* **103** (2009) 102502.
-

- [77] A. Nogga, P. Navrátil, B. R. Barrett, J. P. Vary; *Spectra and binding energy predictions of chiral interactions for 7 Li*; Physical Review C **73** (2006) 064002.
- [78] P. Navrátil, V. G. Gueorguiev, J. P. Vary, *et al.*; *Structure of $A = 10 - 13$ nuclei with two-plus three-nucleon interactions from chiral field theory*; Physical Review Letters **99** (2007) 042501.
- [79] P. Navrátil, G. P. Kamuntavicius, B. R. Barrett; *Few-nucleon systems in a translationally invariant harmonic oscillator basis*; Physical Review C **61** (2000) 044001.
- [80] J. E. Purcell, J. H. Kelley, E. Kwan, *et al.*; *Energy levels of light nuclei $A = 3$* ; Nuclear Physics A **848** (2010) 1.
- [81] D. R. Tilley, H. R. Weller, G. M. Hale; *Energy levels of light nuclei $A = 4$* ; Nuclear Physics A **541** (1992) 1.
- [82] V. Bernard, E. Epelbaum, H. Krebs, U.-G. Meißner; *Subleading contributions to the chiral three-nucleon force: Long-range terms*; Physical Review C **77** (2008) 064004.
- [83] V. Bernard, E. Epelbaum, H. Krebs, U.-G. Meißner; *Subleading contributions to the chiral three-nucleon force II: Short-range terms and relativistic corrections*; Physical Review C **84** (2011) 054001.
- [84] I. Tews, T. Krüger, K. Hebeler, A. Schwenk; *Neutron Matter at Next-to-Next-to-Next-to-Leading Order in Chiral Effective Field Theory*; Physical Review Letters **110** (2013) 032504.
- [85] J. Golak, D. Rozpedzik, R. Skibinski, *et al.*; *A new way to perform partial-wave decompositions of few-nucleon forces*; The European Physical Journal A - Hadrons and Nuclei **43** (2010) 241.
- [86] <http://www.lenpic.org>; *Low-Energy Nuclear Physics International Collaboration*.
- [87] R. Roth, P. Papakonstantinou, N. Paar, *et al.*; *Hartree-Fock and Many-Body Perturbation Theory with Correlated Realistic NN-Interactions*; Physical Review C **73** (2006) 044312.
- [88] D. Oryspayev, H. Potter, P. Maris, *et al.*; *Leveraging GPUs in Ab Initio Nuclear Physics Calculations*; in *Proceedings of the 2013 IEEE 27th International Symposium on Parallel and Distributed Processing Workshops and PhD Forum*; IPDPSW'13; 1365–1372; IEEE Computer Society, Washington, DC, USA (2013).
- [89] P. Navrátil, W. E. Ormand; *Ab initio shell model with a genuine three-nucleon force for the p-shell nuclei*; Physical Review C **68** (2003) 034305.
- [90] E. D. Jurgenson, P. Maris, R. J. Furnstahl, *et al.*; *Structure of p-shell nuclei using three-nucleon interactions evolved with the similarity renormalization group*; Physical Review C **87** (2013) 054312.

-
- [91] P. Maris, J. P. Vary, P. Navrátil, *et al.*; *Origin of the anomalous long lifetime of ^{14}C* ; Physical Review Letters **106** (2011) 202502.
- [92] J. Langhammer; *Consistent chiral three-nucleon interactions in nuclear structure*; Master's thesis; TU Darmstadt (2011).
- [93] A. Calci; *Ab Initio Nuclear Structure with SRG-Transformed Chiral NN plus NNN Interactions*; Master's thesis; TU Darmstadt (2011).
- [94] G. P. Kamuntavicius, R. K. Kalinauskas, B. R. Barrett, *et al.*; *The general harmonic-oscillator brackets: compact expression, symmetries, sums and Fortran code*; Nuclear Physics A **695** (2001) 191.
- [95] P. Maris, H.M. Aktulga, S. Binder, *et al.*; *No Core CI calculations for light nuclei with chiral 2- and 3-body forces*; Journal of Physics: Conference Series **454** (2013) 012063.
- [96] S. Binder; *Coupled-Cluster Theory for Nuclear Structure*; Ph.D. thesis; TU Darmstadt (2014).
- [97] G. Hagen, T. Papenbrock, M. Hjorth-Jensen, D. J. Dean; *Coupled-cluster computations of atomic nuclei*; arXiv:1312.7872 (2013).
- [98] S. Binder, P. Piecuch, A. Calci, *et al.*; *Extension of coupled-cluster theory with a non-iterative treatment of connected triply excited clusters to three-body Hamiltonians*; Physical Review C **88** (2013) 054319.
- [99] J. P. Vary; *The many-fermion dynamics shell-model code* (1992); unpublished.
- [100] P. Sternberg, E.G. Ng, C. Yang, *et al.*; *Accelerating configuration interaction calculations for nuclear structure*; in *Supercomputing Conference*; vol. 0; IEEE Computer Society (2008).
- [101] P. Maris, M. Sosonkina, J.P. Vary, *et al.*; *Scaling of ab-initio nuclear physics calculations on multicore computer architectures*; Procedia Computer Science **1** (2010) 97.
- [102] I. Shavitt, R. J. Bartlett; *Many-body methods in chemistry and physics*; Cambridge University Press (2009).
- [103] R. Roth, T. Neff, H. Feldmeier; *Nuclear Structure in the Framework of the Unitary Correlation Operator Method*; Progress in Particle and Nuclear Physics **65** (2010) 50.
- [104] S. Szpigel, R. J. Perry; *The Similarity Renormalization Group*; in A. N. Mitra (editor), *Quantum Field Theory. A 20th Century Profile*; Hindustan Publishing Co., New Delhi (2000).
- [105] F. J. Wegner; *Flow Equations for Hamiltonians*; Nuclear Physics B Proceedings Supplements **90** (2000) 141.
- [106] Franz J. Wegner; *Flow equations for Hamiltonians*; Physics Reports **348** (2001) 77.
-

- [107] F. Wegner; *Flow Equations for Hamiltonians*; Annalen der Physik (Leipzig) **3** (1994) 77.
- [108] E. R. Anderson, S. K. Bogner, R. J. Furnstahl, R. J. Perry; *Operator evolution via the similarity renormalization group: The deuteron*; Physical Review C **82** (2010) 054001.
- [109] S. Reinhardt; *Unitary Transformations for Nuclear Structure Calculations*; Ph.D. thesis; TU Darmstadt (2013).
- [110] W. Li, E. R. Anderson, R. J. Furnstahl; *Similarity renormalization group with novel generators*; Physical Review C **84** (2011) 054002.
- [111] S. K. Bogner, R. J. Furnstahl, A. Schwenk; *From low-momentum interactions to nuclear structure*; Progress in Particle and Nuclear Physics **65** (2010) 94.
- [112] S. Kehrein; *The Flow Equation Approach to Many-Particle Systems*; vol. 217 of *Springer Tracts in Modern Physics*; Springer, Berlin (2006).
- [113] K. Suzuki, S. Y. Lee; *Convergent Theory for Effective Interaction in Nuclei*; Progress of Theoretical Physics **64** (1980) 2091.
- [114] S. Ôkubo; *Diagonalization of Hamiltonian and Tamm-Dancoff Equation*; Progress of Theoretical Physics **12** (1954) 603.
- [115] H. Feldmeier, T. Neff, R. Roth, J. Schnack; *A Unitary Correlation Operator Method*; Nuclear Physics A **632** (1998) 61.
- [116] R. J. Furnstahl, K. Hebeler; *New applications of renormalization group methods in nuclear physics*; Reports on Progress in Physics **76** (2013) 126301.
- [117] S. Schulz; *SRG-Induced Four-Body Forces in Ab Initio Nuclear Structure*; Master's thesis; Technische Universität Darmstadt (2013).
- [118] A. Calci; *Evolved Chiral Hamiltonians at the Three-Body Level and Beyond*; Ph.D. thesis; Technische Universität Darmstadt (2014).
- [119] Intel® MKL 10.3; *Intel® Math Kernel Library Reference Manual*.
- [120] K. Hebeler; *Momentum-space evolution of chiral three-nucleon forces*; Physical Review C **85** (2012) 021002.
- [121] P. Navrátil, S. Quaglioni, I. Stetcu, B. Barrett; *Recent developments in no-core shell-model calculations*; Journal of Physics G: Nuclear and Particle Physics **36** (2009) 083101.
- [122] S. A. Coon, M. I. Avetian, M. K. G. Kruse, *et al.*; *Convergence properties of ab initio calculations of light nuclei in a harmonic oscillator basis*; Physical Review C **86** (2012) 054002.

-
- [123] R. J. Furnstahl, G. Hagen, T. Papenbrock; *Corrections to nuclear energies and radii in finite oscillator spaces*; Physical Review C **86** (2012) 031301.
- [124] S. N. More, A. Ekström, R. J. Furnstahl, *et al.*; *Universal properties of infrared oscillator basis extrapolations*; Physical Review C **87** (2013) 044326.
- [125] D. H. Glöckner, R. D. Lawson; *Spurious center-of-mass motion*; Physics Letters B **53** (1974) 313.
- [126] S. Binder; *Angular Momentum Projection and Three-Body Forces in the No-Core Shell Model*; Master's thesis; TU Darmstadt (2010).
- [127] I. Mayer; *Simple Theorems, Proofs, and Derivations in Quantum Chemistry*; Kluwer Academic (2003).
- [128] P. Navrátil, W. E. Ormand; *Ab Initio Shell Model Calculations with Three-Body Effective Interactions for p -Shell Nuclei*; Physical Review Letters **88** (2002) 152502.
- [129] Y. Saad; *Numerical Methods for Large Eigenvalue Problems*; Manchester University Press (1992).
- [130] B. N. Partlett; *The Symmetric Eigenvalue Problem*; Prentice-Hall Series in Computational Mathematics (1980).
- [131] Z. Rolik, A. Szabados, P. R. Surján; *On the perturbation of multi-configuration wave functions*; Journal of Chemical Physics **119** (2003).
- [132] P. R. Surján, A. Szabados, D. Köhalmi; *Partitioning in multiconfigurational perturbation theory*; Annalen der Physik **13** (2004).
- [133] E. Caurier, F. Nowacki; *Present Status of Shell Model Techniques*; Acta Physica Polonica B **30** (1999) 705.
- [134] R. J. Bartlett, M. Musial; *Coupled-cluster theory in quantum chemistry*; Reviews of Modern Physics **79** (2007) 291.
- [135] G. Hagen, T. Papenbrock, D. J. Dean, M. Hjorth-Jensen; *Ab initio coupled-cluster approach to nuclear structure with modern nucleon-nucleon interactions*; Physical Review C **82** (2010) 034330.
- [136] S. Binder, J. Langhammer, A. Calci, R. Roth; *Ab initio Path to Heavy Nuclei*; submitted to Physical Review Letters (2014).
- [137] R. Roth, J. R. Gour, P. Piecuch; *Ab initio coupled-cluster and configuration interaction calculations for ^{16}O using the V_{UCOM} interaction*; Physical Review C **79** (2009) 054325.
- [138] K. Kowalski, D. J. Dean, M. Hjorth-Jensen, *et al.*; *Coupled Cluster Calculations of Ground and Excited States of Nuclei*; Physical Review Letters **92** (2004) 132501.
-

- [139] P. Piecuch, M. Wloch; *Renormalized coupled-cluster methods exploiting left eigenstates of the similarity-transformed Hamiltonian*; The Journal of Chemical Physics **123** (2005).
- [140] P. Piecuch, M. Wloch, J. R. Gour, A. Kinal; *Single-reference, size-extensive, non-iterative coupled-cluster approaches to bond breaking and biradicals*; Chemical Physics Letters **418** (2006) 467.
- [141] P. Piecuch, J. R. Gour, M. Wloch; *Left-eigenstate completely renormalized equation-of-motion coupled-cluster methods: Review of key concepts, extension to excited states of open-shell systems, and comparison with electron-attached and ionized approaches*; International Journal of Quantum Chemistry **109** (2009) 3268.
- [142] A. G. Taube, R. J. Bartlett; *Improving upon CCSD(T): Lambda-CCSD(T). I. Potential energy surfaces*; The Journal of Chemical Physics **128** (2008) .
- [143] A. G. Taube; *Alternative perturbation theories for triple excitations in coupled-cluster theory*; Molecular Physics **108** (2010) 2951.
- [144] M. Wang, G. Audi, A. H. Wapstra, *et al.*; *The AME 2012 atomic mass evaluation*; Chinese Physics C **36** (2012) 1603.
- [145] E. D. Jurgenson, P. Navrátil, R. J. Furnstahl; *Evolution of Nuclear Many-Body Forces with the Similarity Renormalization Group*; Physical Review Letters **103** (2009) 082501.
- [146] A. Ekström, G. Baardsen, C. Forssén, *et al.*; *Optimized Chiral Nucleon-Nucleon Interaction at Next-to-Next-to-Leading Order*; Physical Review Letters **110** (2013) 192502.
- [147] D.R. Tilley, C.M. Cheves, J.L. Godwina, *et al.*; *Energy levels of light nuclei $A = 5, 6, 7$* ; Nuclear Physics A **708** (2002) 3.
- [148] D. R. Tilley, J. H. Kelley, J. L. Godwin, *et al.*; *Energy levels of light nuclei $A = 8, 9, 10$* ; Nuclear Physics A **745** (2004) 155.
- [149] F. Ajzenberg-Selove; *Energy levels of light nuclei $A = 11-12$* ; Nuclear Physics A **506** (1990) 1.
- [150] F. Hoyle; *On Nuclear Reactions Occuring in Very Hot STARS.I. the Synthesis of Elements from Carbon to Nickel.*; Astrophysical Journal Supplement **1** (1954).
- [151] C. W. Cook, W. A. Fowler, C. C. Lauritsen, T. Lauritsen; *^{12}B , ^{12}C and the Red Giants*; Physical Review **107** (1957) 508.
- [152] M. Chernykh, H. Feldmeier, T. Neff, *et al.*; *Structure of the Hoyle State in ^{12}C* ; Physical Review Letters **98** (2007) 032501.
- [153] E. Epelbaum, H. Krebs, D. Lee, U.-G. Meißner; *Ab initio calculation of the Hoyle state*; Physical Review Letters **106** (2011) 192501.

-
- [154] T. Neff; *Clusters and halos in light nuclei*; Journal of Physics: Conference Series **403** (2012) 012028.
- [155] E. C. Simpson, P. Navrátil, R. Roth, J. A. Tostevin; *Microscopic two-nucleon overlaps and knockout reactions from ^{12}C* ; Physical Review C **86** (2012) 054609.
- [156] M. C. M. Rentmeester, R. G. E. Timmermans, J. J. de Swart; *Determination of the chiral coupling constants c_3 and c_4 in new pp and np partial-wave analyses*; Physical Review C **67** (2003) 044001.
- [157] P. Büttiker, U.-G. Meißner; *Pion–nucleon scattering inside the Mandelstam triangle*; Nuclear Physics A **668** (2000) 97.
- [158] N. Fettes, U.-G. Meißner, S. Steininger; *Pion-nucleon scattering in chiral perturbation theory (I): Isospin-symmetric case*; Nuclear Physics A **640** (1998) 199.
- [159] V. Bernard, N. Kaiser, U.-G. Meißner; *Aspects of chiral pion-nucleon physics*; Nuclear Physics A **615** (1997) 483.
- [160] R. Skibiński, J. Golak, K. Topolnicki, *et al.*; *Triton with long-range chiral N^3LO three-nucleon forces*; Physical Review C **84** (2011) 054005.
- [161] R. Roth, J. Langhammer, A. Calci, S. Binder; *From Chiral EFT Interactions to Ab Initio Nuclear Structure*; in *Proceedings of the 7th International Workshop on Chiral Dynamics, August 6 - 10, 2012*; vol. PoS(CD12) 015; Jefferson Lab, Newport News, VA, USA (2013).
- [162] H. Krebs, E. Epelbaum, U. G. Meißner; *Nuclear forces with Delta excitations up to next-to-next-to-leading order, part I: Peripheral nucleon-nucleon waves*; The European Physical Journal A **32** (2007) 127.
- [163] E. Gebrerufael; *Multi-Reference Normal Ordering for 3N Interactions*; Master's thesis; TU Darmstadt (2013).
- [164] W. Kutzelnigg, D. Mukherjee; *Normal order and extended Wick theorem for a multi-configuration reference wave function*; Journal of Chemical Physics **107** (1997) 432.
- [165] T. Otsuka, T. Suzuki, J. D. Holt, *et al.*; *Three-Body Forces and the Limit of Oxygen Isotopes*; Physical Review Letters **105** (2010) 032501.
- [166] G. Hagen, M. Hjorth-Jensen, G. R. Jansen, *et al.*; *Continuum Effects and Three-Nucleon Forces in Neutron-Rich Oxygen Isotopes*; Physical Review Letters **108** (2012) 242501.
- [167] C. R. Hoffman, T. Baumann, D. Bazin, *et al.*; *Determination of the $N = 16$ Shell Closure at the Oxygen Drip Line*; Physical Review Letters **100** (2008) 152502.
- [168] G. Audi, A. H. Wapstra, C. Thibault; *The Ame2003 atomic mass evaluation: (II). Tables, graphs and references*; Nuclear Physics A **729** (2003) 337.
-

- [169] G. Hagen, T. Papenbrock, D. J. Dean, M. Hjorth-Jensen; *Medium-Mass Nuclei from Chiral Nucleon-Nucleon Interactions*; Physical Review Letters **101** (2008) 092502.
- [170] D. Rozpedzik, J. Golak, R. Skibinski, *et al.*; *A First Estimation of Chiral Four-Nucleon Force Effects in ^4He* ; Acta Physica Polonica B **B** (2006) 2889.
- [171] H. de Vries, C. W. de Jager, C. de Vries; *Nuclear charge-density-distribution parameters from elastic electron scattering*; Atomic Data and Nuclear Data Tables **36** (1987) 495.
- [172] K. Wildermuth, Y.C. Tang; *A unified theory of the nucleus*; Vieweg & Sohn Verlagsgesellschaft mbH (1977).
- [173] P. Descouvemont, D. Baye; *The R -matrix theory*; Reports on Progress in Physics **73** (2010) 036301, and refernces therein.
- [174] P. G. Burke; *R-Matrix Theory of Atomic Collisions*; Springer Verlag (2011).
- [175] J. M. Blatt, L. C. Biedenharn; *The Angular Distribution of Scattering and Reaction Cross Sections*; Reviews of Modern Physics **24** (1952) 258.
- [176] K. Ulbrich; *Analysierstärke und Spinkorrelationsparameter der elastischen Proton-Proton-Streuung im Energiebereich von 0.5 bis 2.5 GeV*; Ph.D. thesis; Rheinische Friedrich-Wilhelms-Universität Bonn (2005).
- [177] J. R. Taylor; *Scattering Theory - The Quantum Theory of nonreletivistic Collisions*; Dover Publications Inc.' (1972).
- [178] H. Paetz gen. Schieck; *Skriptum Kernphysik mit polarisierten Teilchen*; Institut für Kernphysik, Universität Köln.
- [179] P. Navrátil, R. Roth, S. Quaglioni; *Ab initio many-body calculations of nucleon scattering on ^4He , ^7Li , ^7Be , ^{12}C , and ^{16}O* ; Physical Review C **82** (2010) 034609.
- [180] P. Navrátil, S. Quaglioni; *Ab initio many-body calculations of deuteron- ^4He scattering and ^6Li states*; Physical Review C **83** (2011) 044609.
- [181] P. Navrátil, R. Roth, S. Quaglioni; *Ab initio many-body calculation of the $^7\text{Be}(p,\gamma)^8\text{B}$ radiative capture*; Physics Letters B **704** (2011) 379.
- [182] P. Navrátil, S. Quaglioni; *Ab Initio Many-Body Calculations of the $^3\text{H}(d,n)^4\text{He}$ and $^3\text{He}(d,p)^4\text{He}$ Fusion Reactions*; Physical Review Letters **108** (2012) 042503.
- [183] S. Quaglioni, C. Romero-Redondo, P. Navrátil; *Three-cluster dynamics within an ab initio framework*; Physical Review C **88** (2013) 034320.
- [184] Y. C. Tang, M. LeMere, D. R. Thompsom; *Resonating-group method for nuclear many-body problems*; Physics Reports **47** (1978) 167.

-
- [185] T. Fließbach, H. Walliser; *The structure of the resonating group equation*; Nuclear Physics A **377** (1982) 84.
- [186] K. Langanke, H. Friedrich; *Microscopic Description of Nucleus-Nucleus Collisions*; in John W. Negele, Erich Vogt (editors), *Advances in Nuclear Physics*; chap. 17, 223–363; Springer, New York (1986).
- [187] J. Langhammer; *Consistent chiral three-nucleon interactions in nuclear structure*; Master's thesis; TU Darmstadt (2011).
- [188] D. A. Varshalovich, A. N. Moskalev, V. K. Khersonskii; *Quantum Theory of Angular Momentum*; World Scientific Publishing Company (1988).
- [189] J. Langhammer; *Padé-Resummierte Vielteilchen-Störungstheorie hoher Ordnung für doppeltmagische Kerne mit realistischen Potentialen*; bachelor thesis, TU Darmstadt (2008).
- [190] E. P. Wigner; *Resonance Reactions and Anomalous Scattering*; Physical Review **70** (1946) 15.
- [191] E. P. Wigner; *Resonance Reactions*; Physical Review **70** (1946) 606.
- [192] E. P. Wigner, L. Eisenbud; *Higher Angular Momenta and Long Range Interaction in Resonance Reactions*; Physical Review **72** (1947) 29.
- [193] A. M. Lane, R. G. Thomas; *R-Matrix Theory of Nuclear Reactions*; Reviews of Modern Physics **30** (1958) 257.
- [194] G. Breit; *Encyclopedia of Physics / Handbuch der Physik*; vol. 8 / 41 / 1; 1–407; Springer Berlin Heidelberg (1959).
- [195] D. Baye, P.-H. Heenen; *Generalised mesehs for quantum mechanical problems*; Journal of Physics A: Mathematical and General **19** (1986) 2041.
- [196] *Proceedings of the International Symposium on Nuclear Collisions and their Microscopic Description : Bled, September 26-Oct. 1, 1977.*; Commission for Physics of the Yugoslav Union of Mathematical and Physical Societies and the National Committee of IUPAP, Zagreb (1977).
- [197] C. Bloch; *Une formulation unifiée de la théorie des réactions nucléaires*; Nuclear Physics **4** (1957) 503.
- [198] D. Baye, P. Descouvemont; *Electromagnetic transitions and radiative capture in the generator-coordinate method*; Nuclear Physics A **407** (3) 77.
- [199] D. Baye, M. Hesse, J.M. Sparenberg, M. Vincke; *Analysis of the R -matrix method on Lagrange meshes*; Journal of Physics B: Atomic, Molecular and Optical Physics **31** (1998) 3439.

- [200] L. Malegat; *Lagrange-mesh R-matrix calculations*; Journal of Physics B **27** (1994).
- [201] M. Hesse, J. M. Sparenberg, F. Van Raemdonck, D. Baye; *Coupled-channel R-matrix method on a Lagrange mesh*; Nuclear Physics A **640** (1998) 37.
- [202] M. Hesse, J. Roland, D. Baye; *Solving the resonating-group equation on a Lagrange mesh*; Nuclear Physics A **709** (2002) 184.
- [203] D. Baye; *Lagrange-mesh method for quantum-mechanical problems*; physica status solidi (b) **243** (2006) 1095.
- [204] D. Baye, J. Goldbeter, J. M. Sparenberg; *Equivalence of the Siegert-pseudostate and Lagrange-mesh R-matrix methods*; Physical Review A **65** (2002) 052710.
- [205] Y.C. Tang; *Topics in Nuclear Physics II A Comprehensive Review of Recent Developments*; vol. 145; 572; Springer Verlag (1981).
- [206] K.M. Nollett, S.C. Pieper, R. B. Wiringa, *et al.*; *Quantum Monte Carlo Calculations of Neutron-Alpha Scattering*; Physical Review Letters **99** (2007) 022502.
- [207] G. P. Kamuntavičius, P. Navrátil, B. R. Barrett, *et al.*; *Isoscalar Hamiltonians for light atomic nuclei*; Physical Review C **60** (1999) 044304.
- [208] G.M. Hale; *private communication*.
- [209] P. Navratil; *private communication*.
- [210] M. Drosig; *Interaction of fast neutrons with ^4He , ^3He , and ^1H : additional and improved data. [20 MeV, differential cross sections, angular distributions]*; Tech. Rep. LA-7269-MS W-7405-ENG-36; Los Alamos Scientific Lab., N.Mex. (USA) (1978).
- [211] P. Schwandt, T. B. Clegg, W. Haeberli; *Polarization measurements and phase shifts for p - ^4He scattering between 3 and 18 MeV*; Nuclear Physics A **163** (1971) 432.
- [212] W. B. Broste, G. S. Mutchler, J. E. Simmons, *et al.*; *Polarization Measurements and Analysis in n - ^4He Scattering from 11.0 to 30.3 MeV*; Physical Review C **5** (1972) 761.
- [213] H. Krupp, J. C. Hiebert, H. O. Klages, *et al.*; *$^4\text{He}(\bar{n}, n)^4\text{He}$ analyzing power in the energy range from 15 to 50 MeV*; Physical Review C **30** (1984) 1810.
- [214] A. Kievsky; *Phenomenological spin-orbit three-body force*; Physical Review C **60** (1999) 034001.
- [215] V. D. Efros, P. von Neumann-Cosel, A. Richter; *Properties of the first excited state of ^9Be derived from (γ, n) and (e, e') reactions*; Physical Review C **89** (2014) 027301.
- [216] T. Sasaqui, T. Kajino, G. J. Mathews, *et al.*; *Sensitivity of r -Process Nucleosynthesis to Light-Element Nuclear Reactions*; The Astrophysical Journal **643** (2005) 1173.

-
- [217] I.J. Thompson, F. Nunes; *Nuclear Reactions for Astrophysics*; Cambridge University Press (2009).
- [218] E. Schrödinger; *Quantisierung als Eigenwertproblem*; Annalen der Physik **385** (1926) 437.
- [219] J. Langhammer, R. Roth, C. Stumpf; *Spectra of open-shell nuclei with Padé-resummed degenerate perturbation theory*; Physical Review C **86** (2012) 054315.
- [220] A. Günther, R. Roth, H. Hergert, S. Reinhardt; *Systematics of binding energies and radii based on realistic two-nucleon plus phenomenological three-nucleon interactions*; Physical Review C **82** (2010) 024319.
- [221] K. Hebeler, S. K. Bogner, R. J. Furnstahl, *et al.*; *Improved nuclear matter calculations from chiral low-momentum interactions*; Physical Review C **83** (2011) 031301.
- [222] G. A. Baker; *The Theory and Application of the Padé Approximant Method*; Advances in Theoretical Physics **1** (1965) 1.
- [223] R. Roth, J. Langhammer; *Padé-resummed high-order perturbation theory for nuclear structure calculations*; Phys. Lett. B **683** (2010).
- [224] S.K. Bogner, A. Schwenk, R.J. Furnstahl, A. Nogga; *Is nuclear matter perturbative with low-momentum interactions?*; Nucl. Phys. A **763** (2005) 59.
- [225] G. A Baker, P. Graves-Morris; *Padé Approximants*; vol. 59 of *Encyclopedia of Mathematics and Its Applications*; Cambridge University Press; second edition edn. (1996).
- [226] A. Tichai; *Convergence Behavior of Many-Body Perturbation Series*; Master's thesis; TU Darmstadt (2014).

Danksagung

An erster Stelle danke ich meinem Doktorvater *Prof. Robert Roth* für die Möglichkeit diese Dissertation zu verfassen. Seine Bereitschaft zu ausführlichen Diskussionen und sein beständiges Interesse an den bearbeiteten Themen haben zum Gelingen dieser Arbeit maßgeblich beigetragen. Besonders möchte ich auch für die Möglichkeit der Teilnahme an verschiedenen Workshops in Vancouver, Seattle und Trento danken.

Prof. Jochen Wambach danke ich für die Übernahme des Zweitgutachtens dieser Arbeit.

Desweiteren danke ich *Petr Navrátíl* für die gute Zusammenarbeit, für das Bereitstellen seines Manyeff-Codes und für sein stets offenes Ohr bei diversen Fragen. Außerdem danke ich ihm für die Einladungen zu den Workshops am TRIUMF, Canada in den letzten drei Jahren.

Außerdem danke ich meinen Kollaboratoren *Heiko Hergert, Sofia Quaglioni, Guillaume Hupin*, sowie *James Vary*, der meine Arbeit durch die zur Verfügung gestellte Rechenzeit am National Energy Research Scientific Computing Center, Berkeley unterstützt hat.

Angelo Calci, Sven Binder und *Thomas Krüger* danke ich für die produktive Zusammenarbeit innerhalb des Büros und die aufschlussreichen physikalischen Diskussionen aller Art. Ein besonderer Dank geht an *Sven Binder* und *Angelo Calci* für das sorgfältige Korrekturlesen dieser Arbeit.

Bei der gesamten *TNP++ Arbeitsgruppe* bedanke ich mich für die gute und angenehme Arbeitsatmosphäre.

Der deutschen Forschungsgemeinschaft danke ich für die Unterstützung dieser Arbeit im Rahmen des Sonderforschungsbereichs 634.

Schließlich bedanke ich mich bei meinen Eltern *Elke und Johannes Langhammer* sowie meinem Bruder *Ralph Langhammer* für die Unterstützung während des gesamten Studiums einschließlich der Promotion.

Ein besonders großes Dankeschön geht an *Eva-Maria Christ* für ihr Verständnis, ihre Geduld mit mir und die großartige Unterstützung über die letzten Monate. Ich hoffe wir können einige der in letzter Zeit ausgefallenen Vorhaben bald nachholen.

Lebenslauf

Zur Person

Name	Joachim Langhammer
Geburtstag	01. April 1985
Geburtsort	Groß-Umstadt
Staatsangehörigkeit	deutsch
Eltern	Johannes Langhammer Elke Langhammer, geb. Holschuh

Bildungsweg

1991 - 1995	Lindenfeldschule, Schaafheim/Mosbach Grundschule
1995-1997	Eichwaldschule Schaafheim Förderstufe
1997-2004	Max-Planck Schule, Groß-Umstadt Gymnasium
2004	Abitur
07/2004 - 05/2005	Zivildienst in der Behindertenwerkstatt "Heydenmühle" in Otzberg/Lengfeld
10/2005 - 09/2008	Bachelorstudium Physik, TU Darmstadt
09/2008	Abschluss Bachelor of Science Physik Abschlussnote: mit Auszeichnung bestanden (1.2)
10/2008 - 09/2010	Masterstudium Physik, TU Darmstadt
09/2010	Abschluss Master of Science Physik Abschlussnote: sehr gut (1.16)
seit 10/2010	Promotionsstudium und Anfertigung der Dissertation TU Darmstadt
seit 11/2010	Wissenschaftlicher Mitarbeiter der TU Darmstadt am Institut für Kernphysik

Erklärung zur Eigenständigkeit

Hiermit versichere ich, die vorliegende Dissertation ohne Hilfe Dritter und nur mit den angegebenen Quellen und Hilfsmitteln angefertigt zu haben. Alle Stellen die aus Quellen entnommen wurden sind als solche kenntlich gemacht. Diese Arbeit hat in gleicher oder ähnlicher Form noch keiner Prüfungsbehörde vorgelegen.

Ort

Datum

(Joachim Langhammer)